MILLIMETER ARRAY DESIGN AND DEVELOPMENT PLAN

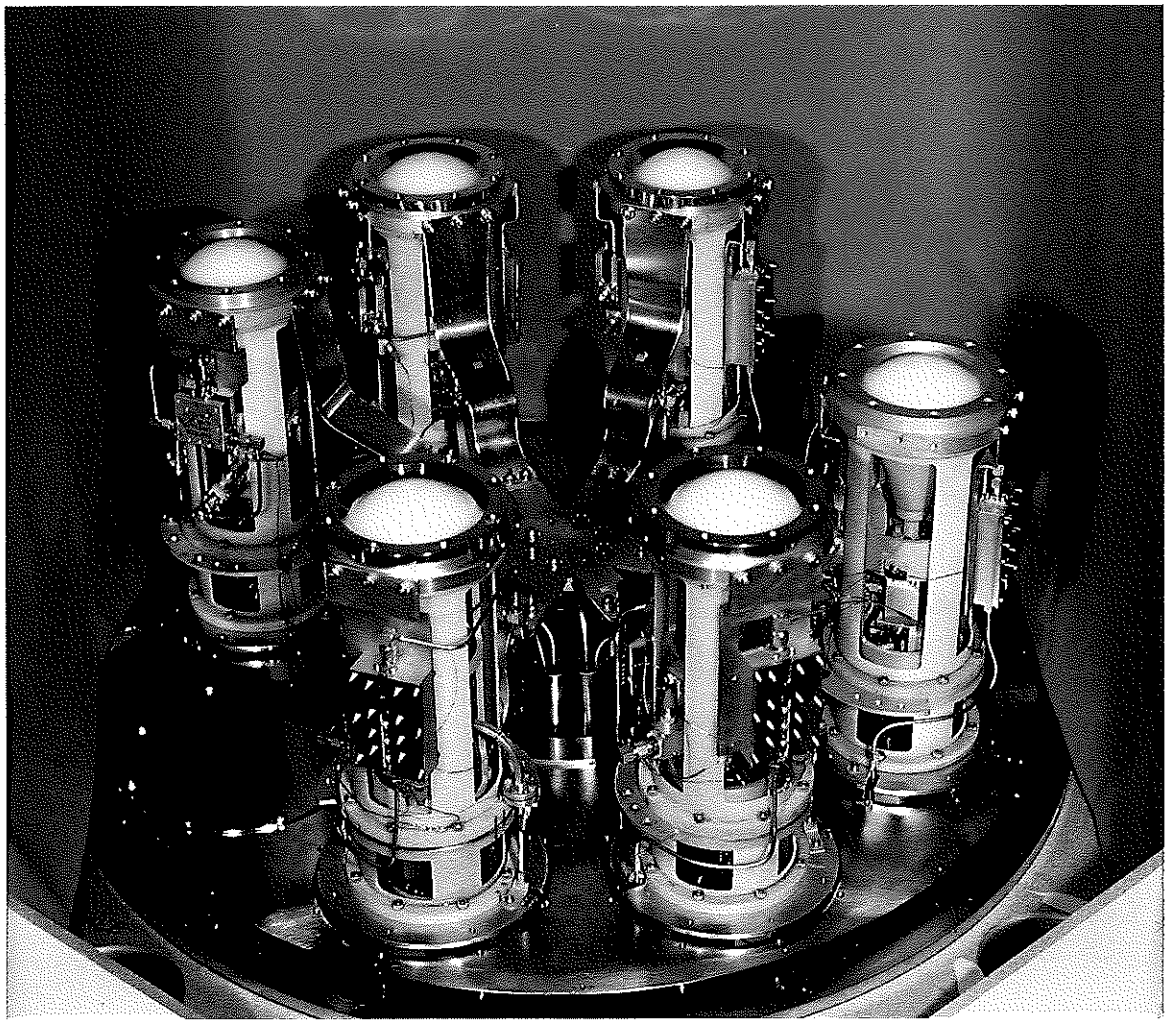

NATIONAL RADIO ASTRONOMY OBSERVATORY

Operated by Associated Universities, Inc., under cooperative agreement with the National Science Foundation.

Millimeter Array
Design and Development Plan

September 1992

National Radio Astronomy Observatory

Cover Illustration: A photograph of the multiband receiver which is currently in use on the NRAO Twelve-Meter Telescope and which will serve as a fiducial design for the packaging of the Millimeter Array receivers. In a single 4-K cryogenic dewar as many as eight receiver inserts can be permanently mounted (six are shown here). Each receiver insert is complete with a focusing lens, feed horn, local-oscillator-injection coupler, mixer, isolator, and intermediate-frequency amplifier. The mixer uses a superconductor–insulator–superconductor (SIS) junction, and the amplifier uses a heterostructure field-effect transistor (HFET) developed at the NRAO.

TABLE OF CONTENTS

CONTENTS

I. INTRODUCTION

The Millimeter Array (MMA) is the first synthesis telescope to be designed as a *complete* imaging instrument, capable of measuring all spatial frequency components of the sky brightness from zero to the longest array baseline. Astronomical images with the highest angular resolution, less than $0\farcs07$, will come from the array in its largest configuration, and will be made using the Fourier-synthesis algorithms that enable the array to simulate an aperture of three-kilometer diameter. Low-resolution images of large regions of the sky will come from a mosaicing mode, using the MMA in its most compact configuration much like a conventional single dish, the MMA antennas rapidly scanning the region to be imaged, in unison. These two capabilities have never been incorporated in a single instrument. The complexity of the sky at millimeter wavelengths and the unique interrelationship of astrophysical phenomena on a wide range of spatial scales that is characteristic of millimeter-wave scientific investigations make the melding of these capabilities a fundamental requirement for the MMA.

In specifying the scientific goals of the MMA, astronomers are calling for an unprecedented combination of sensitivity and angular resolution at short wavelengths, one that will make a wealth of unique astronomical opportunities and new science available for investigation. The MMA realizes these expectations by combining the sensitivity provided by a collecting area equivalent to that of a telescope fifty meters in diameter with an angular resolution superior to the design goals of the Hubble Space Telescope, and operating over a frequency range in which thermal emission processes illuminate the sky. The forty eight-meter antennas of the MMA are transportable. With the antennas spread over a three-kilometer array, astronomers are able to observe in detail the formation of protostars and pre-planetary disks in molecular clouds. With the antennas clumped together in an area no more than seventy meters across, astronomers can observe the chemical evolution in molecular clouds which precedes, or perhaps initiates, star formation. Observations in widely separated frequency bands may be conducted simultaneously in support of studies of molecular excitation, with complete frequency coverage provided in all the atmospheric windows from 9-mm to 0.9-mm wavelength. With forty antennas, the array is sufficiently fast, and the imaging characteristics of such high quality, that the astronomer will be able to see the results and modify the observing program as the observations are being made. The MMA is a unique and powerful instrument.

The burden of designing a powerful and unique instrument is that it requires an extension of existing technology. This is as true for the MMA—with its densely packed mosaicing configuration, broadband sensitive receivers, total-power instrumentation, and precision antennas—as it was for the Keck telescope with its segmented, optical-quality primary mirror, and for the Green Bank Telescope with its unblocked 100-meter aperture and real-time, laser-guided surface metrology. Application of significant technological advances is the *sine qua non* of the design of a forefront scientific instrument.

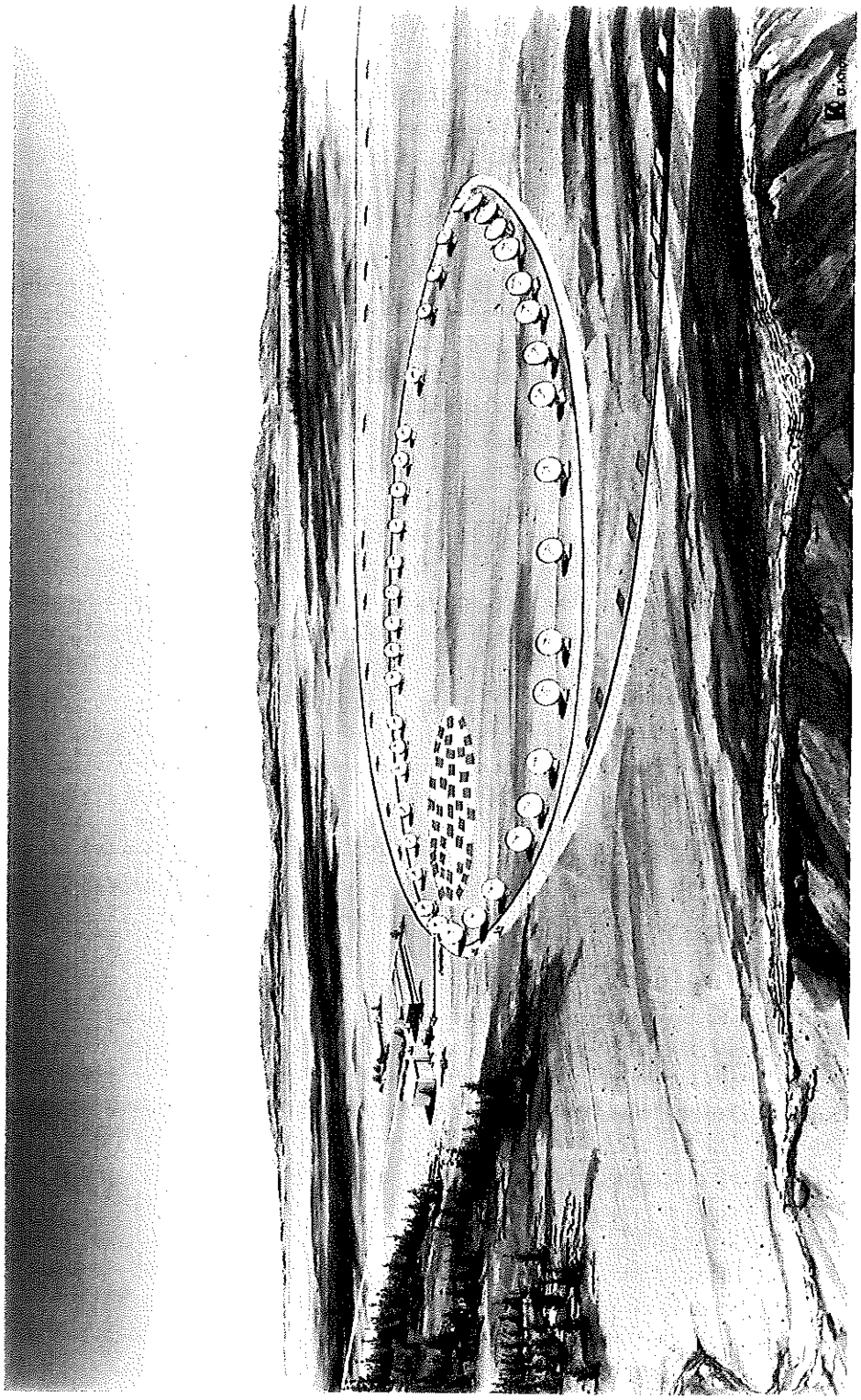

Figure I-1. An artist's concept of the Millimeter Array. The MMA consists of forty eight-meter antennas located on a high-altitude site. The antennas are transportable, giving the array a "zoom-lens" capability. In this drawing the array is shown in one of its largest elliptical configurations, used for high-resolution observations. The antennas may also be moved and packed together on the pad shown on the inside of the ellipse, for wide-field observations.

II. OVERVIEW OF THE MMA DESIGN AND DEVELOPMENT PLAN

Development of the technology needed for astronomical research at short millimeter wavelengths is in large measure defined by two qualitatively different realities: First, the earth's atmosphere has a profound effect on the propagation of millimeter-wave signals and, second, efficient heterodyne detection of such short-wavelength radiation requires high-precision telescope optics and superconducting quantum-effect detectors. The technology development plan for the MMA is a staged approach to deal with these realities. In addition, the MMA as a user facility must accommodate the unique needs of the large number of visiting astronomers who will use the telescope.

The transparency of the earth's atmosphere at millimeter wavelengths varies with altitude, frequency, and time. To make astronomical observations possible during as much of the time and over as much of the frequency range as possible, it is necessary to build the MMA on a high-altitude site above as much of the atmosphere as possible. For this reason, the sites under consideration for the MMA are all above 9,000 feet in elevation. Two sites in the southwestern U.S. have been chosen for extensive study, from a list of fifty potential sites of sufficiently high elevation. All sites in this list except that in the Magdalena Mountains, near Socorro, New Mexico, and the high mesa near Springerville, Arizona, were rejected for reasons of latitude, accessibility, weather conditions, or proximity to environmentally protected areas. The plan to characterize the astronomical quality of these sites and to evaluate them, particularly with respect to environmental impact but also with respect to operational considerations, is given in the next chapter. The schedule leading to the selection and final acquisition of a site is also given there.

Satisfying the MMA requirement for precision optics, implied by the need to observe short-wavelength radiation, is less of a challenge to fundamental design than it is to manufacturing process. Here, development of a transportable eight-meter antenna that will retain a precise figure when fully exposed to the environment is a task eased to a degree by the experience accumulated by university research groups and the interest of several antenna manufacturers. Nevertheless, the needs of the MMA for short-wavelength performance and rapid switching are demanding and must be satisfied by a successful antenna design. Chapter IV discusses the plans for antenna and optics design and development.

The optimum placement of the antennas in the several arrays of the MMA has been studied for the two candidate sites. Configuration design is driven by imaging requirements and performance and is constrained by site topography and transportability of antennas. As site studies and antenna/transporter design proceed, array performance will require continued effort on configuration design.

The MMA is such a fast imaging instrument, particularly in its compact configurations, that many observations can be completed in less than an hour. In any given year many hundreds of astronomers and students will use the MMA for their research. To accommodate a large number of diverse needs, the MMA

software will have to provide the astronomers with a system that is uncommonly flexible, with a real-time display that provides enough information for the astronomer to modify the observations in progress and to supply that information, via computer networks, to the astronomer at his or her home institution.

Finally, the same fluctuating transparency of the atmosphere at millimeter wavelengths that drives the MMA to a high-elevation site makes this part of the spectrum unusable for commercial communications. Consequently, few manufacturers of millimeter-wave instrumentation exist. There is no source of, and as yet no commercial market for, such things as the ultra-low-noise broadband receivers required by the MMA. In collaboration with academic researchers, the MMA devices and ancillary instrumentation will be developed specifically for the MMA as part of this plan. This work will build on the considerable experience at the NRAO and in university groups in millimeter-wavelength electronics. Chapter V presents the extensive development of electronics the MMA requires.

In conducting the design and development program for the MMA, we intend to work closely with university groups through the MMA Joint Development Group (JDG). In each of the areas of the plan the experience and expertise of these groups can be put to effective use. The primary contact between the NRAO and a particular university group is maintained at the working level, between the NRAO engineer and associates responsible for the development in an area and the individuals in a community group that are participating in the effort. Visits, exchanges of technical memoranda, and electronic mail are the means of communication. The current JDG membership and representatives are:

University of California, Berkeley,	W. J. Welch;
Caltech,	J. E. Carlstrom;
University of Illinois,	L. E. Snyder;
University of Maryland,	L. Blitz;
University of Massachusetts,	P. Goldsmith.

To achieve the goals of the *MMA Design and Development Plan*, the following approach will be taken:

- Technical alternatives will be evaluated in detail before a choice is made;
- Prototypes will be constructed and thoroughly tested, so that reliability and functionality can be assessed. This includes both hardware and software prototypes;
- A single-baseline set of electronics will be constructed and tests will be made over a range of environmental conditions;
- A prototype antenna will be designed and constructed so that the special demands of MMA operations can be evaluated and the antenna design refined;
- Prototype software will be made available to users at an early stage so that it can evolve in response to informed criticism.

The *MMA Design and Development Plan* presents a four-year program, 1993–1996, to complete the specific tasks detailed in the sections that follow, anticipating the start of array construction in 1997.

III. SITE

1. Atmospheric Studies

During the last three years we have studied the transparency and stability of the earth's atmosphere at potential MMA sites using 225-GHz tipping radiometers built for this purpose. As detailed in the *MMA Proposal*, there are three potential continental sites for the MMA, one in the Magdalena Mountains of New Mexico, another near Springerville, Arizona, and one near Alpine, Arizona. The radiometer studies were made at the Magdalena Mts. and Springerville sites. In addition, we studied the atmospheric properties from a location adjacent to the Caltech Submillimeter Observatory (CSO) at the summit of Mauna Kea, on the island of Hawaii.

For a common ten-month period in 1990–1991, we measured the atmospheric properties at three places: the New Mexico site, the Springerville site, and Mauna Kea. Measurements of the zenith opacity were made every ten minutes during four-hour periods by scanning the radiometers in zenith angle from one to three airmasses. Every fifth hour the 225-GHz radiometers were directed toward the zenith, and total-power data were sampled in 3.5-second intervals for the hour. After the fact, the fluctuations in the total-power data for time lags between 3.5 and 900 seconds were computed as a means of assessing the stability of the atmosphere.

Figure III-1 is one summary of the atmospheric 225-GHz zenith opacity on each of the three sites, as a function of time of year. The complete body of data may be found in MMA Memorandum No. 79 (see Appendix).

The interpretation of these data in terms of the potential imaging performance of the MMA is an involved task; the first steps in this direction are found in MMA Memoranda Nos. 68, 84, and 88 (see Appendix). The first goal of the interpretation is, of course, to help in the site-selection process. A longer-term goal is to define needed observing techniques and to assess the effect of specific MMA hardware options on the imaging performance of the array (see MMA Memo. Nos. 84 and 86).

2. Environmental Impact Studies

One of the criteria we intend to use in the site-selection process is an assessment of the potential effect of the MMA, and its operation, on each of the sites. The procedure to be followed involves performance of an Environmental Impact Survey (EIS). The format and general content of the EIS is specified in the Code of Federal Regulations 40, paragraphs 1500–1508, supplemented by other applicable laws. For the candidate MMA sites on land administered by the U.S. Forest Service, specific guidance for the EIS will be provided by the Forest Service and the National Science Foundation (NSF).

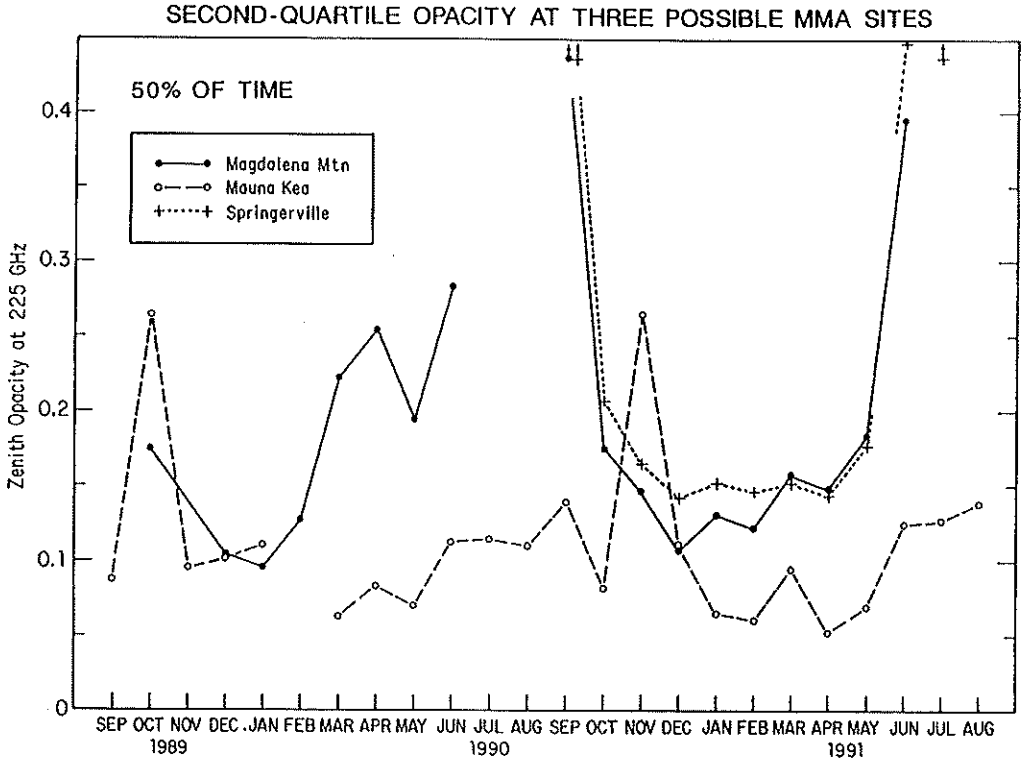

Figure III-1. Atmospheric opacity data, obtained with the 225-GHz tipping radiometers, from three candidate MMA sites. The measured zenith opacity was less than the value indicated for one-half of the time.

The Millimeter Array EIS work will be done under contract and will include, but not be limited to, the following tasks:

(1) Preparation of a Notice of Intent;
(2) Preparation of a Purpose and Need for Action;
(3) Conduct public scoping meetings;
(4) Site survey and determination of field locations;
(5) Site biology assessment;
(6) Geology, hydrology, and sanitary sewer assessment;
(7) Air quality assessment;
(8) Noise and vibration assessment;
(9) Energy use and natural resources assessment;
(10) Occupational safety and health assessment;
(11) Hazardous waste and toxic materials assessment;
(12) Cultural resources management assessment;
(13) Socio-economic assessment;
(14) Preparation of a final EIS report.

The EIS information we compile will be advisory to the NSF.

3. Use Plan

Once it has been determined which site is most satisfactory, but prior to completion of the EIS process, it will be necessary to define in some detail how

the site would be used. Specific information will be needed on where roads would be constructed, how runoff water would be channeled, where culverts would be needed, the location of power cables serving the site, the sizes of buildings and means of access to all buildings, and so forth. Much of this particular information is needed for the EIS process.

Other specific conditions of the site pertain to the ways in which the site can be used for array operations. For example, prototype antenna panels will be crudely assembled in a variety of orientations for ice-loading tests. Wind statistics will be compiled at several locations on the site so that we can have an idea of the patterns of airflow across the site. Snow-cover statistics on the road locations will aid design of the transporter and yield specific information on how frequently the array might be reconfigured in the winter months.

4. Operational Considerations

The mode and cost of MMA operations at each of the candidate sites are other considerations on which the site decision will be based. From experience at the Very Large Array (VLA), the Berkeley–Illinois–Maryland Array (BIMA), the Owens Valley Radio Observatory (OVRO), and elsewhere, it is clear that it will be advantageous to locate the array control center and the astronomers at a conveniently accessible site. An instrument at a remote site can be operated by a modest-sized technical staff who commute daily, or in some cases less frequently, to the array site. The commute is an overhead that is inevitable for the individuals who maintain the array. But it is an overhead that is not necessary for the professional staff who build the next generation of instruments or who deal principally with the observational data. The data can easily be transmitted via networks to a location convenient for nearly all of the professional staff.

Efficient operation of the MMA therefore introduces multiple sites for the array, one for the instrument and one or more for the professional research staff. The astronomers who use the array may find it necessary to be at the array control center, or they may be prepared to use the MMA via networks from their home institutions. All these modes need to be accommodated, and they bring with them somewhat different operations costs, complexities, and possibilities at each of the possible MMA sites.

Finally, each of the candidate sites must be evaluated for considerations such as the cost of electric power, quality of schools, availability of spousal employment opportunities, access to transportation services, cost of employee housing, and so forth. All these factors will be evaluated as part of the MMA site-selection process.

5. Site-Selection Process and Schedule

The information—scientific, atmospheric, operational, and environmental—on which the site selection will be based will be available in a preliminary form in the spring of 1993. At that time it will be reviewed by the MMA Advisory Committee, and the comments of this committee will be used as one guide for further site-evaluation work. After a subsequent period of approximately six months, the committee will meet again, in the expectation that a site recommendation can be made at that time.

Site-Selection Schedule
(Tentative)

2/92 (Continuing)	Environmental Inventory Site Biology Assessment Site Survey and Determination of Field Locations
5/92 – 3/93	Operations Cost Comparisons Staffing Options Power and Communications Roads and Snow Removal Reconfiguration Frequency
1/92 (Continuing)	Imaging Studies: Site Limitations Atmospheric Transparency Atmospheric Stability Mosaicing
11/92 – 3/93	Community Evaluation Housing Schools Transportation Spousal Employment Medical Services
3/93 (approx.)	Site Review: Preliminary Analysis
3/93 (Continuing)	Environmental Impact Studies
9/93 (approx.)	Site Review: Priority Recommendations
1/94 (approx.)	Site Priority Announcement

IV. ARRAY

1. Antenna

The principal scientific specification of the MMA antenna is that it achieve and maintain an rms surface accuracy of 25 microns, together with an rms pointing accuracy of order one-twentieth of the antenna primary beamwidth, so that fast, precision imaging is possible at frequencies as high as 350 GHz. The principal operational specifications of the MMA antenna are that it be reliable, easy to maintain, and that it provide a stable environment in which receivers may be conveniently mounted, replaced, and maintained. The *MMA Proposal* outlines a conceptual design for an antenna with coudé optics, a design which emphasizes a commodious and stable receiver cabin. But there are disadvantages to this approach, the most serious of which is the requirement for a large secondary mirror which may be difficult to nutate. We will re-evaluate the antenna optical design, comparing the coudé system to a more conventional Cassegrainian system, as part of the *MMA Design and Development Plan.*

A second consideration that serves to define the specifications of the MMA antenna is the recognition that, as a facility serving the broad astronomical community, the MMA will be heavily oversubscribed. If we are to make as much observing time as possible available to users, the MMA must perform within specifications at all times of the day and night, including those times of rapid temperature change which occur on a clear, exposed site at dawn and dusk. Moreover, since the capability to observe the sun is a primary scientific specification for the MMA, special care must be taken with the design to allow precision operation during and after pointing at the sun. Control of the antenna distortions introduced by thermal changes or gradients becomes therefore a major operational design goal for the MMA antenna. The design options to be considered are summarized below and are described in detail in MMA Memorandum No. 83 (see Appendix).

The antenna design will proceed in three partially overlapping stages:

(1) Finite-element models of structural designs for the antenna as a whole, and for its constituent parts, will be generated with computer-aided-design-and-analysis tools (such as the MacNeal–Schwendler Corp.'s NASTRAN program). Competitive designs using either steel or carbon-fiber-reinforced-plastic (CFRP) members for the backup structure of the primary mirror will be compared numerically, in the presence of imposed thermal gradients and gravitational distortions. A separation will be made between the gross thermal effects with long time scales, which lead to changes in focus or pointing and can be eliminated by astronomical calibration, and the residual thermal distortions.

(2) Temperature gradients will be measured on existing antennas. Although it is relatively easy to compute the effect that a given

temperature distribution has on the structure, it is very difficult to predict what the actual temperature distribution will be, particularly on scales small compared to the aperture diameter. These small-scale inhomogeneities will impose the ultimate limit on thermal performance. To resolve these questions, and to determine the appropriate input for the computer analysis of the MMA antenna thermal distortion, we will collaborate on the instrumentation of one of the new BIMA antennas with an assemblage of thermistors. Temperature differences and time scales will be evaluated over the varying conditions to which the antenna is exposed. An infrared (IR) camera will be used to photograph the antenna, in order to assess the effects of heating due to the telescope electronics and cryogenic compressor. This work will be done under the auspices of the MMA Joint Development Group.

(3) Based on the design and materials choice made from the above modeling and measurements, a prototype MMA antenna will be built under contract.

The prototype antenna, assembled on a site convenient for testing, will be thoroughly evaluated to verify that it meets the MMA specifications and that its performance agrees with that expected from the computer modeling. In addition, the prototype antenna will allow us to assess:

- Optical design, and the performance of secondary-mirror nutation;
- Mount and servo performance, particularly with regard to the rapid switching required (see Section 6);
- Receiver interface, including receiver-selection optics, electronics support, and cryogenics support;
- Antenna thermal behavior;
- Potential problems in mass production;
- Computer system: hardware and software;
- Pointing instrumentation: laser rangers, quadrant detectors, tiltmeters, thermal monitors, etc.

2. Antenna Transporters

The MMA antennas will be moved each time that the array is reconfigured to change its resolving power. This will occur on time scales of, typically, a month or two, in response to changing atmospheric conditions and the accumulated pressure of proposals for observing time. The antennas will be moved by specialized motorized carriers ("transporters") that will pick up an antenna, move it to a new foundation, and place it in the proper location with the proper orientation. The time required for a typical reconfiguration of the array should not exceed one or two working days. If the average time required for transport of a single antenna during reconfiguration is between approximately one-half hour and one hour, this would necessitate the acquisition of three transporters. The transporters must be:

- Highly maneuverable, to work in and around antennas in the compact configuration;

- Able to traverse safely the grades on the site along the improved site roads;
- Able to function over the conditions that prevail on the site year round.

The design of the transporters is, of course, closely meshed with the design of the antennas, and it is equally, but less obviously, dependent on the site selected. If a rocky site of irregular terrain is chosen, the transporters may need to be tracked vehicles; if a site on open pastureland such as Springerville is chosen, the transporters then could be rubber-tired vehicles. The detailed transporter design needs to be done in phase with the antenna design, recognizing that a wide antenna pedestal is desirable for reasons of stability, but that a more compact structure would be easier to transport. Solid estimates of the width and weight of the antenna, and the width of the transporter, are needed in 1993 so that the requirements for site roads can be defined in sufficient detail for the environmental impact study.

3. Imaging Studies

Ultimately, when all the parts are assembled, the Millimeter Array is an imaging instrument. This means that, in large measure or small, all constituent parts of the array affect the capability of the instrument to make images. When designs are chosen or changed the effect of these actions needs to be assessed. Conveniently this can be done with a computer model of the array that can simulate the imaging performance of the array as it "observes" a model astronomical source. As hardware selections are made or altered the new decisions can be incorporated in the model array and their effect on the images produced can be evaluated. The imaging studies have played a crucial role in the specification of the MMA as described in the *MMA Proposal.* That role must now be expanded in the *MMA Design and Development Plan.*

The MMA imaging studies most needed in the next four years include the following:

(1) *Support for the antenna design work.* Specifications on the antenna are driven in part by the imaging performance needed for the array. As the antenna design progresses we will evaluate the effect of the actual antenna sidelobe pattern on image fidelity and assist the antenna engineering group in setting specifications for such things as acceptable edge tapers, panel gaps, and accuracy of pointing.

(2) *Analysis of the optical design.* As described in the *MMA Proposal,* the MMA makes wide-field images by combining data from rapidly sampled total-power and interferometric mosaic observations. Design of the total-power secondary beam switcher, and the observing technique to support its use, will be a cooperative venture between the imaging group and the antenna design engineers.

(3) *Phase and phase-fluctuation calibration.* Millimeter Array Memorandum No. 84 (see Appendix) outlines the need for us to understand the relationship between the atmospheric phase structure function and the structure function of the calibrated phase if we

are to be in a position to analyze the efficacy of different calibration schemes. This work needs to be extended. Among the calibration schemes that need to be considered in detail are extremely rapid switching between source and calibrator, nutating the subreflector between calibrator and source, simultaneous observations of source and calibrator, phase extrapolation from low to high frequencies, and self-calibration. The ramifications of these studies extend from input to the site-selection process to specification on the antenna and hardware design.

4. Configuration

The MMA has three extended configurations—conceptually, ellipses with nonredundant spacings (see the *MMA Proposal*)—and two closely packed configurations. The imaging performance of each of these configurations needs to be optimized. For the large configurations the optimization for antenna placement involves both the fidelity of MMA images over the full range of source declinations and cognizance of the actual site topography. For the smaller, packed, configurations the optimization for antenna placement involves matching the u-v coverage over a range of hour angles (beneficial for mosaicing applications), and cognizance of the actual antenna design and the resulting physical-space requirement for each antenna. These latter studies feed back to the antenna design and hence should be done in parallel with the antenna design.

5. Control

The software system used to control the MMA will differ significantly, in some of its architectural aspects, from the control systems used for the other large U.S. arrays: the Very Large Array (VLA) and the Very Long Baseline Array (VLBA). The differences stem from both the nature of the MMA hardware and the novel ways in which the MMA will be used in astronomical observations.

In the compact configurations the MMA will be used to image large regions of the sky: entire molecular clouds, nearby galaxies, and the solar disk, for example. These are regions very much larger, in angular size, than the primary beams of the MMA eight-meter antennas. In order to recover all the Fourier components of the emission from such large sources, the MMA will rapidly and repeatedly scan across the source, collecting total-power data from each antenna and cross-power data from all pairs of antennas. The resulting mosaic image will be a Fourier combination of all these data. The control system must not only drive the array antennas but also separate total-power data from interferometric data, keep track of where the array is pointed instant by instant, and adjust the phase center accordingly. When taking data in a mosaicing observation, time spent "setting up" the computer or correlator—as is usually done in array observations—cannot be tolerated for the MMA. Instead, the data will have to be corrected in real time for errors introduced in this demanding observing mode.

In the largest array configuration the interferometric phase fluctuations will be overwhelmingly dominated by fluctuations in the atmospheric phase. Techniques to do effective phase calibration on long baselines is the subject of MMA

Memorandum No. 84 (see Appendix). All these techniques require observations of two sources: the program source and a nearby calibrator. The array, or part of it, must either look at both sources continuously and simultaneously or switch rapidly between the two sources. It may even be desirable to observe the program source at one frequency and the calibrator at another, lower, frequency where the beams are larger and the calibration sources are stronger. These techniques strongly influence the design of the antenna and its optics, and they have a significant impact on the design of the array-control software. The control system must disentangle the time streams of data, determine phase corrections from the calibrator observations, and apply them in real time to the observations of the program source. Design of such a system needs to be done carefully.

Finally, astronomers will sometimes want to divide the forty array antennas into two or more sub-arrays in order to observe a source in different ways simultaneously. An important limiting case is to divide the array into forty sub-arrays: that is, use each antenna as a separate radio telescope. Since each antenna is instrumented as a complete single dish, the forty antennas can be used to observe the same source and the forty autocorrelation spectra be combined into a single spectrum, or the forty antennas can be pointed individually to map an enormous region of sky. In either case, the control system should easily accommodate whatever flexibility the astronomer requires.

6. Data Analysis and Display

The MMA control system will be designed with the capability to calibrate the data continuously as they are taken, whether the array is in its compact mosaicing configuration or an extended, high-resolution configuration. The control system will, if necessary, apply the first-pass calibration, or else pass the needed information along to the data-analysis systems, wherever required (at the MMA site, a remote NRAO site, or the user's home institution). This will be achieved by high-bandwidth networking between the control system and the on-site analysis computers, which in turn will be linked to remote sites by the Internet network (or some successor to Internet). The astronomer will be able to manipulate, analyze, and display the data as they are accumulated. Moreover, because the instantaneous u-v coverage of the MMA will be so complete and because even in the mosaicing mode the entire region to be imaged can be rapidly and repeatedly scanned, the astronomer will be able to watch the full image of the sky emerge from the background with increasing clarity as the data are accumulated. This capability of the MMA has no parallel in existing instruments, and hence much of the software needed to implement it does not yet exist.

The development of software for the MMA will occur as part of two major ongoing efforts. One is an effort, between NRAO and the JDG university partners, to develop real-time imaging systems for use at the Berkeley–Illinois–Maryland Array (BIMA), the Owens Valley Radio Observatory (OVRO), the NRAO 12-Meter Telescope, the VLA, and the GBT. However, the principal activity in display and analysis software is the international collaborative effort to develop AIPS++, a highly improved successor to AIPS. The AIPS++ effort, begun at the end of 1991 by a consortium of institutions from the U.S.,

Australia, the U.K., the Netherlands, Canada, and India, is a modern object-oriented software project which ought to result in a system with a high degree of extensibility and ease of programmability. Approximately one-half of the support for the project is coming from NRAO, and the remaining effort is from the other members of the consortium. Representation of the interests of the millimeter-wave radio-astronomy community is assured by the involvement of NRAO and BIMA in the AIPS++ consortium, as well as by the planned development for instruments such as the James Clerk Maxwell Telescope (JCMT). Representation of the MMA-specific needs will be achieved by an AIPS++ programming group supported by the MMA design and development project. The initial design for AIPS++, which will not be completed until the end of 1992, has already been heavily influenced by the demanding requirements imposed by the MMA's mosaicing mode; this in fact has served as a major focus in the design effort. Since AIPS++ is expected to supersede the AIPS data-processing system sometime in the 1994–1995 time period, the timing of its development is in excellent harmony with our needs for MMA-specific software.

V. MMA ELECTRONICS

1. The Receiving System

Figure V-1 (the fold-out insert between pp. 16 and 17) shows a block diagram of a possible system of electronic interconnection between the antennas and the correlator, representing a current conceptual design. Except for components required for single-dish operation of each antenna, this system satisfies all the requirements outlined in the *MMA Proposal.* However, there are alternative ways in which the receiving system could be assembled (see MMA Memo. No. 71), and Figure V-1 is intended mainly as an example for discussion. Bandpass filters which define the frequency responses are indicated by the symbol "BPF", followed by center-frequency/bandwidth or by the band-edge frequencies. For simplicity, amplifiers in the later intermediate-frequency (IF) stages have been omitted from the diagram. An overview of the electronics system is given in this section; detailed discussion follows in Sections 2 through 8.

1.1. Paths of the Received Signals. Shown at the top left in Figure V-1 is a typical receiver front end, which incorporates a superconducting tunnel-junction mixer circuit (using Superconductor–Insulator–Superconductor—SIS—junctions). There will be approximately six such units to cover a like number of frequency bands in the 130–183-GHz and 195–360-GHz ranges. The details of the quasi-optical package that separates the two polarized components and injects the local-oscillator (LO) signals are not shown. They will depend upon whether linear or circular polarization is required. The SIS mixers are followed by Heterostructure Field-Effect Transistor (HFET) amplifiers with passbands extending from 3 to 4 GHz. This first IF is chosen to provide as large a separation as possible between the sidebands without degrading the system noise temperature. The local oscillator must be tunable in steps of approximately 0.25 GHz so that any desired spectral feature can be converted to appear within the 1-GHz bandwidth of the first IF.

Directly below the SIS front end in Figure V-1 is a typical HFET front end. The feed horn is connected directly to a polarizer in circular waveguide that has outputs for opposite circular polarizations. These go to HFET amplifiers cooled to 15 K. The bandwidths of the amplifiers range between 10 and 15 GHz for the various bands in the 40- to 115-GHz range. The signals are converted down to a first IF that extends from 5 to 20 GHz—i.e., that covers the full HFET amplifier bandwidth. At these frequencies, switches can be introduced to allow selection of any of the five HFET front ends. From the IF band it is then necessary to select bands 1-GHz wide for further processing. Since the bandwidth is wide (15 GHz), provision is made for selection of two independently tunable, 1-GHz-wide bands, from each polarization, to cover different spectral lines. To select a 1-GHz-wide band from the 5–20-GHz band the signal is converted to a second IF which is centered at a frequency greater than 8 GHz to avoid having both the signal and image bands fall within the 15-GHz-wide band at the second mixer.

Also the second IF must not lie within the 5–20-GHz band, or else signals would propagate through the mixer without frequency conversion. Thus the second IF in the diagram is chosen to extend from 24 to 25 GHz. The local oscillator must tune from 30 to 45 GHz in steps of about 0.25 GHz to allow any spectral feature to be selected. After filtering, the signal is converted down to the 3–4-GHz band with a fixed LO of 21 GHz. At this point the outputs from all of the front ends have been reduced to the 3–4-GHz IF band and are brought to a switching network. This network contains switches and power dividers that allow four outputs on the right-hand side in the diagram to be connected to any four of the IF signals at the inputs.

The microwave optics that bring the signals into the feed horns will provide for simultaneous reception in certain pairs of front-end bands, which have not yet been determined. The four outputs from the switching network allow for processing of signals of both polarizations in two frequency bands, or in one frequency band in the case of the HFET front ends. For spectral-line observations the widths of the bands to be processed will depend upon the required frequency resolution. Thus from each of the four signals a band of width variable by factors of two, from 500 MHz on down, is selected. This provides for a maximum total input bandwidth for spectral processing of 2 GHz, which is expected to be about the limit imposed by the capacity of the correlator. The variable-bandwidth channels must be tunable across the 3–4-GHz IF band in small enough steps to allow any desired frequency to be accepted, and in Figure V-1 this is achieved by frequency conversion from 3–4 GHz to 1–2 GHz with an oscillator that is tunable from 4.5 to 5.5 GHz in steps of 20 kHz. The signal then goes to a sideband-separating mixer (i.e., a single-sideband mixer). The output from one sideband of each mixer goes to a baseband (lowpass) amplifier with a cutoff frequency that is variable in the required steps outlined above. The output from the other sideband goes to a baseband amplifier with a fixed 500-MHz lowpass response that can be used to provide increased bandwidth for continuum observations. Since the signal frequencies accepted by the two sidebands cannot be independently tuned, there is little to be gained by making the amplifiers for both sidebands variable in bandwidth for spectral-line observing.

The eight filtered outputs from the four sideband-separating mixers are sampled at a clock rate of 1 GHz, corresponding to the Nyquist rate for a 500-MHz bandwidth, and quantized with a maximum of two bits per sample. Redundant samples can be deleted if desired. The maximum total data rate is 16 Gbit/s. These digital signals are transmitted to the correlator building by means of optical-fiber links. Before the processing in the correlator the timings of the data streams from different antennas must be equalized. This is to compensate for the different geometrical path lengths of the incoming wavefront to different antennas (which vary with time) and the different path lengths of the optical fibers from the antennas to the correlator building (which are fixed). The compensating delays can be implemented electronically by storing the data in digital memory and reading out as required. However, the total electronic memory required can be reduced by performing a few of the longer delay steps in optical fibers switched in and out of the links from the antennas. Thus at the

right-hand end of the signal paths in Figure V-1 both fiber-optic and electronic (digital) delays are shown. The relative amounts of delay implemented by each of these two methods will depend mainly upon the cost of the hardware involved.

The design of the signal paths shown in Figure V-1 involves a number of choices of bandwidths and numbers of signal channels that are somewhat arbitrary, but which have been chosen to match the capacity of the system described in the *MMA Proposal.* The processed bandwidth could be increased by increasing the number of output channels from the switching network to more than four, or by increasing the baseband bandwidths from 500 MHz to 1 GHz. The 500-MHz bandwidth is used in Figure V-1 because, at this time, the required sampling frequency is more easily achievable than is the case for a 1-GHz bandwidth. Testing of some fast samplers will be a necessary part of system development.

1.2. Local Oscillators. The local oscillators at each antenna must be synchronized to a master oscillator system at the correlator building. This is achieved by transmitting reference frequencies to the antennas. In the lower right-hand corner of Figure V-1 the required reference frequencies and timing signals are generated from the output of a frequency standard, and are transmitted by optical-fiber links to each of the antennas. The frequency of 1 GHz, which is multiplied in frequency at the antennas to phase-lock the first LO signals, imposes the most stringent requirements on phase stability. The stability of the outgoing link to the antennas is constantly monitored by returning a component of the 1 GHz to the correlator building and measuring the phase over this round-trip path to each antenna.

At the bottom center of Figure V-1 are two LO units. The fine-tuning LO is tunable over the range 4.5 to 5.5 GHz in 20-kHz steps. This step in frequency is much less than the narrowest baseband filter in the signal channels and so provides sufficient tunability. If the four signal channels are always used in pairs to receive signals with the same frequency and opposite polarization, then only two of the fine-tuning units are required. For greater flexibility, four per antenna could be provided to allow independent fine tuning in each channel. The high-frequency LO unit contains a YIG-tuned oscillator that covers the range 30–45 GHz. A doubler and a tripler are also included to provide a total output range of 30–135 GHz. These units provide both the first and second LO signals for the HFET front-end bands. Other units of this type provide the drive for the LOs in the range 135–360 GHz that are used with the SIS front ends. A total of approximately six of these units would probably be required at each antenna.

In addition to the fine tuning there are two other features that are introduced through the local oscillators. These are phase switching and fringe stopping. Phase switching by $\pi/2$ is required at the first LO for the SIS front ends to enable the sidebands to be separated after correlation. In addition, phase switching by π is required to eliminate DC offsets in the samplers. Thus phase changes of $\pm\pi/2$ and $\pm\pi$ are injected into the first LOs in Walsh-function sequences. The frequency offsets required for fringe stopping can conveniently be introduced at the 1.5-GHz LO as shown in Figure V-1. Although this oscillator should not be widely tunable, to prevent degradation of the sideband separation at the mixer, the offsets for fringe stopping are too small (< 300 Hz)

to have a deleterious effect. (Note that observing in a double-sideband mode would require fringe stopping at the first LO and further offsets at other LOs.)

There are several ways in which it may be possible to simplify the system in Figure V-1. The most interesting idea is outlined in MMA Memorandum No. 85 (see Appendix), which suggests performing all of the signal filtering required for spectral resolution (i.e., the variable baseband filtering) by digital hardware at the correlator location. This would simplify the baseband stages, and the need for tunability in steps finer than about 500 MHz at the antennas would be eliminated. The fine-tuning LO units would not be needed and the number of frequency conversions per channel could be reduced. It would also be possible to perform the fringe rotation digitally, and thus eliminate the analog fringe rotators in the 1.5-GHz LOs in Figure V-1. As well as simplifying the electronic system at the antennas, performing more of the filtering digitally would simplify calibration of the frequency responses of the signal channels since the response of digital logic is more precisely predictable than that of analog circuitry. All of these possibilities are very much more feasible if a correlator of FX type (Fourier transformation first, followed by cross multiplication) rather than a lag (XF) correlator is used. Since the correlator design will not be chosen until a detailed study is completed, the suggested simplifications are not included in Figure V-1. In the case where the fine tuning must remain at the antenna, it may be possible to incorporate it into the high-frequency oscillator units, and again eliminate the special fine-tuning LO units and one of the frequency conversions in each channel. The potential difficulty with this idea is that phase noise that may be introduced in implementation of the fine tuning is enhanced by the frequency multiplication required to attain the high LO frequencies for the first LOs. Measurements on a prototype unit are required to determine whether this would indeed be a problem.

The ability to design the system in modular units, and the desirability of minimizing the number of different types of units, are important factors in consideration of ease of construction and maintainability. The use of identical parallel signal channels in Figure V-1 lends itself to the modular approach. The use of just two different types of modules for the tunable LOs, possibly reducible to only one, also results from a desire for modularity.

2. SIS Mixers

2.1. Design Considerations. In the interests of reliability, it is planned that the SIS mixers used on the MMA should have no mechanical tuning adjustments. To achieve the necessary frequency coverage, integrated-circuit mixers must be used, which will require a considerable development effort. Present indications are that $\geq$ 30% bandwidth should be possible. The approach will be similar to one which has been proposed by Kerr *et al.*[1] Using this approach, we have recently obtained encouraging results over the 200–300-GHz band;[2] see

[1] A. R. Kerr, S.-K. Pan, S. Whiteley, M. Radparvar, and S. Faris, "A Fully Integrated SIS Mixer for 75–110 GHz", *IEEE Int. Microwave Symp. Digest*, pp. 851–854, May 1990.

[2] A. R. Kerr, S.-K. Pan, A. W. Lichtenberger, and D. M. Lea, "Progress on Tunerless SIS Mixers for the 200–300 GHz Band", to appear in *IEEE Microwave & Guided Wave Lett.*, 1992; also MMA Memo. No. 87 (see Appendix).

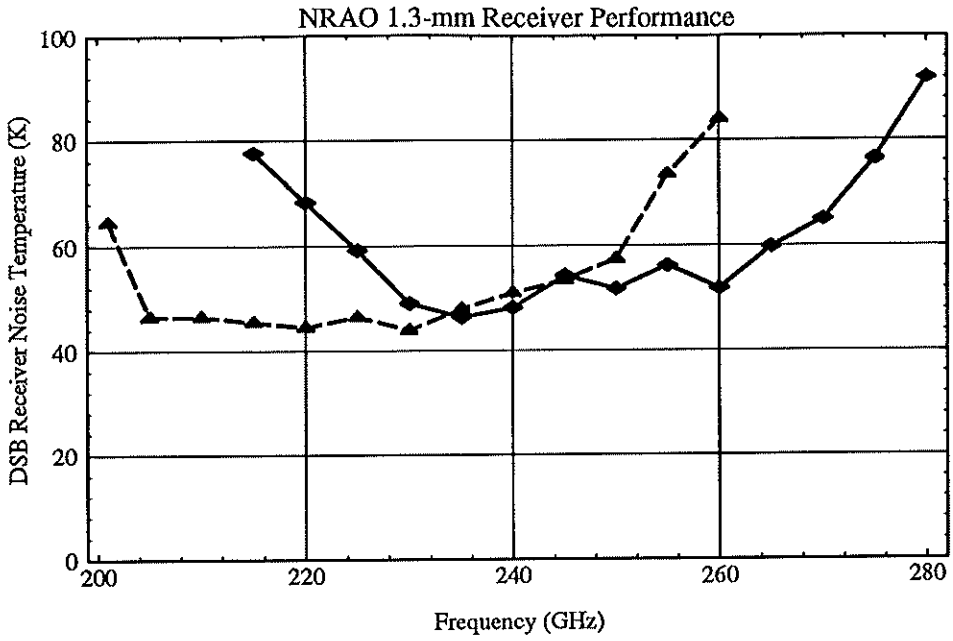

Figure V-2. Receiver noise temperature using an integrated SIS mixer designed at NRAO and fabricated with U. Va. junctions [2]. The dashed curve corresponds to a design that incorporates two tuners. The solid curve corresponds to a tunerless design.

Figure V-2. We propose to develop a range of such tunerless SIS mixers to cover all atmospheric windows up to 366 GHz.

At present the number of frequency bands for which SIS front ends will be required is not certain. This number will depend on the success of two parallel MMA development efforts: (i) transistor amplifiers for 68–90 and 90–115 GHz, which will determine whether SIS front ends will be needed for those bands, and (ii) development of broadband SIS mixers, which will determine the number of mixers needed to cover the 130–183-GHz and 195–314-GHz bands. For these (and other) reasons, it seems wise to concentrate our initial SIS development efforts on the 195–314-GHz bands, then the 330–366-GHz band, and finally the low-frequency bands.

The University of Virginia SIS facility, under Arthur Lichtenberger, appears well suited for fabricating the Nb/Al-Al_2O_3/Nb junctions needed for the MMA. Initially, much of the MMA mixer-development work will fall within the research category, but after one or two years it will be necessary to freeze some of the procedures and establish, on a small scale, a production line to make final mixers for the MMA. In the latter phase of the plan, however, some research work will continue, with emphasis on developing wider-bandwidth integrated mixers, balanced integrated mixers, and image-separation mixers. Developing the needed mixers over a time period of four years will cost about \$300k/yr. In addition, the SIS fabrication facility will require two major items of equipment early in the project, costing a total of \$320k.

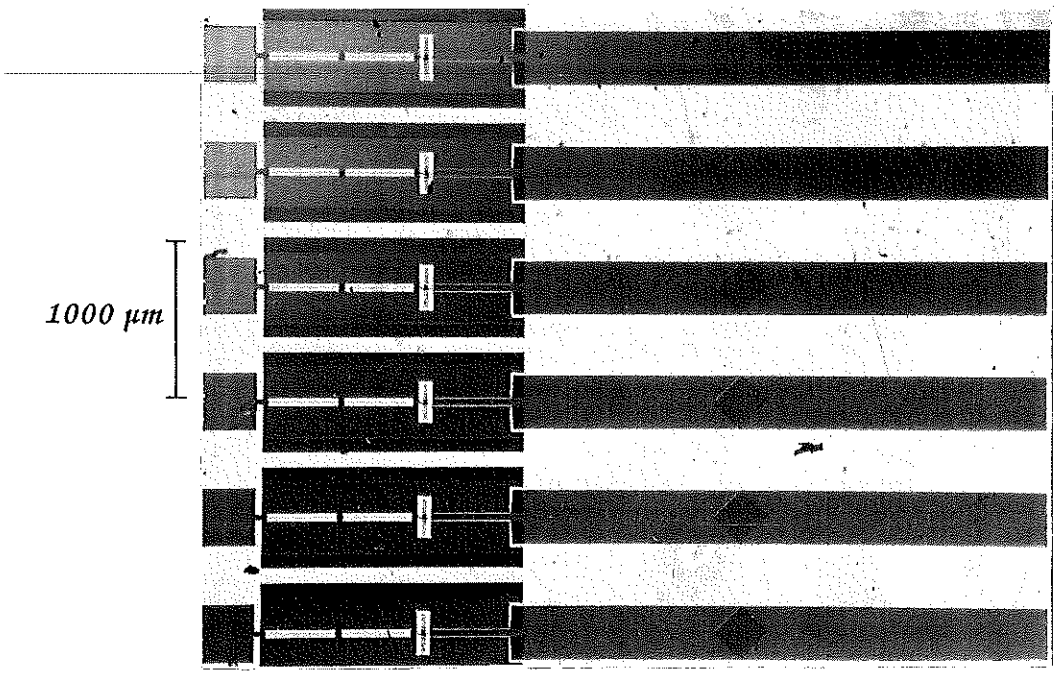

Figure V-3. A view of six fully-integrated 100-GHz SIS mixer circuits on a quartz wafer, prior to cutting. Radiation is coupled from a waveguide (not shown) into the suspended stripline at the right. A transition to coplanar transmission line is visible to the left of center. [Circuit design by A. R. Kerr and S.-K. Pan of NRAO; fabrication by S. Whiteley and M. Radparvar of Hypres, Inc., 1988.]

A microphotograph of six SIS mixer circuits, fabricated upon a quartz substrate, is shown in Figure V-3. Figures V-4 and V-5 show these circuits in finer detail.

2.2. Mixer Development. As stated above, mixer-development work will concentrate initially on the 195–314-GHz range, with concentration on the 130–183-GHz and 330–366-GHz ranges in the final two years. Lower-frequency mixers (68–115 GHz) will be developed only if problems arise with HFET amplifiers for these bands. Development will involve assembly and testing of at least four mixers for each frequency band to provide systems for two antennas, receiving on both polarizations.

We have found that the low end of the useful frequency band of our tunerless SIS mixers in the 200–300-GHz band is limited by an apparent instability in the division of bias voltage between the individual junctions. If we are to make mixers covering a whole waveguide band, it is important to understand this phenomenon and devise a way to avoid it. The analysis of a series array of SIS junctions under the influence of a (large amplitude) local-oscillator signal is a complex nonlinear problem. To date, all analysis of SIS mixers using series arrays of junctions has assumed that all junctions in the array behave identically, so that the array is equivalent to a single junction. The nonlinear analysis is then tractable, though not simple, as is evident from the volume of work published on

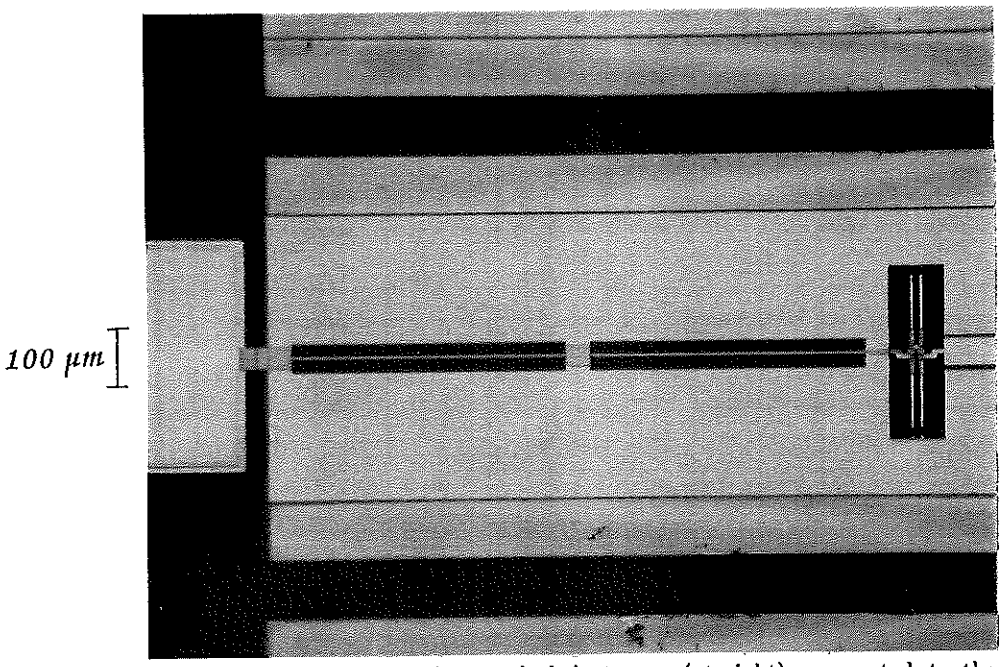

Figure V-4. A view of four SIS junctions and their tuners (at right), connected to the RF choke. The choke consists of two $\sim \lambda/4$ sections of coplanar line and two capacitors to ground. The large rectangle at the left of the picture is a gold bonding pad for the IF and DC connections to the mixer.

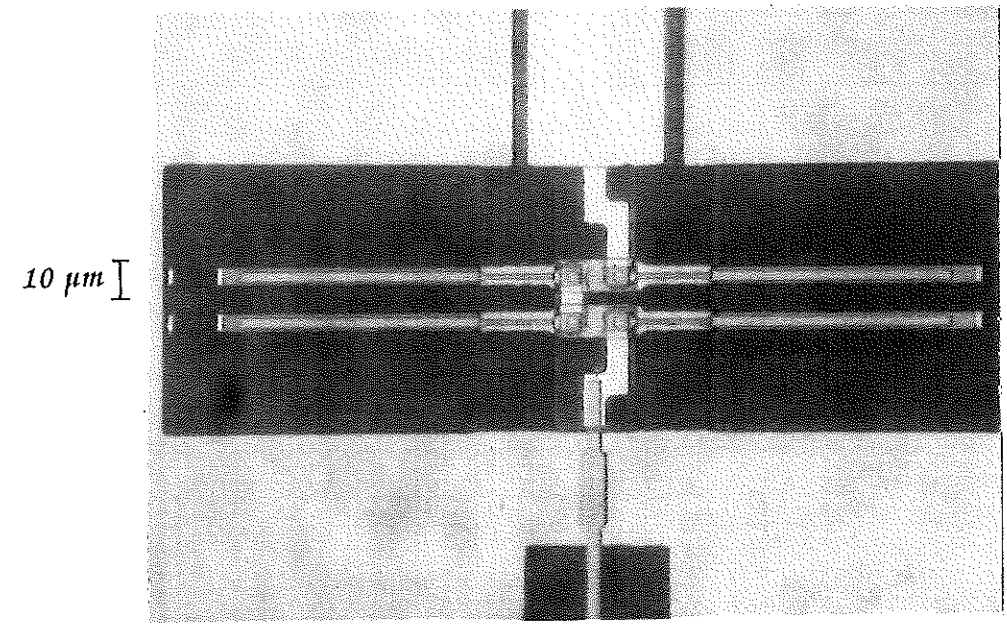

Figure V-5. The coplanar transmission line (top) is connected to an array of four SIS junctions in series (center). Each junction has its own integrated tuning circuit, consisting of a short parallel-plate transmission line terminated in a quarter-wave open-circuit line. Because of the unique properties of superconducting Nb and its oxide, the propagation velocity on the quarter-wave line is only $\sim 0.1c$, which reduces the length of the line to $\sim 1/40$ of a free-space wavelength. The hole in the ground plane containing the four SIS junctions and their tuners adds inductance which is tuned out by the capacitor at the bottom. [This figure is rotated clockwise 90° with respect to Figs. V-3 and V-4.]

the subject. We will investigate this problem in collaboration with university-based JDG researchers and others.

2.3. Balanced and Image-Separation Mixers. Image-separation mixers have certain advantages as front ends on an interferometer (MMA Memo. No. 70; see Appendix). The problem of LO injection in image-separation mixers is nicely solved by using a pair of balanced mixers. Since such an image-separation mixer would not require quasi-optical LO injection or image diplexing, no Martin–Puplett (or other) interferometer would be required in the signal path. Image-separation mixers do not work well with large fractional IF bandwidths. A choice of a 3–4-GHz IF should be acceptable. An investigation of image-separation mixers has been started by D. Woody and J. Carlstrom (both of Owens Valley Radio Observatory/Caltech).

2.4. Quasi-Optical Components. The interface between the telescope optics and the front ends needs careful study, in close collaboration with the mechanical and electromagnetics engineers designing the antenna and its mounting structure. Consideration must be given to polarization requirements (i.e., whether circular polarization is needed; see MMA Memo. No. 72) and which combinations of front ends will be used simultaneously, taking into account the need for quasi-optical-band diplexers, image filters, LO diplexers, polarizers, and refocusing elements, all of which require space and contribute some non-negligible loss in the signal path.

A number of quasi-optical components—vacuum windows, horns, lenses, focusing mirrors, diplexers, and cold loads—will be required for the final MMA front ends. Some of these components are also needed early in the project for front-end testing during the development phase. They are not trivial to design, and are difficult to test. Proper testing facilities do not at present exist at NRAO and must be set up.

2.5. Control and Test Equipment. The SIS front ends for the MMA will require the following control circuits: (i) a mixer bias circuit, consisting of a voltage-control loop within a current-control loop (which adjusts the LO level); (ii) a magnet-control system, to minimize Josephson noise in the SIS mixer by suppressing the Josephson current; and (iii) LO control circuits, including a mechanism for controlling the LO level at each mixer.

A number of specialized items of test equipment will be needed to develop front-end components for the MMA. These include a refrigerator, cryostat, widely tunable signal and LO sources, RF diplexer, cryogenic RF and IF calibration components, a swept-frequency IF receiver, a millimeter-wave network analyzer, and a millimeter-wave spectrum analyzer.

3. HFET Amplifiers

3.1. Introduction. The *MMA Proposal* contains a general description of front ends covering the 30–50-GHz, 68–115-GHz, 130–183-GHz, 195–314-GHz and 330–366-GHz frequency ranges. In the original plan the Heterostructure Field-Effect Transistor (HFET) amplifier was considered for front-end use in only the 30–50-GHz range. However, as a result of recent progress in the technology of

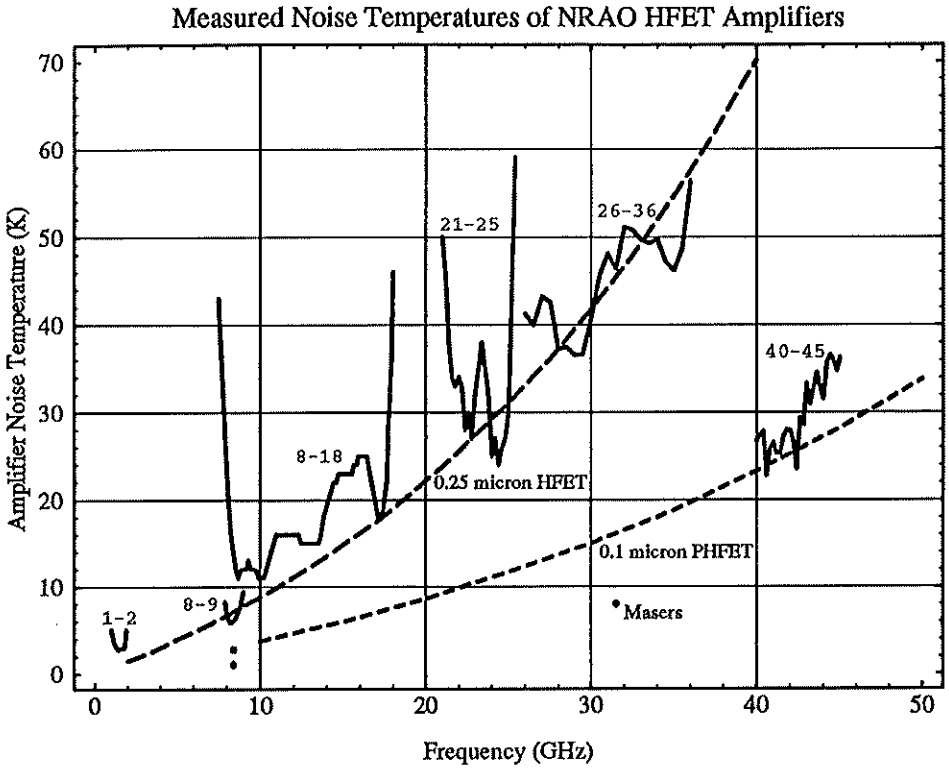

Figure V-6. The noise temperatures of different amplifiers and the minimum noise measures of FHR02X (0.25-μm gate length) and H-CF-100-6 (0.1-μm gate length) HFET amplifiers at a temperature of 12.5 K. The noise performance of three maser amplifiers—two operating at 4 K and one at 1.9 K (the lower point at 8.4 GHz)—is also shown for comparison.

HFETs (5.8 dB small-signal gain for a single device at 140 GHz), it is almost certain that HFET front ends will be competitive in noise performance with those using SIS mixers for frequencies up to 115 GHz (see MMA Memo. No. 67). The main advantages of HFET front ends over those based on SIS mixers are:

(1) The cooling requirements are less stringent (15-K vs. 4-K refrigerators) with a corresponding increase in reliability and serviceability, and lower power consumption;
(2) Image rejection at the first mixer can be effected by the use of a filter, without causing an increase in system temperature;
(3) There is a very graceful degradation of noise performance upon an increase in cold-station temperature;
(4) A large instantaneous bandwidth is possible, allowing for the observation of several lines simultaneously.

These advantages should keep the HFET front-end option under consideration, even for frequency ranges in which HFETs have slightly inferior noise performance to that of SIS mixers, especially in view of the large number of front ends required for the MMA.

3.2. Present and Future HFET Performance. A summary of the typical performance of NRAO cryogenic HFET amplifiers is presented in Figure V-6.

The noise-temperature data are referred to the cold input of the amplifier. The noise performance of these amplifiers is plotted with the minimum noise measure of the FHR02X HFET, a quarter-micron-gate device available from Fujitsu. Also, the noise temperature of the 40–45-GHz amplifier is plotted with the minimum noise measure of the 0.1-μm gate PHFET device from ROHM Research. Data for state-of-the-art 4-K maser amplifiers, developed at the Jet Propulsion Laboratory (JPL), are given for comparison. The amplifier examples demonstrate that for a bandwidth of around an octave or less the amplifier average noise temperature $T_{\rm nav}$ is approximately equal to the minimum noise measure $M_{\rm min}$ at the highest frequency within the band:

$$T_{\rm nav} = \frac{1}{f_{\rm max} - f_{\rm min}} \int_{f_{\rm min}}^{f_{\rm max}} T_{\rm n}(f)\, df \approx M_{\rm min}(f_{\rm max})\,.$$

An excellent agreement between predicted and measured noise performance of the amplifiers[3,4], both at room and cryogenic temperatures, has resulted from the development of a FET noise model.[5,6] This model allows also for a reasonable prediction of future performance. A minimum noise measure vs. frequency of a "futuristic" cryogenic HFET is presented in Figure V-7 for different HFET temperatures. A model of this device was created by assigning to the equivalent circuit of a current experimental HFET the values of equivalent gate and drain temperatures (which determine the noise properties of a device) typical of the 0.1μm ROHM Research HFET routinely used at NRAO (the equivalent gate temperature equal to the ambient temperature and the equivalent drain temperature equal to 1,000 K and 400 K at ambient temperatures of 297 K and 12.5 K, respectively). The "futuristic" device under consideration was the 0.15-μm-long-gate HFET using AlInGa/GaInAs on an InP-wafer structure from General Electric. The published noise-measure data of GE devices at room temperature agree extremely well with the model prediction, as do the data from Hughes and TRW on similar devices. Therefore, the term "futuristic" used for this device reflects only an uncertainty about its cryogenic performance.

A microphotograph of the 0.1μm ROHM Research HFET is shown in Figure V-8.

3.3. Front Ends. The examples of performance of wideband designs are shown in Figures V-9 and V-10, for K_u- and Q-bands, respectively.

---

[3]M. W. Pospieszalski, J. D. Gallego, and W. J. Lakatosh, "Broadband, Low Noise, Cryogenically-Coolable Amplifiers in 1 to 40 GHz Range", in *Proc. 1990 MTT-S Int. Microwave Symp.*, pp. 1253–1256, Dallas, TX, May 1990.

[4]M. W. Pospieszalski, "Cryogenically-Cooled, HEMT Amplifiers and Receivers in 1–50 GHz Range: State-of-the-Art", *IAU Colloquium No. 131: Radio Interferometry—Theory, Techniques and Applications*, Socorro, NM, October 1990. (published in Astron. Soc. of the Pacific Conf. Series, Vol. 19, pp. 60–64, San Francisco, CA, 1991).

[5]M. W. Pospieszalski, "Modeling of Noise Parameters of MESFET's and MODFET's and Their Frequency and Temperature Dependence", *IEEE Trans. on Microwave Theory and Tech.*, Vol. MTT–37, pp. 1340–1350, Sept. 1989.

[6]M. W. Pospieszalski and A. C. Niedzwiecki, "FET Noise Model and On-Wafer Measurement of Noise Parameters", in *Proc. 1991 IEEE MTT-S Int. Microwave Symp.*, pp. 1117–1120, Boston, MA, June 1991.

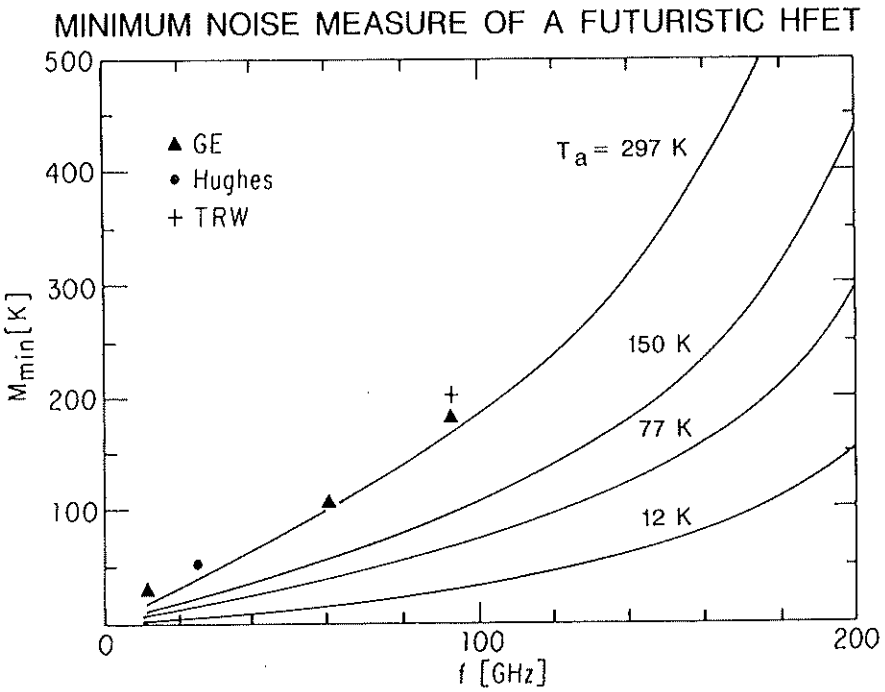

Figure V-7. Plot of the minimum noise temperature of a "futuristic HFET". Experimental results at room temperature for AlInAs/GaInAs on InP HFETs from three different laboratories are also shown.

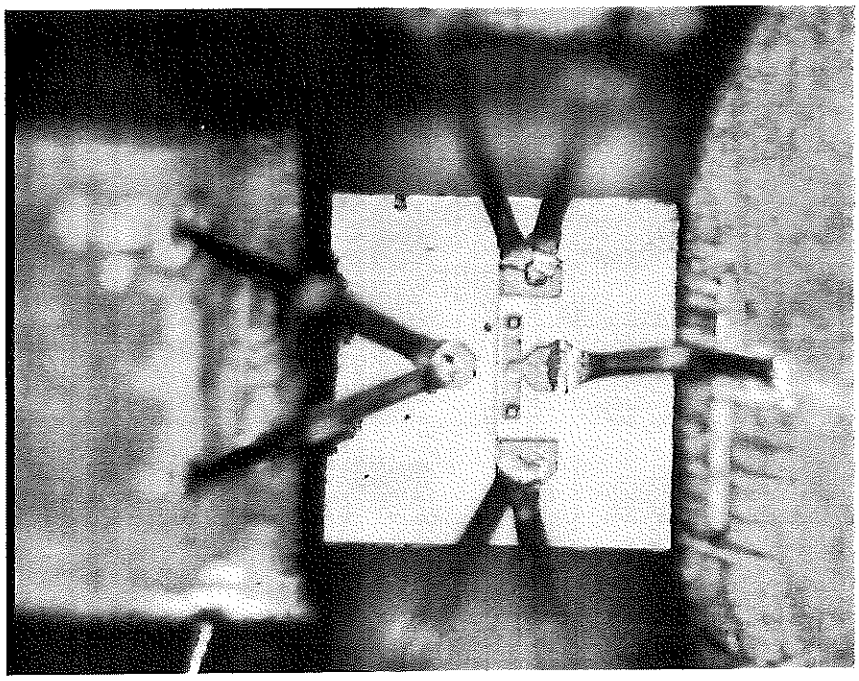

Figure V-8. This device is a ROHM Research HFET, as used in the the 40–45-GHz VLBA amplifiers. The 0.7-mil pure gold wires are attached by a thermo-compression/ultrasonic bonding process. The top and bottom bond wires provide contact to the source pads. The (2) wires at left provide contact from drain to output substrate. The bond wire at right provides contact from gate to input circuit.

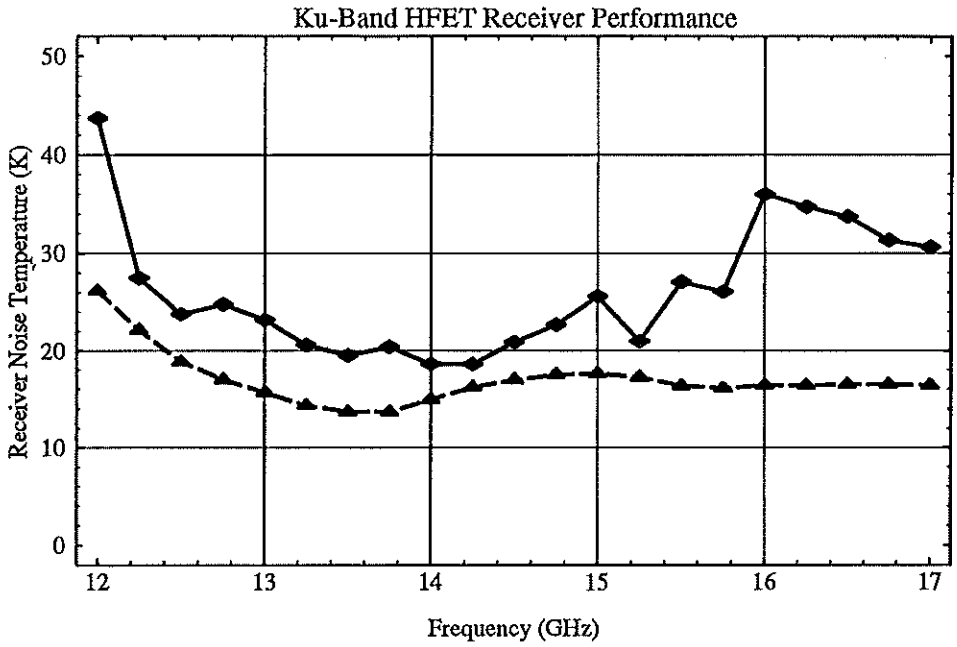

Figure V-9. Noise performance of a cryogenic amplifier *(lower curve)* and receiver *(upper curve)* for use on the VLBA in the 12–15.4-GHz band.

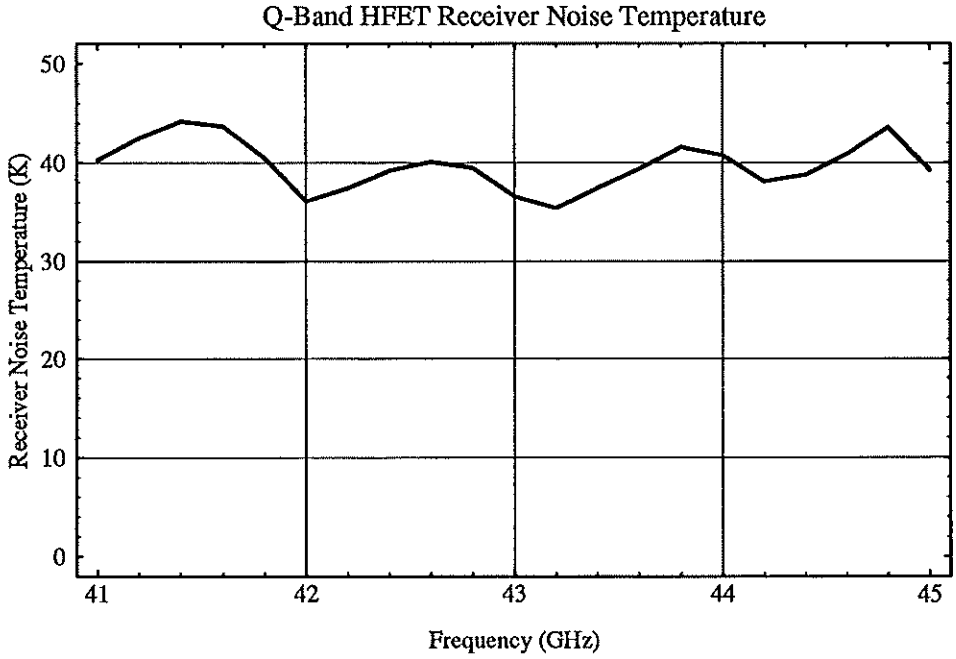

Figure V-10. Noise performance of the Q-band receiver referred to in the text.

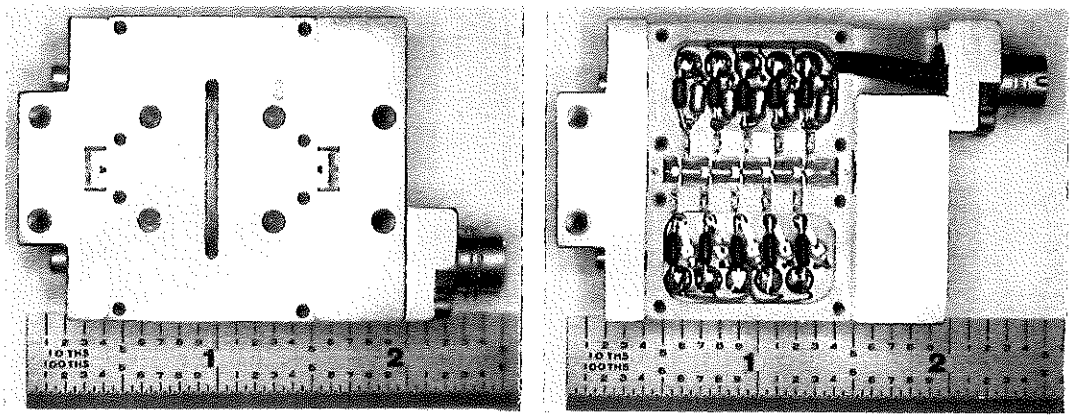

Figure V-11. Photographs of a 40–45-GHz VLBA amplifier. The left-hand photograph shows clearly the input and output waveguides. Small probes in the waveguides provide the transitions to the microstrip circuits shown in the right-hand photograph. The HFETs themselves, as shown in Fig. V-8, are too small to be seen here. They are located in the five narrow vertical ridges visible in the center of the right-hand photograph.

The performance of the 40–45-GHz front end designed for the VLBA antennas is the best yet reported for HFET units in this frequency range and is comparable to that of SIS mixers. The noise temperature of the front end is determined by the cryogenic-amplifier noise temperature ($\leq$ 30 K) and by the losses of the waveguide components (polarizer, coupler, and isolator) preceding the amplifier. Photographs of this amplifier are shown in Figure V-11.

Further improvements are possible if the expected cryogenic performance of AlInAs/GaInAs on InP HFETs is confirmed experimentally. A comparison of NRAO HFET and SIS front ends is shown in Figure V-12. The expected performance of HFET front ends built with current experimental devices is also shown, indicating that their performance should soon be competitive with that of SIS mixers at 3-mm wavelength.

Conceptual designs of HFET front ends for the MMA are similar to the design of the 40–45-GHz front end for the VLBA. The main difference is that in the concept for the MMA the bandwidth (15 GHz) of the first IF circuitry is equal to, or only slightly smaller than, the bandwidth of the preceding RF amplifier. There are several advantages to this approach:

(1) A full HFET bandwidth is available for processing at frequencies not much greater than 20 GHz. Therefore, all analog signal processing (image rejection, local-oscillator tuning, and IF bandwidth determination) can be done fairly inexpensively, as a result of Monolithic Microwave Integrated Circuit (MMIC) development driven by commercial and military markets.

(2) No tuning of any millimeter-wavelength component is required.

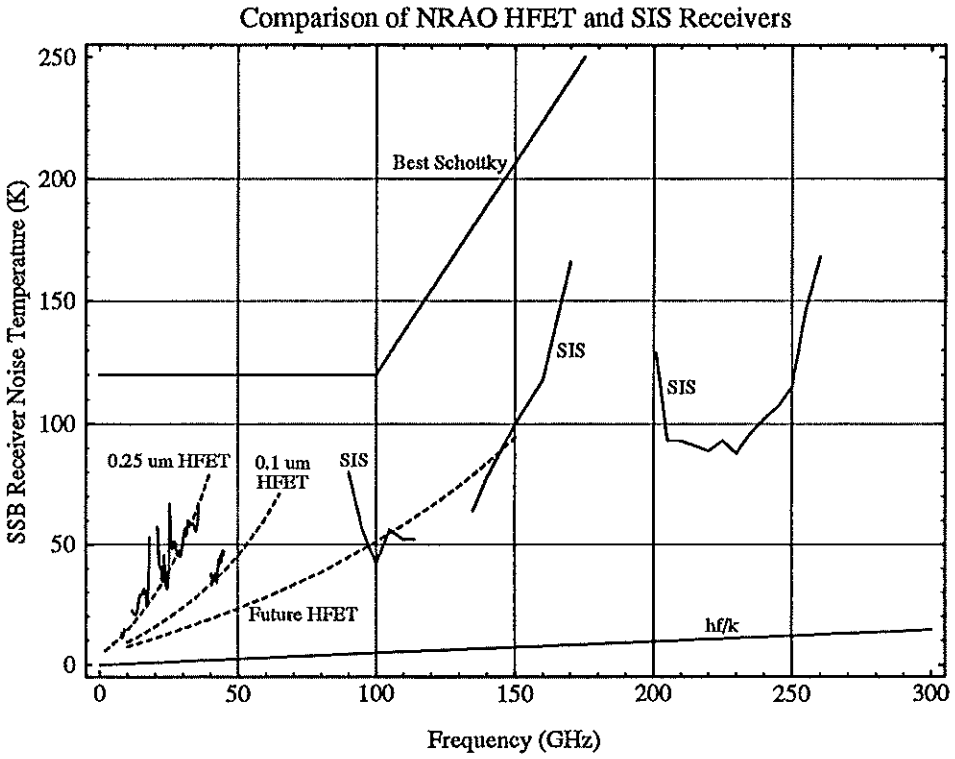

Figure V-12. A comparison of NRAO HFET and SIS receiver performance with that expected from the current experimental devices ("futuristic HFETs").

(3) Image rejection for the first frequency conversion can be obtained naturally by the proper choice of waveguide size (chosen so that the image frequency is below the waveguide cutoff frequency) or by a conventional filter.

The expected noise temperatures of different front ends are summarized in Table V-1. The crucial element of each of the front ends is the HFET RF amplifier, which will employ lattice-matched AlInAs/GaInAs HFETs. Their cryogenic performance has not yet been demonstrated. However, the excellent performance of the VLBA 40–45-GHz amplifiers employing AlGaAs/InGaAs pseudomorphic devices is a good indicator that projected performance can be achieved.

The feasibility of the remaining components of the front ends—i.e., horns, orthomode transducers, and wide-bandwidth mixers and IF amplifiers—has already been demonstrated. Some additional development work may be required on circular polarizers and isolators.

3.4. Research and Development Plan. The development plan is based on the assumption that the 33–50-GHz and 68–115-GHz bands will be subdivided into five subbands: 32–40 GHz, 40–50 GHz, 68–85 GHz, 85–100 GHz, and 100–115 GHz, following the scheme proposed in the previous section. The following research issues need to be addressed:

Table V-1. Expected Noise Performance of 32–115-GHz Front Ends

Frequency Range	Maximum Noise Temperature
32–40 GHz	25 K
40–50 GHz	32 K
68–85 GHz	55 K
85–100 GHz	65 K
100–115 GHz	75 K

3.4.1. Evaluation of HFETs. Evaluation, testing, and establishment of device models for HFETs at millimeter wavelengths and at cryogenic temperatures is required. This should be an ongoing effort, until the beginning of the construction phase, involving one full-time engineering position. Although there exists a significant research effort into room-temperature millimeter HFETs in industry (GE, TRW, Hughes, Avantek/HP) as a result of primarily military funding, it is somewhat unlikely that this will produce a spillover into commercial markets. Therefore, the purchase of millimeter-wavelength devices at fairly low commercial market prices, as has been done for VLBA front ends, may not be possible. An establishment of a contractual relation between NRAO and one of the leading research laboratories may be required.

3.4.2. Measurement Systems. Test systems for the 60–140-GHz frequency range must be assembled before testing of prototype amplifiers can proceed. Components include test dewars with refrigerators and vacuum systems, sweep oscillators, noise sources, isolators, etc. The plan calls for these systems to be completed during the first year of the development period.

3.4.3. Prototype Amplifier Development. Design and development of prototype amplifiers will follow the completion of the test systems, starting with the 68–90-GHz range to confirm, as early as possible, the feasibility of the HFET concept at the higher frequencies.

4. Cryogenics

4.1. Introduction. The requirement for 4-K and 15-K cryogenic refrigerators (cryocoolers) for the SIS mixers and HFET amplifiers necessitates a serious study of the available options. Although cryogenics is an area that is not new to NRAO and other radio-astronomy organizations, it is one that has presented the community with problems in the past and some worries for the future. The reliability and the high electrical power consumption of the coolers are probably the areas that demand the most study.

The first priority of a serious study and development program is the hiring of an engineer who has a significant background in cryogenics. Ideally, this engineer should have a thorough understanding of cryocoolers and also some background in construction of cryogenic components and systems. This person would review the various options, evaluate prototype coolers, and be responsible for any in-house fabrication of cryogenic systems.

4.2. Areas for Development Activity.

4.2.1. Gifford–McMahon 15-K Cryocoolers. There should be a review of current Gifford–McMahon coolers for 15 K. These will be used for cooling HFET amplifiers and perhaps as pre-coolers for Joule–Thompson (JT) systems (see below). The Molecular Resonance Imaging (MRI) community has selected coolers from other manufacturers than the primary one to have served the radio-astronomy community. The recent availability of 6.5-K coolers from Balzers (USA) makes these devices particularly attractive for JT coolers.

4.2.2. Standard Joule–Thompson Coolers. These are the standard 4-K coolers used by the Jet Propulsion Laboratory (JPL) and the NRAO for at least twenty years. Although these coolers have proved satisfactory, they have a reputation for poor reliability. NRAO's recently manufactured JT circuits, used together with scroll compressors, have resulted in an improvement in reliability. The efficiency (electrical power input for a given cooling capacity) is not good and would result in the cryogenics being a very significant component of the operations power usage for the MMA.

However, despite these shortcomings, this type of system could be the cooler of choice for the Millimeter Array. It is proposed, as part of the MMA development program, that five complete 4-K systems be built for long-term testing. These would be used in laboratory setups as well as in the MMA prototype receivers. At the same time, there are other options which, while less developed, hold promise of a system that would better meet the requirements of the MMA. Table V-2 lists specifications of an ideal cooler for the MMA; most, but not all, of these specifications are met by the "standard" JT cooler systems.

Table V-2. Summary of Cryogenics Requirements

Final Stage:	
Temperature	≤ 3.5 K
Short-term temperature stability	± 50 mK
Cooling capacity	1 to 5 W
Intermediate Stage:	
Temperature	~ 60 K (max.)
Cooling capacity	~ 30 W (min.)
System Efficiency:	
Input electrical power for 1 W cooling @ 3.5 K	$\leq 1,000$ W
Routine Maintenance:	
Period between seal replacement	$\geq 10,000$ hr
Mean Time Between Failures (MTBF):	$\geq 10,000$ hr
Orientation:	
Should meet specs over at least a 90° change of vertical orientation	

4.2.3. Gifford–McMahon Cooler with Er_3Ni Regenerator. The use of Er_3Ni regenerator material has been shown to reduce the temperature of a Gifford–

McMahon cooler second stage to below 4 K. This work has been reported by several organizations.[7,8,9] However, at the moment, there are no commercially available systems. There are several problem areas with these coolers. Due to the difficult nature of the regenerator material, the long-term reliability needs to be demonstrated. The temperature stability is not good, the cooling capacity is limited, and the overall cooler efficiency is much lower than that of the standard JT coolers. It may be that the real potential of these systems is as pre-coolers for a conventional JT system. Such a system has been reported in the literature and showed a very high efficiency and high cooling capacity at 4.5 K.[10] Some support, by the MMA Joint Development Group, of the work at the University of California, Berkeley, may accelerate the progress in this area.

4.2.4. Boreas Cooler, Single Cold Station. Boreas, Inc., has developed a new 4-K cooler that promises to provide an efficient, reliable cooling system that does not require the multiple compressors used by JT coolers. Prototype models are expected to be available for shipment to customers at the beginning of 1993. NRAO will purchase one of these units for evaluation.

4.2.5. Boreas Cooler, Two Cold Stations. The major limitation of the cooler above is the lack of an intermediate temperature station for heat sinking input/output lines, in order to minimize thermal loads at 4 K. However, Boreas plans to market such a machine sometime within the 1993–1994 time frame.

5. Local Oscillators

5.1. LO Design Philosophy. LO signals are required in the frequency range between 30 and 360 GHz. Because of the finite bandwidth of frequency multipliers and other components, it is expected that six LO bands will be required to provide complete coverage of this range (MMA Memo. No. 69; see Appendix). Block diagrams of some LO subsystems are shown in Figures V-13 and V-14. The primary design goals for the LO system are as follows (in order of importance):

(1) To meet the MMA requirements with regard to tunability, phase stability, power levels and flatness, and phase switching.

(2) To design the LO system in a modular manner. This permits configuration versatility and reduces the number of specialized subsystems (e.g., modules used for producing the 30- to 120-GHz LO can also be used to derive the LO above 120 GHz by frequency

[7]H. Nakagome, "Two-Stage GM Refrigerator with Er_3Ni Regenerator for Helium Liquefaction", in *Proceedings of the Sixth International Cryocoolers Conference*, Plymouth, MA, Oct. 25–26, 1990

[8]T. Inaguchi, M. Nagao, and H. Yoshimura, "Two-Stage Gifford–McMahon Cycle Cryocooler Operating at about 2 K", in *Proceedings of the Sixth International Cryocoolers Conference*, Plymouth, MA, Oct. 25–26, 1990

[9]M. Nagao, T. Inaguchi, H. Yoshimura, S. Nakamura, T. Yamada, and M. Iwamoto, "Generation of Superfluid Helium by a Gifford–McMahon Cycle Cryocooler", in *Proceedings of the Sixth International Cryocoolers Conference*, Plymouth, MA, Oct. 25–26, 1990

[10]H. Nakagome, R. Hakamada, M. Takahashi, and T. Kuriyama, "High Efficient 4 K Refrigerator (GM Refrigerator with JT Circuit) Using Er_3Ni Regenerator", in *Proceedings of the Sixth International Cryocoolers Conference*, Plymouth, MA, Oct. 25–26, 1990

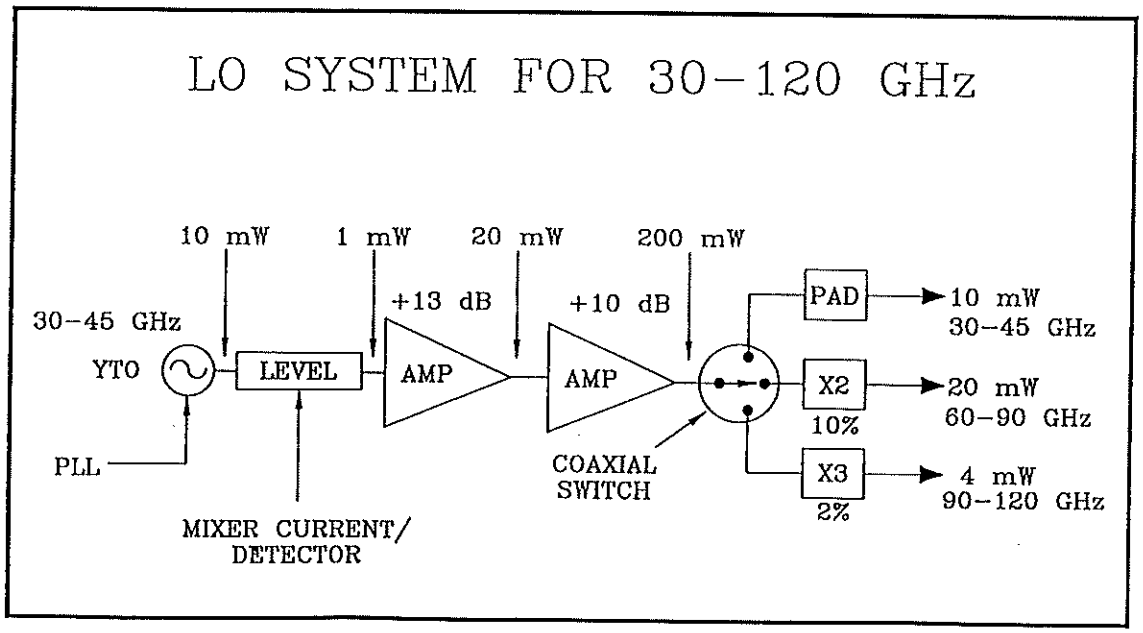

Figure V-13. Block diagram of the local-oscillator system for lower-frequency operation of the MMA (30–120 GHz).

multiplication). This is a cost-effective approach which improves construction and testing efficiency and enhances maintainability of the system in the field.

(3) To design highly reliable components that minimize the number of mechanical moving parts, such as sliding-short tuners. Emphasis will be on wide-bandwidth components with mechanically fixed backshorts and electronic tuning. This also greatly reduces the complexity of the monitor and control required in the LO system.

(4) That the components should not contain fragile mechanical contacts, such as whiskers, which would compromise the reliability. The design approach involving discrete planar diodes in Microwave Integrated Circuits (MICs)—i.e., hybrids—should be explored as an alternative to the whisker. This is currently a very active area of research.[11]

(5) To explore the use of Monolithic Microwave Integrated Circuits (MMICs) for the LO system. The potential benefits of such circuits are (i) to reduce greatly the number of intricate wiring connections requiring highly specialized procedures, (ii) to minimize the weight and size of the components, (iii) to improve on the reliability by reducing the number of interconnections, and (iv) to reduce the component-to-component performance variation, since the critical circuit layout is produced photolithographically. Research in this

[11] R. Bradley, *The Application of Planar Monolithic Technology to Schottky Varactor Millimeter-Wave Frequency Multipliers*, Dept. of Electrical Engineering, U. Va., Charlottesville, VA, March 1992.

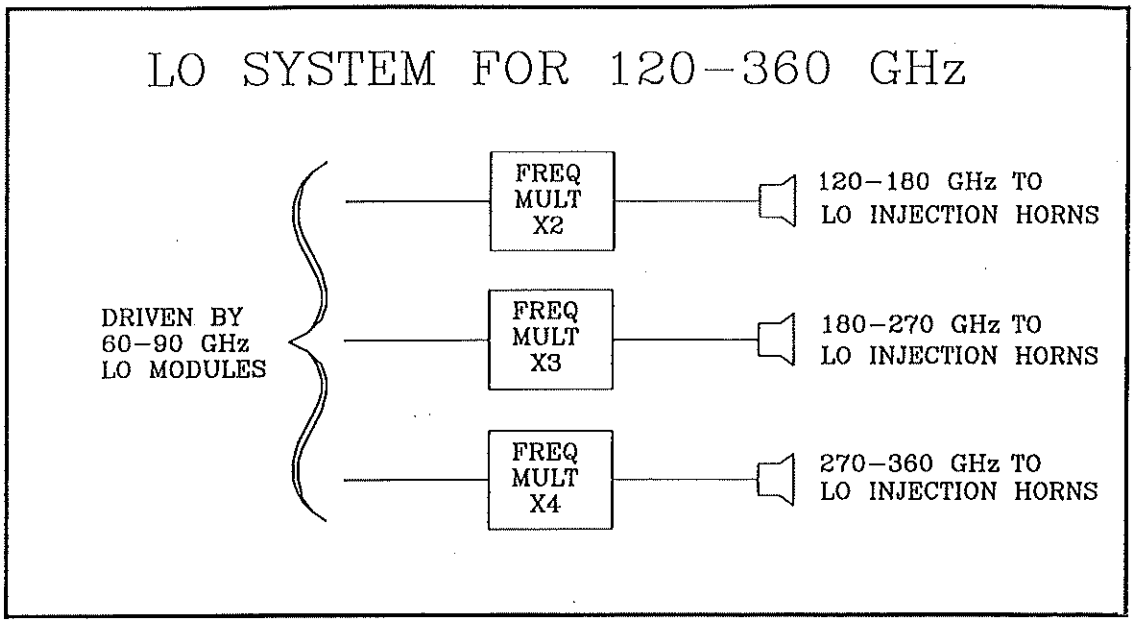

Figure V-14. Block diagram of the local-oscillator system for the higher-frequency bands of the MMA (120–360 GHz).

area is also quite active, with emphasis placed on circuits up to 120 GHz.[11]

It is very important to assess the state of the art for the various components quite early in the development phase, thus allowing the creation of a preliminary framework for the research and development tasks. Some of the LO components can be purchased directly from commercial vendors, while others will require extensive research and development.

5.2. Development Plan. The lower-frequency LO modules (30 to 120 GHz) are of prime importance since (i) the inherent phase-locked loops are a major factor in the overall LO phase stability and (ii) the higher-frequency LOs are derived from the 30–120-GHz modules through frequency multiplication. Therefore, careful phase-stability measurements of proposed 30–120-GHz LO schemes must be performed very early in the development stage in order to verify that adequate phase stability will be achieved for acceptable array operation. Work on the lower-frequency modules will progress to the pre-production stage in early 1996. Furthermore, supporting work on frequency multipliers as well as design and test of filters, levelers, amplifiers, etc., will also begin within this time frame. Design of the higher-frequency LO systems will commence in early 1994 and will progress through the prototype stage in mid-1996. Throughout 1996, the bulk of the LO work will concentrate on integrating the LO system with the LO reference distribution, receivers, and monitor/control systems.

The fiducial LO design illustrated here is an extension of the approach which has already been adopted for other millimeter-wave telescopes. However, as noted in the *MMA Proposal*, there are a number of promising technologies that

ultimately may lead to a better solution for the LO system. We will investigate these developments and adopt alternative approaches as appropriate.

6. Front-End Packaging

6.1. Introduction. The packaging task consists of integrating the HFET and SIS front ends in refrigerated dewars, along with the feed horns, first mixers and IF stages, the LO injection, polarizers, etc. Image-rejection devices for the SIS mixers and polarizers are also required. The feed horns must be arranged to allow switching between front ends by adjusting an element of the microwave optics, usually a plane reflector, to direct the focused radiation into the appropriate feed. For the SIS mixers the local-oscillator switching is also by means of an optical element, but for the HFET front ends it is by means of waveguide switches. A possible arrangement would be to put all of the HFET front ends into one dewar cooled to 15 K and all the SIS front ends into another cooled to 4 K. All of the technology required is within the experience of NRAO in the instrumentation of the twelve-meter antenna at Kitt Peak. A description of the techniques that would be involved is given by Payne.[12]

6.2. Current Design for Millimeter-Wavelength Front-End Packaging. An arrangement now in use on the NRAO Twelve-Meter Telescope uses eight front-end inserts in a ring-shaped configuration in a circular dewar; see Figure V-15. These front ends are SIS mixer units, and the dewar is cooled to 4 K. Two inserts are used for each frequency band, one for each polarization. A pair of crossed grids and two Martin–Puplett interferometers enable two linear polarizations to be separated and the image band to be terminated in a cold load; see Figure V-16. The pair of inserts for each frequency are positioned at opposite sides of the dewar, and the circular arrangement is designed to allow bands to be selected by rotating an arrangement of quasi-optical mirrors. The front-end inserts are easily interchanged for maintenance, and the spares that are used to replace defective ones can first be adjusted in a test dewar to minimize down time of the antenna. Image rejection of greater than 20 dB at frequencies up to 270 GHz has been obtained with this system. The system has been in use for more than a year on the Twelve-Meter Telescope, and has been very reliable.[13,14]

6.3. Design and Development Plan. Some details of the overall front-end specification remain to be finalized at this time. These include the precise numbers of front ends to cover the various frequency ranges, and verification that HFET amplifiers can be developed up to a frequency of 115 GHz. However, present best estimates are satisfactory as a basis for initial design studies. The arrangement for the Twelve-Meter Telescope described above has been sufficiently reliable and satisfactory that a similar design will be adopted for the

[12] J. M. Payne, "Millimeter and Submillimeter Wavelength Radio Astronomy", *Proc. IEEE*, Vol. 77, pp. 993–1017, 1989.

[13] J. M. Payne, "Millimeter Wavelength SIS Receivers", *Program and Abstracts*, National Radio Science Meeting (URSI), Boulder, CO, Jan. 1990, p. 273

[14] J. W. Lamb, J. M. Payne, and N. Bailey, "New Millimetrewave Receivers at NRAO", to appear in *Proceedings of the European Microwave Conference*, Helsinki, Aug. 24–28, 1992.

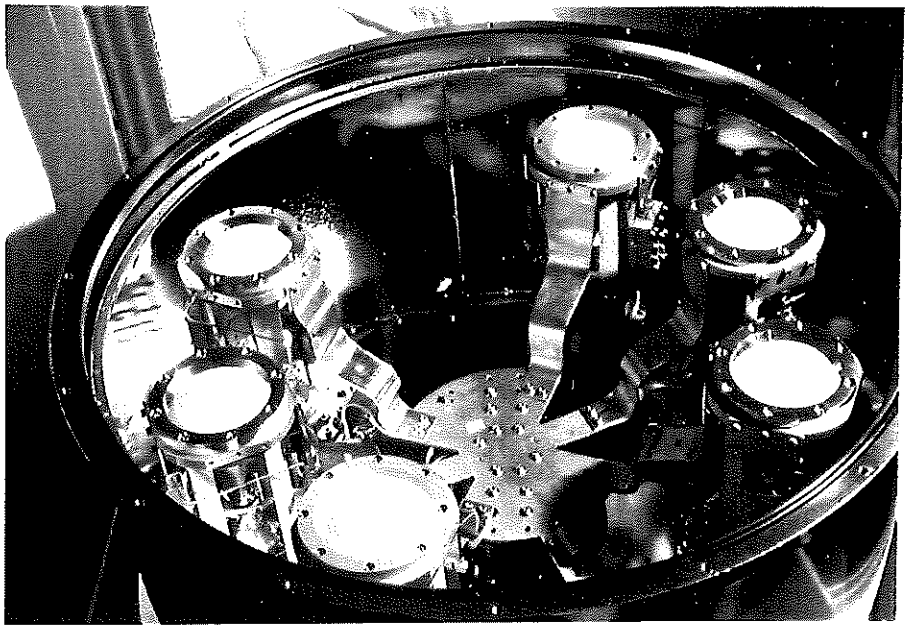

Figure V-15. The multiband SIS receiver on the NRAO 12-Meter Telescope, which will serve as a fiducial design for the MMA receiver. Eight individual SIS receivers are accommodated in a single 4-K dewar. Six SIS receiver inserts are shown installed in this photograph.

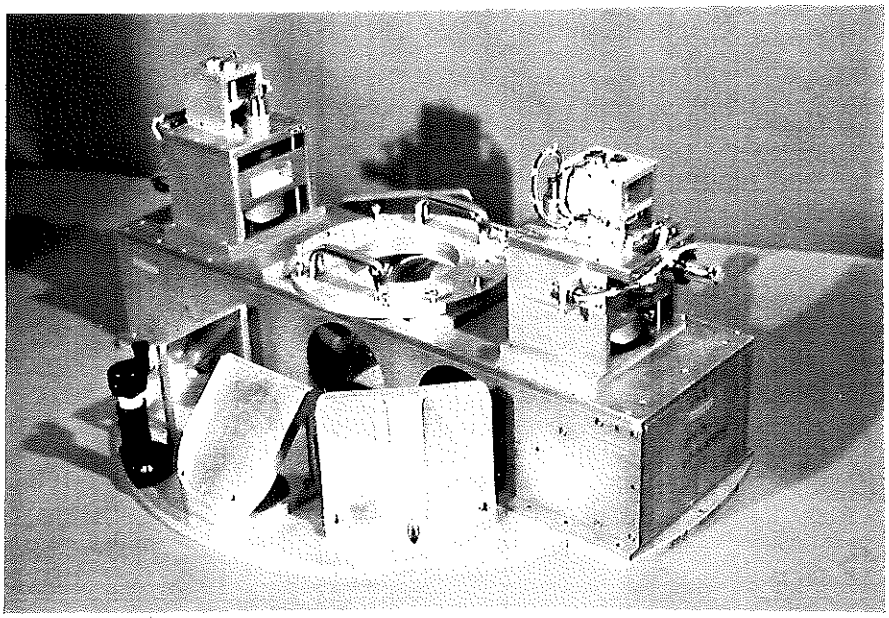

Figure V-16. The optics package for the multiband SIS receiver on the 12-Meter Telescope. A pair of crossed grids and two Martin–Puplett interferometers separate the two linear polarizations and reject the image band.

MMA. The complexity of the total system of quasi-optical elements used for image rejection, polarization separation, signal switching, etc., is the factor that most influences the design of the whole front-end package. Considerations of the antenna with regard to the Cassegrainian optics and the physical space available to accommodate the front-end packages are also important factors. Prototype modules will undergo thorough testing within the laboratory. After approval of these modules, two complete front-end systems will be assembled. One system will be installed on the prototype MMA antenna, and the other will be available for laboratory tests until such time as the next antenna is procured.

7. Fiber-Optic Transmission, IF Processing, Monitor and Control, Etc.

The development reviewed here is concerned mainly with the part of the electronics between the front ends and the correlator. This subject is addressed in additional detail in MMA Memorandum No. 65 (see Appendix).

7.1. Reference-Frequency Transmission. A small number of reference frequencies must be transmitted from the central electronics complex to each antenna to provide phase references for the LO signals required there. The use of more than just one frequency allows for a necessary degree of tunability of the LOs. The primary reference frequency will be multiplied to several hundred GHz, and must therefore be transmitted to the antennas with the highest possible phase stability. One or more optical fibers, of single-mode type, will be used for the transmission. Some questions that must be addressed as part of the design are as follows: Is it necessary to use (expensive) high-stability fiber, or is round-trip measurement with regular fiber adequate? How are the two directions in the round-trip scheme best separated: via different optical wavelengths, different modulation frequencies, or different fibers? What are the factors that limit the accuracy of the round-trip measurement? What are the best reference frequencies to transmit? To address these questions we will set up a small optical-fiber laboratory and measure performance with various arrangements. This will involve one engineer and one technician. Two years will be devoted mainly to development and design, and about another two years to building and testing a two-antenna prototype system. Other tasks that will be performed by the same group include design of the phase-locked loops for control of the high-frequency local oscillators and design of the circuitry for phase switching and frequency offsets used to provide fringe stopping. The development of the oscillators (i.e., the units that generate the required microwave power) is one of the tasks of the millimeter development group, and the LO group envisaged here will work with the millimeter-wave engineers in designing the phase-locked loops.

7.2. IF Processing. The received signals must be converted in frequency to an IF of a few GHz. They must then be converted again one or more times to select the required bands for processing. These filtered signals must then be sampled and digitized. To provide the basic performance expected of the array there should be at least four IF channels, to allow for observing with two frequency bands and two polarizations.

The use of four IF channels to cover 2 GHz of total bandwidth (one GHz each per polarization) will require a maximum bandwidth of 500 MHz per channel. Factors related to the choice of correlator design will determine whether further analog filtering before the samplers is required to obtain the highest spectral resolution (approximately 6 kHz). In the conversion of the signals to baseband for sampling it is advantageous to use a single-sideband mixer to reduce the response to unwanted sidebands. Sideband rejection in such mixers is often only marginally adequate, but may be improved by avoiding tunability in the LO for the baseband conversion. This is an area in which some development will be required. Selection and testing of fast samplers to digitize the received signals will also be necessary, since bandwidths of 500 MHz or perhaps 1 GHz will need to be sampled. This task is considered in the correlator section since experience with fast digital logic is required.

7.3. IF Transmission System. The design of the optical-fiber transmission system to convey the digitized signals to the correlator location should require less laboratory study than that for the LO reference transmission, since the phase stability is not so critical and digital data transmission is a straightforward application of fiber technology. Some detailed questions such as the bit rate per fiber and the optimum optical wavelength will need to be considered. Also, it has been suggested that lengths of optical fiber could be used to implement the longer pieces to the variable delay lines required to compensate for the geometrical delays in the system. Alternatively the variable delays could be entirely digital. The choice will depend largely upon cost, and if the optical fiber delay is to be pursued some tests of switches for optical fibers will be necessary.

7.4. Monitor and Control. A monitor-and-control system will be required to provide the necessary data transfer between many parts of the system and the control computer. A system of this type was designed for the VLBA, based on an interface card that connects through a bus to the local control computer. The card can be included in any module as an interface, but its use has been limited by the amount of power that the card consumes and the interference that it could produce. A similar concept, with some improvements in these areas, should be feasible for the MMA.

7.5. Other Systems-Engineering Areas Requiring Design Effort. The following are some areas not mentioned above in which some careful design and testing will be necessary to achieve optimum performance:

(1) Shielding of IF input stages and filtering of bias leads, etc., is important to protect against radio-frequency interference. Note that the late IF stages are likely to fall in the most heavily used range of the radio spectrum (< 4 GHz), and the site will be on a high plateau and thus not well sheltered from interference. Extensive laboratory tests with simulated interference should be made.

(2) All parts of the electronics should be examined for sensitivity to temperature variations, to determine whether they will perform adequately within the usual range of temperature control

($\pm 1^\circ$ C). This is particularly important for the LO system and high-frequency parts of the analog-signal channels.

(3) A total-power measurement scheme is required on all antennas. This will involve a nutating subreflector on the antenna, and it will require a power-linear detector and a synchronous detector for each IF channel.

8. Correlator Development

8.1. Introduction. The design of the correlator can be separated into two steps: the concept-development phase and the detailed design phase. The first phase will resolve basic design issues. The detailed design phase will use the results of the concept-development phase and combine them into a design for the entire correlator.

The primary concept decision that will drive the MMA correlator development is the choice of an FX or XF architecture. The selection of the primary architecture will be strongly driven by the level of integration possible on a custom or semi-custom chip. Each architecture has a number of advantages and disadvantages (MMA Memo. Nos. 66 and 85; see Appendix). Similarly, each approach has inherent efficiencies and inefficiencies that will affect the size, cost, power consumption, and reliability of the final correlator. Therefore, a very thorough strawman design of each is required to make an appropriate choice. The strawman design will include the first stages of custom/semi-custom chip design. At sometime during the chip design effort it will be possible to choose one architecture. Thereafter, work on one approach will be ended, with all effort continuing on the preferred architecture.

8.2. Development Timetable. The VLSI technology applicable to the correlator construction is probably advancing more rapidly than most other areas encountered in the MMA. Arguments can therefore be made in favor of leaving the design of the correlator as late as is possible in the array construction. However, it is also clear that a correlator to handle signals from a number of antennas will be needed at an early stage of construction. If the construction is spread out over, say, five years, then one might expect that within the second year there would be as many as ten antennas outfitted for receiving in some if not all bands. It would then be very important to have a correlator to allow testing, investigation of atmospheric effects on imaging, and even some preliminary astronomy. If a correlator were not available until the end of the array construction, more and more antennas would have to wait unused as the construction progressed.

Ideally, a small usable correlator should become available early in the construction period, and its capacity should approximately keep pace with the completion of antennas. Unfortunately, correlator construction does not easily fit such a scenario. Custom-designed integrated circuits (ICs) are usually obtained in a single procurement, and software must be largely complete to allow any operation at all. Thus unless an interim, possibly throw-away, system is built, there are arguments for a timetable in which the correlator would be completed by about two years into the construction of the antennas. Detailed design of

the correlator would then have to start several years before the commencement of construction of antennas. A possibility would be to build a continuum correlator for the early operation, and to use it to provide extra bandwidth for continuum observing after the spectral-line correlator is completed. The question of whether to build an interim system or to complete the final system early needs careful study, including an appraisal of existing correlator ICs and the chances that significant advances in the technology are imminent. A study of these points should commence as early as possible.

8.3. Strawman XF/FX. Two separate efforts should be started to design a suitable instrument applying both architectures. The resulting designs will be used to guide the custom/semi-custom chip development. This development effort should try to use the advantages of VLSI designs to reduce the required number of connectors and the amount of support electronics. In other words, this effort should be geared towards guiding the chip development to produce an optimum VLSI chip. Included in the overall design should be a consideration of the desirability of building a separate continuum correlator to provide greater bandwidth for continuum observations. The goal would be to maximize continuum sensitivity while retaining the desired performance in the spectral correlator, and possibly to provide a correlator for initial testing of the array, as discussed above.

8.4. FX Simulations. The architecture of the FX correlator has enough complexity to warrant some computer simulations. One important result of this program is to optimize data representation. This program can use the VLBA simulations as a starting point.

8.5. XF/FX Chip Design. During development of the strawman design, it should be possible to design a custom chip. The XF chip will include the correlators and as much mode-selection hardware as is feasible. The most likely approach will be a fully customized design using the metal-oxide-semiconductor implementation service (MOSIS). The FX chip will implement the Fast Fourier Transform algorithm in silicon. The most likely approach is an advanced gate array, although a full-custom design should be considered.

8.6. Sampler Development. The maximum signal bandwidths to be processed, 500 MHz or perhaps 1 GHz, will require sampling frequencies of 1 GHz or 2 GHz, respectively. Testing of available sampler ICs, and possibly some development, will be necessary and can probably best be done within the correlator group.

VI. SCHEDULE, PERSONNEL, AND COST

To assist in formulating a cohesive project-management program for the *MMA Design and Development Plan*, the whole of the essential activities described in the preceding chapters has been subdivided into a group of specific and distinct tasks, and the interrelationships of these tasks, especially with regard to scheduling, have been considered in detail. Summary presentations of the project-management data pertinent to each task are included below. The staffing/labor requirements for each task, and the appropriate time period for completion thereof, are shown in the attached Gantt chart (Table VI-1). As this is a research and development program, the timing and estimated durations of the tasks should be considered as current best estimates, and they are likely to be altered as the program evolves. The current "baseline" plan does enable us to formulate a reasonably accurate overall cost estimate for labor.

The "resources" indicated in the Gantt chart—E7, T9, C2, and so forth—refer to individuals with the specific skills required of the labor force as defined in Table VI-2 below. The labor effort indicated in the Gantt chart, and summarized by year in Table VI-2, is incremental to the NRAO staff working at present on the MMA.[1] For example, the NRAO scientists and engineers who now are working on millimeter-wave instrumentation that may be of benefit to the MMA as well as to other observatory activities are not charged to the MMA design and development effort in Table VI-2. Neither is there any overhead or institutional levy. Quite the reverse: the observatory resources are, and will be, fully available to the MMA team.

The total cost of the MMA design and development phase is summarized in Table VI-3. Labor costs include employee fringe benefits. As is characteristic of research and development programs in general, approximately half of the costs shown in Table VI-3 are for labor, and the other half for materials. For the development of the Millimeter Array in particular, half of the development cost is allocated to the two items presenting the greatest technical challenges—the wideband, tunerless superconducting mixers, and the precision antennas—the other half covers all other aspects of the MMA.

In 1997, when the MMA design and development work is concluded and array construction begins, the development program whose costs are outlined in Table VI-3 will have established much of the laboratory infrastructure necessary for fabrication and testing of the array electronics. To this end, an important task of the design and development phase will be construction of test setups and verification of test procedures. The test equipment needed for this facility and for the tasks noted throughout the *MMA Design and Development Plan* is substantial. A summary of the major equipment needs is shown in Table VI-4.

[1]The incremental labor may be new NRAO employees or, where appropriate, labor supplied under the auspices of the JDG at participating universities.

Task Name	Resources	Start Date	End Date
ADMINISTRATION		4-Jan-93	30-Dec-96
Project Management		4-Jan-93	30-Dec-96
Engineering	E28	4-Jan-93	30-Dec-96
Science	S3	4-Jan-94	30-Dec-96
Purchasing/Contracts	C1	3-Jan-95	30-Dec-96
Project book milestone		1-Jul-93	1-Jul-93
SITE EVAL,ACQSN & USE PLAN		4-Jan-94	31-Dec-96
Site Engineering	E23	4-Jan-94	2-Jan-96
Detailed site plan	E23, E24	2-Jan-96	31-Dec-96
Site selection milestone		4-Jan-94	4-Jan-94
ANTENNA DEVELOPMENT		4-Jan-93	31-Dec-96
Thermal Studies	E20	4-Jan-93	31-Dec-96
Optics Design	E20	4-Jan-93	31-Dec-93
Instrumentation	E20, T16	4-Jan-93	2-Jan-96
Receiver Interface	E20	4-Jan-93	2-Jan-96
Programming Support	P3	4-Jan-94	31-Dec-96
Structure/Panel Design	E21	4-Jan-94	3-Jan-96
Nutating Secondary	E8	4-Jan-94	3-Jan-95
Drives/Encoders	E8	4-Jan-94	3-Oct-94
Control System	T17, E9	4-Jan-94	2-Jan-96
Bids for prototype	E8	3-Oct-94	3-Jan-95
Build prototype	T18, E8	3-Jan-95	2-Jan-96
ARRAY IMAGING STUDIES		4-Jan-93	31-Dec-96
Antenna Specifications	S1	4-Jan-93	31-Dec-93
Config. & Observ. Techniques	S1, S2	4-Jan-94	31-Dec-96
SIS MIXER DEVELOPMENT		4-Jan-93	31-Dec-96
SIS Mixer Design	E3, M1	4-Jan-93	31-Dec-96
Mixer Assy and Test		4-Jan-94	31-Dec-96
195-260/260-314GHz	E4, T3	4-Jan-94	3-Jan-95
130-183/330-366GHz	E4, T3	3-Jan-95	31-Dec-96
68-90/90-115GHz	E5, T4	2-Jan-96	31-Dec-96
Balanced mixer study	E5, T4	4-Jan-94	3-Jan-96
Quasioptical components	E6, M1	4-Jan-94	31-Dec-96
Test/Control equipment	E7, T5, E27	4-Jan-94	31-Dec-96
HFET AMPLIFIERS		4-Jan-94	31-Dec-96
HFET Evaluation	E13, T15	4-Jan-94	31-Dec-96
Measurement Systems(60-140GHz)	E14, T9	4-Jan-94	14-Oct-94
Prototype Development		4-Jan-94	4-Apr-96
Design	E14	4-Jan-94	30-Jun-94
Prototype 68-85GHz	E14	1-Jul-94	4-Oct-94
Prototype 85-100GHz	E14, T9	3-Oct-94	13-Apr-95
Prototype 100-115GHz	E14, T9	3-Apr-95	6-Oct-95
Prototype 40-50GHz	E14, T9	2-Oct-95	8-Jan-96
Prototype 32-40GHz	E14, T9	2-Jan-96	4-Apr-96
LOCAL OSCILLATOR		4-Jan-93	31-Dec-96
Prototype PLLs 30-120GHz		4-Jan-93	2-Jan-96
Design	E10	4-Jan-93	25-Mar-94
Construction	T6, M2	1-Jul-93	1-Apr-94
Evaluation/Pre-Prod.	E10, T6	1-Apr-94	2-Jan-96
Multiplier Development		4-Jan-94	31-Dec-96
Design	E11	4-Jan-94	4-Jan-95
Construction	T7, M2	4-Jan-95	3-Jan-96
Evaluation	E11, T7	4-Jan-96	31-Dec-96
Component Development		1-Jun-94	30-Dec-96
Design	E12	1-Jun-94	30-Jun-95
Construction	T8, M2	3-Jul-95	1-Apr-96
Evaluation	E12, T8	3-Apr-96	30-Dec-96
Subsystems to 360GHz		4-Apr-94	31-Dec-96
Design	E10	4-Apr-94	1-Apr-96
Construction	T6, M2	2-Jan-96	30-Sep-96
Evaluation	E10, T6	1-Oct-96	31-Dec-96
System Integration		2-Jan-96	31-Dec-96

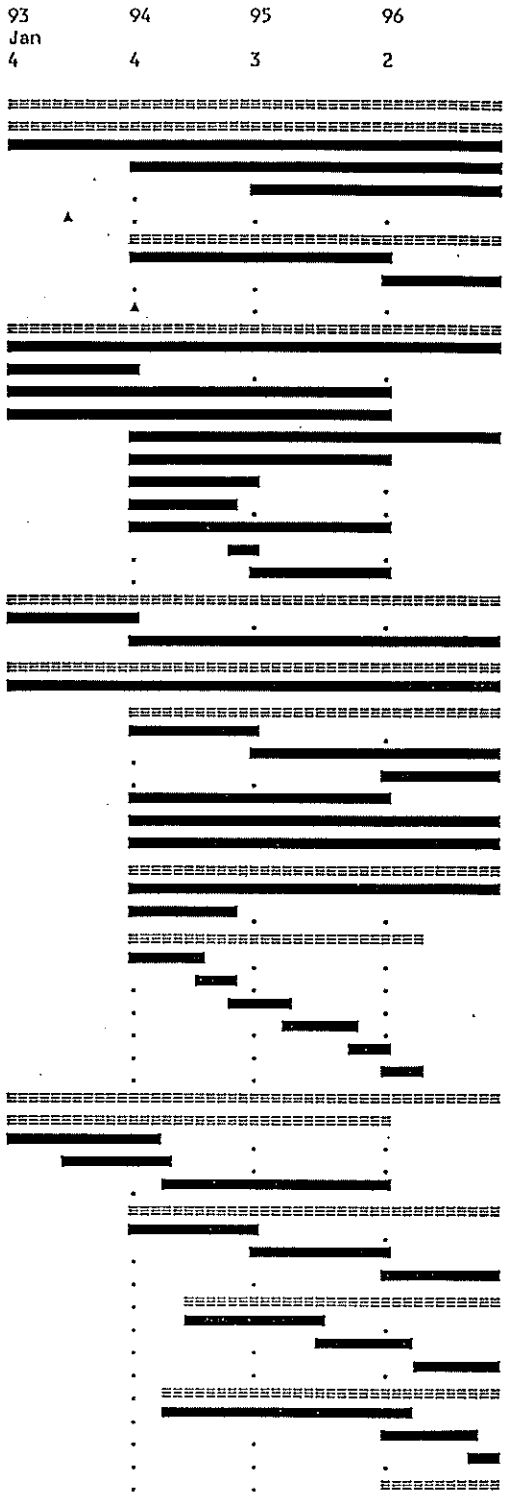

Table VI-1. Gantt chart showing task descriptions and time schedules for the *MMA Design and Development Plan.* *(Continued on next page)*

Task Name	Resources	Start Date	End Date
With LO Ref. Dist.	E12, T8	3-Apr-96	31-Dec-96
With Receiver	E11, T7	2-Jan-96	31-Dec-96
REFERENCE FREQ. TRANSMISSION		4-Jan-93	31-Dec-96
Phase stable link study	E16, T11	4-Jan-93	3-Jan-95
Construct/Test Prototype	E16, T11	3-Jan-95	31-Dec-96
IF PROCESSING		4-Jan-93	31-Dec-96
SSB mixer study	E16, T11	4-Jan-93	3-Jan-95
IF Filtering	E17, T12	3-Jan-95	31-Dec-96
DATA TRANSMISSION		4-Jan-94	24-Dec-96
Sampler/Fiber/Delay	E18, T13	4-Jan-94	24-Dec-96
MONITOR & CONTROL		4-Jan-94	31-Dec-96
Construction	E19, T14	27-Dec-94	31-Dec-96
Software	P1, P2	4-Jan-94	31-Dec-96
AIPS++ COMPUTING		4-Jan-93	31-Dec-96
Phase 1	P4, P5	4-Jan-93	30-Dec-93
Phase 2	P4, P5, P6	4-Jan-94	31-Dec-96
CORRELATOR		4-Jan-93	31-Dec-96
Strawman XF/FX Design	E25	4-Jan-93	31-Dec-93
XF/FX chip development	E26	4-Jan-94	3-Aug-94
Final chip development	E26, E25	4-Aug-94	3-Aug-95
Correlator detail design	E25, E26, T19	3-Aug-95	31-Dec-96
CRYOGENICS		4-Jan-94	31-Dec-96
JT System Evaluation		4-Jan-94	31-Dec-96
Construct 5 Systems	T10	4-Jan-94	3-Jan-95
Control/monitor	E15, T10	4-Jan-94	3-Jan-95
Long term test	T10, E15	4-Jan-95	2-Jan-96
Improve Reliability	E15, T10	3-Jan-96	31-Dec-96
Evaluate Boreas coolers	E15	4-Jan-94	23-Jan-95
PROTOTYPE RECEIVER		4-Jan-94	5-Jan-96
Receiver Specifications	E1	4-Jan-94	7-Apr-94
Optical Design	E2	4-Jan-94	12-Jul-94
Dewar Design	E1	8-Apr-94	11-Jul-94
Detailed Receiver Des.	E2, E1	12-Jul-94	24-Mar-95
Construct Prototype Rx	E2, T1, T2, E1	27-Mar-95	5-Jan-96
SYSTEM TESTING		2-Jan-96	30-Dec-96
Test prototype Antenna	E9, E21	2-Jan-96	30-Dec-96
Test Prototype Receiver	E2, T1, T2, E1	2-Jan-96	30-Dec-96

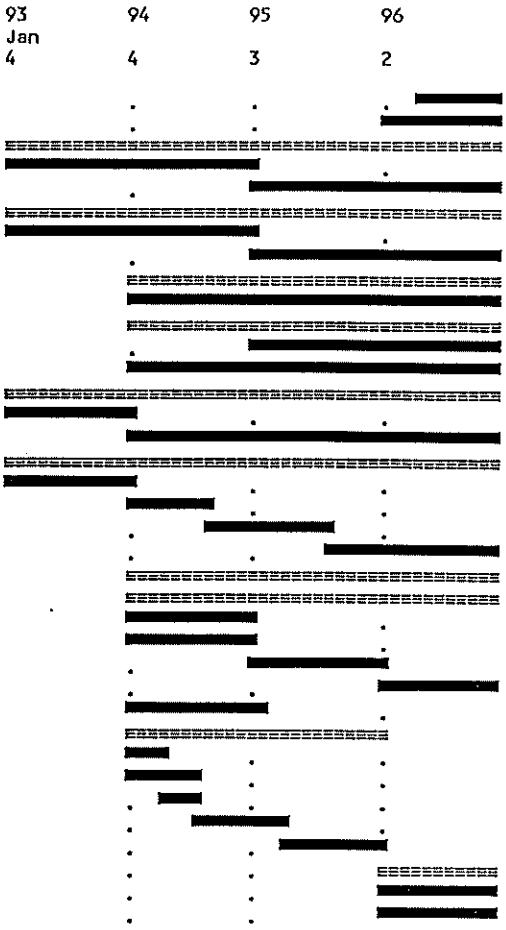

Detail Task Summary Task Baseline
(Progress) (Progress) Conflict
(Slack) (Slack) Resource delay
Progress shows Percent Achieved on Actual Milestone
Scale: 4 weeks per character

Table VI-1. *(Continued)*

Table VI-2. Total Labor Requirements (Work Years)

	1993	1994	1995	1996	Total
Contracts (C)			1.0	1.0	2.0
Engineer (E)	4.5	21.2	23.7	24.0	73.4
Technician (T)	2.5	10.5	16.9	15.3	45.2
Programmer (P)	2.0	6.0	6.0	6.0	20.0
Scientist (S)	0.5	2.5	2.5	2.5	8.0
Machinist (M)	1.0	1.2	1.7	1.5	5.4
Total Labor by Year	10.5	41.4	51.8	50.3	

TOTAL COST OF PROPOSED MMA DEVELOPMENT PROGRAM

	1993	1994	1995	1996	SUBTOTAL	TOTAL
ADMINISTRATION						$1,226,125
Labor	$32,901	$65,540	$131,080	$131,604	$361,125	
Lab/Office space		$130,000	$130,000	$130,000	$390,000	
Refurbish Shop Equipment		$50,000	$50,000	$50,000	$150,000	
Materials/Travel	$25,000	$100,000	$100,000	$100,000	$325,000	
SITE EVAL,ACQSN & USE PLAN						$1,337,800
Labor		$32,770	$32,770	$132,260	$197,800	
EIS contract	$350,000	$350,000	$100,000		$800,000	
Material cost	$40,000	$50,000	$50,000	$200,000	$340,000	
ANTENNA DEVELOPMENT						$4,450,404
Labor	$112,167	$403,806	$450,117	$84,314	$1,050,404	
Material cost	$25,000	$125,000	$125,000	$125,000	$400,000	
Study Contracts		$200,000	$150,000	$150,000	$500,000	
Build Prototype Antenna			$2,500,000		$2,500,000	
ARRAY IMAGING STUDIES						$497,190
Labor	$32,901	$131,080	$131,080	$132,129	$427,190	
Material Cost	$10,000	$20,000	$20,000	$20,000	$70,000	
SIS MIXER DEVELOPMENT						$4,605,663
Labor	$88,965	$522,100	$522,547	$583,031	$1,716,663	
Material cost	$50,000	$430,000	$450,000	$420,000	$1,350,000	
Contracts						
UVA SIS Mixer fab.	$150,000	$303,000	$303,000	$303,000	$1,059,000	
Hypres second source		$100,000	$100,000	$100,000	$300,000	
Other		$60,000	$60,000	$60,000	$180,000	
HFET AMPLIFIERS						$1,120,582
Labor		$226,544	$229,696	$144,342	$600,582	
Material cost	$35,000	$70,000	$20,000	$20,000	$145,000	
HFET Contracts		$125,000	$125,000	$125,000	$375,000	
LOCAL OSCILLATOR						$1,560,127
Labor	$112,352	$226,255	$248,627	$302,893	$890,127	
Material cost	$35,000	$190,000	$190,000	$255,000	$670,000	
REFERENCE FREQ. TRANSMISSION						$551,500
Labor	$56,083	$55,860	$111,943	$112,614	$336,500	
Material cost	$10,000	$35,000	$100,000	$70,000	$215,000	
IF PROCESSING						$596,500
Labor	$56,083	$55,860	$111,943	$112,614	$336,500	
Material cost	$10,000	$50,000	$100,000	$100,000	$260,000	
DATA TRANSMISSION						$504,266
Labor		$111,720	$111,720	$110,826	$334,266	
Material cost		$20,000	$75,000	$75,000	$170,000	
MONITOR & CONTROL						$710,410
Labor		$132,868	$242,800	$244,742	$620,410	
Material cost		$20,000	$30,000	$40,000	$90,000	
AIPS++ COMPUTING						$802,513
Labor	$131,080	$196,620	$196,620	$198,193	$722,513	
Material cost	$20,000	$20,000	$20,000	$20,000	$80,000	
CORRELATOR						$644,305
Labor	$32,901	$92,280	$150,446	$178,678	$454,305	
Material cost	$30,000	$100,000	$30,000	$30,000	$190,000	
CRYOGENICS						$647,758
Labor		$111,720	$113,424	$112,614	$337,758	
Material cost	$40,000	$100,000	$85,000	$85,000	$310,000	
PROTOTYPE RECEIVER						$667,299
Labor		$131,342	$202,382	$3,575	$337,299	
Material cost		$60,000	$200,000	$70,000	$330,000	
SYSTEM TESTING						$355,938
Labor				$355,938	$355,938	
TEST EQUIPMENT	$100,000	$1,000,000	$899,190			$1,999,190
LABOR TOTAL					$9,079,380	
GRAND TOTAL	$1,585,453	$6,204,365	$6,999,385	$5,488,367		$22,277,570

Table VI-3. Total Cost of the *MMA Design and Development Plan.*

MODEL	Description	no	Cost	
HP 85106C	Millimeter wave network analyzer		$132,500	
	Includes HP 83621A Synthesizer			
	HP 8350B/83540A(2-8.4GHz Source)			
	Option.010 Time Domain			
HP V85104A	Test Set Modules(*2)(50-75GHz)		$64,000	
HP W85104A	Test Set Modules(*2)(75-110GHz)		$70,000	
	WR-6 90-140 GHz RF modules		$31,275	est
	WR-6 110-170 GHz RF modules		$36,225	est
	WR-4 170-260 GHz RF modules		$41,375	est
	WR-3 220-325 GHz RF modules		$52,500	est
	Printer		$1,500	est
HP 8517A	S-Parameter Test Set(0.045-50GHz)		$41,000	
HP 83651A	Synthesized source(.01-50GHz)		$49,900	
HP 8566B	Spectrum Analyzer(100Hz-325GHz)		$64,500	
HP 11974Q	Preselected mm mixer(33-50GHz)		$14,600	
HP 11974V	Preselected mm mixer(50-75GHz)		$16,500	
HP 11970W	Harmonic Mixer(75-110GHz)		$3,270	
	Harmonic Mixer(110-170GHz)		$5,000	est
	Harmonic Mixer(170-260GHz)		$5,000	est
	Harmonic Mixer(220-325GHz)		$5,000	est
HP 8595A	Spectrum Analyzer(9KHz-6.5GHz)	3	$62,250	
HP 54504A	Digitizing Oscilloscope	3	$20,250	
HP 3561A	Signal Analyzer(0.000125Hz-100KHz)		$13,500	
	Keating Power meter(30GHz-1.2THz)		$15,000	
	Mask Aligner(3" wafers)		$200,000	
	Load-locked Scanning Electronic Microscope		$120,000	
HP8508A	Phase Meter(Vector Voltmeter)		$7,500	
HP8158B	Optical Attenuator		$7,570	
HP8100BS	Optical Power Splitter	4	$17,360	
HP81210L1	Optical Isolator	4	$17,400	
HP81310L1	Optical Isolator	4	$17,400	
HP8153A	Lightwave Multimeter		$16,100	
HP11982A	Amplified Lightwave Converter		$13,300	
	Oven for component testing		$10,000	
	General Purpose Oscilloscopes	3	$6,000	
	IF sweeper		$8,000	
	IF power meter		$3,000	
	VXI Boxes/Modules	3	$33,000	
	MM-Wave signal sources(YTO/mult)	6	$210,000	
WLTN563	Scalar Network Analyzer		$8,000	
	X-Y plotters	3	$9,000	
HP5345A	Frequency counter(DC-110GHz)		$35,000	
	RF Power meters(10-350GHz)	6	$60,000	
HP5508A	Measurement Display		$7,040	
HP5518A	Laser Head		$7,040	
HP10751A	Air Sensor		$4,400	
HP10754A	Dimensional Metrology Analysis Software		$1,200	
HP10777A	Optical Square		$4,500	
HP10793A	Laser Head Cable		$240	
HP55280A	Linear Measurement Kit		$4,400	
HP55281A	Angular Optics Kit		$4,900	
HP55282A	Flatness Accessory Kit		$2,900	
HP55283A	Straightness Measurement Kit		$7,400	
MVNA 8-350	Millimeter Vector Analyzer		$140,000	
HG-D	Millimeter Harmonic Generator		$8,200	
HM-D	Millimeter Harmonic Mixer		$8,200	
R3271	Spectrum Analyzer(26 GHz)		$32,000	
OS3702	IR Thermometer		$2,745	
HP6674A	Programable Power Supply		$4,300	
HP54504A	Digitizing Oscilloscope		$6,750	
	E-size Electrostatic Plotter		$9,000	
	Miscellaneous Equipment		$200,000	
	TOTAL TEST EQUIPMENT		$1,999,190	

Table VI-4. Major items of test equipment that are required.

VII. MANAGEMENT

Management of this entire activity provides genuine challenges and requires human resources. Figure VII-1 illustrates the organizational structure of the MMA design and development program, with some of the responsible individuals named.

The MMA organization is patterned after the organization used successfully by the NRAO for construction of the VLA and the VLBA. There is, however, one novel addition to the MMA organization: the Joint Development Group (JDG), the function of which is described below.

Ultimate responsibility for the conduct of the *MMA Design and Development Plan* rests with the NRAO Director. He is guided by the MMA Advisory Committee, a body of knowledgeable scientists unaffiliated with the NRAO which meets annually to review progress. The advisory committee, or some subgroup thereof, also meets on an *ad hoc* basis to address critical and pressing issues.

The Project Manager and Project Engineer oversee the activities of the scientists and engineers involved with the MMA development work. It is their responsibility to define tasks, establish priorities, allocate resources, and communicate progress both to others involved with the program and to the community at large. They are assisted in these tasks by the advice of two Project Scientists, one of whom is a specialist in the specific requirements for spectroscopic observations and the other in the demands of continuum observations.

Development of the MMA receiving system is a multifaceted program involving two different cryogenic front-end subsystems—HFET amplifiers and SIS mixers—which are provided with a common local-oscillator source and a common intermediate-frequency transmission system. Integrating the development of the capabilities of the front ends, the IF, and the correlator is the responsibility of the Systems Engineer. Work on the specific aspects of the receiving system is carried out by focused engineering groups working under the leadership shown in Figure VII-1.

Antenna design and design of the telescope optics will be carried out in Tucson, Arizona, by a small engineering group which is to be augmented in later years by engineers working at present on the design and construction of the Green Bank Telescope. MMA site development, and coordination where necessary with the antenna-transporter design, is the responsibility of engineers and scientists based in Socorro, New Mexico. Similarly, the MMA imaging simulations, configuration studies, and definition of the software requirements for the MMA will be coordinated by the individuals responsible for the development of many of the imaging algorithms now in common usage at synthesis telescopes worldwide. Development of MMA imaging software is also an area where the JDG will have an extensive involvement.

The Joint Development Group is a mechanism by which the experience in university groups can be brought to bear on specific MMA development issues. We expect to see JDG university participation in essentially all the activities

shown in Figure VII-1. As with all the activities shown, the JDG work will be coordinated by the Project Manager and the Project Engineer, but the day-to-day contact between the NRAO and cooperating JDG university groups will be at the working-group level. The JDG concept is new to the NRAO. It has the potential to provide an efficient way to "recruit" experienced millimeter-wave astronomers and instrument builders to the MMA project without disrupting their personal lives or professional careers. If the JDG model is successful it has a natural extension to the operational phase of the instrument. Working together with the university groups, we expect, during the MMA development phase, to define the role and guide the fruitful evolution of the JDG.

With the four years of effort described in the previous sections having passed, design and prototyping of all the critical MMA technical components will have been completed. A prototype antenna will exist, instrumented with prototype receivers and ancillary instrumentation. Tests of the performance of the antenna under a variety of changing environmental conditions will have been made and the operational modes demanded of the antenna (e.g., beam switching, rapid positioning) will then be evaluated. The sensitivity, tunability, and flexibility of the receiving equipment will be assessed in light of the MMA requirements.

The prototype MMA hardware is the most visible "product" of the MMA design and development program. Less visible but equally important are the people available and trained in the construction of MMA instrumentation through their work in fabricating the prototypes. In fact, a major rationale for constructing prototypes is that it provides us an opportunity to establish the fabrication and test facilities that will allow us to construct, reproducibly, the MMA instrumentation. In 1997 the technical designs will exist, the prototype fabrication/test facilities will exist, the fabrication techniques will have been established, and experienced people responsible for MMA construction will be well prepared.

An important management concern in a large construction project, like the one at hand, is to provide not only the resources but also the focus for the individuals responsible for construction. Thus there should be minimal involvement (i.e., no obligatory entanglement) with other observatory activities. Once the site for the MMA has been chosen, efforts will be made to concentrate much of the MMA design and development team in the community nearest the site. The array staffing, technical effort, and management will grow from this nucleus to become the group building the MMA in 1997.

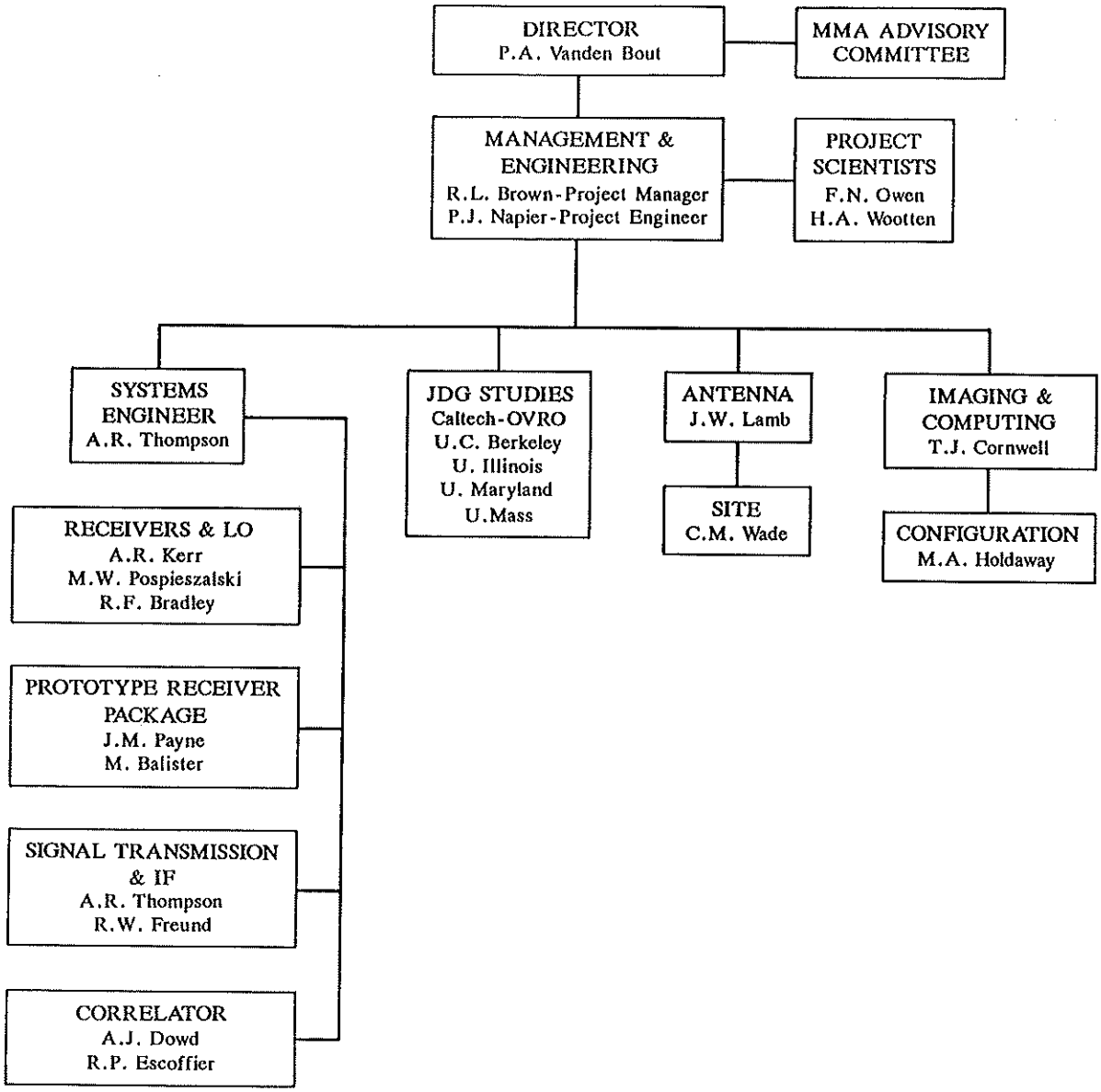

Figure VII-1. Organization chart for the *MMA Design and Development Plan.*

VIII. APPENDIX

Copies of those Millimeter Array Memoranda (Nos. 65–72, 79, and 83–88) which were referenced in the preceding sections are appended below.

MILLIMETER ARRAY
MEMO NO. 65

Some Considerations on the IF and Transmission System of the Millimeter Array.

A. R. Thompson

April 19, 1991

This memo outlines some preliminary ideas for the part of the receiving system of the MMA that takes the signals from the front-end outputs and delivers them in digital form to the inputs of the correlator. The IF amplifiers following the SIS mixers used in the highest frequency bands will probably have frequency passbands from 1 to 2 GHz, and the outputs of FET front ends can easily be converted to the same band. It will therefore be assumed that the front end outputs consist of two or four such IF bands carrying signals of two frequency bands and/or polarizations. It will also be assumed that the inputs of the correlator consist of four level (two-bit) digital data covering a total signal bandwidth of 2 GHz, divided into at least eight bands. These figures are consistent with the specifications in the MMA proposal document. They are intended to provide a basis for preliminary discussion of system details, and may well be changed several times as the system evolves. Note that much of the following discussion would also be applicable to an upgrade of the VLA receiving system.

(1) A System with Analog Signal Transmission.

Some insights on possible system arrangements can be obtained by considering how similar problems are handled in the VLA and VLBA. In the VLA the signal is transmitted in analog form in the waveguide. A diagram of a system for the MMA using analog transmission in optical fibers is shown in Fig. 1. A total of 2 GHz is selected from the four IF bands and modulated onto an optical fiber transmission line that runs from the antenna to the central building where the correlator is located. The 2 GHz bandwidth can probably be accommodated on a single fiber, so the IF signals could be combined in a frequency multiplex system, and demultiplexed at the output of the optical receiving system. Sideband separating mixers would be used to convert each 500 MHz-wide IF signal into two baseband channels with maximum upper cutoff frequency of 250 MHz. The samplers would run at a clock speed of 500 MHz. The specifications of the correlator given in the proposal document indicate that the 2 GHz bandwidth would be analyzed into 1024 spectral channels of width 2 MHz. Discussion at the meeting on 4/11/91 in Socorro indicated that the finest spectral resolution likely to be required is about 6 kHz, which corresponds to a velocity resolution of 0.02 km/s at 100 GHz. Thus it would be necessary to reduce the spectral channel bandwidth by a factor of about 340 which could be achieved in a recirculating correlator by a reduction in the input bandwidth by a factor of 18. Switchable filters would thus be required in the baseband amplifiers to cover bandwidths of 250, 125, 62.5, 31.25, 15.62 and possibly 7.81 MHz. With the reduced filter bandwidths the frequencies converted to baseband would be tuned across the IF passbands by varying the local oscillator used in the baseband conversion. The oscillator should be tunable in increments of no more than a few spectral bandwidths, say, 10 kHz. The same oscillator could be used for the corresponding IF band from all antennas (so long as fringe rotation is not introduced at this oscillator: see section 3). In the VLA a set of Fluke synthesizers in the Electronics Room of the Control Building perform the corresponding function.

The scheme outlined in Fig. 1 has the advantage of being about the simplest that one could devise. The serious disadvantage of it is that it involves long paths of analog signal transmission which produce some distortion, including time variation of the signal passbands resulting from temperature effects etc. Experience with the VLA has shown that passband mismatching is a source of closure errors, and that variation of the passbands is a possible limit on the calibration of closure errors (see the paper by Bagri and Thompson in the Proceedings of the VLA 10 th Anniversary Symposium, 1990). It is not easy to make a quantitative estimate of the likely limits on dynamic range imposed by variability in the transmission system, but such a limit must occur, and it can be avoided entirely by transmitting the signals in digital form. Although errors occur in digital systems also, error rates are readily measurable and can be made almost arbitrarily small. Since the signals must be digitized before correlation, there seems to be every reason to digitize them at the antennas and transmit them in digital form. One may therefore ask why analog transmission was chosen in the case of the VLA. Three reasons can be given, as follows. (1) Putting the baseband conversion, filtering, and sampling at the antennas would have increased the complexity of the equipment at the antennas which can be located as far as 21 km away from the central maintenance area, requiring access times of over an hour. (2) Tuning the narrow baseband responses to cover specific frequencies of spectral lines would have required local oscillator tunability in increments of about 1 kHz or less, and generating such LO signals with synchronous phases at each of the antennas is a complicated procedure. Note that the larger tuning increments required for the MMA greatly simplify this problem. (3) At the time that the VLA system was designed the requirements of dynamic range and the effects of closure errors were not understood.

(2) A System with Digital Signal Transmission.

Since the development of the VLA the range of signal processing functions that can be performed digitally has increased greatly, in large part due to the development of large custom design IC's based on gate arrays and of circuits with programmable functions. Also the commercial development of optical fiber components has been aimed largely, but not exclusively, at digital signal transmission. Thus to take maximum advantage of the accuracy and flexibility of state-of-the-art techniques, it would appear to be advantageous to perform essential analog processing and then get the signals into digital form as soon as possible after they are received.

A system based on digital signal transmission from the antennas is shown in Fig. 2. This system is based on that developed for the VLBA. The unit in which conversion to baseband, filtering, and amplification are performed is the Baseband Converter (BBC), which is shown in more detail in Fig. 3. By means of the input switch each BBC can be assigned to any of the four IF signals as required by the particulars of the observation. The digital outputs of the samplers go to a formatter which performs splitting or interleaving of the bit streams that may be required by the optical transmission system. Parity bits for monitoring the transmission error rates may be added at this point. The optical fiber link would have a capacity of 8 Gb/s to accommodate a 2 GHz signal bandwidth with four-level sampling. Four fibers would probably be required for each antenna. At the correlator location the data are reconstituted into eight output streams, corresponding

to the baseband signals, for further digital processing. The deformatter could also perform the parity checking mentioned above. This need not be done continuously, but would be useful as a periodic check, especially as the connectors of optical fibers are commonly a source of problems. Alternatively a check of the error rate could be obtained by transmission of a reproducible sequence of pseudo-random code.

In the BBC block diagram in Fig. 3 the local oscillator is tunable in increments of 10 kHz, which corresponds to a velocity increment of 0.03 km/s at 100 GHz, and should be fine enough for any observations with the MMA. If the required LO frequency is N times 10 kHz, a part of the oscillator output is divided by N and then compared with a 10 kHz reference to phase-lock the oscillator. The 10 kHz reference is easily established at all antennas, and for any given frequency the oscillators at the different antennas always maintain the same phase relationships. Note, however, that this scheme will only work successfully if N is not too large since the frequency division results in some generation of phase jitter in the LO. An oscillator with division from 1 GHz to 10 kHz has been satisfactorily used in Alan Rogers' design of the BBC's for the VLBA. (If the 10 kHz intervals are not fine enough other possibilities would include reconstituting the signals in analog form at the central location and then applying further filtering and resampling, as in the Australia telescope, or distributing finely tunable signals to the antennas from the central location.) The baseband filter bandwidths from 250 MHz down to about 15 MHz are too large to be implemented using operational amplifiers and switched resistors as in the VLBA design, so all of the filters would probably be implemented as custom L-C filters. The synchronous detectors in the unit are required to measure the gain by detecting the signal from a switched noise source at the receiver input (these would also be required in the system in Fig. 1). The BBC also contains a monitor and control (M/C) interface for setting of the input selector switch, the LO frequency, and the baseband bandwidths, and for readout of the synchronous detector voltages. For system maintenance there are significant advantages in placing the components of the BBC together in a single module. Each BBC processes a certain fraction of the total bandwidth, and a breakdown of one unit should not affect the others. Spare units would be available for replacement, or, better still, an additional BBC and sampler could be in place at each antenna and could be brought into operation remotely to replace a failed unit. Configuring the components in some other arrangements could save the use of an individual M/C interface for each baseband pair, but very little else. If the signals were transmitted in an analog form from the antennas the only saving would be in the 1-2 GHz LO's, for which separate units would not be required for each antenna. For the full array of 40 antennas a total of 160 BBC's would be required for operation, with perhaps another 40 spares. Although this is a rather complicated module, careful design with attention to minimization of required adjustments should make production of such numbers by NRAO a practical proposition.

(3) Fringe Rotation.

Rotation of the fringe pattern to slow to zero the fringe oscillations at the correlator outputs can be performed by inserting phase shifts at a required rate into one of the local oscillators. For each band that is processed, the fringes are stopped for the frequency that is brought to zero

in the conversion to baseband. Fringes at other frequencies within the baseband are then also stopped by the phase shifts introduced by the compensating delays. With receiving bandwidths of 1 GHz or more it is necessary to break the bandwidth down into smaller bands (eight in the schemes considered here for the VLBA) which are processed in parallel. Each of these requires different fringe offsets to stop the fringes precisely. To accomplish fringe stopping by means of LO offsets would necessitate applying a different offset to each of the oscillators used in the conversion to baseband. The full fringe rotation could be applied at these oscillators, or else the major part could be applied at an earlier LO which would be within the front end block in Figs. 1 and 2. If double sideband reception is used in the front end, the fringe stopping would be applied for a signal frequency equal to the first LO. In the system under consideration, signals within the upper or lower receiving bands are all within 2 GHz of this LO frequency. Thus if the maximum distance of an antenna from the phase reference point (taken to be at the center of the array) is 1.5 km, the maximum additional frequency offset for any baseband is 0.73 Hz. These offsets could be applied at the conversion to baseband, or digitally in the correlator, either before or after cross correlation. Stopping the additional fringe frequency after correlation would probably be the simplest. The maximum additional frequency for any antenna pair would be 2x0.73 = 1.46 Hz. The correlator output could be averaged over about (+/-) 5° of phase, i.e. 40 ms of time. Every 40 ms, for each frequency band, it would be necessary to apply a small (and different) phase shift to each of the 40x39/2 = 780 cross correlator outputs. The disadvantage of this method is that it does not accommodate phasing of the array as used in VLBI observations since the full correction is applied only to the cross products of the signals. Digital frequency correction before cross correlation may be the optimum method.

(4) Conversion to Baseband.

In the conversion of signals to baseband a sideband separating mixer (sometimes called a single-sideband mixer) is generally used. In such an arrangement the outputs corresponding to the signal and image channels of the input are separated by applying precise phase shifts, and the best isolation that is achievable is a little more than 30 dB. John Archer obtained about 32 dB consistently for the baseband mixers of the VLA, using carefully selected diodes, and hybrids and baseband quadrature networks designed and made at NRAO. After about ten years, some of these mixers have been remeasured and typically show isolation in the range 26-30 dB, presumably as a result of ageing of the components. In the sideband separating mixers of the VLBA BBC's an isolation of 26 dB can just be achieved with some difficulty, and we have no experience of how this may degrade with time. In the VLBA system, commercial mixers and hybrids are used with an IF phasing network designed by Alan Rogers. The lower isolation relative to the VLA is due, at least in part, to the wider bandwidth over which the input is tuned: 500 to 1000 MHz for the VLBA and only 100 to 150 MHz or 200 to 250 MHz in the case of the VLA. These examples illustrate a general problem: sideband separating mixers require careful design, and a great deal of time and effort to adjust, and then are little more than marginally acceptable.

An alternative to the sideband separating mixer would be the use of a regular mixer with very careful filtering to allow only one sideband in the

baseband output. Two frequency conversions would be necessary as in the scheme in Fig. 4. A band of width 250 MHz is selected from the input band of 1000 to 2000 MHz, and can be tuned over this band by conversion with a 750 to 1500 MHz oscillator. The resulting signal is passed through a sharp-sided filter covering 2500 to 2750 MHz (9.5% bandwidth). This could be converted to baseband with an LO at 2500 MHz, but it will ease the specifications of the 2500-2750 MHz filter if instead it is converted to 250-500 MHz using an LO at 2250 MHz. In this latter case bandpass sampling would be used, but the sampling frequency would be the same since it depends upon the bandwidth to be sampled. In this type of system each converter unit produces only one output band rather than two as in the case of the sideband separating mixer. However, since the two bands of the sideband separating case are not independently tunable, one can equally well process the same signal band by using the scheme of Fig. 4 with a bandwidth twice that of the lowpass filters used with a sideband separating mixer.

For a given total signal bandwidth and a given number of baseband converters, a design using sideband separating mixers uses twice as many samplers as a design based on Fig. 4, but the latter requires a sampling frequency higher by a factor of two. In the first of these schemes the critical parameters are the matching of the phase and amplitude responses of the mixers and phasing networks, and in the second the selectivity of the filters. The scheme in Fig. 4 would cost more in commercially obtainable components but should require much less adjustment during assembly. Further investigation is required to clarify the choice between these schemes.

(5) Conclusions.

(1) Digital transmission offers minimum distortion of the signals and no serious problems in its implementation have been identified.

(2) Large bandwidths require correspondingly large numbers of IF conversions to baseband (or to a low frequency passband) for sampling, and the hardware involved will comprise a fairly large part of the signal processing equipment. Adequate time should be allowed for investigating and testing the approaches discussed in section (4), in order to obtain a well engineered design before the main construction phase of the MMA is started. Configuration of the required components in a form similar to the BBC in Fig. 3 offers some practical advantages.

(3) Fringe rotation (stopping) could be performed in an analog manner in the LO's, digitally in the correlators, or by a combination of both methods. A different rotation is required for each signal band that is sampled, and further study of the system design is required before a specific scheme can be recommended. The feasibility of fringe rotation in the correlator will depend upon whether an FX or a lag design is chosen.

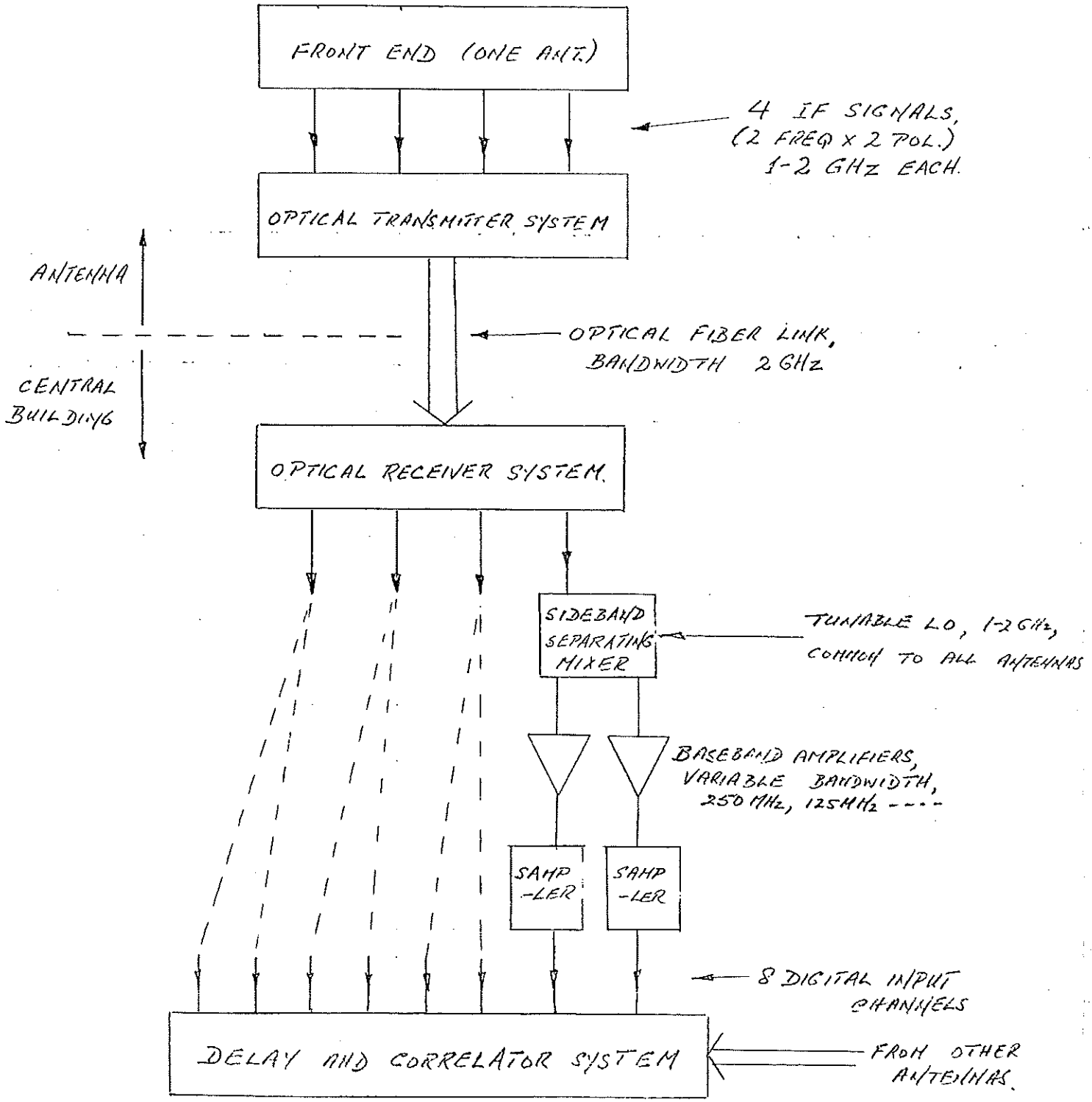

Fig. 1. System with analog signal transmission.

ART 4/18/91

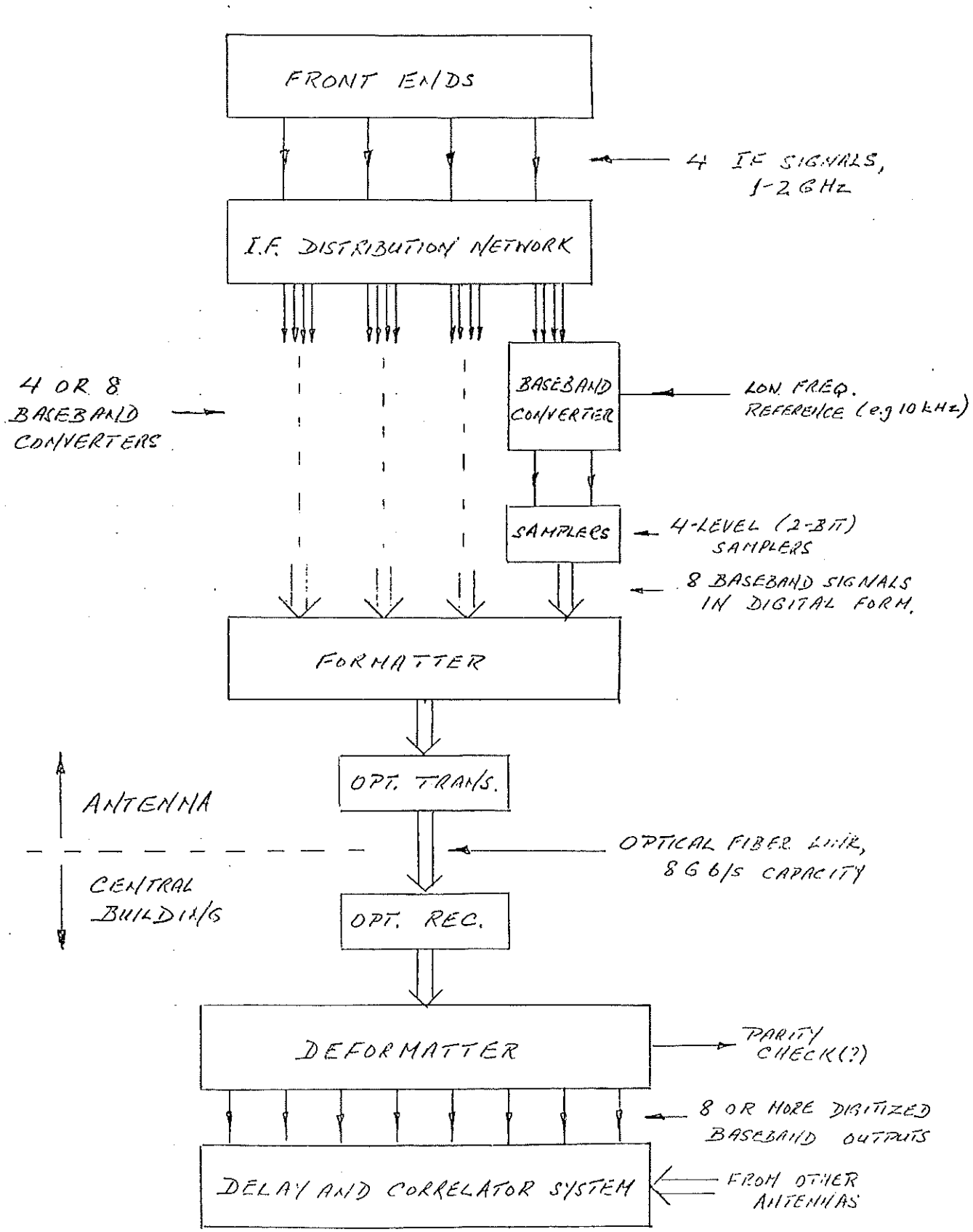

Fig. 2. System with digital signal transmission configured to include a Baseband Converter unit as in the VLBA.

ART 4/8/91

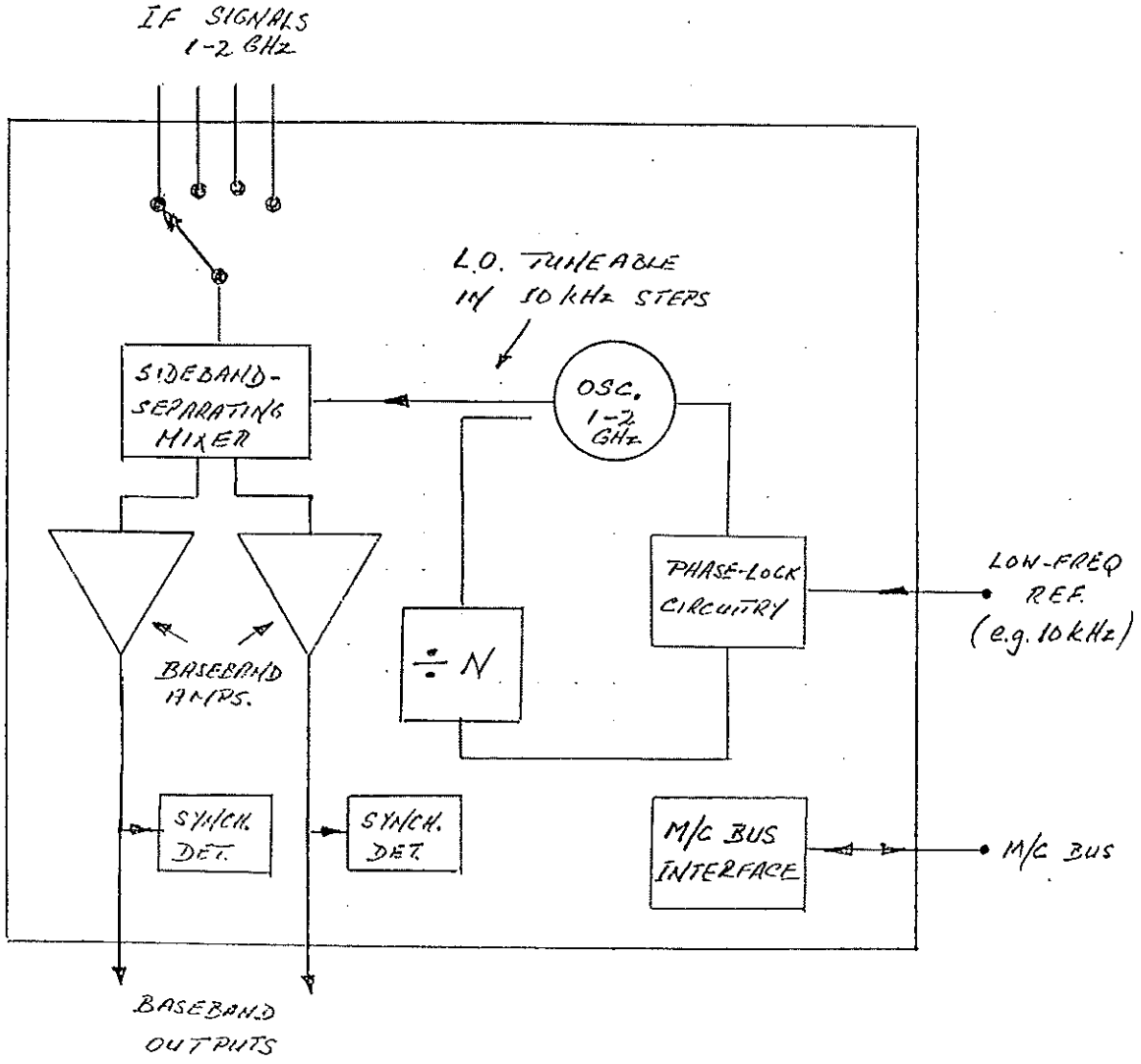

Fig. 3. Details of Baseband Converter unit in Fig. 2. The baseband amplifiers have selectable bandwidths of 250 MHz, 125 MHz, 62.5 MHz, etc.

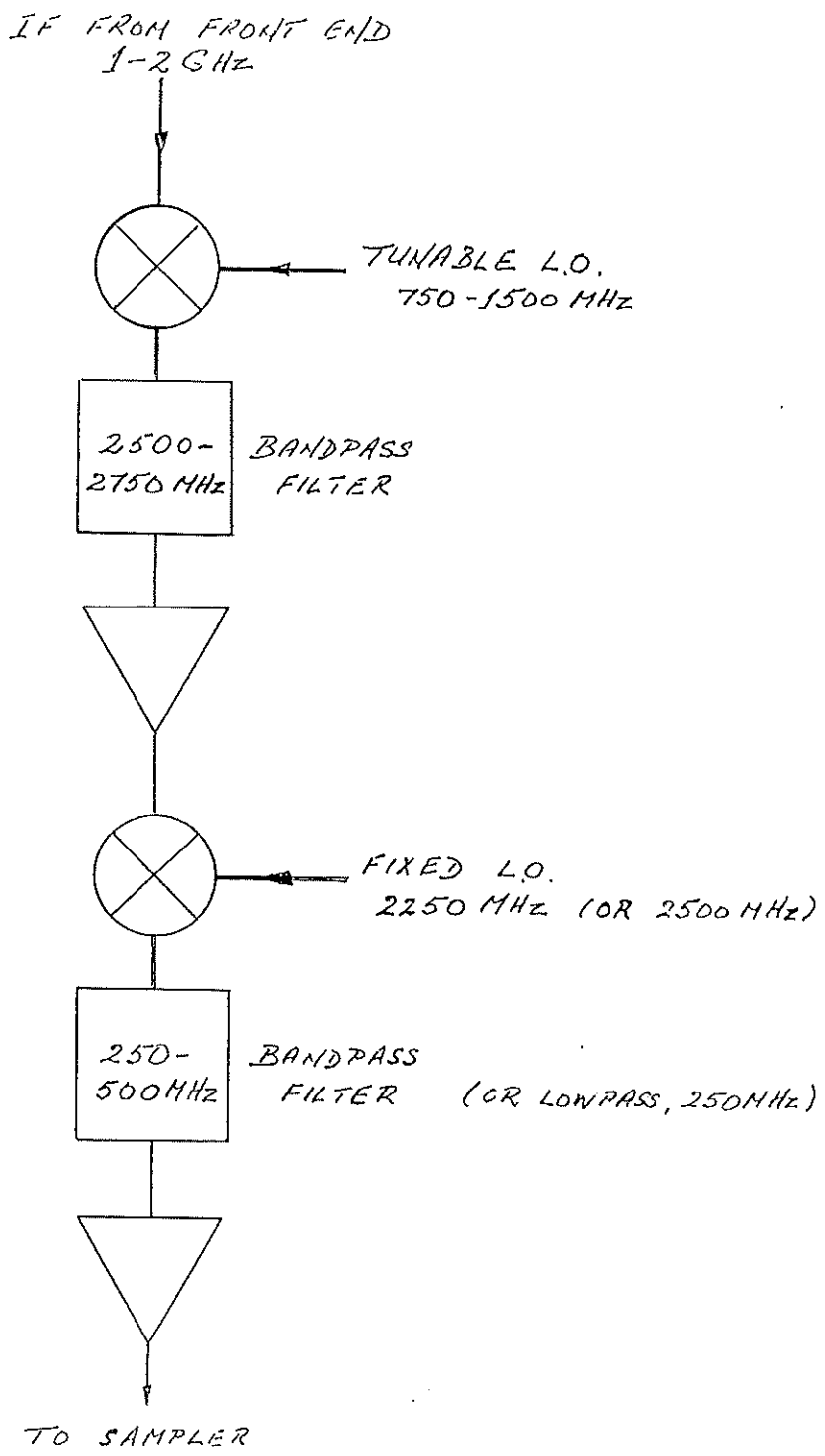

Fig. 4. Possible scheme for conversion to a baseband or bandpass spectrum for sampling, without the use of a sideband-separating mixer.

MILLIMETER ARRAY
MEMO NO. 66

MMA Correlator

Some Design Considerations

Andrew Dowd

I. Introduction

The intention of this memo is to continue the correlator discussion which began at the April meeting in Socorro. Many points were raised at that meeting. Most comments involved pushing the specifications to include more capability. Naturally, increased capability translates into greater cost. So a happy medium must be reached that gets the most bang for the buck. This paper will roughly address some of the costs associated with increased capability. On a related topic, I will initiate a discussion on the possibility of using a fiber optic system to implement the delay network.

II. Specifications

For reference, I've repeated the design specifications of the MMA correlator:

1. Number of telescopes	: N = 40
2. Maximum total bandwidth per antenna; two polarizations of 1 GHz each	: BW = 2 GHz
3. IF frequency agile separation of bandwidth, i.e., at least 500 MHz pieces of passband	: $J \geq 4$
4. Spectral frequency resolution at max. BW	: b = 2.0 MHz
5. Cross polarization mode possible at reduced capacity of BW,b or N^2	
6. Sideband separation mode (if necessary)	

III. Full Cross-Polarization

The proposal as written, specifies cross-polarization but only at reduced capacity. Some people felt it was inappropriate to force cross-polarization observations to suffer reduced capacity. Naturally, building a full-bandwidth cross-polarizing correlator will increase the size and cost of the correlator. How much additional expense is justified for this technique is a question for the astronomical community. I'll summarize some of the tradeoffs.

First, let me mention the correlator, as originally proposed, that would be operated at reduced capacity for cross-polarization. When the correlator is not performing cross-polarization, each of the polarizations from the telescope are treated like another frequency band. The difference between a single-polarization system and the proposed two-polarization system is roughly double, regardless of implementation technique. A reduced capacity cross-polarization mode does not affect the number of operations per second figure-of-merit, however, it does

increase cabling and multiplexing hardware. The proposal lists several parameters which could be reduced in order to implement the cross-polarization mode. If the correlator were required to handle any tradeoff possibility, it would greatly increase the interconnection capability. It would be beneficial to limit the tradeoff possibilities.

Naturally, to provide a full capacity cross-correlating system would increase the complexity of the system. The following table lists some of the possible configurations and the effective number of baselines that must be processed by the correlator system. This table also includes the consequences of including a total power mode which operates simultaneously with the spectroscopy mode (i.e., measuring the auto power spectra of each telescope, all the time). Note the baseline value includes these autocorrelations. This is not completely appropriate, but will be discussed in greater detail in the next section.

Table 1. Correlator Options

Fixed Parameters: 40 Antennas

1. Standard Spectroscopy, One Polarization, No Total Power Mode

   This is the classic calculation of baselines, with only one polarization measured (or both polarizations combined).

   Baselines = $40 \times 39 / 2 = 780$

2. Standard Spectroscopy, Two Polarizations, No Total Power Mode

   This is the instrument sketched by the MMA proposal. Information about polarizations is separated, but cross polarizations are only available in a reduced capacity mode.

   Baselines = $2 \times 40 \times 39 / 2 = 1560$

3. Standard Spectroscopy, Two Polarizations, Total Power Mode.

   Includes a continuous measurement of total power spectra, along with the cross power calculation.

   Baselines = $2 \times 40 \times 39 / 2 + 80 = 1640$

4. Standard Spectroscopy, Two Polarization with Full Cross Polarization, No Total Power.

   Essentially this is the same as 80-station cross correlation with 40 missing baselines, i.e., the cross polarization of the same telescope.

   Baselines = $2 \times 2 \times 40 \times 39 / 2 = 3120$
   [or $(80 \times 79 / 2) - 40$]

5. Standard Spectroscopy, Two Polarizations with Full Cross Polarization, plus Total Power AND Cross Polarization from same telescope.

Essentially a full implementation of every possible distinct cross and auto correlation.

Baselines = 80 × 80 / 2 = 3200

The follow-up question to the previous discussion of options is how they affect the size of the correlator. Well, for the two-cent answer: more baselines translate into a bigger, more expensive correlator. There are two components to consider. First, increasing the number of baselines increases the operations per second required of the digital logic. This effect is different for FX and XF type correlators. This effect is fairly easy to quantify. The other less obvious effect is in complexity. In this application, I'll use the word complexity to indicate how different modes increase the need for more hardware interconnections. This does not appear in the operations per second, but more cables and multiplexing mean greater cost and complexity.

First, the simple problem of operations per second. The XF correlator does calculations on a per baseline basis. Cross correlations cost the same as autocorrelations. Therefore, the number of operations per second will be directly proportional to the number of baselines, as defined in Table 1.

The FX correlator is not so simple. First, the FX correlator does its frequency conversion on a per station basis. In one respect, this gives the total power spectra for free. It is calculated automatically and does not require any additional hardware. In truth,some additional storage is required, but this should be a nominal increase in hardware.

Conversely, increasing the cross-polarization will increase the operations per second. However, the effect will be isolated to the cross-multiplication circuitry. The number of Fourier transform engines will not be affected. The operations per second can be quantified with the following expression [2]:

$$r_{FX} = r_{F(X)} + r_{(F)X} = r_0 \left[n_S \, n_P \, 2 \log_2 (n_T) + (n_X - n_A) \right]$$

where:

r_0 = Input sample rate (total).

n_S = Number of antennas

n_P = Number of polarizations per antenna

n_T = Number of frequency samples required

n_X = Total baselines as given in Section I.b.

n_A = any "Auto" baselines, i.e., total power spectra.

Note: *the equation does not account for separation into frequency bands, which is a proportionality constant.*

The fact that total power mode is relatively free is indicated by subtracting n_A from the baselines. The effect on correlator size of adding cross polarization will depend on whether the cross-multiplier or Fourier engine dominates the size of the spectrometer. By inserting some realistic numbers for the MMA as proposed, the addition of cross-polarization will increase the correlator size about 1.5 times. This compares to 2 times for the XF case.

Given:

$n_S = 40$
$n_P = 2$
$n_T = 1024$
$n_X - n_A$ (proposed) = 1560
$n_X - n_A$ (full cross) = 3120

Then

r_{FX} (full cross) / r_{FX} (proposed) = 1.49

The question of complexity is more difficult to quantify. But in some ways this would tend to lean towards a full cross-polarization correlator. This seems counter-intuitive, but relates to the reduction of different operating modes. Building a correlator that operates in only one mode is simpler to construct, than a fully configurable system. This is especially relevant at the operating frequencies that might be required to construct the MMA correlator. Quantifying the effects of different operating modes will be an important result of more detailed design study.

IV. Separate Wide Bandwidth Continuum Correlator

At the meeting in April, there was interest in extremely wide-bandwidth continuum observations. Building the continuum correlator into the spectroscopy correlator (like the VLA) has some nice features. However, if extremely wide bandwidths are required, it might be easier to build a separate continuum correlator.

Several things must be considered before making a determination on this issue. First, increasing the bandwidth to handle a wide-bandwidth continuum correlator has a strong influence on the IF system and receivers. Also, will the resulting continuum correlator require some minimum frequency resolution, or could a single channel analog correlator suffice?

V. Delay Lines

During my recent visits to OVRO and BIMA, I was intrigued by their delay subsystem. In both cases they use a very simple coax delay network. For their next generation of arrays, both sites are considering a delay system built on fiber optic delay networks. It is essentially identical to the coax network, but replaces the coax with fiber. It has some nice features, and we should at least consider a similar technique for the MMA.

Some rough numbers:

Maximum delay should be related to the geometry of the telescope,about 3000 m. Conversely, the smallest delay should be around the sampling period of the AD conversion. (Shorter delays will be handled in the correlator). This gives a minimum delay period of 0.5 nsec (for 2 GHz sampling, i.e., 1 GHz bandwidth per polarization). [1]

Assume a fiber optic material with n = 1.5. Therefore, 0.5 nsec translates into about 0.1 meters of cable. If we ignore the switches required to change the delay, the MMA would need a 14-section delay line matrix.

1 = 0.1 m	16 = 1.6 m	256 = 25.6 m	4096 = 409.6 m
2 = 0.2 m	32 = 3.2 m	512 = 51.2 m	8192 = 819.2 m
4 = 0.4 m	64 = 6.4 m	1024 = 102.4 m	16384 = 1,638.4 m
8 = 0.8 m	128 = 12.8 m	2048 = 204.8 m	

Minimum delay = 0.5 nsec
Maximum delay = 16.4 usec

A fiber optic delay line does not remove the need for a fractional sampling correction, but it does take care of the really long delays that would be difficult to buffer at the sampling rates required of the MMA correlator. Also, if a hybrid system is built, the digital delay circuit would be repeated for each sampler, and not each telescope like a fiber optic delay system. A fiber optic delay system could be built as an extension to the signal transmission system. If suitable switches can be obtained, the signal does not even need to leave the light domain.

Another interesting bonus of this system is it might simplify the addition of a wideband continuum correlator. It is possible that a fiber delay network could be built with plenty of bandwidth to satisfy its needs, without much additional effort. However, this would depend on several systematic questions, like the method of signal transmission.

Naturally, the big unknown in this scheme is the stability and linearity of the fiber and switches. To its favor, many of these questions must be answered for the signal transmission issue, so the two problems can be addressed together. Also, we can gain experience on the problems from the new efforts at OVRO and BIMA. I see this as an area for positive application of joint cooperation.

VI. Sampling Frequency

There has always existed a gray area in digital circuitry (roughly between 20 MHz and 80 MHz) where it was inconvenient to build large digital systems. This zone was between the competing techniques of TTL logic and ECL logic. Building a circuit within the grey area either meant pushing TTL beyond its limit or using the costlier and more power hunger ECL at a relative crawl.

During recent discussions with several correlator builders, in particular Steve Padin at OVRO, it appears another grey area might exist at a higher frequency range. The frequency range in question is not a problem for available

chip technology, instead for connector technology. For systems below about 150 MHz, it is possible to use high density, fairly simple connectors. It is even possible to use edge connectors for short jumps. However, above this point, the connectors must revert to more traditional coax techniques such as SMA, etc. On circuit boards, the signals must be impedance matched to give a good 50-ohm transmission line.

Naturally, all these arguments are dependent on the distance the signal must travel. To a certain point, increases in chip level integration will improve the situation. However, within the limits of present integrated chip design, it is difficult to use simple connector techniques above 150 MHz.

The consequence of this situation is to affect the operating clock rate of the correlator. The clock rate should be held below 150 MHz to take advantage of the simpler technology. Conversely, if the clock rate is to be above this value, it should be pushed higher to take advantage of the circuit gains associated with higher operating speeds. In other words, it might be better to use a 500 MHz sampling speed over 250 MHz. Once the difficulty of a high sampling rate is accepted, the maximum benefit should be engendered.

VII. References:

[1] Thompson, et al. *Interferometry and Synthesis in Radio Astronomy*, Section 7.3, page 200, "Delay Setting-Tolerances"

[2] Romney, Jonathan, VLBA Correlator Memo 60, "Introduction to the Spectral-Domain ('FX') Correlator", May 5,1986.

MILLIMETER ARRAY
MEMO NO. 67

HFET'S AND RECEIVERS FOR THE MILLIMETER-WAVE ARRAY

M. W. Pospieszalski
August 12, 1991

1. Introduction

There has been considerable progress in the performance of HFET's (or as they are known by other names: MODFET's, HEMT's, TEGFET's) at millimeter wavelengths in the past several years. This memorandum attempts to assess the possible impact of these developments on the design of receivers for the Millimeter-Wave Array and to identify important research issues pertaining to HFET's which should be answered before the electronics design phase begins.

2. HFET Amplifiers

A summary of the typical performance of NRAO cryogenic HFET amplifiers is presented in Figure 1. The noise temperature data are referred to the cold input of the amplifiers [1], [2]. The noise performance of these amplifiers is plotted with the minimum noise measure of the FHR02X HEMT, a quarter-micron gate device available from Fujitsu. Also, the noise temperature of the 38-45 GHz amplifier is plotted with the minimum noise measure of the .1 μm gate PHEMT device from ROHM Research [3], [4]. The data for the 4 K masers [5]-[7] are given for comparison. The amplifier examples demonstrate that for a bandwidth of around an octave or less the amplifier average noise temperature is equal to the minimum noise measure at the highest frequency within the band.

An excellent agreement between predicted and measured noise performance of the amplifiers [1], both at room and cryogenic temperatures, was a result of the development of a FET noise model [8]-[10]. This model allows also for a reasonable prediction of future performance. A minimum noise measure vs. frequency of a "futuristic" HFET is presented in Figure 2 for different ambient temperatures. A model of this device was created by assigning to the equivalent circuit of a current experimental HFET [11] the values of equivalent gate and drain temperatures (which determine the noise properties of a device) measured on the best devices currently being used in the construction of amplifiers at NRAO.

The "futuristic" device under consideration was the .15 μm long gate HFET using AlInGa/GaInAs on an InP wafer structure from GE [11]. The published room temperature noise measure data of GE devices [11] fit extremely well the model prediction, as do the data from Hughes and TRW on similar devices [12], [13]. The data for this device at other ambient temperatures were obtained under the assumption that the equivalent gate and drain temperatures behave like those for .15 μm ROHM Research HFET routinely used in our laboratory. Therefore, the term "futuristic" used for this device reflects only an uncertainty about its cryogenic performance.

3. HFET's as Sources of Millimeter-Wave Power

The output power of state-of-the-art HFET's for frequencies up to 100 GHz is now comparable with that of Impatt diodes and better than Gunn diodes [14]. Recent HFET results are summarized in Figure 3 [14] (an extensive comparison with other sources is given in [15]). Current millimeter-wave systems are using phase-locked Gunn oscillators and whisker-contacted Schottky-diode frequency multipliers as the sources of local oscillator power. Both Gunn oscillator and multipliers require mechanical tuning. A notable exception is the design of LO chain for the FCRAO 15-element array [16] in which a phase-locked YIG is followed by a wideband FET power amplifier and a cryogenic, fixed-tuned multiplier to deliver more than 4 mW of over 88 to 115 GHz range [16]. Not much information is available on fundamental FET oscillators in W-band and above, although FET oscillators or oscillator-(multiplier)-power amplifier chains are replacing diode oscillators (Gunn, Impatt) in most applications at lower microwave frequencies. Also, no information is available on cryogenic properties, either on FET fundamental oscillators or power amplifiers, but it is expected that their performance should greatly improve upon cooling.

4. Impact of Advances in HFET Technology on the Design of Receivers for the Millimeter-Wave Array

A reasonable attempt to predict the future in a rapidly developing field of technology should be based on:

- an assessment of the rate of development of a given field which, in most cases, is determined by the interest it generates from the point of view of military and commercial applications;

- an understanding of the limitations of current technology.

Both low-noise HFET's and power HFET's are in the focus of many research programs and their development will continue to be strongly driven by military and commercial markets. An understanding of their noise, small signal and large signal characteristics and underlying technology limitations is now emerging. Computer-aided design tools, both commercial and in-house, are now available.

The consequences of this progress on the development of receivers for the MMA cannot be overestimated. It is interesting to recall that the first paper on cryogenic properties of HFET's was published in 1985 [17]. It reported on X-band measurements of a couple of experimental HFET's developed at Cornell University. Today all receivers for the VLBA employ HFET's amplifiers. The performance of these receivers and also of SIS/HFET IF [20] receivers is compared in Figure 4 (courtesy of A. R. Kerr) with the predicted performance of receivers employing <u>current</u> experimental devices (compare Figure 2). It becomes rather obvious that HFET receivers would be the preferred solution, not only in the 9-mm window atmospheric window but also in the 3-mm window. (The MMA proposal suggests the use of SIS receivers in the 3-mm window [18].)

A successful demonstration of the model-predicted performance at cryogenic temperatures of a current experimental HFET could have a tremendous impact not only on the design of the 68-115 GHz receivers, but also on receivers for other frequency bands: 130-183 GHz, 195-314 GHz and 330-366 GHz. It stems from the observation that the device capable of exhibiting ~ 50 K noise measure at 100 GHz could be used to build 10-20 GHz IF amplifiers with an average noise of 6 K. Even larger bandwidths are possible, for instance, 20-40 GHz with average noise of 20 K or so. This could facilitate the use of SIS junctions as wideband frequency converters with considerably relaxed requirements for LO tuning. Not only would it allow the instantaneous access to a large bandwidth for radio astronomy observations, but also it would greatly simplify the separation of sidebands. Both of these issues are now perceived as challenging design and engineering problems in the current MMA design concept [19].

Finally, HFET's could provide sufficient local oscillator power at frequencies in excess of 100 GHz, and probably under cryogenic cooling up to 200 GHz. Also, a combination of HFET amplifiers and varactor (or HFET) multipliers (possibly also cryogenically-cooled) for local oscillator applications throughout millimeter-wave range is ultimately to be extremely competitive with current solutions.

5. Conclusion

There are several areas in which a concentrated NRAO effort should be strongly encouraged:

- evaluation, testing and establishment of small signal and noise models of currently available experimental HFET's at room and cryogenic temperatures (an effort similar in scope to that established during the development of receivers for the Voyager/Neptune encounter),

- evaluation, testing and establishment of nonlinear device models (also for cryogenic temperatures) for power HFET's at millimeter wavelengths,

- a study of SIS junctions as frequency converters with high IF frequency (the properties may differ from those of current low-IF mixers due to the fact that IF frequency energy quanta are no longer negligible compared with the band-gap energy; also the impedances at both sidebands would be drastically different [19]), and

- a study of the interaction between an SIS mixer and its IF amplifier with high IF and wide bandwidth (*e.g.*, 10-20 GHz or 20-40 GHz). This interaction can profoundly affect the overall noise performance of the receiver [19].

HFET technology, both in low-noise and power applications, is the most dynamically developing field among those likely to influence the design of the MMA. Answers to the questions posed in the preceding could influence the design of SIS mixers (wideband IF vs. narrow-band IF), local oscillators (HFET power amplifiers and HFET oscillators vs. Gunn diode oscillators), cryogenic

systems (4 K vs. 12 K coolers), optics (sideband separation), multiple-frequency operation, and signal transmission (IF bandwidth). In essence, HFET and related development may not be viewed as possibly leading to a replacement of one building block with another, but as having a profound effect on the whole MMA receiver design.

6. References

[1] M. W. Pospieszalski, J. D. Gallego, and W. J. Lakatosh, "Broadband, Low-Noise, Cryogenically-Coolable Amplifiers in 1 to 40 GHz Range," in *Proc. 1990 MTT-S Int. Microwave Symp.*, pp. 1253-1256, Dallas, TX, May 1990.

[2] M. W. Pospieszalski, "Cryogenically-Cooled, HEMT Amplifiers and Receivers in 1-50 GHz Range: State-of-the-Art," *IAU Colloquium No. 131: Radio Interferometry - Theory, Techniques and Applications*, Socorro, NM, October 1990.

[3] R. E. Lee, *et al.*, "Ultra-Low-Noise Millimeter-Wave Pseudomorphic HEMT's," *IEEE Trans. on Microwave Theory and Tech.*, vol. MTT-37, pp. 2086-2092, Dec. 1989.

[4] S. Weinreb, *et al.*, "Millimeter-Wave Noise Parameters of High Performance HEMT's at 800 K and 17 K," in *Proc. 1989 IEEE Int. Microwave Symp.*, pp. 813-816, Long Beach, CA, June 1989.

[5] S. M. Petty and D. L. Trowbridge, "Low-Noise Amplifiers," in *Deep Space Network - Radio Communications Instrument for Deep Space Exploration*, JPL Publication 82-104, Jet Propulsion Laboratory, California Institute of Technology, Pasadena, CA, July 1983.

[6] J. Shell and D. Neff, "A 32 GHz Reflected-Wave Maser Amplifier with Wide Instantaneous Bandwidth," in *Proc. 1988 IEEE MTT-S Int. Microwave Symp.*, pp. 789-792, New York, NY, June 1988.

[7] J. Shell, private information, 1991.

[8] M. W. Pospieszalski, "A New Approach to Modeling of Noise Parameters of FET's and MODFET's and Their Frequency and Temperature Dependence," National Radio Astronomy Observatory Electronics Division Internal Report No. 279, Charlottesville, VA, July 1988.

[9] M. W. Pospieszalski, "Modeling of Noise Parameters of MESFET's and MODFET's and Their Frequency and Temperature Dependence," *IEEE Trans. on Microwave Theory and Tech.*, vol. MTT-37, pp. 1340-1350, Sept. 1989.

[10] M. W. Pospieszalski and A. C. Niedzwiecki, "FET Noise Model and On-Wafer Measurement of Noise Parameters," in *Proc. 1991 IEEE MTT-S Int. Microwave Symp.*, pp. 1117-1120, Boston, MA, June 1991.

[11] K. H. Duh, *et al.*, "W-Band InGaAs HEMT Low-Noise Amplifiers," in *Proc. 1990 Int. Microwave Symp.*, pp. 595-598, Dallas, TX, May 1990.

[12] S. E. Rosenbaum, *et al.*, "AlInAs/GaInAs on InP HEMT Low-Noise MMIC Amplifiers," in *Proc. 1991 Int. Microwave Symp.*, pp. 815-819, Boston, MA, June 1991.

[13] P. D. Chow, *et al.*, "Ultra Low-Noise High Gain W-Band InP-Based HEMT Downconverter," in *Proc. 1991 Int. Microwave Symp.*, pp. 1041-1044, Boston, MA, June 1991.

[14] P. M. Smith, *et al.*, "Microwave and Millimeter-Wave Power Amplification Using Pseudomorphic HEMT's," *Microwave Journal*, vol. 33, p. 71, May 1990.

[15] R. Bradley, Ph.D. thesis, to be published.

[16] N. R. Erickson, *et al.*, "15-Element Imaging Array for 100 GHz," in Proc. 1990 Int. Microwave Symp., pp. 973-977, Dallas, TX, May 1990.

[17] S. Weinreb and M. W. Pospieszalski, "X-Band Noise Parameters of HEMT Devices at 300 K and 12.5 K," in *Proc. 1985 IEEE/MTT-S Int. Microwave Symp.*, pp.539-542, St. Louis, MO, May 1985.

[18] "The Millimeter Array," NRAO proposal to the National Science Foundation, July 1990.

[19] A. R. Kerr, private communication.

[20] A. R. Kerr and S.-K. Pan, "Some Recent Developments in the Design of SIS Mixers," *Int. J. Infrared & Millimeter Waves*, vol. 11, no. 10, pp. 1169-1187, Oct. 1990.

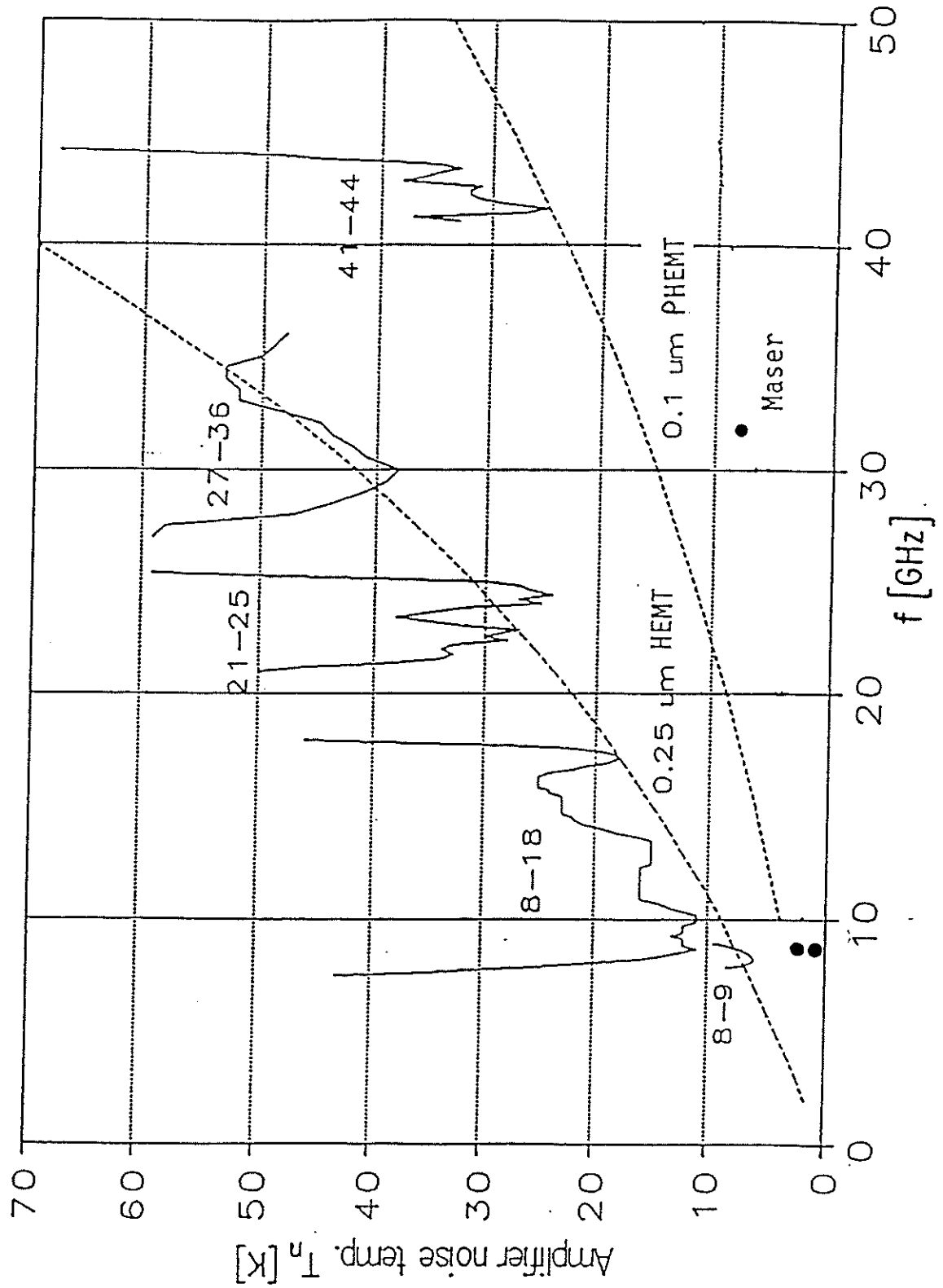

Fig. 1. Noise temperature of different amplifiers and minimum noise measure of FHR02X (.25 μm gate length) and H-CF-100-6 (.1 μm gate length) at T_a = 12.5 K. The noise performance of masers at 4 K and 1.9 K (a lower point at 8.4 GHz) is also shown for comparison.

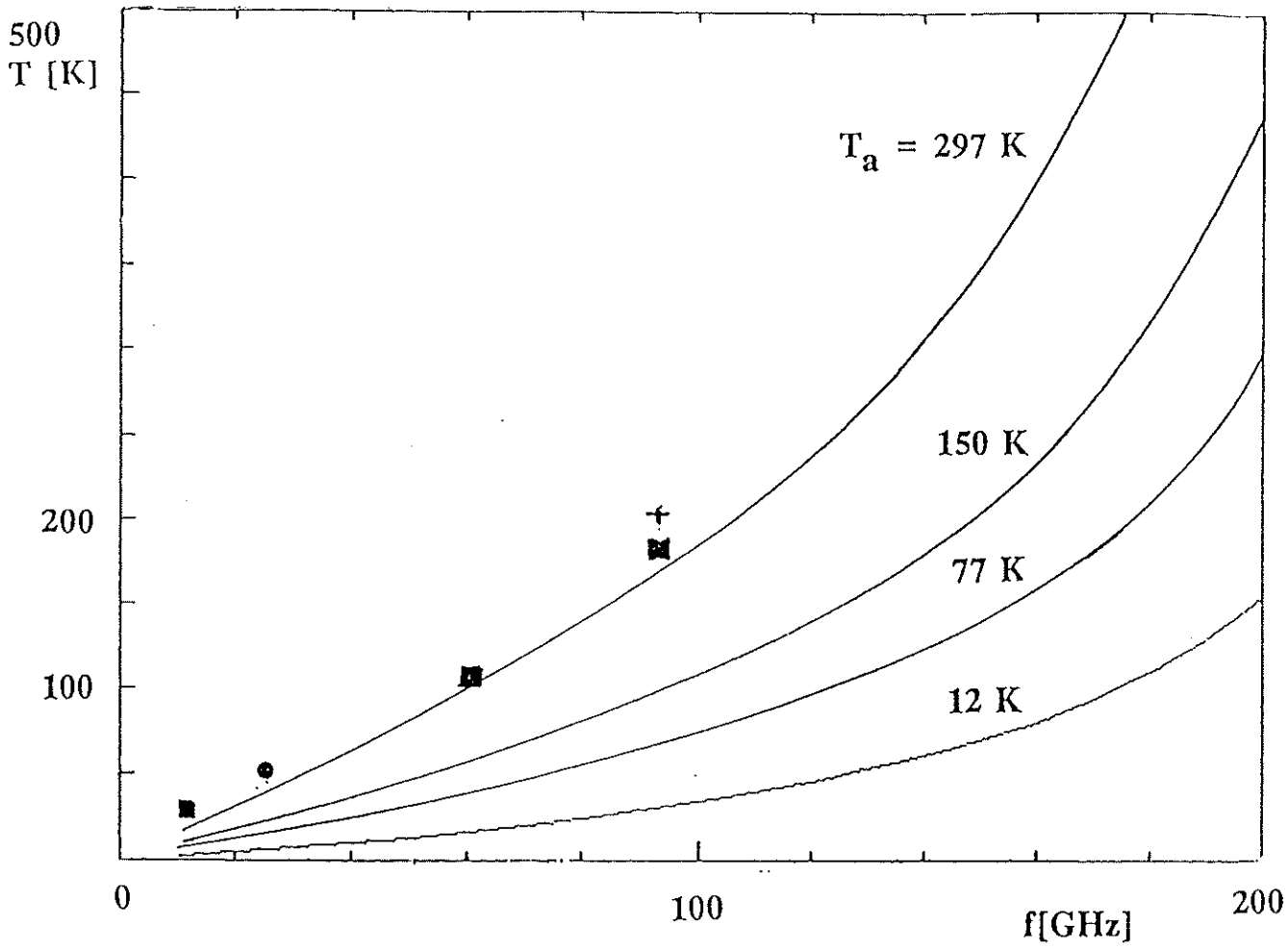

Fig. 2. A minimum noise measure of a "futuristic" HFET. Experimental results at room temperature for AlInAs/GaInAs on InP HFET's from three different laboratories are also shown: "■" GE [11], "•" Hughes [12], "+" TRW [13].

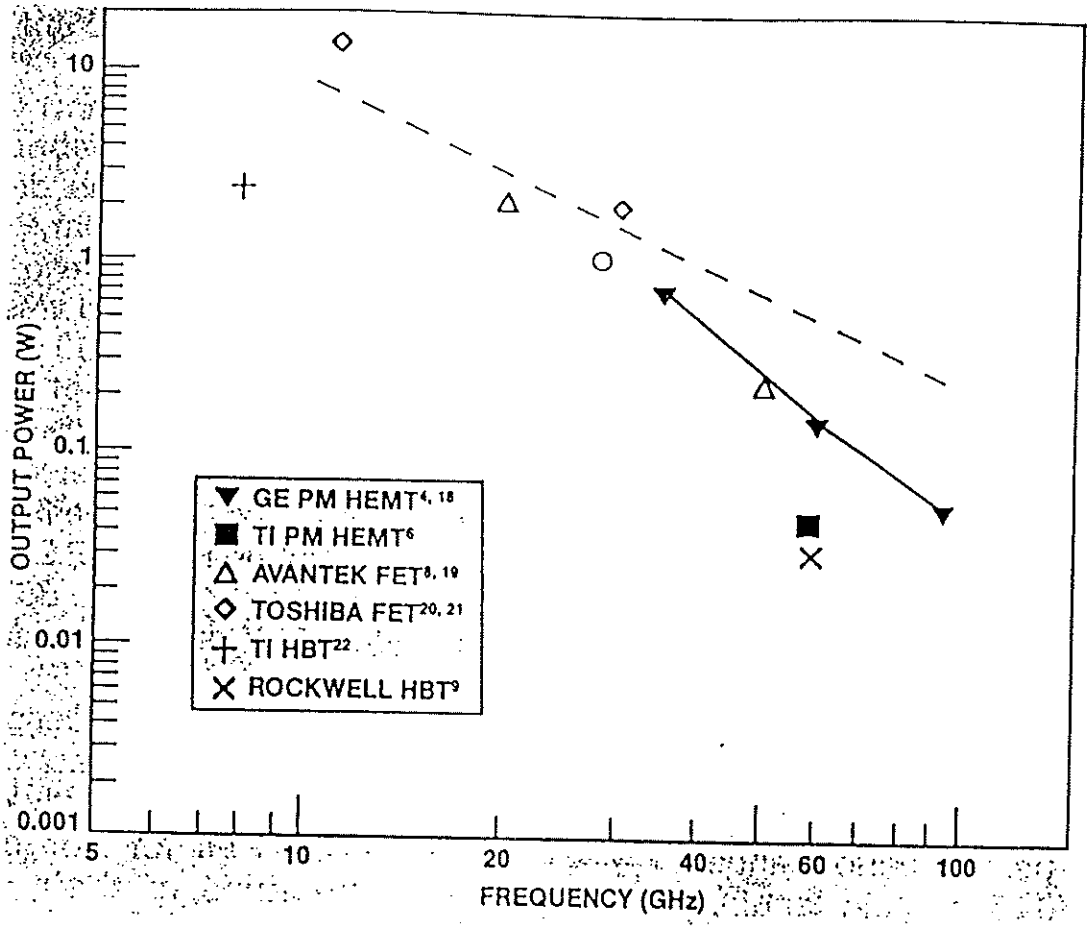

Fig. 3. A summary of the power performance of microwave and millimeter-wave transistors [14].

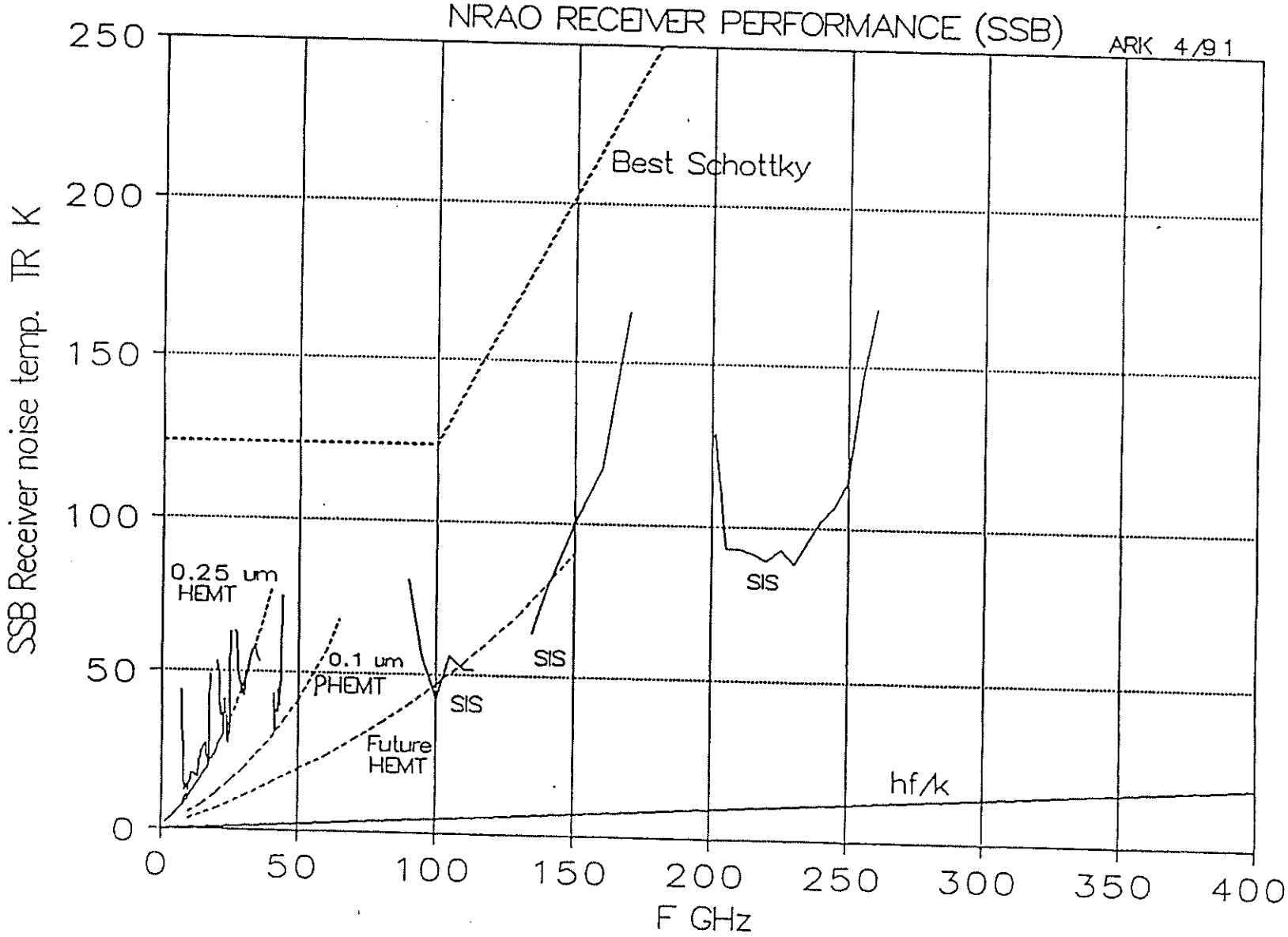

Fig. 4. A comparison of NRAO receiver performance with that expected from the current experimental devices ("future HEMT's").

MILLIMETER ARRAY
MEMO NO. 68

A Millimeter λ Phase Stability Analysis of the South Baldy and Springerville Sites

M.A. Holdaway

November 22, 1991

1 Abstract

Site testing for the Millimeter Array has been underway at South Baldy, NM for about four years and at Springerville, AZ for about two. In addition to opacity measurements, the tipping radiometers at each site have performed stability measurements at 230 GHz which yield the Allan standard deviation at various averaging times of the sky brightness temperature fluctuations. The Allan standard deviation is related to the phase structure function $D_\phi(\rho)$ if the velocity is known (Treuhoft and Lanyi, 1987), so in principle we could take the Allan standard deviation "profiles" and determine the behavior of an interferometer of baseline ρ. The details of this problem do not lend themselves to an analytic solution, so we have turned to computer simulations.

The simulations indicate that South Baldy is a better 1 mm site than Springerville. At 230 GHz, the two sites are comparable in the most compact configuration and in the large configurations when selfcalibration is possible. When selfcalibration is not an option, phase stable interferometry in the A and B configurations would be possible at South Baldy between 10% and 20% of the winter time. At Springerville, phase stable observing in the two large arrays would be very rare.

2 The Data

2.1 *A priori* Information

The first piece of data we have is really a piece of belief: the turbulent atmosphere has a Kolmogorov power spectrum. A Kolmogorov power spectrum will lead to a phase structure function which varies with baseline length as $\rho^{5/3}$ for ρ less than the width of the turbulent layer, and $\rho^{2/3}$ for ρ greater than the turbulent layer (slopes of 5/6 and 1/3 in the rms phase variations over a sufficiently large time). Bester et al see a spectrum of ρ^1 (a random power spectrum in the phase fluctuations) over baselines of 10 m

at infrared wavelengths during conditions of excellent atmospheric stability. Also, the interferometric phase stability measurements of Sramek (1989) with the VLA indicate that the break from 5/3 to 2/3 power laws occurs on baselines less than 1 km. When the atmospheric data are ambiguous, we will rely upon this *a priori* information for guidance.

2.2 Wind Velocity and Height of the Turbulent Atmosphere

The velocity of the turbulent layer and the height above the array of the turbulent layer are needed to run the simulation program. Surface wind velocity data was taken concurrently with the atmospheric stability data at the two sites. During the very best observing conditions, surface wind velocities at both sites are about 4 m/s. For other conditions, the average surface winds are about 7 m/s at South Baldy and about 2 m/s at Springerville. The low winds at Springerville are likely due to the local topography, but it seems that the generally high wind speeds at South Baldy suggest that South Baldy is reaching up into the jet stream. Hence, the low surface winds during the best conditions at South Blady suggest that these conditions may be produced by low wind speeds. The consequences of erroneous assumptions about the wind velocity will be discussed later.

The velocity of the pattern of turbulent water vapor is likely to be different from the surface wind velocity. Radiosonde measurements of wind velocities at 4200 m (about 1000 m above the array) have been averaged over the last 20 years for Albuquerque, NM and Winslow, AZ (Schwab, 1991). Also, the average velocity as a function of time of year has been determined at 3400 m, 4200 m, and 5000 m over 1 year for both radiosonde sites. The South Baldy MMA site is about 100 miles south of the Albuquerque radiosonde site, and the Springerville MMA site is about 100 miles SE of Winslow and 150 miles SW of Albuquerque. The median wind velocity at 4200 m for the months of November through February is about 12 m/s at Winslow and about 14 m/s at Albuquerque. Wind speeds increase by about 15% for every 800 m of elevation gain. Hence, the altitude of the turbulent layer is not critical for the stability simulations. A wind velocity of 12 m/s was used for all simulations presented here. The height of the turbulent layer above the array was taken to be 1000 m for most cases, with all exceptions noted explicitly.

2.3 Water Vapor Radiometer Data

The water vapor radiometers measure the total power emitted by the sky at zenith every 3.51 s for one hour. Since the unevenly mixed water vapor in the turbulent atmosphere leads to variations in the total power measured by the water vapor radiometer as well as the phase fluctuations in an interferometer, it should be possible to determine the latter from the former. A naive calculation indicates that

$$\Delta\phi \approx 150 \cdot \Delta T_B$$

(McKinnon, 1988), but it is unclear on what time scales ΔT_B is to be measured and on what baselines $\Delta\phi$ is applicable to. Such a treatment ignores the detailed shape of the distribution of power on various scales in the atmosphere, so a more complicated analysis must be used.

The stability data which we used consisted of the Allan standard deviation (square root of the Allan Variance) of the radiometer time series calculated for averaging times of $2^{n-1} \cdot 3.51$ s for n = 1 to 9. Nominally, this yields information about the atmospheric turbulence on scales ranging from 3.51 s · 12 m/s = 42 m to 898 s · 12 m/s = 11000 m. Weaknesses in the data at both ends of this range impair our ability to predict the phase stability for the shortest and longest baselines (see below), but the *a priori* information about the behavior of atmospheric turbulence sometimes enables us to extrapolate at both ends.

In the southwest United States, the winter months offer the lowest opacity and best atmospheric stability. Hence, the ASD profiles were compiled for the months of November, December, January and February of 1990-1991 for the South Baldy and Springerville sites. To improve the statistics of the profiles without introducing confusion among different atmospheric conditions, the Allan standard deviation profiles were binned by the value of the Allan standard deviation at 56 s averaging time. The number of stability runs which fell into each bin are summarized in Table 1, while the average Allan standard deviation profiles are plotted on a log-log plot in Figures 1 and 2. Each average Allan standard deviation profile is named by the upper limit of the Allan standard deviation at 56 s averaging time (the profile formed by averaging all profiles with 0.04 < ASD(56 s) < 0.07 is labeled by 0.07).

2.4 Relative Abundances of Atmospheric Conditions

Data were selected by opacity ($\tau < .2$) and stability (ASD(56 s)<0.30). For higher opacities, the atmosphere is not optically thin and the emission from higher altitudes would be partially absorbed by the water vapor at lower elevations, a complication we would rather not deal with at this point. For high ASD values, the atmospheric emission may include substantial amounts of water droplets, which requires a different physical model. These selection criteria eliminate half of the winter observing time. As the simulations will show, much of the time eliminated by these criteria will permit 3 mm and 9 mm observations in all configurations, as well as some 1 mm observing in the compact array.

Consider the amount of time during which the very best stability conditions occur at the two sites. Tables 1 and 2 indicate that both sites have approximately equal amounts of time with ASD(56 s) better than 0.30, 0.20, and even 0.13. However, South Baldy has almost twice as much time than Springerville better than 0.07, half of which is better than 0.04. Springerville has essentially no time with ASD(56 2) better than 0.04. So, if the meaning of the ASD(56 s) values are assumed to have the same meaning at the two sites under consideration, it is clear that South Baldy comes out ahead if ASD(56 s) less than 0.07 is required for a substantial fraction of the observations that could be made with the MMA. The results of the simulations will shed new light on this data in two ways. The simulations will indicate just what phase stability is associated with a given ASD(56 s). Also, due to the differing natures of the turbulence at the two sites, the simulations will show that the same value for ASD(56 s) at the two sites *doesn't lead to the same phase stability!*

2.5 The Measured Allan Standard Deviation Profiles

The two sites show very different Allan standard deviation profiles in Figures 1 and 2. Unreliable points (points in which the errors in the removal of the instrumental function are clearly greater than the ASD value) are set equal to the next suspected reliable value. The last ASD point (896 s averaging time) is not significant as it is the average of only two numbers. When plotted on an appropriately scaled log-log plot against averaging time, the Allan standard deviations show the same behavior as the square root of the phase structure function plotted against distance. The conversion from time to distance is accommodated by the velocity of the turbulent atmosphere.

The best conditions at South Baldy show a slope of 0.5, consistent with a random spectrum of atmospheric turbulence, while less stable conditions show a slope of 0.83 breaking to 0.33, consistent with a Kolmogorov spectrum of turbulence. Modeling the atmosphere at the Baldy site is fairly straightforward.

The best conditions at the Springerville site are consistent with a Kolmogorov spectrum of turbulence, but all other cases show a complicated three part power spectrum. For each stability bin, the values of ASD(56 s) are required by the selection process to be equal for the Baldy and the Springerville data. However, the ASD for both shorter and longer averaging times is higher in the Springerville profiles than the South Baldy profiles. This indicates that the phase stability at Springerville will be worse than at Baldy on the both the shortest and the longest baselines. The upturn at the three longest averaging times (224 s, 448 s, and 896 s) indicates that the phase stability will be dramatically worse at Springerville on $\sim$2.5 km to 10 km baselines. (The ASD measurements have no information on baselines longer than 10 km, and the 10 km information may not be reliable.) Springerville would not be an appropriate site for an extended (baselines $>$ 3 km) array. The high ASD on the shortest three averaging times indicates that the phases may be rather poor on baselines shorter than 200 m. Springerville's higher ASD numbers at small averaging times should be interpreted with caution. Generally, they do not display the 0.83 power law slope ascribed to Kolmogorov turbulence. The error in the instrumental function subtraction is greater than the true atmospheric signal for the shortest averaging times at the best conditions. However, even at the worst conditions where such an error would be dominated by the true signal, the ASD profile remains flat for small averaging times suggesting that this behavior is true. Finally, while the radiometers used to measure the time series at the two sites were virtually identical and produced virtually identical results when operated on the same site (Baldy), the calibrated Springerville data seems to be quantized. This effect shows up on the shortest averaging times on the best conditions. These caveats must be considered when the Springerville atmosphere is modeled.

2.6 Possible Causes of Differences in the Allan Standard Deviation Profiles

Even without the simulations to guide us, it is apparent that the strength of the turbulence is often lower at South Baldy (indicated by the percentage

of time very good stability occurs), and that the nature of the turbulence is quite different at the two sites (indicated by the shapes of the ASD profiles). The qualitative and quantitative differences in the turbulence above the two sites is likely due to the local topography at the sites. The Baldy site sits on the top of a 3200 m mountain which overlooks 2200 m plains to the west. There are no features higher than 2800 m for at least 100 km to the west/northwest, the direction from which good weather comes. There are no local features which would cause anomalous turbulence.

The Springerville site is on a high plateau at 2900 m. A series of high mountains ranging from 3100 to 3500m sit 30 km to the west and northwest of the site. As the weather blows in from the west or northwest, these local features could generate large scale (>10 km) turbulent eddies. The excess power at long averaging times of the ASD could be due to transfer of power from the largest scale turbulence down to ~1 km eddies. Such large scale turbulence would not die out in the vicinity of the site where the stability measurements were taken, *ie*, all three of the sites which are topographically and politically feasible in this area would be adversely affected. On the other hand, the short averaging time or small spatial scale anomaly seen in the Springerville ASD profiles could be due to a local feature within a few hundred meters of the location of the measurements. If this were the case, the other two possible sites may not be affected. In the event that the Baldy site were ruled out, stability testing at the second Springerville site and the Alpine site would be important to determine if ant site in the area does not have problems on the short spacings.

3 The Simulation Program

We have undertaken a simple suite of atmospheric simulations which can relate the observed Allan standard deviations (ASD) to the interferometer phase fluctuations on various baselines and time scales.

- First, a model atmosphere is generated with the program ATMOMAKE. As will be explained later, this model atmosphere is chosen to be consistent with some observed Allan standard deviation profile in strength of turbulence and the relative amounts of power on various scales. The model atmosphere is a two dimensional representation of a three dimensional turbulent layer. The units of the pixel values are "millimeters of precipitable water vapor". The atmosphere is the Fourier transform of $\sqrt{F_\phi(\kappa)} \sim \kappa^{-\alpha}$, where $F_\phi(\kappa)$, the two dimensional

spectral power density, is defined by Tatarski (1961) as

$$D_\phi(\rho) = 4\pi \int_0^\infty (1 - J_o(\kappa\rho)) F_\phi(\kappa)\kappa d\kappa. \quad (1)$$

Input parameters to ATMOMAKE include inner and outer scale lengths of the atmospheric turbulence, a two part broken power law for $\sqrt{F_\phi(\kappa)}$ and the scale at which the power laws switch over, and the strength of the turbulence. In a three dimensional atmosphere, $D_\phi(\rho)$ will have a kinked power law form due to a change from 3-D turbulence on short spacings to 2-D turbulence on long spacings. The kink in the 2-D model atmosphere's spectrum serves to simulate this effect.

- Next, the program ATMOPHAS simulates a water vapor radiometer and an array of antennas observing a geostationary point source through the atmospheric phase screen moving with constant velocity. The atmosphere is in the near field of the interferometric elements, and the near field radiation pattern is assumed to be a cylinder which samples the atmosphere above each antenna in the direction of the source. Antenna based phase errors

$$\Delta\phi = 6.5\frac{2\pi}{\lambda}\frac{mm_{H_2O}}{1000}$$

are introduced here. The atmosphere is in the far field of the radiometer and an Airy disk samples the atmosphere, measuring $(1-e^{-\tau})T_{sky}$, where $\tau = .06$ times the column density of water in millimeters. Input parameters of the ATMOPHAS program include T_{sky} (253 K), the atmospheric height, the atmospheric velocity (12 m/s), the observing frequency (230 GHz), the declination (the point source is essentially frozen at transit for the entire observation), and the length of the observation (1024 scans of 3.51 s). The output of the ATMOPHAS program consists of a time series from the radiometer, from which the Allan standard deviation profile can be calculated, and a visibility database which lists the complex visibilities as a function of baseline and time.

- The visibilities are processed by the PHRMS program. Here, the phases are "rewound" and binned by some time interval. The RMS of all phases about the mean within each time interval is calculated for each baseline and a range of binning times ranging from 30 s to

3600 s. Assuming sufficient averaging has occurred (high enough velocity, long enough observation time), $\sqrt{D_\phi(\rho)}$ is approximated by the rms phase at maximum binning time (3600 s) as a function of baseline. The power law slopes and breaks in the power laws of $\sqrt{D_\phi(\rho)}$ are mimicked by the Allan standard deviation profile. In fact, if plotted on the correct scale, the power laws are the same for the two. If the velocity is known, the breaks in the power laws show very good correspondence as well. This allows us to say something immediately about the atmosphere simply by looking at the raw Allan standard deviations.

A test of the simulation method will be carried out by comparing the simulated interferometer phases derived from Allan standard deviation profiles taken with a radiometer at the VLA site with concurrent VLA data. Twenty four such concurrent observations were taken in the winter of 1988-1989, but the data have not yet been analyzed with the methods presented here. The results of this investigation will be written up as a separate MMA memo.

4 Simulation Results

A trial and error process guided by numerically integrating Equation 1 leads us to the model parameters which describe an atmosphere which yields simulated Allan standard deviation profiles which are consistent with the measured (averaged) Allan standard deviation profiles. The simulated Allan standard deviation profiles are shown in Figures 3, 4, and 5. When the simulated and measured Allan standard deviations agree sufficiently in form and scale, the rms phases can be calculated for an arbitrary interferometer. Phase matrices which list the rms phase for several baselines and averaging times are presented for each model atmosphere studied (see Tables B, S1, and S2). Also, an example of $\sqrt{D_\phi(\rho)}$ for the BALDY.13 case is given in Figure 6. The short baseline slope is 0.81 and the long baseline slope is 0.40, consistent with the Kolmogorov values of 5/6 and 1/3. One point of interest is the turnover from 0.81 to 0.40. Sramek does not see this turnover in his VLA data, but it is clear that it does *not* exist in any data longer than 1000 m. There is a steepening of the rms phase to 0.59 for baselines less than 1000 m when all observations limited by the stability of the electronics are eliminated. Hence, the evidence is that the turnover occurs *somewhere*

below 1000 m, contrary to the conventional wisdom that the turnover occurs at 5000 m, the scale height of the turbulent troposphere. Our simulated structure function indicates the turnover occurs at only 250 m. The turnover could occur further out if our estimate for the velocity (12 m/s for South Baldy) is too low. The low turnover suggests that the thickness of the tropospheric turbulence is isolated to *thin* layers, on the order of 250 m think.

The atmospheric model which fit the South Baldy data is simple and is in line with the Kolmogorov theory. For 60 second averaging times for both the interferometer phase and the Allan standard deviation, the rms phase fluctuations on the longest spacings at South Baldy are more aptly described by

$$\Delta\phi = 200 \cdot \Delta T_{sky},$$

To fit the Springerville Allan standard deviation data at long averaging times, two independent atmospheric phase screens were used, one which generally agreed with the standard Kolmogorov theory, and one which had very little power on short scales and a steep power law on long scales, dominating the atmospheric fluctuations. There was no evidence for placing these two layers at different atmospheric heights or at different velocities (though this is by no means excluded by the data), so the standard values for the height (1000 m) and velocity (12 m/s) have been used. The short averaging time end of Springerville's Allan standard deviation profiles is not as steep as the Kolmogorov model and leads to greater phase fluctuations on short baselines. Because of potential problems with the measurement of the three shortest averaging times, two models for the atmosphere above Springerville have been produced. Springerville model 1, which actually agrees with the ASD data, shows poorer than expected phase stability on the shorter baselines. Springerville model 2 assumes a Kolmogorov model for short baselines, leading to lower phase fluctuations on the shorter baselines, and should be considered a "best case". Hence, if there is reason to doubt the short integration time ASD values, or if the small scale turbulence which causes the anomalously high ASD values at small integration times turns out to be local to the immediate area in which the radiometer data were obtained, then Springerville model 2 is more representative of what may be possible at the Springerville site.

A few points should be kept in mind:

- The last point on the Allan standard deviation plots is *not significant.* A bootstrap analysis of several simulations indicates that this point is in error by $\sim 25\%$.

- These simulations were performed with a linear array with wind velocity parallel to the array. Simulations with nonlinear arrays yield very similar results, with rms phases within about 20% of the phases computed for a linear array.

- These simulations were performed at the zenith. Phases must be multiplied by 1/ sin(elevation) to consider other declinations. For a source near the galactic center, this term is about 2.

- Before and after a source transits, the array will be observing through more airmass than at transit. It is assumed that MMA observations will proceed out to 1.4 times the transit airmass. Hence, in addition to the secant elevation term, the phases must be further multiplied by the average excess airmass due to change in elevation, about 1.2. Hence for a full integration on a source at δ = 35, the phases must be multiplied by 1.2, while for a source at δ = -25, the phases must be multiplied by 2.4.

4.1 Reliability of the Phase Stability Simulations

Short of a systematic error in the simulation programs or the radiometers, the simulations seem to be fairly robust by atmospheric standards. Phase stability on 1-3 km baselines is not very model dependent. Internal errors are less than 30% on these baselines. For the short baselines (< 200 m) at Springerville, the two models give results which differ by a factor of 2. As mentioned earlier, the altitude is not a critical parameter because the velocity changes slowly with altitude. Furthermore, the altitude has no effect on the simulated interferometer phases and only a minor effect on the simulated sky temperature fluctuations at short averaging times.

If the true velocity of the atmospheric phase pattern is significantly different from the assumed value of 12 m/s (as may be possible for the 0.04 bin on South Baldy), then the measured Allan standard deviation profiles indicate different phase stability than these simulations have produced. First, any kink in the phase structure function will move; a lower true velocity will cause the kink to move to smaller spatial scales. Since the 0.04 South Baldy ASD has no kink, this is not a problem. Second, since not as much atmosphere passes over the array, there will not be sufficient averaging on the longer baselines and the determined shape of the structure function will not be accurate. Third, to account for the the lower ASD in conjunction with the low velocity, the turbulence must be somewhat stronger than that

which is used in the model. These two effects, lower velocity and stronger turbulence, will approximately cancel out in both the ASD and the rms phases.

4.2 Interpretation of the Simulations

Looking at the phase stability for the worst atmospheric conditions included in this study ($0.20 < \mathrm{ASD}(56\ \mathrm{s}) < 0.30$), it is clear that 3 mm or 9 mm observations will have no problem at either the Baldy or Springerville sites. Even low elevation observations in the A array will present no problems at 3 mm if selfcalibration is possible. This means that the A array at either site will be usable for *at least* 50% of the winter time at frequencies of 100 GHz and lower. A better estimate of the time cannot be made given the selection criteria we have applied to the stability data. However, it is clear the A array will not sit around idle while waiting for the very best observing times to come around.

At 100 GHz, the two sites are quite comparable. At higher frequencies, we must look to better and better atmospheric conditions and we must consider both how good the atmosphere is at each site as well as how often these conditions occur.

Table 1 indicates the percent of time the ASD(56 s) is less than a given value at the Baldy and Springerville sites. However, in light of the fact that the same ASD(56 s) at Baldy and Springerville translate to different phase stabilities and the behavior with baseline is complicated, it is important to try to fold the simulation results back into the amount of time each condition range occurs at the two sites. In doing so, we will have a much better idea about what sorts of observations can be done and how often they can be done.

We estimate that interferometry will work with 30° rms phase errors. Observations of the galactic center at transit will have an airmass of two, so zenith phase fluctuations of 15° are required. For phase stable interferometry, we require the rms phase fluctuations over 3600 s to be less than or equal to 30° or 15°. On the other hand, if the target source is bright enough to detect on shorter times (selfcalibration is possible), then phase fluctuations of 30° or 15° over the detection time are acceptable. (For a 30 s integration time, a continuum source must be a few hundred mJy for selfcalibration to work.) These are the four cases we will examine: phase stable interferometry looking to the zenith and looking to the galactic center, and observations of strong sources which can be detected on each baseline in

30 s, looking to the zenith and to the galactic center.

The South Baldy model and the two Springerville models are considered in this light (the second Springerville model is the more optimistic). We know the fraction of time the ASD(56 s) falls into each bin, and we know the rms phase on the pertinent baselines and averaging times for the median atmosphere of each bin. It is assumed that the simulation results represent the median conditions of the corresponding bin. If we also assume that the occurrence of some phase fluctuation on some baseline is linear in time (cumulative time at which the atmosphere is better than that phase) between the midpoints of bins which straddle the phase in which we are interested (30° or 15°), a linear interpolation gives an estimate of the percent time the atmosphere will be better than that phase on that baseline.

Table 3 indicates the amounts of time interferometry would work if selfcalibration averaging times of 30 s were possible on 60 m, 210 m, 700 m, and 2000 m baselines, looking towards the galactic center and towards the zenith, at the Baldy and Springerville sites. These baselines were chosen because they are fairly long baselines in the D, C, B, and A arrays respectively, and will indicate how often observations in those arrays will succeed. Table 4 indicates the amounts of time phase stable interferometry would work on 60 m, 210 m, 700 m, and 2000 m baselines, looking towards the galactic center and towards the zenith, at the Baldy and Springerville sites. Interpolation errors are on the order of 1% as indicated by interpolation verses extrapolation. Errors inherent to the modeling procedure may contribute up to 3% as indicated by inconsistencies in Table 4, and for some portions of these tables, such as where the percentages are low and are dominated by the fraction of time given conditions occur, the errors will be much lower.

We draw the following conclusions from Tables 3 and 4:

- For zenith observations in which selfcalibration is possible, there is very little difference between the Baldy and Springerville sites.

- For zenith observations in which selfcalibration is possible, D array observations would be possible from both sites for all conditions which were not rejected by the selection criterion: selected D array observations will be possible *more than half of the winter observing period.*

- For higher airmass observations in which selfcalibration is possible, suitable atmospheric conditions exist roughly twice as often at Baldy than at Springerville.

- The most dramatic differences between the sites become evident when more difficult observations are considered. Phase stable observing in the A and B arrays at Springerville will be rare (except perhaps for looking overhead on 700 m baselines). The Baldy A and B arrays will be phase stable a reasonable amount of time (5% to 25%, depending upon the airmass and configuration).

While there is only a small amount of time at South Baldy which permits phase stable interferometry at 230 GHz in the A array, the stability data indicates that these good atmospheric conditions tend to last more than 5 hours (the time between consecutive stability measurements), sometimes lasting more than 24 hours but interrupted by unstable conditions in the afternoons.

Both sites are appropriate for 100 GHz work, for compact array work, and for work in which selfcalibration is a possibility, though Baldy is marginally better than Springerville for these observations. The most challenging experiments which require high resolution imaging of very weak sources appear to be possible only at the South baldy site.

Table 1: Number of stability measurements in each of the stability divisions at South Baldy and Springerville.

ASD(56 s) range	Baldy		Springerville	
<0.04	43	9.8%	5	1.1%
0.04 - 0.07	37	8.5%	41	9.0%
0.07 - 0.13	64	14.6%	89	19.6%
0.13 - 0.20	43	9.8%	60	13.2%
0.20 - 0.30	38	8.7%	32	7.0%
rejected	212	48.5%	227	50.0%

Table 2: Percentage of time at which the stability measurements are better than some value of the Allan standard deviation at 56 s.

ASD(56 s)	Baldy	Springerville
<0.04	9.8%	1.1%
<0.07	18.3%	10.1%
<0.13	33.0%	29.7%
<0.20	42.8%	43.0%
<0.30	51.5%	50.0%

Table 3: Percentage time at which rms phase error are less than 15° and 30° on 30 s integration times at South Baldy and Springerville. Selfcalibration required.

Baseline	15°			30°		
	B	S1	S2	B	S1	S2
60 m	40%	20%	34%	>52%	47%	>50%
210 m	26%	10%	14%	41%	31%	45%
700 m	26%	12%	15%	41%	34%	45%
2000 m	27%	11%	14%	43%	32%	44%

Table 4: Percentage time at which rms phase error are less than 15° and-30° on 3600 s integration times at South Baldy and Springerville. Phase stable.

Baseline	15°			30°		
	B	S1	S2	B	S1	S2
60 m	38%	18%	27%	>52%	44%	>50%
210 m	21%	7%	10%	36%	23%	30%
700 m	14%	2%	2%	26%	13%	16%
2000 m	6%	0%	0%	16%	2%	2%

Figure 1: Scaled log-log plot of the Allan standard deviation profiles from South Baldy, binned by conditions.

Figure 2: Scaled log-log plot of the Allan standard deviation profiles from Springerville, binned by conditions.

Figure 3: Simulated Allan standard deviation profiles for South Baldy.

Figure 4: Simulated Allan standard deviation profiles for Springerville, Model 1.

Figure 5: Simulated Allan standard deviation profiles for Springerville, Model 2.

Figure 6: Simulated phase structure function from one of the South Baldy model atmospheres.

BALDY.04.RMS.2

Baseline, m	Averaging Time, s 30.	60.	120.	240.	480.	960.	3600.
16.0	0.9	0.9	0.9	0.9	0.9	0.9	0.9
24.0	1.1	1.1	1.1	1.1	1.1	1.1	1.1
40.0	1.5	1.5	1.5	1.5	1.5	1.5	1.6
60.0	1.9	2.0	2.0	2.1	2.1	2.1	2.1
84.0	2.3	2.4	2.5	2.5	2.5	2.5	2.5
100.0	2.4	2.6	2.7	2.7	2.7	2.7	2.8
150.0	2.8	3.1	3.3	3.4	3.4	3.4	3.4
210.0	3.0	3.5	3.8	3.9	3.9	4.1	4.0
250.0	3.1	3.7	4.0	4.2	4.3	4.4	4.4
350.0	3.2	4.1	4.8	5.0	5.1	5.4	5.3
400.0	3.5	4.5	5.0	5.3	5.5	5.8	5.7
500.0	3.5	4.6	5.6	6.1	6.2	6.6	6.5
600.0	3.5	4.6	6.0	6.6	6.8	7.2	7.1
700.0	3.5	5.0	6.1	6.7	7.2	7.5	7.7
750.0	3.3	5.1	6.4	7.1	7.5	8.0	8.0
800.0	3.4	5.2	6.3	7.1	7.8	8.0	8.1
900.0	3.6	5.1	6.7	7.7	8.1	8.8	8.8
1000.0	3.5	4.9	6.8	8.0	8.5	9.3	9.3
1200.0	3.4	5.0	6.7	8.0	9.0	9.8	10.2
1400.0	3.4	4.8	6.7	8.5	9.5	10.7	11.0
1600.0	3.3	4.5	6.5	8.6	10.0	11.3	11.9
2000.0	3.3	5.2	6.9	9.2	11.5	12.6	13.5
2200.0	3.4	5.1	7.0	9.8	11.6	13.6	14.5
2400.0	3.3	5.0	6.9	9.9	12.4	14.2	15.2
3000.0	3.5	5.2	7.7	10.8	13.7	16.2	17.4

BALDY.07.RMS.2

Baseline, m	Averaging Time, s 30.	60.	120.	240.	480.	960.	3600.
	30.	60.	120.	240.	480.	960.	3600.
16.0	1.8	1.9	1.9	1.9	1.9	1.9	1.9
24.0	2.3	2.3	2.3	2.4	2.4	2.4	2.4
40.0	3.1	3.2	3.3	3.3	3.3	3.2	3.3
60.0	4.1	4.3	4.3	4.4	4.4	4.4	4.4
84.0	4.8	5.1	5.2	5.3	5.3	5.3	5.3
100.0	5.2	5.5	5.6	5.7	5.7	5.7	5.8
150.0	6.0	6.6	6.9	7.0	7.0	7.1	7.1
210.0	6.3	7.3	7.8	8.1	8.1	8.4	8.3
250.0	6.5	7.7	8.3	8.7	8.8	9.0	8.9
350.0	6.8	8.5	9.8	10.2	10.4	10.8	10.6
400.0	7.2	9.2	10.2	10.8	11.1	11.7	11.5
500.0	7.3	9.4	11.4	12.3	12.5	13.1	13.0
600.0	7.3	9.5	12.1	13.3	13.6	14.3	14.2
700.0	7.2	10.2	12.3	13.5	14.4	14.8	15.2
750.0	6.9	10.4	12.8	14.2	14.9	15.9	15.8
800.0	6.9	10.5	12.7	14.1	15.5	15.8	16.0
900.0	7.3	10.3	13.4	15.3	16.1	17.4	17.3
1000.0	7.3	10.0	13.6	15.9	16.8	18.2	18.2
1200.0	7.1	10.1	13.4	15.8	17.6	19.1	19.7
1400.0	7.1	9.8	13.3	16.7	18.6	20.7	21.3
1600.0	6.8	9.1	12.9	16.9	19.5	21.9	22.9
2000.0	6.9	10.4	13.8	18.1	22.1	24.2	25.8
2200.0	7.1	10.3	13.9	19.1	22.4	25.9	27.5
2400.0	6.8	10.0	13.7	19.2	23.9	27.1	28.9
3000.0	7.2	10.5	15.1	21.0	26.2	30.8	33.0

TABLE B

BALDY.13.RMS.2

Baseline, m	Averaging Time, s 30.	60.	120.	240.	480.	960.	3600.
16.0	3.3	3.5	3.5	3.6	3.6	3.6	3.6
24.0	4.2	4.5	4.6	4.6	4.6	4.6	4.6
40.0	6.0	6.5	6.6	6.6	6.7	6.6	6.6
60.0	8.1	8.7	8.9	9.0	9.0	8.9	9.0
84.0	10.3	11.3	11.5	11.7	11.7	11.7	11.7
100.0	11.3	12.6	12.8	13.0	13.1	13.0	13.0
150.0	13.8	15.7	16.3	16.6	16.7	16.6	16.7
210.0	15.2	18.1	18.9	19.4	19.6	19.5	19.5
250.0	15.4	19.1	20.2	20.8	21.0	21.0	21.0
350.0	14.6	19.0	21.4	22.5	23.2	23.6	23.4
400.0	14.2	20.3	22.4	23.0	23.9	24.7	24.1
500.0	14.1	20.5	23.4	24.9	26.0	26.8	26.4
600.0	14.3	21.5	24.6	26.5	27.8	28.9	28.2
700.0	15.7	20.9	24.9	27.1	28.0	29.6	29.3
750.0	14.2	19.0	24.6	26.8	29.3	30.5	29.9
800.0	15.1	20.2	25.3	27.8	28.1	30.0	29.8
900.0	14.3	19.1	24.4	27.3	30.5	31.8	31.3
1000.0	14.2	18.8	24.0	27.5	31.2	32.5	31.9
1200.0	14.4	19.1	23.9	28.2	30.5	33.9	33.6
1400.0	14.3	18.4	22.8	27.9	33.7	36.3	35.2
1600.0	13.7	17.9	22.6	28.5	33.5	38.2	37.1
2000.0	14.0	18.9	25.4	31.0	34.5	42.4	42.1
2200.0	15.4	19.5	24.7	32.1	40.4	45.4	44.7
2400.0	14.3	18.5	24.2	31.0	37.4	45.9	45.5
3000.0	13.8	19.5	23.4	31.7	42.0	50.7	50.6

BALDY.20.RMS.2

Baseline, m	Averaging Time, s 30.	60.	120.	240.	480.	960.	3600.
16.0	5.4	5.7	5.8	5.9	5.9	5.8	5.8
24.0	6.9	7.3	7.5	7.6	7.6	7.6	7.6
40.0	9.8	10.6	10.7	10.8	10.9	10.7	10.8
60.0	13.2	14.3	14.5	14.7	14.8	14.6	14.7
84.0	16.8	18.4	18.8	19.1	19.2	19.1	19.1
100.0	18.4	20.5	20.9	21.3	21.4	21.2	21.3
150.0	22.6	25.6	26.6	27.1	27.3	27.2	27.2
210.0	24.8	29.5	30.9	31.7	32.0	31.8	31.9
250.0	25.1	31.3	33.0	34.0	34.4	34.3	34.3
350.0	23.9	31.0	35.0	36.7	37.9	38.6	38.3
400.0	23.2	33.2	36.6	37.5	39.0	40.3	39.3
500.0	23.0	33.5	38.2	40.7	42.5	43.8	43.1
600.0	23.4	35.1	40.2	43.3	45.4	47.1	46.1
700.0	25.7	34.1	40.7	44.3	45.7	48.4	47.9
750.0	23.1	31.0	40.1	43.7	47.9	49.8	48.9
800.0	24.6	33.0	41.3	45.4	45.9	49.0	48.6
900.0	23.3	31.1	39.8	44.6	49.9	52.0	51.1
1000.0	23.2	30.8	39.2	44.9	50.9	53.1	52.1
1200.0	23.6	31.2	39.0	46.0	49.9	55.3	54.9
1400.0	23.3	30.1	37.3	45.6	55.1	59.2	57.5
1600.0	22.4	29.2	37.0	46.6	54.7	62.4	60.5
2000.0	22.9	31.0	41.5	50.7	56.3	69.3	68.7
2200.0	25.1	31.9	40.4	52.4	66.1	74.2	73.0
2400.0	23.3	30.3	39.6	50.7	61.0	74.9	74.4
3000.0	22.6	31.8	38.2	51.7	68.6	82.9	82.7

TABLE B

BALDY.30.RMS.2

Baseline, m	Averaging Time, s 30.	60.	120.	240.	480.	960.	3600.
16.0	8.3	8.7	8.8	8.9	8.9	8.8	8.9
24.0	10.5	11.2	11.4	11.5	11.5	11.5	11.5
40.0	14.9	16.1	16.3	16.5	16.5	16.3	16.5
60.0	20.1	21.7	22.0	22.3	22.5	22.2	22.4
84.0	25.5	28.0	28.6	29.0	29.1	29.0	29.0
100.0	28.0	31.2	31.8	32.4	32.6	32.2	32.4
150.0	34.3	39.0	40.5	41.2	41.5	41.3	41.4
210.0	37.7	44.9	47.0	48.2	48.6	48.4	48.5
250.0	38.2	47.5	50.1	51.6	52.3	52.2	52.2
350.0	36.3	47.2	53.2	55.9	57.6	58.7	58.2
400.0	35.3	50.5	55.6	57.1	59.4	61.4	59.8
500.0	34.9	50.9	58.2	61.9	64.6	66.7	65.5
600.0	35.6	53.3	61.1	65.8	69.1	71.7	70.1
700.0	39.0	51.8	61.9	67.4	69.4	73.6	72.9
750.0	35.2	47.1	61.0	66.5	72.8	75.8	74.4
800.0	37.5	50.2	62.8	69.1	69.8	74.6	73.9
900.0	35.5	47.4	60.6	67.9	75.9	79.0	77.6
1000.0	35.3	46.8	59.6	68.3	77.4	80.8	79.2
1200.0	35.8	47.5	59.3	69.9	75.8	84.1	83.5
1400.0	35.4	45.7	56.7	69.4	83.8	90.1	87.5
1600.0	34.0	44.4	56.2	70.9	83.2	94.8	92.0
2000.0	34.8	47.1	63.0	77.0	85.7	105.4	104.5
2200.0	38.1	48.4	61.4	79.7	100.4	112.8	111.0
2400.0	35.4	46.0	60.2	77.0	92.8	114.0	113.1
3000.0	34.4	48.3	58.1	78.7	104.3	126.0	125.7

TABLE B

SPRING.04.RMS.2

Baseline, m	Averaging Time, s 30.	60.	120.	240.	480.	960.	3600.
16.0	1.1	1.1	1.2	1.2	1.2	1.2	1.2
24.0	1.3	1.3	1.3	1.3	1.3	1.4	1.4
40.0	1.8	1.9	1.9	1.9	2.0	2.0	2.0
60.0	2.4	2.5	2.5	2.6	2.6	2.7	2.7
84.0	2.9	3.0	3.1	3.1	3.2	3.3	3.3
100.0	3.1	3.3	3.3	3.4	3.5	3.6	3.6
150.0	3.5	3.8	3.9	4.0	4.2	4.3	4.4
210.0	3.8	4.2	4.4	4.6	5.0	5.0	5.2
250.0	3.9	4.4	4.7	5.0	5.4	5.5	5.8
350.0	3.8	5.1	5.4	5.8	6.5	6.7	7.0
400.0	3.9	4.8	5.5	6.3	7.1	7.2	7.6
500.0	4.0	5.6	6.0	6.8	8.0	8.2	8.8
600.0	3.9	5.7	6.3	7.3	8.8	9.1	10.0
700.0	3.8	5.2	6.9	8.6	10.0	10.3	11.1
750.0	4.0	5.3	6.6	8.4	10.4	10.6	11.8
800.0	3.9	5.1	7.0	9.6	10.7	11.3	12.5
900.0	4.0	5.5	6.9	9.0	11.7	12.0	13.5
1000.0	4.0	5.7	7.1	9.4	12.5	13.0	14.6
1200.0	4.1	5.7	8.9	11.6	14.5	15.1	16.9
1400.0	4.1	6.1	8.6	11.5	15.9	16.6	19.1
1600.0	4.2	5.9	9.8	13.3	17.8	18.6	21.2
2000.0	4.2	6.2	9.7	15.8	20.6	22.1	25.3
2200.0	4.3	6.1	9.9	14.0	21.9	23.3	27.1
2400.0	4.2	6.4	10.5	16.7	23.3	25.1	29.0
3000.0	4.3	6.6	10.3	16.3	26.5	28.8	34.1

SPRING.07.RMS.2

Baseline, m	Averaging Time, s 30.	60.	120.	240.	480.	960.	3600.
16.0	2.8	2.9	2.9	3.0	3.0	3.0	3.0
24.0	3.5	3.7	3.7	3.7	3.7	3.8	3.8
40.0	5.0	5.2	5.2	5.3	5.3	5.4	5.3
60.0	6.6	6.9	7.1	7.2	7.2	7.3	7.2
84.0	7.9	8.4	8.5	8.7	8.8	8.9	8.7
100.0	8.6	9.2	9.4	9.6	9.7	9.8	9.6
150.0	9.6	10.6	11.1	11.5	11.6	11.8	11.6
210.0	10.5	12.1	12.9	13.4	13.6	13.7	13.6
250.0	10.7	12.6	13.6	14.2	14.5	14.5	14.6
350.0	10.8	13.7	15.2	16.3	16.8	16.9	17.1
400.0	10.7	13.9	15.7	16.8	17.4	17.4	18.0
500.0	10.2	13.6	16.2	17.8	18.7	18.9	19.6
600.0	10.0	13.3	16.6	18.7	19.9	20.1	21.1
700.0	10.0	14.1	17.4	19.5	21.4	21.4	22.6
750.0	10.1	14.1	17.3	20.1	21.8	22.4	23.8
800.0	10.1	14.2	18.5	21.0	21.6	22.6	23.7
900.0	10.0	13.9	17.3	20.9	23.1	24.3	25.9
1000.0	10.0	13.4	17.2	21.4	24.0	25.4	27.3
1200.0	9.9	13.9	17.9	21.3	26.3	27.3	29.6
1400.0	9.9	14.5	18.9	22.6	27.9	30.1	33.2
1600.0	10.5	14.3	19.3	22.4	29.8	31.4	35.3
2000.0	10.3	14.8	19.1	26.1	32.3	35.0	39.4
2200.0	10.6	15.0	19.8	23.4	34.6	37.3	43.1
2400.0	10.1	14.0	18.6	24.7	33.7	37.0	43.5
3000.0	10.0	14.3	18.9	24.5	37.6	41.6	50.5

TABLE 5 1

SPRING.13.RMS.2 Baseline, m	Averaging Time, s 30.	60.	120.	240.	480.	960.	3600.
16.0	6.6	6.8	6.9	7.0	7.0	7.0	6.9
24.0	8.4	8.7	8.7	8.7	8.8	9.0	8.8
40.0	11.9	12.2	12.2	12.3	12.3	12.6	12.3
60.0	15.7	16.1	16.4	16.5	16.6	16.8	16.4
84.0	18.4	19.1	19.3	19.6	19.6	19.9	19.5
100.0	19.7	20.6	20.9	21.2	21.2	21.5	21.0
150.0	21.4	23.0	23.6	24.1	24.2	24.6	24.0
210.0	22.3	24.9	25.9	26.5	26.7	26.9	26.5
250.0	22.2	25.3	26.6	27.3	27.6	27.6	27.5
350.0	21.8	26.4	28.5	29.8	30.3	30.5	30.4
400.0	21.7	26.7	29.0	30.4	31.0	30.9	31.3
500.0	20.6	25.8	29.2	31.1	32.0	32.0	32.7
600.0	20.1	25.1	29.5	31.9	33.1	33.1	34.2
700.0	20.4	26.4	30.6	33.1	35.3	34.9	36.3
750.0	20.6	25.9	30.4	33.7	35.5	36.0	37.5
800.0	20.7	26.6	31.6	34.9	35.5	36.5	37.4
900.0	20.5	25.8	30.3	34.4	36.8	38.2	39.8
1000.0	20.3	25.3	30.3	34.9	37.7	39.3	41.4
1200.0	20.2	25.6	30.6	34.8	40.6	41.9	44.3
1400.0	20.2	26.3	31.8	35.9	42.0	44.8	48.3
1600.0	21.1	26.2	32.0	35.8	44.6	46.4	51.1
2000.0	21.0	27.1	32.4	41.0	48.1	51.4	56.1
2200.0	21.3	27.6	33.5	37.2	50.6	53.9	60.8
2400.0	20.6	25.9	30.9	38.2	48.9	52.9	60.5
3000.0	20.4	26.0	31.6	37.9	53.5	58.3	69.0

SPRING.20.RMS.2 Baseline, m	Averaging Time, s 30.	60.	120.	240.	480.	960.	3600.
16.0	10.3	10.6	10.8	10.9	11.0	11.0	10.9
24.0	13.1	13.5	13.5	13.6	13.6	14.0	13.7
40.0	18.3	18.8	18.9	19.0	19.0	19.4	19.0
60.0	23.9	24.7	25.1	25.3	25.4	25.6	25.2
84.0	27.7	28.8	29.2	29.6	29.6	30.0	29.4
100.0	29.4	30.8	31.4	31.9	32.0	32.3	31.7
150.0	31.9	34.5	35.6	36.4	36.7	37.1	36.4
210.0	33.9	38.2	40.0	41.0	41.4	41.6	41.2
250.0	34.0	39.3	41.5	42.7	43.2	43.2	43.1
350.0	33.8	41.4	45.1	47.5	48.3	48.3	48.4
400.0	33.5	41.8	46.1	48.4	49.4	49.1	50.0
500.0	31.9	40.8	46.9	50.4	51.9	51.7	52.9
600.0	31.2	39.7	47.6	51.9	53.9	53.8	55.6
700.0	31.4	41.8	49.5	54.0	57.5	56.8	59.0
750.0	31.8	41.3	49.1	55.1	57.9	58.5	61.0
800.0	31.9	42.0	51.5	57.0	58.0	59.5	61.0
900.0	31.6	40.8	48.9	56.3	60.2	62.2	64.9
1000.0	31.3	39.9	48.7	57.1	61.7	64.2	67.5
1200.0	31.1	40.7	49.6	57.0	66.5	68.5	72.1
1400.0	31.2	41.9	51.7	59.3	69.0	73.4	78.8
1600.0	32.6	41.5	52.2	58.9	73.0	75.8	83.0
2000.0	32.3	43.0	52.3	67.3	78.7	83.7	90.6
2200.0	32.9	43.6	54.1	60.8	82.4	87.4	98.1
2400.0	31.7	40.8	50.1	62.7	79.7	85.6	97.1
3000.0	31.3	41.0	51.0	61.6	86.6	93.5	110.3

TABLE S1

SPRING.30.RMS.2

Baseline, m	Averaging Time, s 30.	60.	120.	240.	480.	960.	3600.
16.0	12.6	13.0	13.3	13.4	13.5	13.5	13.3
24.0	16.0	16.6	16.6	16.7	16.8	17.3	16.9
40.0	22.5	23.2	23.4	23.6	23.7	24.2	23.6
60.0	29.6	30.8	31.4	31.7	31.8	32.1	31.5
84.0	34.9	36.6	37.1	37.7	37.8	38.2	37.5
100.0	37.4	39.5	40.3	41.0	41.2	41.6	40.7
150.0	41.3	45.0	46.7	47.9	48.2	48.7	47.8
210.0	44.3	50.4	53.1	54.6	55.1	55.3	54.7
250.0	44.7	52.2	55.5	57.2	57.8	57.8	57.6
350.0	44.8	55.6	61.0	64.3	65.3	65.3	65.3
400.0	44.4	56.4	62.4	65.9	67.1	66.5	67.7
500.0	42.1	54.9	63.8	68.7	70.6	70.3	71.8
600.0	41.1	53.3	64.9	70.9	73.5	73.2	75.5
700.0	41.4	56.2	67.6	73.9	78.5	77.4	80.0
750.0	41.9	56.0	67.0	75.5	79.0	79.7	82.7
800.0	41.9	56.5	70.5	77.7	79.0	80.9	82.6
900.0	41.6	55.0	66.6	77.2	82.0	84.5	87.7
1000.0	41.1	53.4	66.1	78.2	84.0	87.1	91.0
1200.0	40.8	54.8	67.5	78.0	90.2	92.7	96.8
1400.0	40.9	56.4	70.4	81.2	93.4	99.0	105.4
1600.0	43.0	55.8	71.3	80.8	98.8	102.2	110.7
2000.0	42.4	57.9	71.1	91.9	106.1	112.1	119.8
2200.0	43.4	58.5	73.3	82.9	110.2	116.5	129.3
2400.0	41.6	54.7	68.1	85.3	106.6	113.6	127.2
3000.0	41.1	55.1	69.0	83.3	114.6	122.6	143.2

TABLE S-1

SPRING.04.RMS.3

Baseline, m	Averaging Time, s 30.	60.	120.	240.	480.	960.	3600.
16.0	1.1	1.1	1.2	1.2	1.2	1.2	1.2
24.0	1.3	1.3	1.3	1.3	1.3	1.4	1.4
40.0	1.8	1.9	1.9	1.9	2.0	2.0	2.0
60.0	2.4	2.5	2.5	2.6	2.6	2.7	2.7
84.0	2.9	3.0	3.1	3.1	3.2	3.3	3.3
100.0	3.1	3.3	3.3	3.4	3.5	3.6	3.6
150.0	3.5	3.8	3.9	4.0	4.2	4.3	4.4
210.0	3.8	4.2	4.4	4.6	5.0	5.0	5.2
250.0	3.9	4.4	4.7	5.0	5.4	5.5	5.8
350.0	3.8	5.1	5.4	5.8	6.5	6.7	7.0
400.0	3.9	4.8	5.5	6.3	7.1	7.2	7.6
500.0	4.0	5.6	6.0	6.8	8.0	8.2	8.8
600.0	3.9	5.7	6.3	7.3	8.8	9.1	10.0
700.0	3.8	5.2	6.9	8.6	10.0	10.3	11.1
750.0	4.0	5.3	6.6	8.4	10.4	10.6	11.8
800.0	3.9	5.1	7.0	9.6	10.7	11.3	12.5
900.0	4.0	5.5	6.9	9.0	11.7	12.0	13.5
1000.0	4.0	5.7	7.1	9.4	12.5	13.0	14.6
1200.0	4.1	5.7	8.9	11.6	14.5	15.1	16.9
1400.0	4.1	6.1	8.6	11.5	15.9	16.6	19.1
1600.0	4.2	5.9	9.8	13.3	17.8	18.6	21.2
2000.0	4.2	6.2	9.7	15.8	20.6	22.1	25.3
2200.0	4.3	6.1	9.9	14.0	21.9	23.3	27.1
2400.0	4.2	6.4	10.5	16.7	23.3	25.1	29.0
3000.0	4.3	6.6	10.3	16.3	26.5	28.8	34.1

SPRING.07.RMS.3

Baseline, m	Averaging Time, s 30.	60.	120.	240.	480.	960.	3600.
16.0	1.5	1.6	1.7	1.7	1.7	1.7	1.7
24.0	1.9	2.0	2.1	2.1	2.1	2.2	2.2
40.0	2.8	3.0	3.1	3.2	3.2	3.3	3.2
60.0	3.7	4.1	4.3	4.4	4.5	4.5	4.5
84.0	4.8	5.3	5.6	5.7	5.8	5.9	5.8
100.0	5.4	6.0	6.3	6.6	6.7	6.7	6.7
150.0	6.5	7.6	8.2	8.6	8.7	8.9	8.8
210.0	7.5	9.1	10.0	10.6	10.9	10.9	11.1
250.0	7.9	9.8	10.9	11.6	12.0	12.0	12.3
350.0	8.3	11.2	12.9	14.1	14.6	14.8	15.1
400.0	8.3	11.6	13.5	14.8	15.5	15.5	16.2
500.0	7.9	11.4	14.3	16.1	17.1	17.3	18.1
600.0	7.8	11.2	14.8	17.2	18.5	18.8	19.9
700.0	7.8	12.0	15.6	17.9	20.1	20.1	21.4
750.0	7.9	12.3	15.6	18.8	20.6	21.3	22.7
800.0	7.8	12.1	17.0	19.6	20.2	21.3	22.6
900.0	7.7	11.9	15.6	19.7	22.1	23.3	25.0
1000.0	7.7	11.3	15.4	20.3	23.1	24.5	26.5
1200.0	7.7	12.1	16.5	20.2	25.4	26.4	28.8
1400.0	7.6	12.6	17.5	21.7	27.2	29.5	32.6
1600.0	8.2	12.4	18.1	21.6	29.2	30.8	34.8
2000.0	8.0	12.8	17.5	25.0	31.5	34.2	38.8
2200.0	8.2	12.7	18.0	22.4	34.0	36.7	42.6
2400.0	7.8	12.0	17.3	23.9	33.3	36.5	43.1
3000.0	7.8	12.4	17.5	23.7	37.2	41.2	50.2

TABLE S2

SPRING.13.RMS.3 Averaging Time, s

Baseline, m	30.	60.	120.	240.	480.	960.	3600.
16.0	5.2	5.3	5.4	5.5	5.5	5.6	5.4
24.0	6.7	6.9	7.0	7.0	7.0	7.3	7.1
40.0	9.6	10.0	10.0	10.1	10.2	10.5	10.1
60.0	13.0	13.5	13.7	13.9	13.9	14.2	13.8
84.0	16.1	16.8	17.0	17.2	17.3	17.6	17.1
100.0	17.5	18.4	18.7	19.0	19.1	19.5	18.9
150.0	19.7	21.4	22.0	22.5	22.7	23.1	22.5
210.0	20.6	23.3	24.3	25.0	25.2	25.4	25.0
250.0	20.5	23.7	25.1	25.8	26.1	26.2	26.0
350.0	20.3	24.9	27.1	28.5	29.0	29.2	29.1
400.0	20.3	25.4	27.8	29.2	29.8	29.8	30.2
500.0	19.0	24.4	27.9	29.9	30.9	30.9	31.6
600.0	18.6	23.7	28.3	30.7	32.1	32.1	33.3
700.0	18.8	24.9	29.4	31.9	34.2	33.8	35.2
750.0	19.1	24.5	29.2	32.6	34.6	35.1	36.6
800.0	19.1	25.1	30.4	33.7	34.4	35.4	36.4
900.0	18.9	24.3	29.1	33.3	35.9	37.3	39.0
1000.0	18.7	23.8	29.1	33.8	36.9	38.5	40.6
1200.0	18.7	24.3	29.5	33.8	39.7	41.1	43.5
1400.0	18.5	24.9	30.5	34.9	41.3	44.1	47.7
1600.0	19.7	25.0	31.1	35.1	44.0	45.9	50.5
2000.0	19.3	25.7	31.2	40.1	47.4	50.7	55.5
2200.0	19.7	26.2	32.3	36.3	50.0	53.3	60.2
2400.0	19.0	24.6	29.9	37.5	48.4	52.4	60.0
3000.0	18.9	24.9	30.6	37.3	53.1	58.0	68.7

SPRING.20.RMS.3 Averaging Time, s

Baseline, m	30.	60.	120.	240.	480.	960.	3600.
16.0	6.4	6.6	6.8	6.9	6.9	6.9	6.8
24.0	8.1	8.5	8.5	8.6	8.6	8.9	8.7
40.0	11.5	12.1	12.2	12.4	12.4	12.7	12.4
60.0	15.4	16.2	16.6	16.9	17.0	17.1	16.8
84.0	18.7	19.9	20.4	20.8	20.9	21.2	20.8
100.0	20.4	22.0	22.6	23.1	23.2	23.5	23.0
150.0	23.3	26.0	27.3	28.1	28.4	28.8	28.3
210.0	25.6	29.8	31.9	33.1	33.5	33.7	33.5
250.0	26.2	31.4	33.9	35.3	35.8	35.9	35.9
350.0	26.7	34.2	38.2	40.8	41.7	41.8	42.0
400.0	26.5	35.0	39.5	42.2	43.3	43.0	44.2
500.0	25.1	34.1	40.8	44.7	46.4	46.4	47.8
600.0	24.5	33.2	41.9	46.8	49.0	49.1	51.1
700.0	24.6	35.2	43.7	48.7	52.6	52.1	54.4
750.0	25.0	35.5	43.5	50.2	53.4	54.3	56.8
800.0	24.9	35.4	46.3	51.9	53.0	54.8	56.6
900.0	24.7	34.5	43.3	51.8	56.1	58.2	61.1
1000.0	24.4	33.3	42.9	52.8	57.8	60.5	64.0
1200.0	24.2	34.6	44.5	52.6	62.7	64.7	68.6
1400.0	24.2	35.9	46.7	55.5	65.8	70.4	75.9
1600.0	25.8	35.4	47.7	55.2	70.1	73.0	80.2
2000.0	25.2	36.7	46.9	63.2	75.4	80.3	87.8
2200.0	25.9	36.8	48.4	56.7	79.4	84.5	95.5
2400.0	24.7	34.5	45.5	59.2	77.1	83.0	95.0
3000.0	24.4	35.1	46.0	58.0	84.1	91.2	108.4

TABLE S2

SPRING.30.RMS.3

Baseline, m	Averaging Time, s 30.	60.	120.	240.	480.	960.	3600.
16.0	7.0	7.3	7.5	7.6	7.6	7.7	7.6
24.0	8.8	9.3	9.4	9.5	9.6	9.9	9.6
40.0	12.7	13.5	13.8	14.0	14.0	14.4	14.0
60.0	17.1	18.4	18.9	19.4	19.5	19.7	19.3
84.0	21.3	23.2	23.9	24.5	24.7	25.0	24.5
100.0	23.6	26.0	26.9	27.7	27.9	28.2	27.6
150.0	27.9	31.8	33.8	35.0	35.4	35.8	35.3
210.0	31.4	37.4	40.5	42.2	42.8	43.0	42.8
250.0	32.6	39.9	43.6	45.7	46.4	46.5	46.6
350.0	33.8	44.4	50.2	53.8	55.1	55.0	55.4
400.0	33.6	45.7	52.2	56.2	57.5	57.0	58.6
500.0	32.1	48.2	57.3	60.3	63.3	62.2	64.4
600.0	31.1	43.6	56.1	63.1	66.0	66.0	68.4
700.0	31.2	46.3	58.8	65.8	70.9	70.1	72.8
800.0	31.4	46.4	62.6	69.9	71.3	73.6	75.7
900.0	31.1	45.4	57.9	70.2	75.5	78.0	81.6
1000.0	30.8	43.4	57.1	71.5	77.8	81.1	85.2
1200.0	30.5	45.7	59.8	71.2	84.1	86.4	91.0
1400.0	30.4	47.4	62.7	75.4	88.2	94.0	100.5
1600.0	32.6	46.4	64.4	75.0	93.7	97.3	105.7
2000.0	31.7	48.2	62.7	85.1	100.4	106.3	114.6
2200.0	32.7	47.9	64.4	76.3	105.0	111.1	124.4
2400.0	31.1	45.1	60.9	79.7	102.0	108.8	123.0
3000.0	30.8	46.0	61.2	77.4	110.0	118.1	139.2

TABLE S2

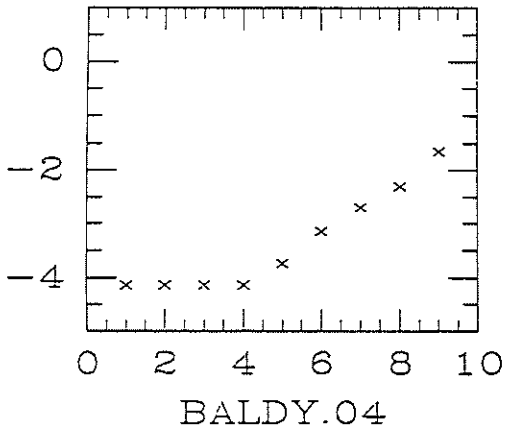

BALDY.04

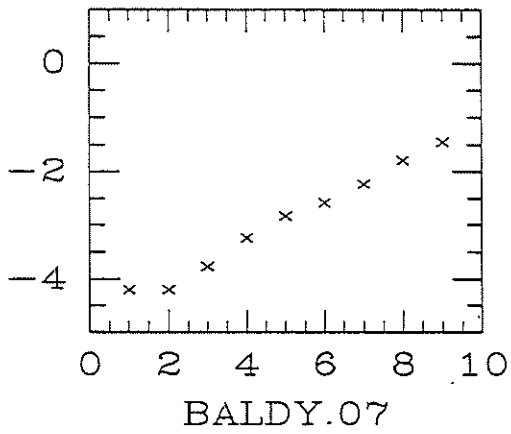

BALDY.07

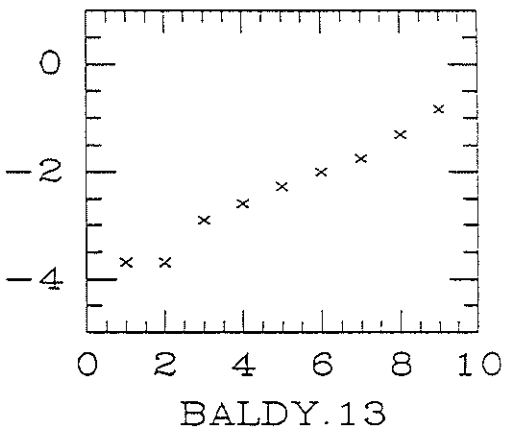

BALDY.13

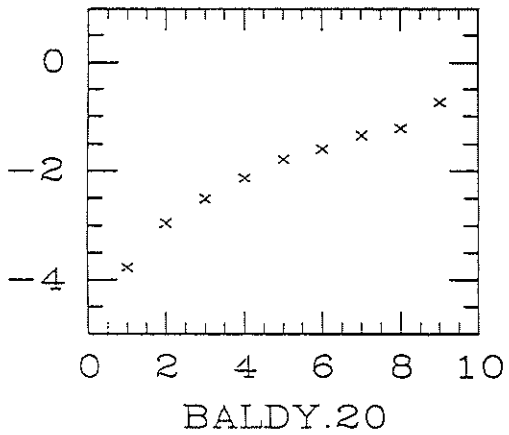

BALDY.20

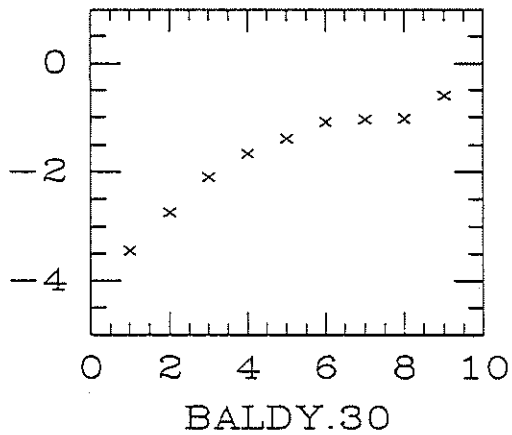

BALDY.30

Fig 1

Truth

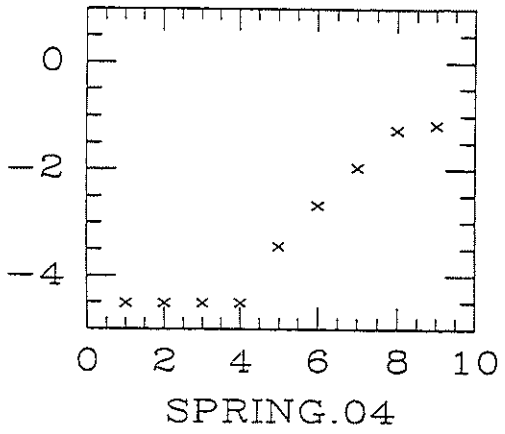

SPRING.04

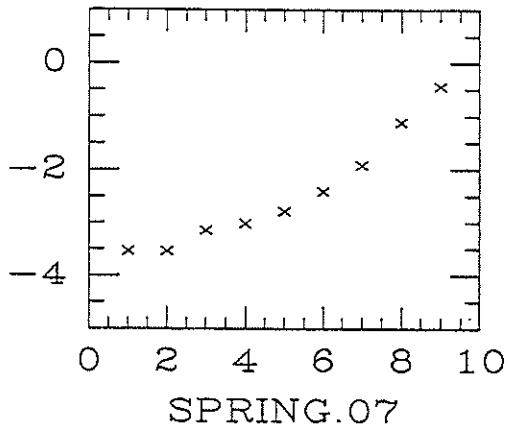

SPRING.07

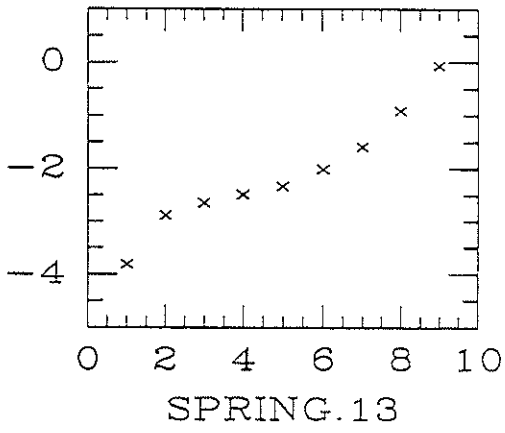

SPRING.13

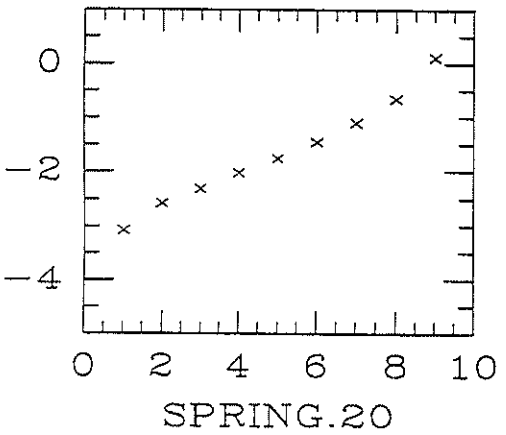

SPRING.20

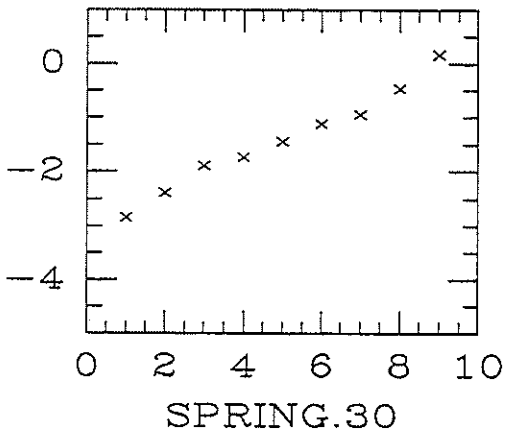

SPRING.30

Truth

Fig 2

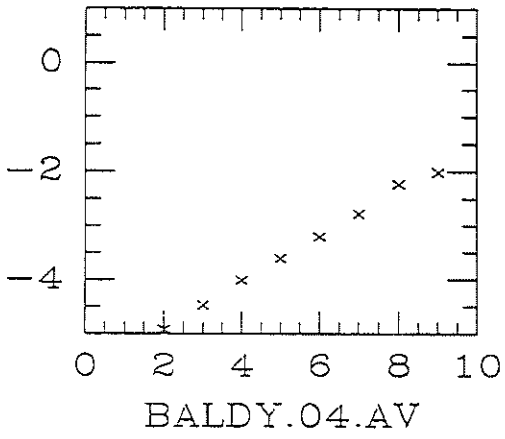
0
−2
−4
0 2 4 6 8 10
BALDY.04.AV

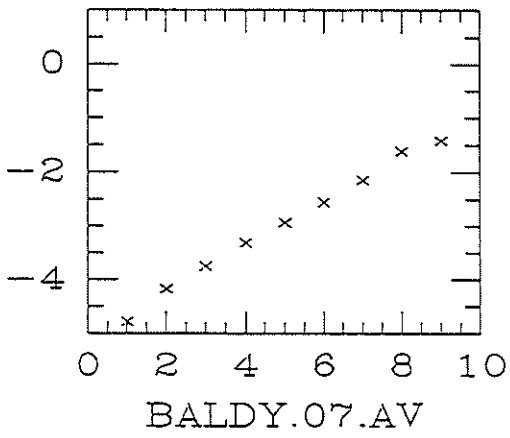
0
−2
−4
0 2 4 6 8 10
BALDY.07.AV

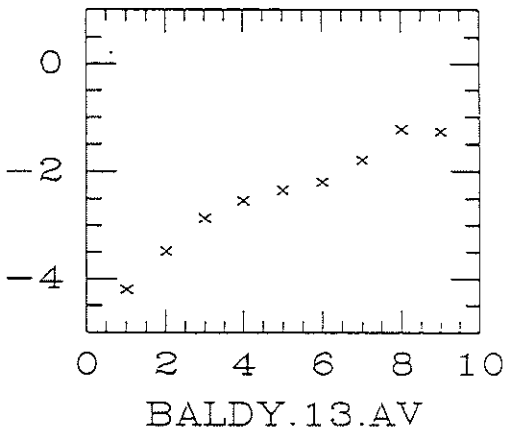
0
−2
−4
0 2 4 6 8 10
BALDY.13.AV

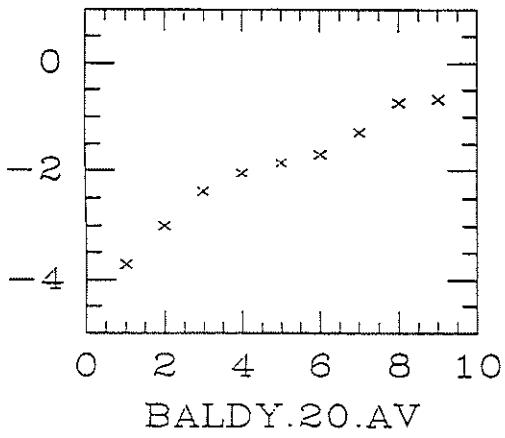
0
−2
−4
0 2 4 6 8 10
BALDY.20.AV

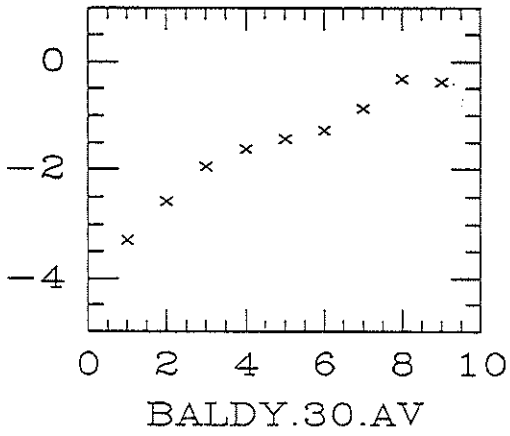
0
−2
−4
0 2 4 6 8 10
BALDY.30.AV

SIM 2

Fig 3

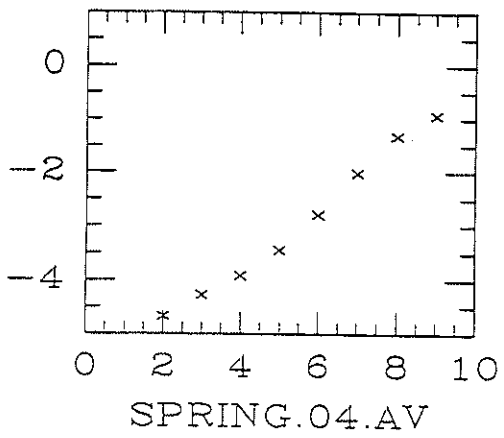
0
−2
−4
0 2 4 6 8 10
SPRING.04.AV

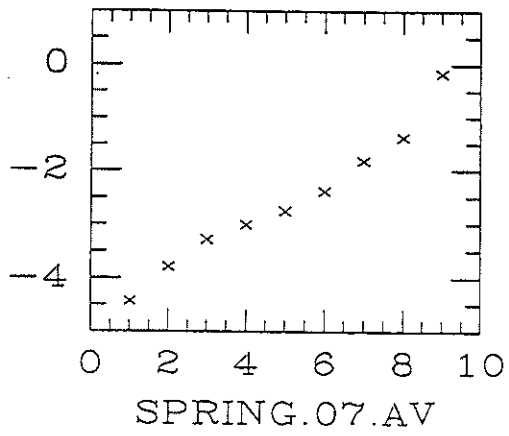
0
−2
−4
0 2 4 6 8 10
SPRING.07.AV

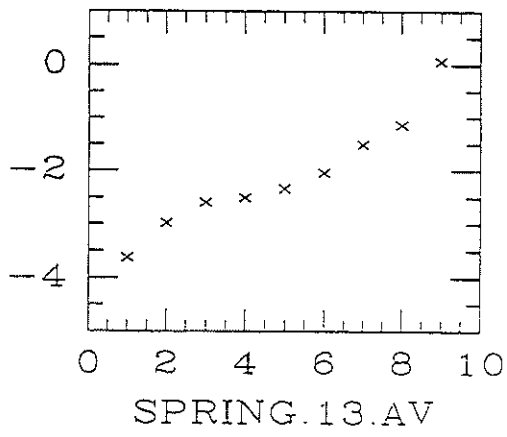
0
−2
−4
0 2 4 6 8 10
SPRING.13.AV

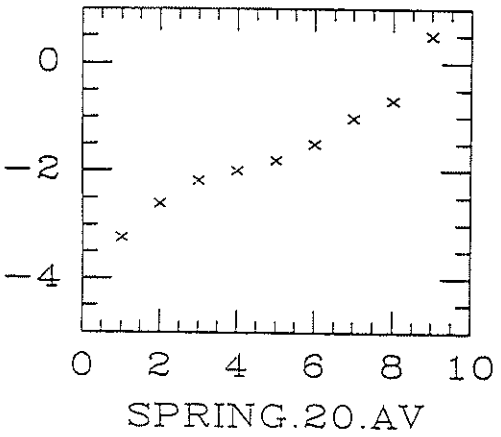
0
−2
−4
0 2 4 6 8 10
SPRING.20.AV

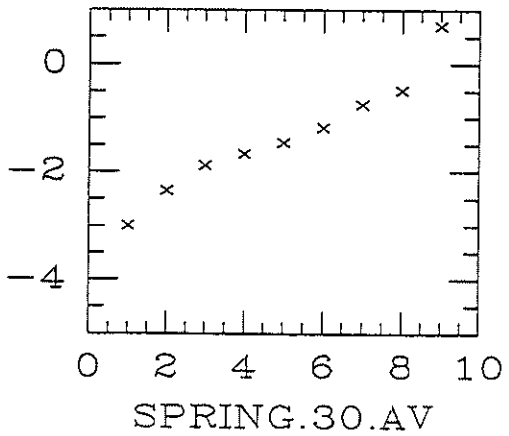
0
−2
−4
0 2 4 6 8 10
SPRING.30.AV

Fig 4

SIM1

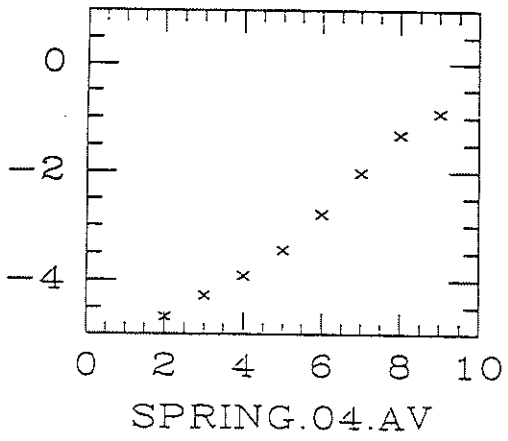
0
−2
−4
0 2 4 6 8 10
SPRING.04.AV

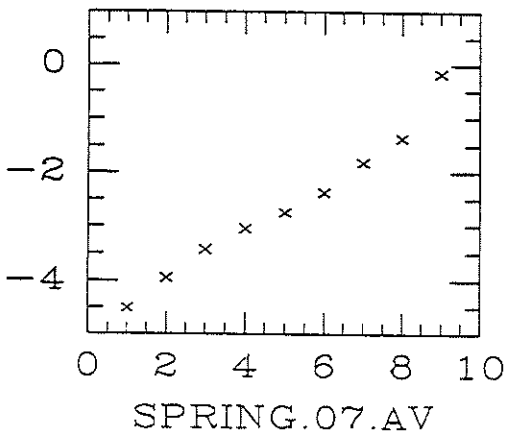
0
−2
−4
0 2 4 6 8 10
SPRING.07.AV

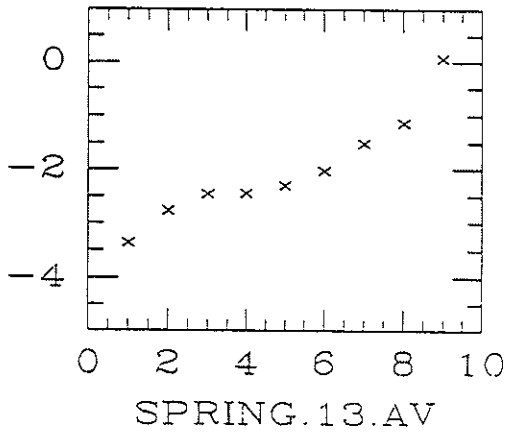
0
−2
−4
0 2 4 6 8 10
SPRING.13.AV

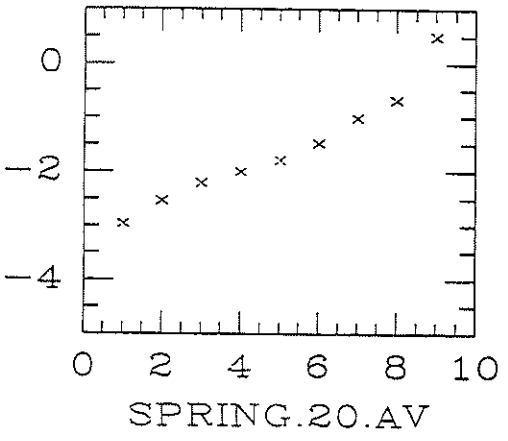
0
−2
−4
0 2 4 6 8 10
SPRING.20.AV

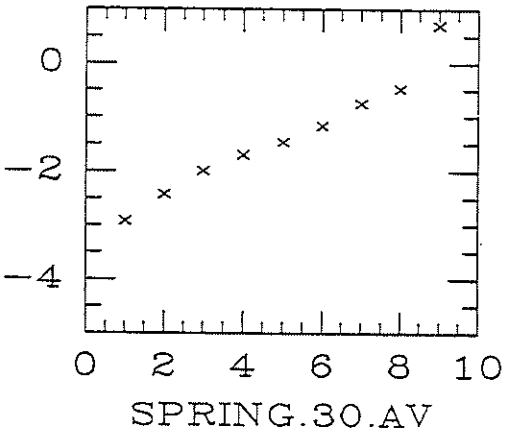
0
−2
−4
0 2 4 6 8 10
SPRING.30.AV

Fig 5

sim 2

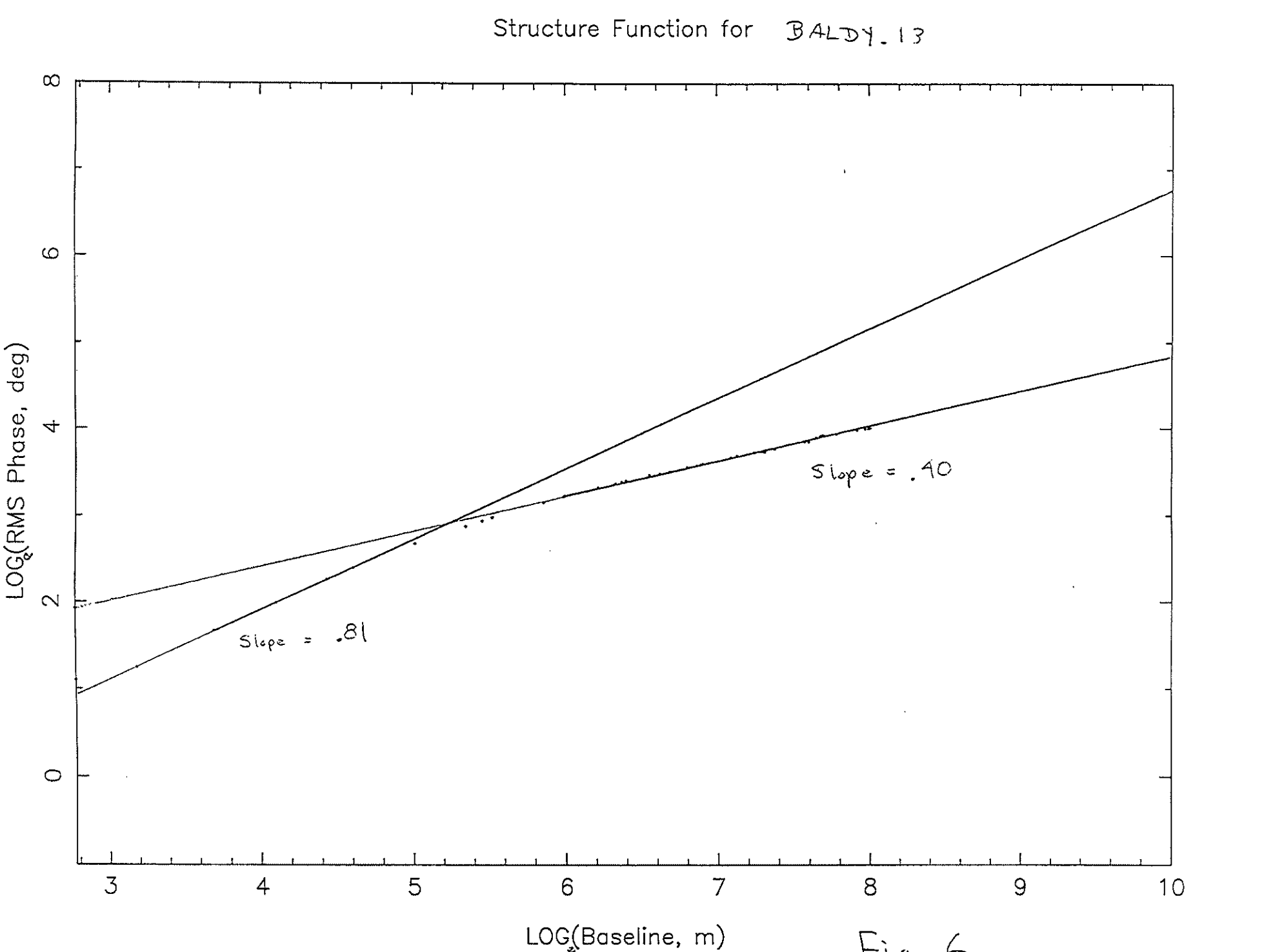

Fig 6

mholdawa 21-Oct-1991 17:19

MMA MEMORANDUM # 69

SIS MIXER & LO OPTIONS FOR THE MILLIMETER ARRAY

A. R. Kerr
5 December 1991

This memorandum is based on a document sent last August to members of the MMA Joint Development Group. Its purpose was to initiate discussion amongst those interested in SIS receiver and local oscillator development for the MMA.

Appendices 1 and 2 list some of the options that might be appropriate for SIS mixer and LO development. The items that seem most promising for further study and development, when MMA funding becomes available, are printed in italics.

In Appendix 3, an initial conservative SIS receiver design is described. It consists of components which we are reasonably confident could be made a few years from now in the quantities needed for the MMA.

MMA receivers for 30-50 GHz, probably 68-90 GHz, and possibly 90-115 GHz, will use transistor amplifiers, whose development will be managed by Marian Pospieszalski. For the present discussion, it will be assumed that SIS receivers will be used at all frequencies above 90 GHz.

The total number of receivers required to give the MMA its intended spectral coverage depends on the outcome of the preliminary SIS mixer and transistor amplifier development efforts. At present we are reasonably confident that amplifiers and SIS mixers will each be able to cover ~20% bandwidths. Each MMA antenna would then need 11 receivers (x 2 polarizations), packaged in 3-5 cryostats, to give full coverage of the desired bands. With additional effort, 30-40% bandwidth (approximately a full waveguide band) may eventually be possible, reducing the required number of receivers to 7 (x 2 polarizations).

For SIS receiver development to proceed at an acceptable rate, substantial sustained funding is needed for junction fabrication. Our only real source of junctions at present is UVA, and their SIS project is almost crippled by insufficient support. Support for SIS junction fabrication should be of the highest priority as we cannot hope to develop wideband SIS mixers without a responsive source of junctions.

Wideband frequency multipliers for the first LO will require considerable development of both circuits and planar diodes. This, too, should be a high priority. At present, NRAO supports no work, internally or elsewhere, on frequency multipliers or other LO sources.

Appendix 1: SIS Mixer Options for the MMA

(Items in italics are initial suggestions for further development.)

- Coupling
  - Quasi-optical
  - *Horn-waveguide*
- Tuning
  - *Fixed*
  - *Adjustable*
    - Mechanical
      - W/g short circuit(s)
      - Other
      - Actuators
        - Lead-screw
        - Cam
        - Piezoelectric
    - Electronic
      - *Varactor*
      - JJ inductor
      - Kinetic inductance
- Junction type
  - *Nb*
  - NbN
  - Pb-alloy
- Mixer type
  - Fundamental
    - *Single-ended*
    - *Balanced* (may be useful for image separation mixers)
  - Harmonic
  - *Image-separation*
  - Single-sideband (i.e., reactive image termination)
  - *High IF* (e.g., 20-40 GHz) vs low IF
- Additional areas needing study:
  - *Multiple bias points in series arrays.*
  - *Suppression of Josephson noise ???-360 GHz in mixers with series arrays.*
  - *Effects of a high IF (e.g., 20-40 GHz) on SIS mixer performance.*
  - *The need for an IF isolator; how does it depend on mixer design?*
  - *Integration of the IF amplifier into the mixer block.*
  - *Optimization (L, T_M, bandwidth) of fixed-tuned mixers.*

Appendix 2: Millimeter Local Oscillator Options for the MMA
(Items in italics are initial suggestions for further development.)

- Fundamental Source (or pump for multiplier)
  - Transistor
    - *YTO*
    - Other
  - *Gunn*
  - Transit-Time (IMPATT, Tunnett, etc.)
  - Quantum-well
  - Solid state vacuum triode
  - Josephson oscillator

  - X-Y Distributed (grid oscillators)
  - Z-Distributed (travelling-wave)

  - Tuning method -- see mixers

- Upconverter
  - Varactor (or varistor) diode
  - Transistor

  - Distributed (travelling wave)

- Multipliers
  - Discrete
    - *Tunable*
    - *Tunerless*
  - X-Y Distributed (grid multipliers)
  - Z-Distributed (travelling wave multipliers)
    - *Nonlinear transmission line (soliton)*

  - Diodes for multipliers
    - Whisker-contacted
    - *Planar diodes*

    - *Schottky*
    - *δ-doped*
    - Quantum-well
    - Other

  - Tuning method -- see mixers

- *Power amplifiers* (to drive multipliers)

- Additional areas needing investigation
  - *Noise (AM, FM, and ϕM) in oscillators, multipliers, power amplifiers.*
  - *Design of broadband multipliers.*
  - *Optimization of diodes for multiplier chains (e.g., δ-doped for low power stages).*

Appendix 3: An Initial Conservative Receiver Configuration

Room temperature optics

Input multiplexer	Martin-Puplett interferometer tuned for 3 dB LO loss while terminating the image in a 4 K load.
Vacuum window	?

Cryogenic optics

I/R filter (50 K)	Grooved teflon or polyethylene.
Lens	Polyethylene.
Horn	Corrugated horn for longer wavelengths. Potter horn for short wavelengths?
Image Cold-Load	?

Mixer

SIS mixer	Single-ended, broadband, waveguide mixer with integrated tuning. No mechanical tuning. Fundamentally pumped. Useable bandwidth not yet clear.

IF Components

Isolator	Probably necessary unless the IF amplifier can be integrated with the mixer. At L-band an isolator would restrict the bandwidth. Prefer, therefore, an IF of 2-3 GHz.
Amplifier	30 dB gain, 3 stages, 30 mW dissipation (+ 20 mW if LED's are required).

Local Oscillator

Fundamental source	ϕ-lockable YIG-tuned oscillator, 30-45 GHz.
Power leveller	(servoed to DC junction current)
Amplifier	30-45 GHz, 100 mW
Doubler(s) Tripler(s)	Output 68-90 GHz Output 90-120 GHz
Amplifier(s)	65-90 GHz, 50 mW
Doubler(s) Tripler(s) Quadrupler(s)	Output 130-170 GHz Output 200-270 GHz Output 270-360 GHz

MMA MEMORANDUM # 70

IMAGE FREQUENCY SUPPRESSION ON THE MMA

A. R. Kerr
12 December 1991

There has been some discussion of the need for image suppression on the MMA. Image suppression (or separation) is required with the MMA's mixer receivers for two reasons: to remove atmospheric noise received in the image band, which would otherwise substantially degrade the overall system sensitivity, and to remove (or separate) signals from astronomical sources received in the image band which would contaminate the image produced by the array.

To remove atmospheric noise, an image rejection ≥10 dB across the band should be acceptable. However, to produce good images, the MMA will need to reject astronomical image-frequency signals by ≥30 dB.

There are three ways to obtain image suppression (or separation): (i) A filter can be used ahead of the mixer. This could be a two-port filter, or a four-port filter which would allow the image to be terminated in a cold load. (ii) Walsh function phase switching of the LO's allows signal and image signals arriving at the antennas to be separated digitally in the back end. (iii) Image separation mixers provide separate IF outputs for the upper and lower sidebands at each receiver.

The choice of the first intermediate frequency is important if an image filter is used in front of the receiver. However, other factors also affect the choice of IF, including: the desired IF bandwidth (1 GHz for each polarization), the need for an IF isolator between the mixer and IF amplifier, and the penalty in noise temperature of using a higher IF.

This memorandum addresses the following questions:

- Should the image response be suppressed at the front end, either by an image filter or using an image separation mixer?
- Should we plan to include quadrature phase switching of the first local oscillator as a means of image separation?
- What first IF should be used?

IMAGE SUPPRESSION/SEPARATION

RF Input Filtering

The choice of input filter is governed in part by the requirements of the SIS mixers. The tunerless SIS mixers needed for the MMA will operate best when connected to the same optimum value of source impedance at the signal and image frequencies. A simple two-port (reactive) filter is therefore not appropriate, and a four-port filter with a frequency-independent input impedance must be used. The most suitable four-port filter appears to be the quasi-optical Martin-Puplett interferometer [1], which has been widely used in millimeter wave receivers both as a sideband filter and as a LO diplexer [2,3]. The filter is simply tuned by moving a single reflector, and can be adjusted to suppress either upper or lower sideband, or to allow both to be received. Its image port can be coupled quasi-optically to a cold load.

With a Martin-Puplett image filter, the image rejection can be very large at the center frequency, but degrades rapidly towards the band edges. Figs. 1 and 2 show the transmission, as a function of frequency, of M-P image filters operating in receivers with IF's of 1-2 GHz and 2-3 GHz. The image rejection at the band edges is 12 dB and 16 dB, respectively. A 3-4 GHz IF would give an image rejection $\geq$19 dB across the band, with little penalty in receiver noise temperature.

The theoretical insertion loss at the edges of the signal band for the same three examples is 0.30 dB (1-2 GHz), 0.11 dB (2-3 GHz), and 0.05 dB (3-4 GHz). A loss of 0.3 dB would cause an unacceptable degradation in sensitivity.

Phase Switching

Phase switching of the LO, using different Walsh functions at each antenna, allows upper- and lower-sideband signals from astronomical sources to be separated digitally in the back end. Atmospheric noise in the image band, which is not correlated between the antennas of the array, cannot be removed in this way, however.

Image Separation Mixers

Only by using image separation mixers can MMA observations be made simultaneously in the upper and lower sidebands while suppressing atmospheric image noise.

An image separation mixer uses two simple mixers in parallel, driven by a quadrature-phased LO. The input signal, upper and lower sideband, is divided equally between them, and their IF outputs are combined in a quadrature hybrid coupler. Upper- and lower-sideband information appears at separate ports of the IF hybrid.

In an image separation mixer, the image rejection depends on the phase and amplitude balance through the two paths of the mixer. Using current technology, I would expect it to be difficult to produce image separation

mixers with image rejection much above 10 dB across the full IF bandwidth and over the full RF tuning range. This is being investigated by D. Woody.

If image separation mixers turn out to be feasible for the MMA, they may influence the choice of IF. The need for good amplitude and phase balance in the two parallel channels of an image separation mixer is likely to support the use of a moderately high IF (a few GHz) with a correspondingly smaller fractional bandwidth.

IF CONSIDERATIONS

Isolators

It is most likely that IF isolators will be needed for the MMA receivers. SIS mixers do not generally operate well with their output port impedance-matched. The out-going noise wave from the IF amplifier will therefore be reflected by the mixer back into the amplifier, degrading its noise temperature, unless an isolator is used.

Isolators may not be required if it is possible to integrate the IF amplifier into the SIS mixer block. However there are potential difficulties in doing this, not the least of which is the thermal design of the mixer block to prevent the amplifier heating the SIS junctions above 4 K. (With Nb junctions, even a 0.5 K increase in the junction temperature can significantly raise the receiver noise temperature). Another difficulty may arise from the change of output impedance of a tunerless SIS mixer as the LO is tuned; the integrated IF amplifier may be required to maintain a low noise temperature over a wide range of source impedances, which may not be possible. These matters need to be investigated during the preliminary development phase of the MMA.

A conservative initial receiver configuration should therefore include an IF isolator. Cryogenic isolators with 1 GHz bandwidth are commercially available [4] for operation at center frequencies $\geq$3 GHz.

IF Amplifiers

Cryogenic transistor amplifiers at present can be made with a maximum noise temperature of ~3 K over the 2-3 GHz band, and ~4 K over the 3-4 GHz band, and these figures may improve somewhat in the future.

It has been suggested [5] that a very high IF, possibly 20-40 GHz, could be used for the SIS receivers on the MMA, and would reduce the required tuning range of the first local oscillators. This would carry a penalty in receiver noise temperature whose severity would depend on the conversion loss of the SIS mixer. Such a very high IF may make it difficult to provide desirable embedding impedances at both signal and image frequencies for the SIS junctions, thereby degrading the mixer performance. Furthermore, at 40 GHz the photon energy is sufficiently large that new quantum effects can be expected in an SIS mixer. This is a completely unexplored area at present.

CONCLUSIONS

To achieve acceptable image rejection for both atmospheric noise (≥10 dB) and astronomical signals (≥30 db), we should plan to use LO phase switching together with either RF input filtering or sideband separation mixers. The choice between RF input filtering and sideband separation mixers will depend on developments in the latter during the next few years.

A conservative initial design for the SIS mixer receivers on the MMA might have a 3-4 GHz first IF, and should include IF isolators.

REFERENCES

[1] D.H. Martin and E. Puplett, "Polarized interferometric spectrometry for the millimeter and submillimeter spectrum," Infrared Physics, vol. 10, pp.105-109, 1969.

[2] N. R. Erickson, "A Very Low-Noise Single-Sideband Receiver for 200-260 GHz," IEEE Trans. Microwave Theory Tech., vol. MTT-33, no. 11, pp. 1179-1188, Nov. 1985.

[3] J. M. Payne, "Millimeter and submillimeter wavelength radio astronomy," Proceedings of the IEEE, vol. 77, no. 7, pp. 993-1017, July 1989.

[4] G. Grund, Pamtech, Inc., Canoga Park, CA 91304, private communication.

[5] M. Pospieszalski, "HFET's and receivers for the millimeter-wave array," Millimeter Array Memo No. 67, National Radio Astronomy Observatory, Charlottesville, VA 22903, Aug. 1991.

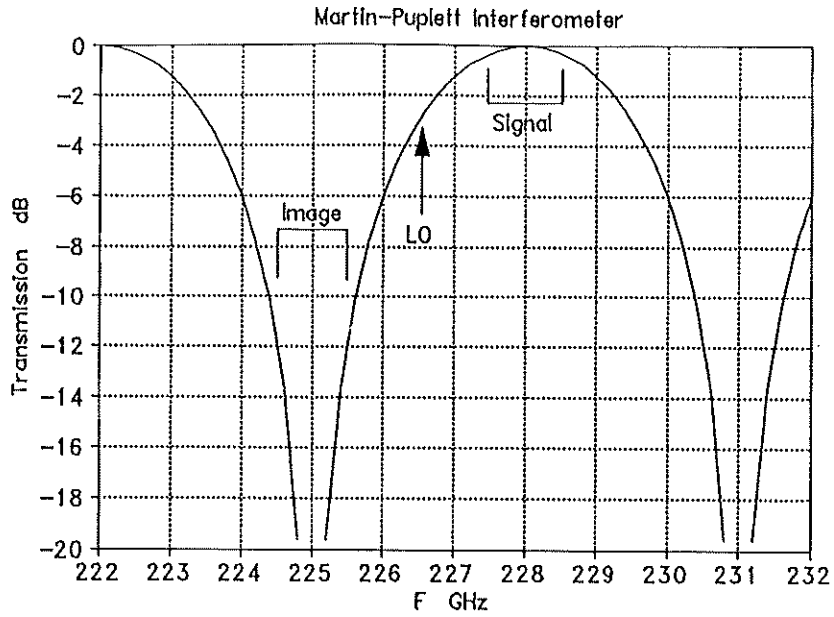

Fig. 1. Response of a Martin-Puplett image filter with 1-2 GHz IF.

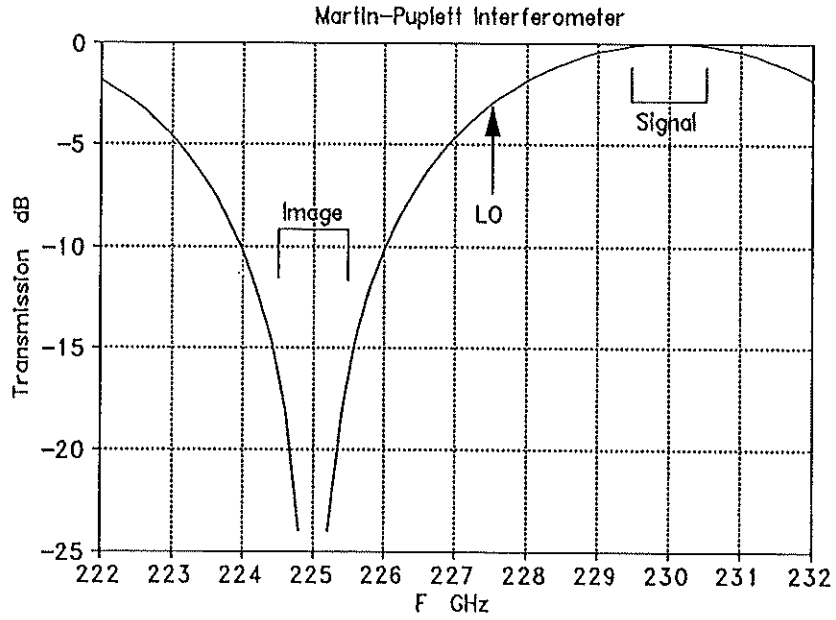

Fig. 2. Response of a Martin-Puplett image filter with 2-3 GHz IF.

MILLIMETER ARRAY
MEMO NO. 71

MMA Systems Engineering Questions and Comments

A. R. Thompson

December 1, 1991

The major parameters of the Millimeter Array that define the overall capability have been specified in the proposal document. These include such things as the number and size of the antennas, the range of antenna spacings, and the observing frequency bands. Now, as we are beginning to think about the design of the hardware, it is necessary to consider the receiving system in greater detail. The goal is to produce a block diagram that shows details of the signal flow and breaks the hardware down into units with well defined characteristics that are feasible to construct. Developing this block diagram is a task of the Systems Engineering group.

This memorandum outlines some of the questions that are encountered at a fairly simple level of detail when considering such a block diagram. A number of these questions concern the way in which the received signals are handled between the front ends and the correlator. The questions have been discussed by NRAO staff involved in the MMA project and many of the resulting ideas are included below. However, this memorandum is intended to stimulate discussion rather than to indicate that any firm decisions have yet been made. Initial answers obtained can in many cases be expected to be modified before the array is built, as techniques and components improve. Thus the aim is to produce and maintain an optimum plan for implementation of the receiving system, revising it as necessary.

(1) First Intermediate Frequency and Bandwidth.

It will be assumed that the front ends contain mixers and the outputs are at an intermediate frequency. What are the frequencies and bandwidths of the IF's at this point? The proposal indicates a total bandwidth of 2 GHz per antenna, so the bandwidth for single-band observing would be 1 GHz for each polarization. It has been pointed out in MMA Memo 67 that a wide bandwidth for the first IF could reduce the required tuning range of the first LO. This would require IF bandwidths of tens of GHz, and the resulting high intermediate frequencies could also result in increased system temperature. Use of a high IF seems to be a future possibility that would require some development. It has been recommended that with a 1 GHz bandwidth the IF center frequency should be 2.5 GHz (rather than 1.5 GHz) to reduce the fractional bandwidth of the IF input circulator, if one is needed. More importantly, the higher intermediate frequency would improve the image rejection obtainable with a Martin-Puplett interferometer. Note that the 1 GHz bandwidth, which can be used for planning at this early stage, is a minimum requirement and is likely to be increased as the technology allows.

(2) Image Suppression.

For most spectral line observations, and for continuum observations in the larger configurations, the array will be required to operate in a single sideband mode. However, for continuum operation, simultaneous reception in both sidebands reduces the receiver noise temperature by an approximate factor of two. It also results in increased bandwidth smearing, and so would probably only be usable at the smallest configurations. The front ends should therefore be designed to allow operation in either double or single sideband

modes.

In single sideband operation, how will the image response be suppressed? Image suppression could be implemented at the front end by means of a Martin-Puplett interferometer or by development of a sideband separating configuration for the SIS mixer. With a Martin-Puplett interferometer the image rejection increases with the intermediate frequency: for a signal frequency near 230 GHz the image rejection at the band edges is 12, 16 or 19 dB for IF bands 1-2, 2-3 or 3-4 GHz respectively (see memo by T. Kerr, 9/19/91). Degradation of the system noise temperature would limit the IF to a few GHz. Also, the achievable image rejection with a sideband separating mixer might be no better than 10 dB at some points in the band. Image rejection in the range 10-20 db would be sufficient to prevent degradation of the system temperature by atmospheric noise at the image frequency, which is an important requirement. However, it would not be sufficient for the required spectral dynamic range. Thus sideband separation at the correlator (which does not remove atmospheric noise) may also be required. This technique involves quadrature phase switching of the first LO and doubling the number of integrators at the correlator output. It appears that we should plan to include both image suppression by hardware at the front end and by phase switching. A Martin-Puplett interferometer at the front end would be remotely adjustable to allow the rejection band to be placed over the unwanted sideband for any particular local oscillator tuning. It could also be adjusted to allow both sidebands to be accepted by the mixer when required.

(3) First LO Tunability.

With an IF bandwidth of 1 GHz the minimum tuning increment of the first LO should be about 500 MHz which will require an LO reference of the same frequency. A scheme like that used for the VLBA in which the lock frequencies are (Nx500 +/- 100) MHz is convenient to implement and would be appropriate. At the highest observing frequencies the multiplication factor for a 500 MHz reference frequency would exceed 700, so considerations of phase noise may require a use of an additional, higher reference frequency. Note that distributing fixed reference frequencies and synthesizing required frequencies at the antennas should, in practice, result in better phase stability than distributing tunable reference frequencies. Also, in a complicated system it can be extremely difficult to avoid spurious responses if tunable reference frequencies are used.

(4) Number of IF Signals at each Antenna.

The project book indicates that dual band observing using a dichroic system at the feeds is a requirement of the array. The number of IF's to be handled at each antenna should thus be no less than four to allow for simultaneous observations at two frequencies, each with dual polarization.

(5) Channelization.

Should the 1 GHz-wide IF bands be further subdivided into narrower channels before digital sampling? If the observer wants to use only a part of the full 1 GHz IF bandwidth then narrower channels must be provided that will be tunable across the IF bands to allow the desired frequencies to be selected. There should perhaps be more than one channel for each IF to allow for cases in which two or more parts of the IF band are of interest. A system with one

or two such channels per IF (i.e. this means four or eight per antenna) was suggested in MMA Memo No.65. It has been noted that with modern circuitry it should be possible to sample and digitize a bandwidth of one or two GHz with a single sampler. This would be good for continuum observing, but breaking the IF down into a number of tunable narrower channels is likely to be necessary to provide flexibility of bandwidth for line observations. Filtering by digital techniques would add considerable complexity to the system. Channelization considerations also depend upon the design of the correlator. A preliminary figure for the minimum spectral channel bandwidth (i.e. the spectral resolution) that has been mentioned in earlier discussions is 6 kHz. (This figure is equal to the Doppler shift for a radial velocity of 0.02 km/s at 100 GHz.) If the correlator produces 1000 spectral channels, the IF channels prior to sampling would require bandwidths variable down to 6 MHz.

(6) Analog or Digital Transmission.

Should the signals be transmitted from the antennas to the correlator location in analog or digital form? The advantage of analog transmission is that it simplifies the equipment at the antennas since selection of the final frequency channels and sampling can then be performed at the correlator location. Advantages of digital transmission are that distortion in the analog transmission system is avoided, high linearity of the transmission system is not necessary to maintain high dynamic range, and after digitization the signals are not susceptible to pickup of low-level spurious components. Also, the stability of the delay in the transmission is less important because, in principle, the time at which each sample was taken is known. In the VLA, which uses waveguide as an analog transmission medium, the dependence of the passbands on the flatness of the waveguide response is a limiting factor in the dynamic range achievable in the images. Of the advantages given above, those of digital transmission seem to outweigh those of analog.

It also appears that for fiber optic systems digital transmission can, in some circumstances, handle a higher signal bandwidth than analog transmission. In analog transmission the noise introduced in the laser diode imposes a lower limit to the power spectral density of the signal at the modulator input to avoid degradation of the signal-to-noise ratio. In addition, there is a maximum input power limit set by linearity requirements. The effect of these two limits is a limit on the bandwidth. This bandwidth limit depends inversely upon the required signal-to-noise ratio and the dynamic range required in the link. Since a lower signal-to-noise ratio and dynamic range can be tolerated for digital bits, the signal bandwidth transmitted in the digital case can be higher if the number of bits per sample is not too high. However, for the MMA the limit on the analog bandwidth resulting from this effect should be at least several gigahertz, and so it may not be an important consideration.

(7) Use of Fiber Optics in the Delay System.

The possibility of using switched lengths of fiber optic transmission line as delay elements has been pointed out in MMA Memo No. 66. If the signals are carried in digital form in the transmission line, adding further sections for delay purposes would not cause distortion. This would be an analog delay of a digital signal. The relative advantages of performing some delay steps in the transmission line rather than making the whole delay system in digital

circuitry are mainly related to cost and reliability, so a choice would rest largely on engineering considerations. With analog signal transmission the temperature coefficient of the delay in the fiber would be important. The practicability of the fiber optic delay system would depend strongly on the availability of fiber optic switches with adequate performance.

(8) What is the Minimum Tuning Increment for the Final LO?

This tuning increment determines how closely the channels discussed in (5) could be set relative to a particular frequency in the IF band. This should be some fraction, say 1/10, of the narrowest analog bandwidth which, as suggested in (5) above, might be 6 MHz. Thus the LO should be tunable in increments of about 0.5 MHz.

(9) Fringe Rotation.

How should the fringe rotation be implemented? Possible methods are by offsetting a local oscillator, or digitally in the correlator as in VLBI. Fringe rotation in a lag correlator usually involves a small loss in sensitivity as a result of the use of a two- or four-level representation of the waveform with which the signal is multiplied. More importantly, it has been pointed out in VLBA Memo No. 593 that phase shifting after coarse quantization does not compensate accurately for phase shifts incurred before sampling. It works alright in most cases, but calculations in the Memo demonstrate that for high correlation coefficients (>0.2), which could occur in observations of maser lines, spectral dynamic range is lost. These problems are avoided by fringe rotation at one of the local oscillators, as in the VLA. The system for fringe rotation in a local oscillator also provides a means of real time phasing of the array, which is presumably a requirement for the MMA. Discussions in some early VLA memos (VLA Electronics Memoranda Nos. 116 and 122) concluded that both fringe rotation and phase switching should be introduced in an early LO in the receiver chain. Fringe rates for the MMA will be very similar to those for the VLA, in which a fringe frequency synthesizer at each antenna is used to offset the reference in an LO phase-locked loop. Is there any reason not to use a similar scheme for the MMA? It should be noted that since the VLA may be re-outfitted in the foreseeable future, it would simplify design and maintenance if some units were identical in both instruments. The fringe rate generator is a possible case for such a unit.

(10) A Special Wideband Correlator for Continuum Observing?

Data processing for spectral line observing will be done in a digital correlator, the capacity of which will limit the bandwidth that can be used for continuum observations. To obtain wider bandwidths for maximum sensitivity in continuum observing it is likely to be cheaper to build a special continuum correlator rather than to expand the spectral correlator. The continuum correlator would perform only multiplying and integrating functions without lags or real time FFT's. Correlation of wide bandwidth signals in a single channel has the effect of smearing the image in the outer parts of the field of view. With the 3 km configuration of the array the smearing would begin to be noticeable at a bandwidth of about 1/200 of the observing frequency, e.g. 500 MHz for the 3 mm band. Thus to obtain an overall bandwidth of several GHz at the larger configurations several narrower channels would be processed in parallel. For the purpose of detecting narrow,

weak sources some degradation in the resolution would be acceptable in return for higher sensitivity. However, these factors need to be carefully weighed to decide what the maximum channel bandwidth for a continuum correlator should be. Although the additional correlator would perhaps be a feature to be added later in the design of the array, it should be considered at this point because it would affect the bandwidth requirements of the signal transmission system.

In principle, a continuum correlator could be implemented in either analog or a digital hardware. An analog system would also require analog signal transmission and compensating delays. A bandwidth of 1 GHz, for example, would require delay adjustment to an accuracy of 31 ps (1/32 of the reciprocal bandwidth, as in the VLA delay system) which is equivalent to an air path length of 9.7 mm. To avoid rapid switching of short lengths of optical fiber the fine delay elements might have to use moving mirrors to provide a variable path length. The usefulness of an analog system would depend upon how accurately the signal passbands could be maintained, and the extent to which bandpass mismatch would limit the dynamic range achievable in imaging. The reason for considering an analog correlator is that it might be somewhat cheaper since some parts of the system such as the signal multiplying elements could be quite broadband. However, if image smearing considerations require that the overall bandwidth be broken down into a number of parallel channels, the possible advantage of the analog approach is reduced, since very broad bandwidth components would no longer be needed. As in the case of double sideband observation, the size of the array configuration should be included in any consideration.

(11) Total Power Measurements.

Measurement of the total power received at each antenna is required for a number of purposes. These are, (1) determination of total flux density from an area being mapped, (2) pointing calibration, as an alternative to interferometer-mode pointing, (3) measurement of system temperature, (4) operation of the array as a set of independent single dishes. Measurement of system temperature is a way of monitoring variations in the atmospheric component noise power, and might in the future provide a correction for atmospheric phase. Four total power measurement units should be provided at each antenna to cover the four IF channels mentioned in section (4). Each total power unit would contain a square-law detector, and also a synchronous detector to extract the switched component from a noise source or nutating subreflector. This system would provide for continuum measurements of total power. If spectral line measurements of total power are required these would have to be implemented in the correlator using an autocorrelation mode. They would therefore be made on the IF signals after digital sampling. The level of the IF signals at the sampler input will be controlled by an ALC circuit, but a measurement of the unlevelled IF power would be provided by the continuum total power system.

(12) Pulse Calibration Scheme.

A feature that may be desirable for the MMA is a pulse calibration scheme to facilitate bandpass calibration of the IF signal channels from the antennas to the correlator. This would be similar to the calibration systems used in VLBI in which a series of narrow pulses is injected into the front end inputs. The

spectrum of such a pulse train is a series of lines that are harmonics of the pulse repetition frequency, which is commonly one or five megahertz, i.e. a comb spectrum. In VLBI the pulses are derived from the maser at each antenna site, and can be used to calibrate the instrumental phase responses. The pulse generators use tunnel diodes to produce pulses of width approximately 25 ps, which result in a useful comb spectrum up to about 30 GHz. It is not within the current state of the art to generate trains with lines of useful strength as high as the observing frequencies of the MMA, but pulses could certainly be injected into the IF stages immediately following the SIS mixers. The system would not help to calibrate drifts in the first local oscillator, but a series of lines across the passband could be used to measure the variations in amplitude and relative phase with frequency. During spectral line programs such calibration could be performed at convenient intervals since one would not generally want the calibration lines present when astronomical data was being taken. Measurement of the calibration lines might be done in the correlator, or a special line-frequency extraction system, and these considerations would determine whether it would be possible to calibrate all antennas and all IF's simultaneously. Pulse calibration schemes were considered for the VLA but never implemented, and various possibilities are described in VLA Electronics Memo No. 172.

MMA MEMORANDUM # 72

CIRCULAR POLARIZATION AND MULTI-BAND OPERATION: IMPLICATIONS FOR MMA RECEIVER DESIGN

A. R. Kerr
9 January 1992

It is desirable that the MMA operate with circular polarization. Also, the ability to operate simultaneously in two frequency bands is important for some astronomical measurements. This note considers these requirements from the viewpoint of receiver design.

On a millimeter-wave radio telescope a number of operations can be performed quasi-optically before the signal beam enters single-mode waveguide. These include:

- Separation of the incoming beam into individual frequency bands for routing to different receivers.
- Conversion of left and right circular polarization to two linear polarizations, as required by most millimeter wave mixers and amplifiers.
- Termination of the image frequency in a cold load to prevent atmospheric image noise degrading the system sensitivity during spectral line observations.
- Coupling the local oscillator power into the receiver.

While it is possible, in principle, to perform most of these functions in single-mode waveguide or TEM circuits, it is probably not practical at millimeter wavelengths, especially where wide tuning ranges are required. Quasi-optical components are fairly easy to design and construct, have very low loss, and are easily tunable over wide frequency ranges. They are also relatively easily moved into and out of the optical path as needed.

Fig. 1 shows three possible arrangements of quasi-optical components which would perform all or most of the above functions. Fig. 1(a) allows observations with dual circular polarization using a frequency band diplexer with circularly polarized input and output beams (e.g., a dichroic plate). Fig. 1(b) is also for dual circularly polarized observations, but in this case the beam from the telescope is split into its left and right circular components using a circular polarizer with linearly polarized output beams (e.g., a Martin-Puplett interferometer). Fig. 1(c) is used for dual linearly polarized observations. The incoming beam is split into its linear polarization components using a linearly polarized beam splitter (e.g., a wire

grid). The realization of each functional block is considered below.

The discussion here applies primarily to receivers with single-ended double-sideband mixers. If image separation mixers turn out to be practical, an image filter will not be needed. If balanced mixers can be developed, the LO diplexer will not be necessary. Low noise transistor amplifiers will eventually eliminate the need for both at the longer millimeter wavelengths.

The Martin-Puplett Interferometer

Most of the functions in the above list can be performed very well by the quasi-optical Martin-Puplett interferometer [1], an easily fabricated device which has been widely used in millimeter wave receivers as a sideband filter and as a LO diplexer [2,3]. The interferometer is simply tuned by moving a single reflector. As a circular polarizer, it can receive left and right circularly polarized signals from the telescope and convert them to linearly polarized signals at separate output ports. As an image filter, it can be adjusted to suppress the upper or lower sideband, or to allow both to be received. Its image port can be coupled quasi-optically to a cold load. It can also operate as frequency band diplexer.

The M-P interferometer is normally operated with a polarizing grid at its output (or input) port to separate (or combine) two linear polarizations. Linear polarization is necessary as there is no circularly polarized equivalent of the wire polarizing grid.

Polarization Diplexers

Linear Input Polarization/Linear Output Polarization. For separation of two linear polarizations, a wire grid is almost ideal. It is easily made, and can have a useful frequency range of several octaves. A pair of intersecting grids can perform the same function, with the advantage of added symmetry: both polarizations pass through and are reflected off grids and emerge perpendicular to the input beam, having traversed identical path lengths. This dual-grid type of beam splitter has been successfully used on SIS receivers on the NRAO 12-m telescope [4]. (Formulas and programs for the design of wire grid beam splitters and polarizers are given in [5]).

Circular Input Polarization/Linear Output Polarization. For separation of left and right circular polarizations, at centimeter wavelengths, septum-type square waveguide polarizers give dual linear outputs in separate waveguides with an axial ratio AR $\leq$ 1 dB over ~20% bandwidth (about half a waveguide band). At millimeter wavelengths, the use of this kind of polarization diplexer would preclude the use, ahead of the feed horn, of (practical) quasi-optical image filters and LO diplexers, which are linearly polarized. Furthermore, because of their small critical dimensions, it is probably impractical to make septum-type circular polarizers for wavelengths less than a few millimeters.

At millimeter wavelengths, an attractive circular polarization diplexer is the Martin-Puplett interferometer. The left and right circular inputs are converted to linear outputs at separate ports. An axial ratio less than 1 dB is possible over a 15% bandwidth, as shown in Fig. 2.

The Martin-Puplett polarization diplexer can be tuned to operate simultaneously in dual frequency bands. Fig. 3 shows the frequency coverage for which the axial ratio is under 1 dB. Frequency is normalized to the center of the upper band. The interferometer path difference, shown on the vertical axis, is increased in steps of half a wavelength at the upper frequency. The horizontal bars indicate the bands over which the axial ratio is less than 1 dB. It is seen that most frequency combinations are possible, but that a number of integer-ratio frequencies are not possible. Does this make this form of polarization diplexer inappropriate for use on the MMA? For dual-frequency observing, is it essential to be able to operate at frequencies with these particular integer ratios?

Frequency Band Diplexers

Dichroic Plates. Dichroic plates can be designed to operate with circular or linear polarization. For circular polarization, the axial ratio can be under 1 dB over a bandwidth of ~10% when operated at an angle of incidence of 30° [6]. For linear polarization, wider operating bands should be possible.

Martin-Puplett Interferometer. The frequency coverage of a Martin-Puplett interferometer operated as a frequency band diplexer is shown in Fig. 4. Frequency is normalized to the center of the upper band. The interferometer path difference, shown on the vertical axis, is increased in steps of half a wavelength at the upper frequency. The horizontal bars indicate the bands over which the diplexer loss is less than 0.1 dB. It is seen that complete frequency coverage is possible except for a small gap at $f = 0.33$.

Image Filter and Local Oscillator Diplexer

Each of these functions can be performed quasi-optically by a Martin-Puplett diplexer. Two arrangements are possible: the LO diplexer can be inserted between the image cold load and the image filter, as shown in Fig. 1, or it can be between the image filter and the mixer. The former is preferable as the loss of the LO diplexer is removed from the main telescope signal path. With the configuration of Fig. 1, the loss between the LO and mixer is ~3 dB (or 0 dB if the image filter is tuned for DSB operation).

The image rejection bandwidth of a Martin-Puplett interferometer depends on the choice of IF [7]. For a 1-2 GHz IF, the image rejection is only 16 dB at the band edges. For a 3-4 GHz IF, the image rejection $\geq$ 19 dB across the band.

Other options: On SIS receivers at some observatories, the LO power is injected by reflection from a thin mylar sheet inclined at 45° to the signal beam. The thickness of the mylar is usually chosen to give ~20 dB LO coupling loss and ~0.04 dB signal loss. Present SIS receivers on the NRAO 12-m telescope use waveguide LO couplers with ~20 dB LO loss. For the MMA with its very wide frequency coverage, LO power will be at a premium, and it would be unwise to plan on an unnecessary LO loss of ~20 dB.

Discussion

Figs. 5-7 show three possible MMA receiver configurations corresponding to those in Figs. 1(a)-(c). In Fig. 5, the incoming circularly polarized signals are split into separate frequency bands, still circularly polarized, using a dichroic plate. These beams are converted to linear polarization by a Martin-Puplett interferometer. In Fig. 6, the incoming circularly polarized signals in both desired frequency bands are converted to linear polarization using a Martin-Puplett interferometer. Each resulting linearly polarized beam is separated into the desired frequency bands by a second Martin-Puplett interferometer. In Fig. 7, the linearly polarized input signals are separated by a wire grid (or pair of crossed grids [4]), and each resulting linearly polarized beam is separated into its desired frequency bands by a Martin-Puplett interferometer.

The choice of receiver configuration for the MMA will depend on detailed studies of these and other possible configurations. The implications for multi-frequency operation of the small gaps in the frequency coverage of the Martin-Puplett interferometer when used as a broadband circular polarizer or as a frequency band diplexer, must be assessed.

The possibility of using linearly polarized receivers and synthesizing circular polarization at the back end needs to be considered. This would permit the simplest receiver configuration, that of Fig. 7, to be used.

This discussion has assumed ideal quasi-optical components with negligible ohmic, scattering, and diffraction loss . However, with so many grids and mirrors in series, loss may turn out to be significant. Ohmic loss, and its noise contribution, could be reduced by cryogenically cooling the quasi-optical components, an option to be avoided if possible.

References

[1] D.H. Martin and E. Puplett, "Polarized interferometric spectrometry for the millimeter and submillimeter spectrum," Infrared Physics, vol. 10, pp.105-109, 1969.

[2] N. R. Erickson, "A Very Low-Noise Single-Sideband Receiver for 200-260 GHz," IEEE Trans. Microwave Theory Tech., vol. MTT-33, no. 11, pp. 1179-1188, Nov. 1985.

[3] J. M. Payne, "Millimeter and submillimeter wavelength radio astronomy,"

Proceedings of the IEEE, vol. 77, no. 7, pp. 993-1017, July 1989.

[4] J. M. Payne, private communication.

[5] A. R. Kerr, "Programs for analysis of wire grid beam-splitters and the folded Mach-Zehnder diplexer", Electronics Division Technical Note No. 148, National Radio Astronomy Observatory, Charlottesville, VA 22903, October 20, 1988.

[6] S. Srikanth, private communication.

[7] A. R. Kerr, "Image frequency suppression on the MMA," Millimeter Array Memorandum #70, National Radio Astronomy Observatory, Charlottesville, VA, Dec. 1991.

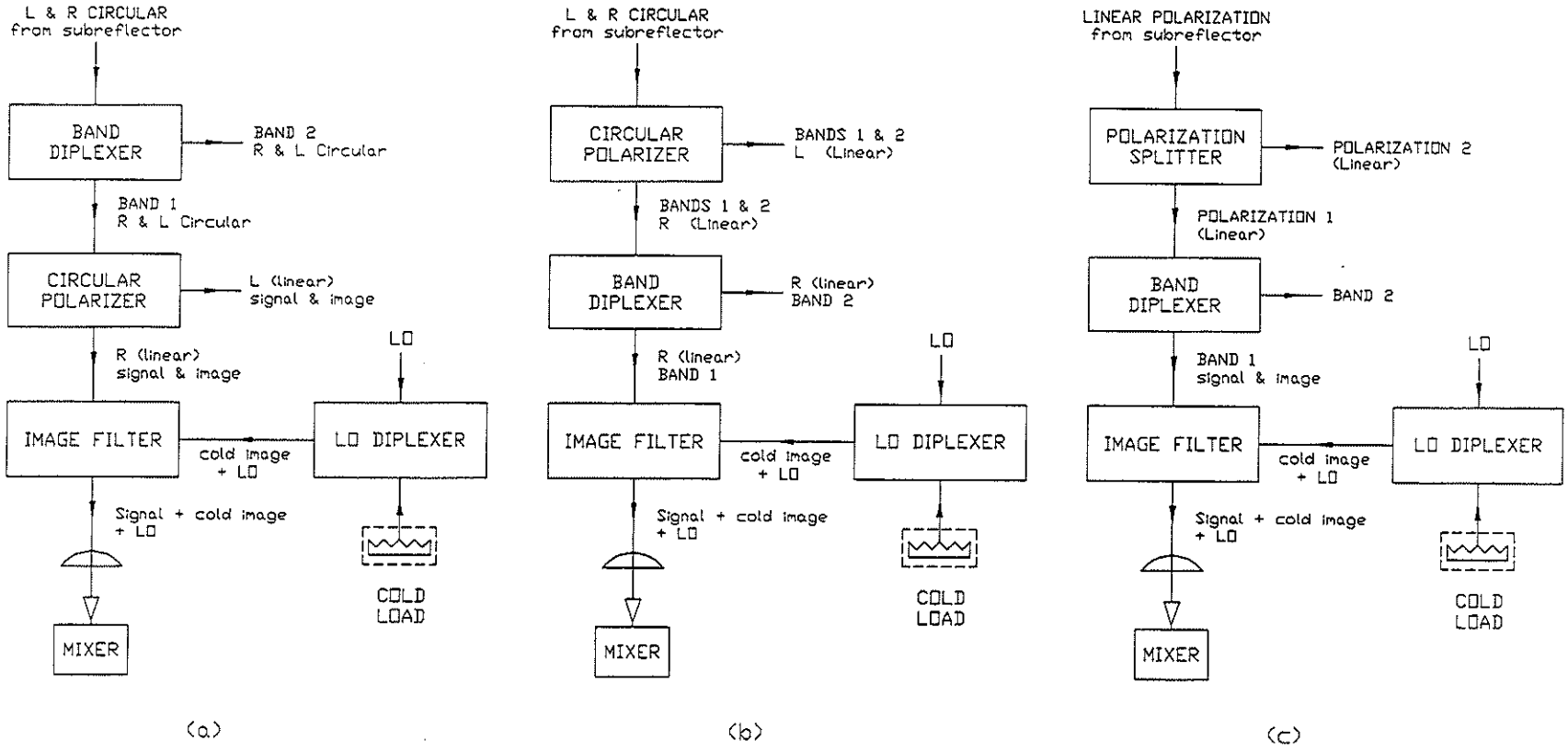

Fig. 1. Three possible arrangements of quasi-optical components.

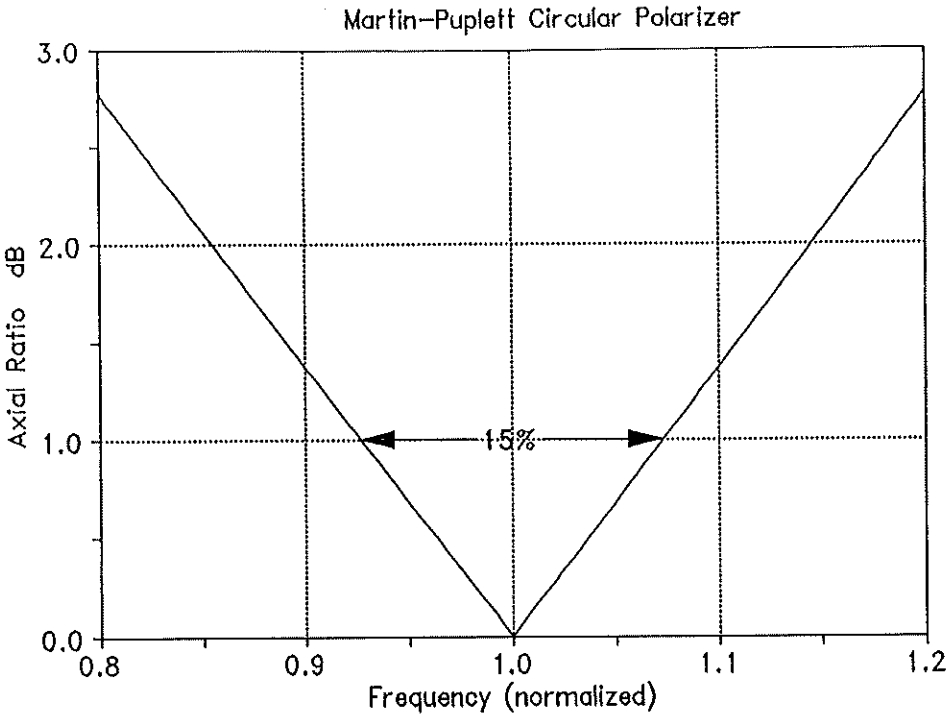

Fig. 2. Axial ratio of a Martin-Puplett interferometer used as a circular polarizer. L & R circular input signals are converted to linear outputs.

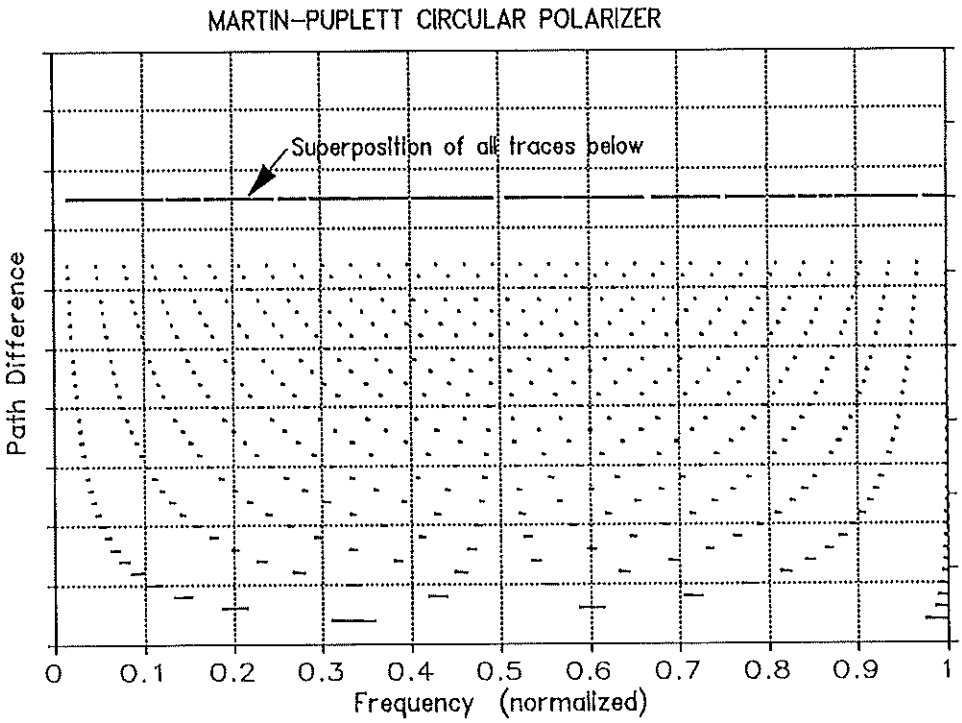

Fig. 3. Frequency coverage of a Martin-Puplett circular polarizer, as a function of interferometer path difference. Axial ratio ≤ 1 dB.

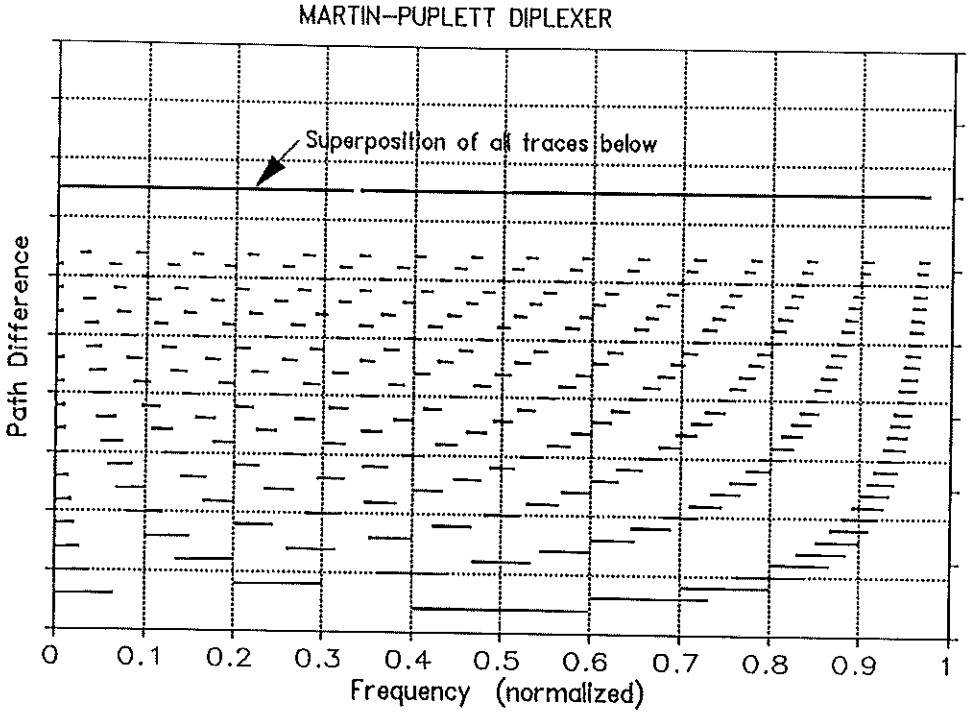

Fig. 4. Frequency coverage of a Martin-Puplett frequency band diplexer, as a function of interferometer path difference. Transmission loss $\leq$ 0.1 dB.

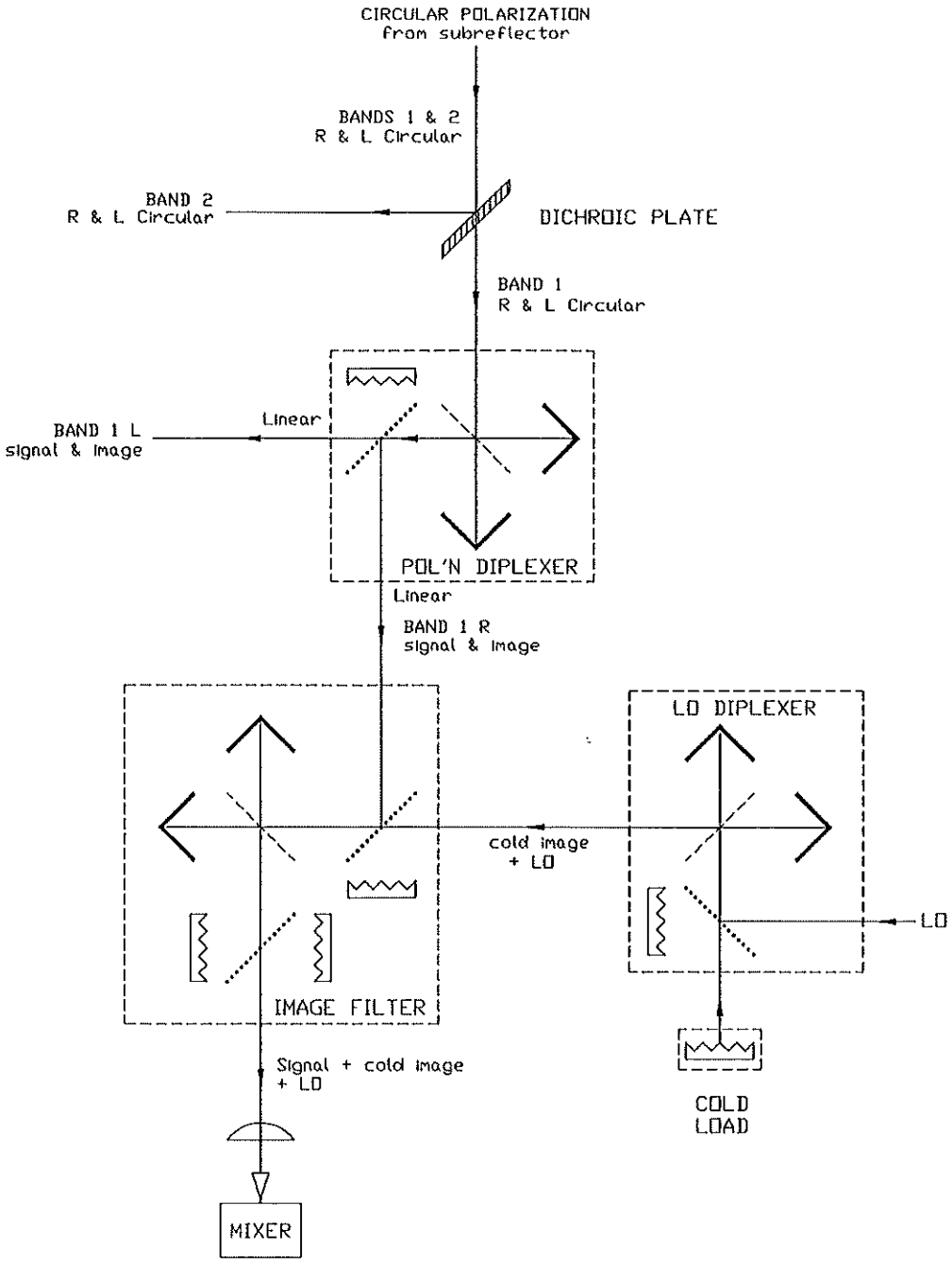

Fig. 5. A possible MMA receiver configuration corresponding to that in Fig. 1(a). The incoming circularly polarized signals are split into separate frequency bands, still circularly polarized, using a dichroic plate.

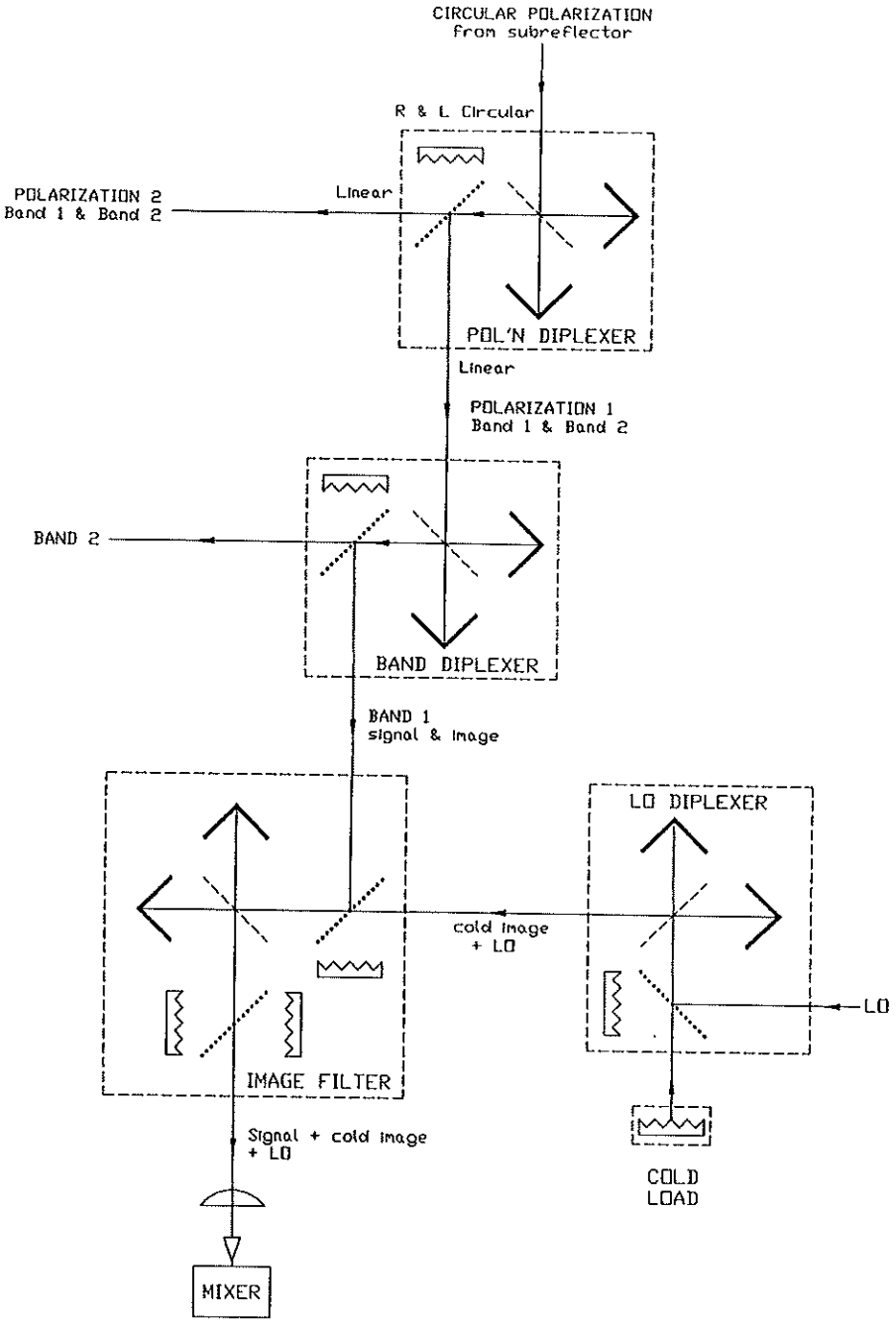

Fig. 6. A possible MMA receiver configuration corresponding to that in Fig. 1(b). The incoming circularly polarized signals in both desired frequency bands are converted to linear polarization using a Martin-Puplett interferometer.

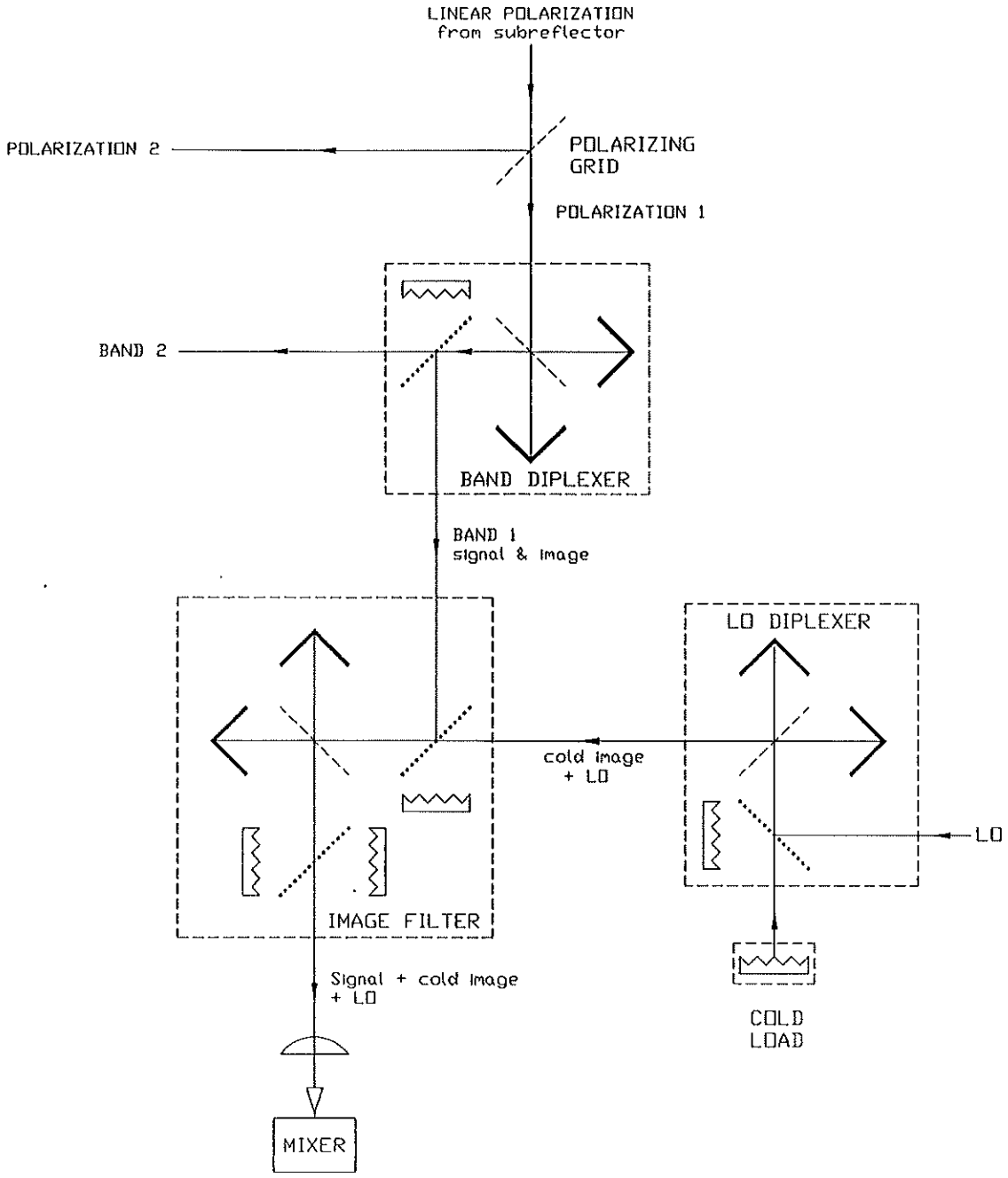

Fig. 7. A possible MMA receiver configuration corresponding to that in Fig. 1(c). The linearly polarized input signals are separated by a wire grid (or pair of crossed grids [4]).

MILLIMETER ARRAY
MEMO NO. 79

A Summary of the Data Obtained During the mmA Site Survey

D. E. Hogg

February 26, 1992

Abstract: A radiometer was developed in 1986 to test potential sites for the proposed Millimeter Array. The atmospheric transparency and the stability at three sites have now been evaluated using several of these devices. This report presents a summary of the data obtained.

Introduction: After the millimeter array concept had been explored and discussed with the scientific community, a project group was formed to develop the concept into a proposal which could be forwarded to the National Science Foundation. One of the critical questions concerned the possible site for the array. It was soon realized that it would be necessary to make accurate measurements of the atmospheric conditions at prospective sites in order to properly evaluate their potential for the mmA.

About ten years ago John Payne developed a radiometer operating at 225 GHz with the intention of using it to monitor the sky transparency at Kitt Peak, as a guide to observers at the 12 meter telescope. This design was modified and further developed in Charlottesville by S. Weinreb and Z-Y Liu, and four of the devices were built. After two years of observations (1986-1988), the devices were modified and upgraded by G. Petencin, and returned to service in the fall of 1989. Data are available for the Magdalena Mountains (also called South Baldy) and the VLA Site from the earlier period, for the Magdalena site and Mauna Kea for 1989-1991, and for Springerville for 1990-1991.

This report will present the data in sufficient detail that interested readers will be able to develop a good feel for the uncertainties involved in the measurements. A few graphs will be used to summarize the data, but the comparative analysis will be given elsewhere. Some studies based on the earlier data have been given by McKinnon (1987), Hogg, Owen, and McKinnon (1988), Owen and Hogg (1990), Schwab, Hogg, and Owen (1990), and Owen (1991).

The Instrument: The detailed technical description of the basic radiometer system is given by Liu (1987), and a more general discussion of the instrument, operation, and tipping-scan data analysis is found in McKinnon (1987). Briefly, the receiver uses a room temperature Schottky mixer operating at 225 GHz as the primary element. The LO is derived from a 75 GHz Gunn using a tripler. The rf and if components are maintained in a small temperature-controlled box. The signal is received by a small primary mirror located outside the box, and is directed into the mixer through a chopper wheel by means of a secondary mirror. The primary mirror can be rotated through 360 degrees in elevation, enabling the sampling of the atmosphere over a wide range of zenith angle. The chopper wheel alternates the receiver input between the sky, a load at 45 C, and a load at 65 C. The two stable temperature loads permit internal calibration of the system gain.

As originally designed the units operated from line power, and required periodic visits to retrieve the data stored on a local disk. During the course of the site tests extensive developments were made by G. Petencin, to the point that the Springerville unit operated remotely on solar power and the data were retrieved by interrogation using a cellular phone.

During the first two years the units were used only to estimate the zenith opacity at 225 GHz using a tipping technique which measured the sky temperature at a series of zenith angles. During the later trials the units also measured the atmospheric stability by recording the sky temperature fluctuations at the zenith over the course of a hour, such samples being taken every fifth hour.

Anemometers were installed at the Magdalena Mountain and Springerville sites during the course of the later trials, thus giving a limited sampling of the wind statistics for these places.

Operations and Data Archival: The operations and data processing for the entire site survey was under the supervision of F. Owen. During the first period, from November 1986 to June 1988 the operations and initial data retrieval and analysis were conducted by M. McKinnon (McKinnon 1987). For the second period the systems were extensively upgraded by G. Petencin, who also looked after their operations. The introduction of the sky fluctuation measurements, and the data retrieval, was done by a number of students working for F. Owen. The archiving of the data was done primarily by Theresa Calavini.

It is important to note that the observations at the Magdalena Mountains and at Springerville were made near the center of the proposed array site and should therefore be representative of the conditions that the array might operate under. In contrast, the observations at Mauna Kea were conducted in cooperation with the Smithsonian Astrophysical Observatory and the California Institute of Technology at the CSO site in the "millimeter valley." At 4080 m, this site is 355 m higher than the potential array site, which lies near the VLBA site. If the scale height of water vapor is 2000 m at high altitudes on Mauna Kea, the opacity (for small values) at the potential array site would be about 20 percent greater than the value measured at the summit. The effect on the radio path length inferred may be greater than this by another factor which is difficult to estimate but which also depends on opacity. The total water vapor may be systematically underestimated, since the opacity caused by a given amount of water vapor will be less at the higher altitude because of the smaller pressure broadening.

The Zenith Opacity Data: The measurement of the zenith opacity consisted of a series of 11 observations taken over zenith angles between 7 and 70 degrees corresponding to airmasses between one and three. Here the opacity tau is defined so that the fractional atmospheric attenuation is given by exp(-A*tau), where A is the airmass normalized to unity at the zenith. The details of the algorithms used for the extraction of tau from the tipping scans are given by McKinnon (1987).

During the first period a tipping measurement was made every ten minutes, twenty-four hours per day. The tipping runs for each hour were reduced to give the opacity, and the median value of the six runs was defined to be the opacity value characteristic of that hour. In the second period the tipping runs were interrupted every fifth hour in order to make a stability run, as will be described in the next section.

In general the data required little editing. There were of course times when the tipper was broken. Occasionally, perhaps following a storm, the tipper gave unreasonably small values for the zenith opacity, indicating that there was little change in sky temperature, presumably because there was a layer of snow or moisture on the primary mirror. Such times were assigned either to the category "broken" or to the category "high opacity" if the occurrence was short-lived and was surrounded by valid measurements showing high opacity.

All of the hourly medians for the three sites sampled in the second period are given in Figure 1. A striking feature of the continental sites is the almost periodic fluctuation of the opacity on a time scale of a few days. On each site there are long periods during which the zenith opacity at 225 GHz is low (i.e., below 0.1). It is evident that the number of such periods is greater for the Magdalena Mountains than it is at the Springerville site. The data for Mauna Kea show less regular structure, and the site has more periods of low opacity than either of the continental sites.

In order to make quantitative evaluations of the sites, the data have been analyzed to show the frequency of occurrence of a given value of the zenith opacity. Figure 2 gives a summary of all such data for the three sites from the second period, with the data grouped by three months, for brevity. Also shown for completeness are the data from the Magdalena Mountains for the first period.

An abstract of the data from the last period is given in Figure 3. Displayed for each of the three sites are contours giving the fraction of the time the opacity lies below certain selected values, as a function of time. All sites have significant amounts of time during which the zenith opacity at 225 GHz lies below 0.1, though Mauna Kea has the most such time and Springerville the least.

Figure 4 compares the opacities that obtain for 25 percent of the time and for 50 percent of the time at the three sites.

The Zenith Fluctuation Data: Every fifth hour the 225 GHz radiometers were directed towards the zenith, and the total power was sampled every 3.51 seconds. The fluctuations thus observed are characterized by the Allan standard deviation (ASD), calculated for lags between 3.5 sec and 898 sec, in steps of a factor of two.

Included in the Allan standard deviation are components of the variation due to sky fluctuation and due to radiometer instability. To separate these effects, every fifth fluctuation run was taken with the primary

mirror directed toward the ground, rather than toward the zenith. These reference measurements were plotted as a function of time, and a value for the instrumental fluctuation at each lag was estimated from the lower envelope of the plotted values. This procedure probably results in a slight overestimate of the instrumental contribution, since the total system temperature is higher when pointed at the ground, and indeed the resultant Allan variance is occasionally negative, especially for small values of lag where the instrumental term is a much greater fraction of the observed fluctuations. However, for the larger lag values the procedure appears to be satisfactory.

Intuitively, it is clear that the lower the fluctuations the better the site will be for interferometry. However, to make the distinction quantitative is a difficult task, because it involves knowledge of the wind and a model of the atmosphere. These considerations are reviewed and a preliminary analysis of selected fluctuation data is given in the recent report by M. Holdaway (1991).

The fluctuation data are summarized in Figure 5, which shows for each site the fraction of the time that the ASD lies below a given value. For brevity, the data are grouped into intervals of three months. The quality of the data in general was high and needed little editing. However, the data for the last ten weeks at Mauna Kea are inconsistent with earlier observations, and perhaps should be discarded even though the radiometer was apparently working. Note that the negative values are included in the frequency-of-occurrence statistics, since these are probably times when the ASD is the smallest, even though the precise value was not accurately measured.

As Holdaway (1991) notes, a crucial parameter of the fluctuation study is the dependency of the magnitude of the ASD on the value of the lag. To illustrate the data, we have grouped the ASD values for the Magdalena Mountains by the value of the ASD at a lag of 56 seconds. Figure 6 shows the value of the ASD as a function of lag for three groups of data. Also shown is plus and minus one standard deviation in the mean. The groups have $0.04 < ASD56 < 0.08$; $0.16 < ASD56 < 0.20$; and $0.28 < ASD56 < 0.32$. The points at lags of 3.5 sec and, to a lesser extent at 7.0 sec are seriously influenced by the instrumental term. The points at a lag of 898 sec are poorly determined, since the lag is one-fourth of the total duration of the observation. With these caveats, the spectrum of the ASD appears to be similar over the range of ASD(56 sec) chosen for the analysis. The spectrum is somewhat steeper than the value 0.33 expected for very long lags, but is consistent with a random power spectrum in the phase fluctuation (Holdaway 1991).

It is also of interest to examine the spectra of the three sites, to see if the vastly differing terrain has had an influence on the atmospheric structure. Figure 7 compares the spectra for two different selections of the ASD at 56 seconds. The spectra for the three sites appear to be similar at the times of the large fluctuations, but the spectrum of the fluctuations at Springerville is steeper at the longer lags during periods of low fluctuation.

In order to compare the nature of the fluctuations at the three sites, we show in Figure 8 the fraction of the time that the fluctuations at the sites are less than two selected values, as a function of time. Very crudely, the ASD(56 sec) of 0.04 corresponds to a phase fluctuation on the longer baselines of the mmA of 8 degrees, and the ASD(56) of 0.20 to 40 degrees. In general, Mauna Kea has the greatest fraction of the time with low fluctuations, and Springerville has the lowest incidence of low fluctuations.

Finally, it is of interest to explore the atmospheric transparency during times of good phase stability. Figure 9 shows the distribution of the zenith opacities for all times at the three sites for which the Allan standard deviation at 56 seconds was less than 0.1 K. As might be expected, such periods are characterized by superior transparency. It should be noted that the observations at Mauna Kea and the Magdalena Mtns spanned nearly two years, while only one year's worth of data were obtained at Springerville.

The Wind Data: Wind data were recorded for possible use in the interpretation of the fluctuation data. However, since they may also be of value in the design of the telescope as well as in the planning of operations, we present a summary of the data for the Magdalena Mountains and for Springerville. No data were obtained for Mauna Kea.

Figure 10 gives the frequency of occurrence of wind values for each site. The data have been grouped into intervals of three months. The winds at the Magdalena site are often higher than at the Springerville site, and occasionally exceeded 70 mph. The winds at Springerville are relatively light.

Acknowledgement: The program of site evaluation was developed and led by Frazer Owen. He performed the initial calibration of the devices as they were received from the Central Development Lab, and supervised the surveys conducted at the VLA and Magdalena Mountains between 1986 and 1988. He then evaluated the performance of the devices, and, with G Petencin, undertook a program of rebuilding and upgrade which materially improved the reliability and stability of the systems. Finally, he supervised the survey from 1989 to 1991, the results of which are compiled in this report.

References

Hogg, D. E., Owen, F. N., and McKinnon, M. 1988, MMA Memo No. 45
Holdaway, M. A. 1991, MMA Memo No. 68
Liu, Z-Y. 1987, MMA Memo No. 41 (EDIR No. 271).
McKinnon, M. 1987, MMA Memo No. 40
Owen, F. N. 1991, in Radio Interferometry: Theory, Techniques, and Applications, ed. T. J. Cornwell and R. A. Perley, IAU Colloq. No. 151, p 124.
Owen, F. N. and Hogg, D. E. 1990,in URSI/IAU Symp. on Radio Astronomical Seeing, ed.
Wang Shoguan and Yang Ti-Pei, Chinese Acad. Sci.,Beijing, p 42.
Schwab,F. R., Hogg, D. E., and Owen, F. N. 1990, ibid, p 116.

Figure Captions

Figure 1. Observations of the zenith opacity at 225 GHz as a function of time. Plotted are all valid measurements of the hourly median which were obtained during the survey 1989-1991.
(a) Magdalena Mountains (South Baldy). (b) Mauna Kea.
(c) Springerville.

Figure 2. Frequency of occurrence of opacity values, averaged over intervals of three months. Values obtained at the Magdalena Mountain site between 1986 and 1988 are also shown.
(a) Magdalena Mountains. (b) Mauna Kea. (c) Springerville.

Figure 3. Frequency of occurrence of selected values of zenith opacity as a function of the time of year.
(a) Magdalena Mountains. (b) Mauna Kea. (c) Springerville.

Figure 4. A comparison of opacity values at the three sites as a function of the time of year.
(a) Opacities are lower than indicated value 25 percent of the time. (b) Opacities are lower than indicated value half the time.

Figure 5. The fraction of the time the Allan standard deviation (ASD) is less than a given value. The data have been grouped in intervals of three months.
(a) Magdalena Mountains. (b) Mauna Kea. (c) Springerville.

Figure 6. A comparison of the variation of the Allan standard deviation (ASD) with lag. The data have been selected for three ranges of the ASD at a lag of 56 seconds. Only data from the Magdalena Mountains taken when the zenith opacity was less than 0.2 are included in this figure.

Figure 7. The spectrum of the Allan standard deviation at the three survey sites, for two ranges of the ASD at 56 seconds.

Figure 8. A comparison of the atmospheric fluctuations at three sites. The lines show the fraction of the time the Allan standard deviation is less than a given value.
Upper: ASD at 56 seconds less than or equal to 0.20 K.
Lower: ASD at 56 seconds less than or equal to 0.07 K.

Figure 9. The distribution of values of the zenith opacity during times of low fluctuations for the three sites.

Figure 10. The wind at the two continental sites. Shown is the fraction of the time the wind speed is less than a given value, for data grouped in intervals of three months.
(a) Magdalena Mountains. (b) Springerville.

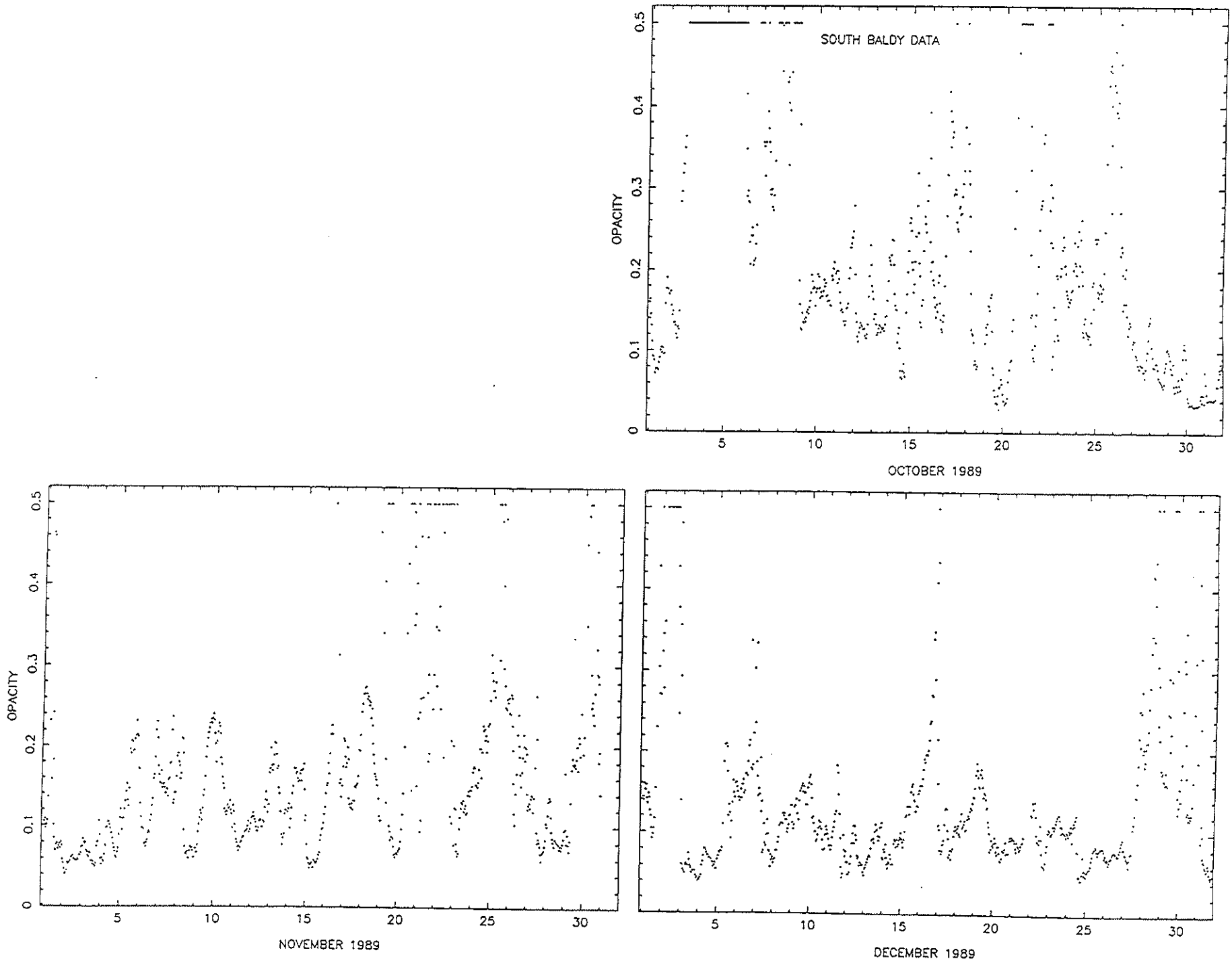
SOUTH BALDY DATA
OPACITY
0
0.1
0.2
0.3
0.4
0.5
5
10
15
20
25
30
OCTOBER 1989
NOVEMBER 1989
DECEMBER 1989

Figure 1a

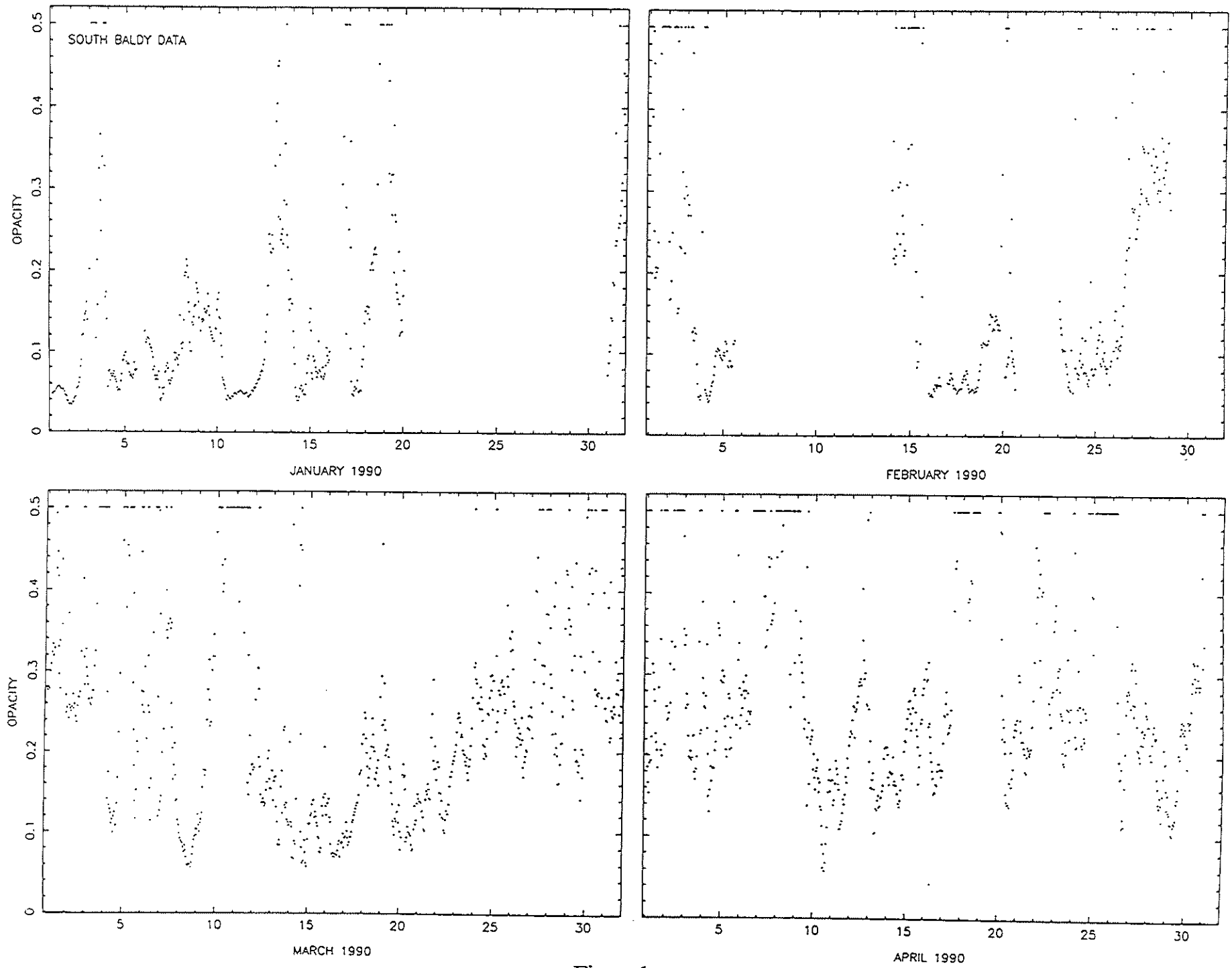
SOUTH BALDY DATA
OPACITY
0
0.1
0.2
0.3
0.4
0.5
5
10
15
20
25
30
JANUARY 1990
FEBRUARY 1990
MARCH 1990
APRIL 1990

Figure 1a

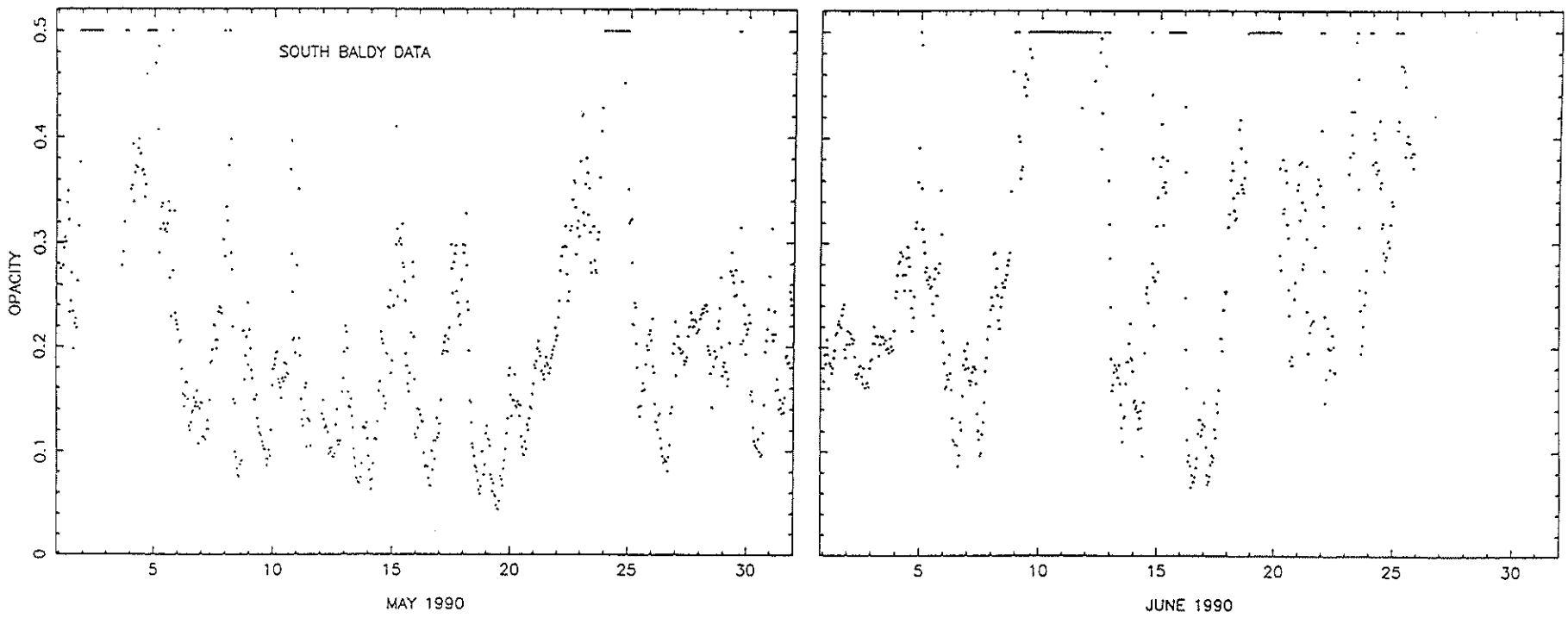
SOUTH BALDY DATA
OPACITY
0
0.1
0.2
0.3
0.4
0.5
5
10
15
20
25
30
MAY 1990
JUNE 1990

Figure 1a

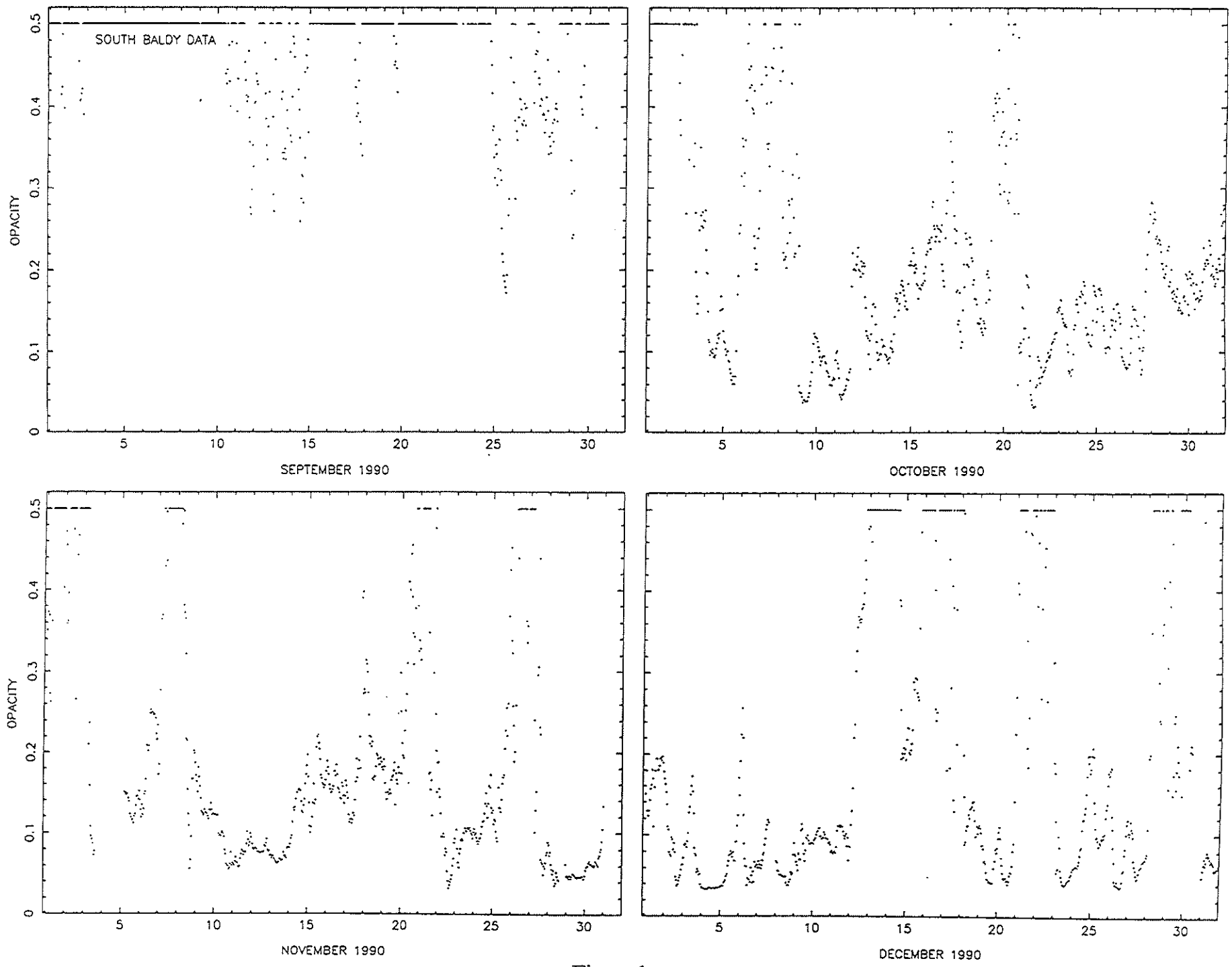
SOUTH BALDY DATA
OPACITY
0
0.1
0.2
0.3
0.4
0.5
5
10
15
20
25
30
SEPTEMBER 1990
OCTOBER 1990
NOVEMBER 1990
DECEMBER 1990

Figure 1a

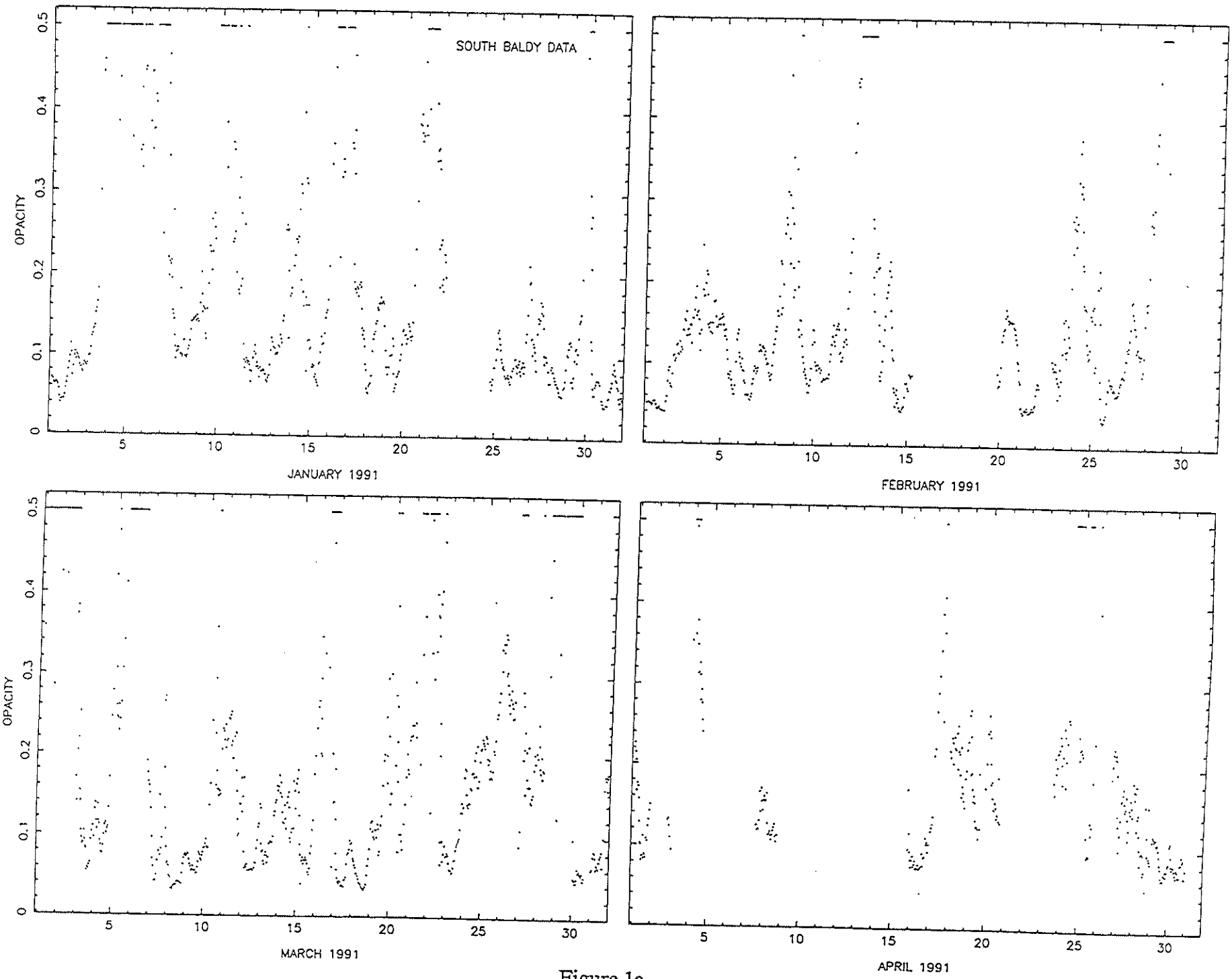
SOUTH BALDY DATA
OPACITY
0
0.1
0.2
0.3
0.4
0.5
5
10
15
20
25
30
JANUARY 1991
FEBRUARY 1991
MARCH 1991
APRIL 1991

Figure 1a

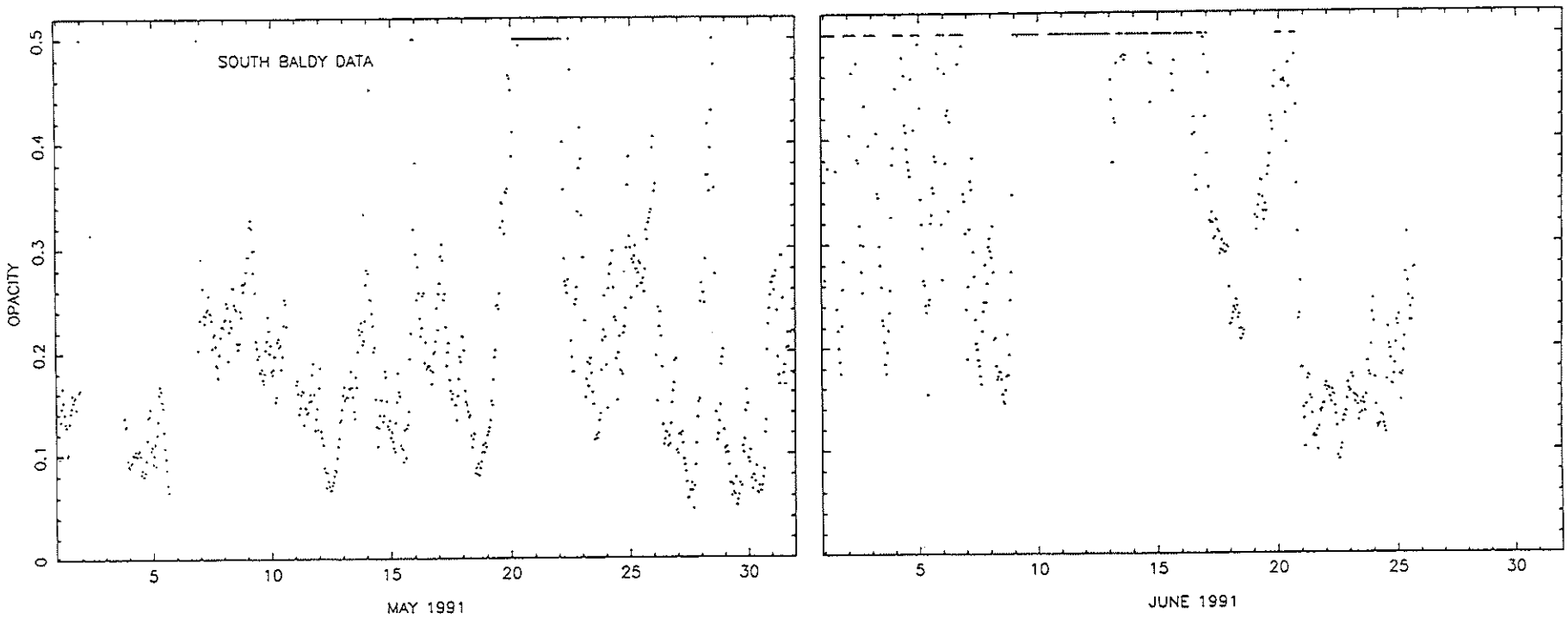
SOUTH BALDY DATA
OPACITY
0
0.1
0.2
0.3
0.4
0.5
5
10
15
20
25
30
MAY 1991
JUNE 1991

Figure 1a

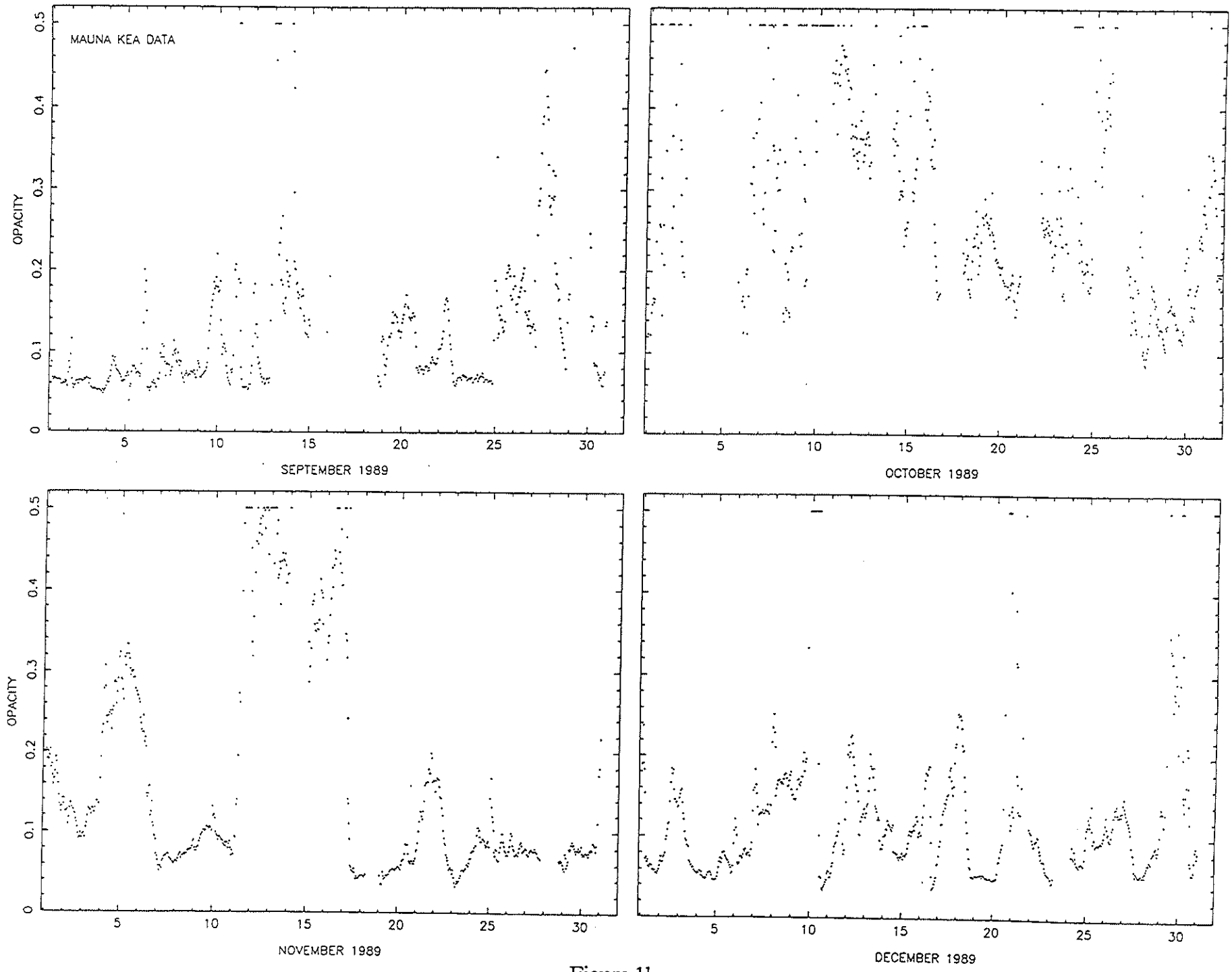
MAUNA KEA DATA
OPACITY
0
0.1
0.2
0.3
0.4
0.5
5
10
15
20
25
30
SEPTEMBER 1989
OCTOBER 1989
NOVEMBER 1989
DECEMBER 1989

Figure 1b

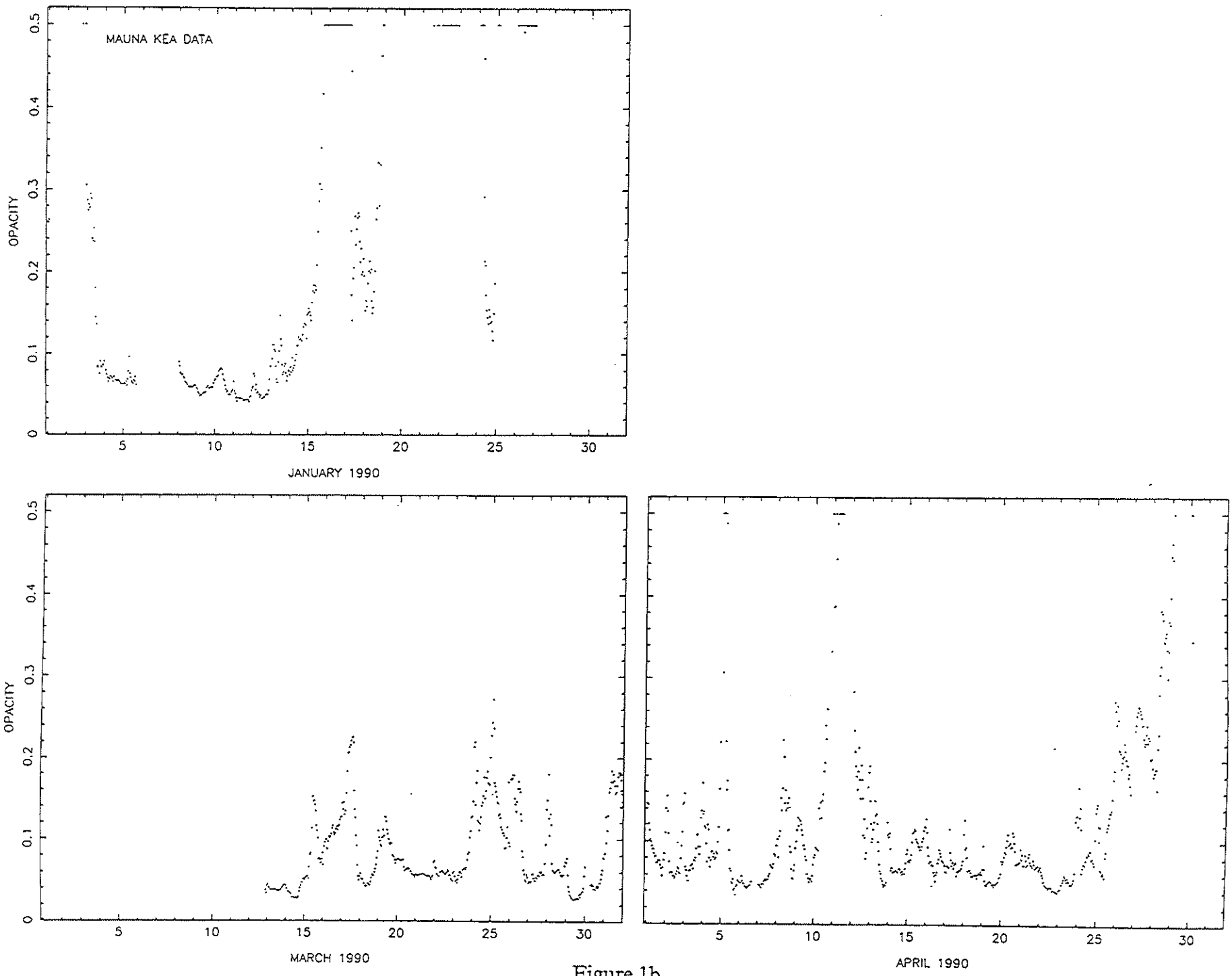
MAUNA KEA DATA
OPACITY
0
0.1
0.2
0.3
0.4
0.5
5
10
15
20
25
30
JANUARY 1990
MARCH 1990
APRIL 1990

Figure 1b

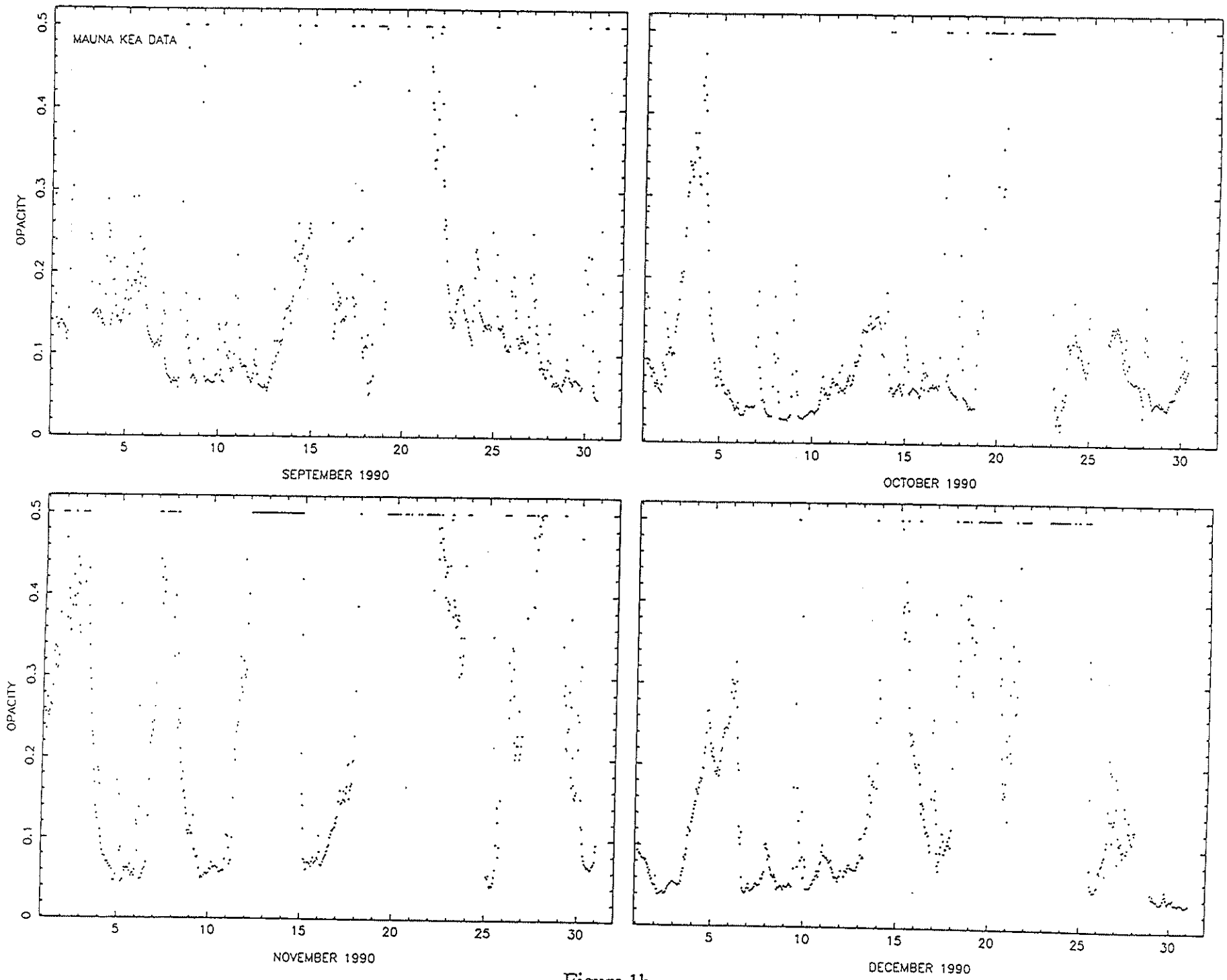
MAUNA KEA DATA
OPACITY
0
0.1
0.2
0.3
0.4
0.5
5
10
15
20
25
30
SEPTEMBER 1990
OCTOBER 1990
NOVEMBER 1990
DECEMBER 1990

Figure 1b

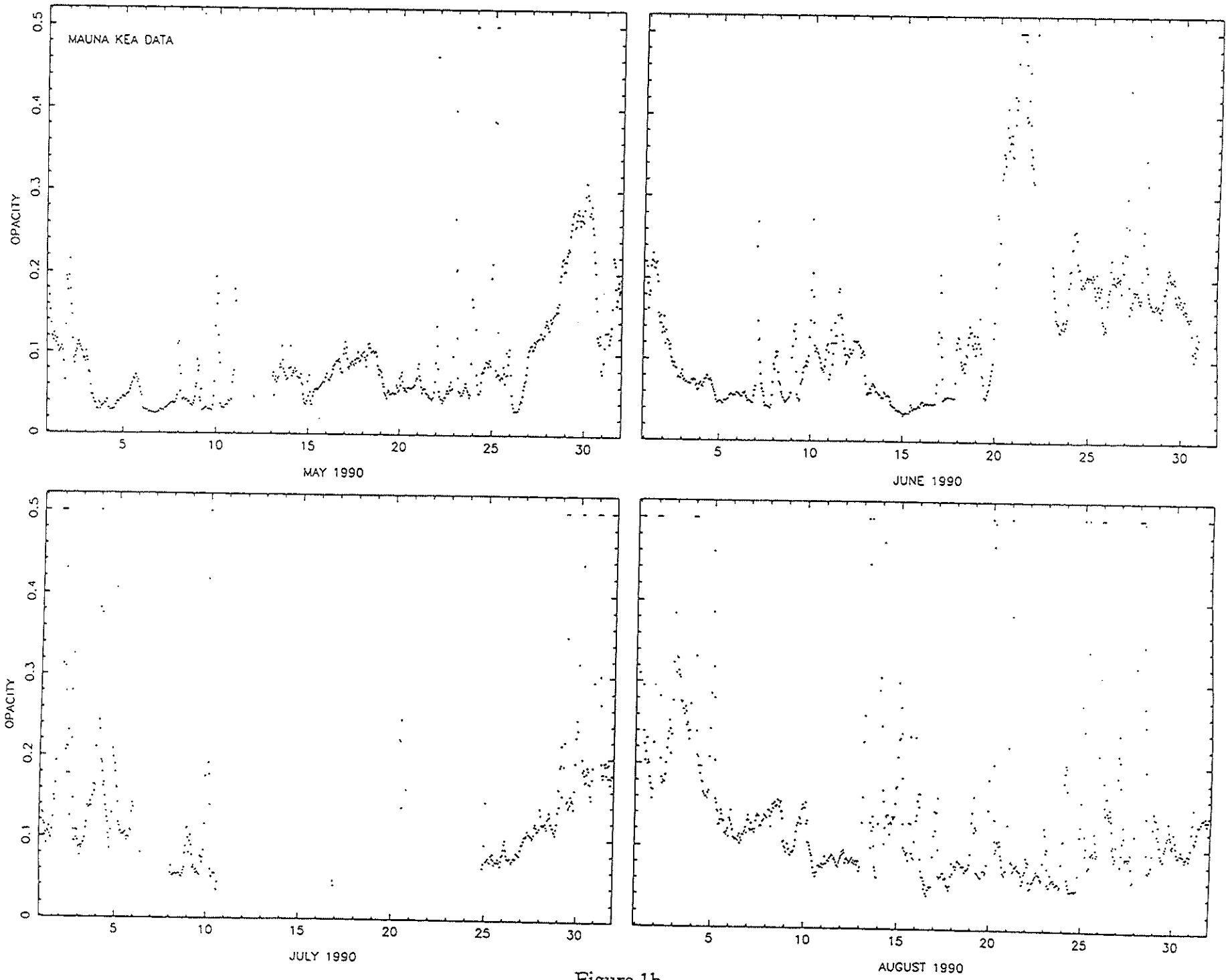
MAUNA KEA DATA
OPACITY
0
0.1
0.2
0.3
0.4
0.5
5
10
15
20
25
30
MAY 1990
JUNE 1990
JULY 1990
AUGUST 1990

Figure 1b

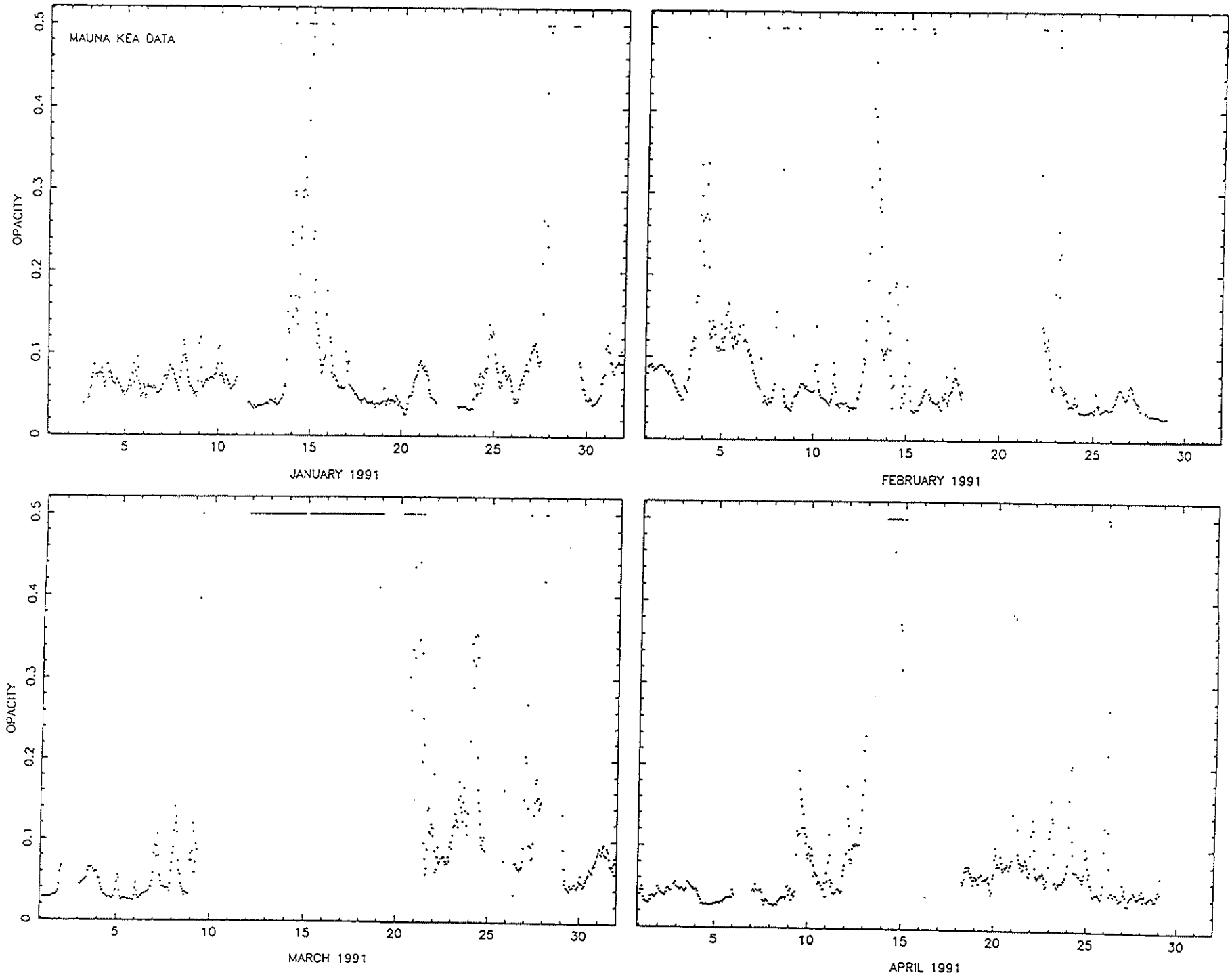
MAUNA KEA DATA
OPACITY
0
0.1
0.2
0.3
0.4
0.5
5
10
15
20
25
30
JANUARY 1991
FEBRUARY 1991
MARCH 1991
APRIL 1991

Figure 1b

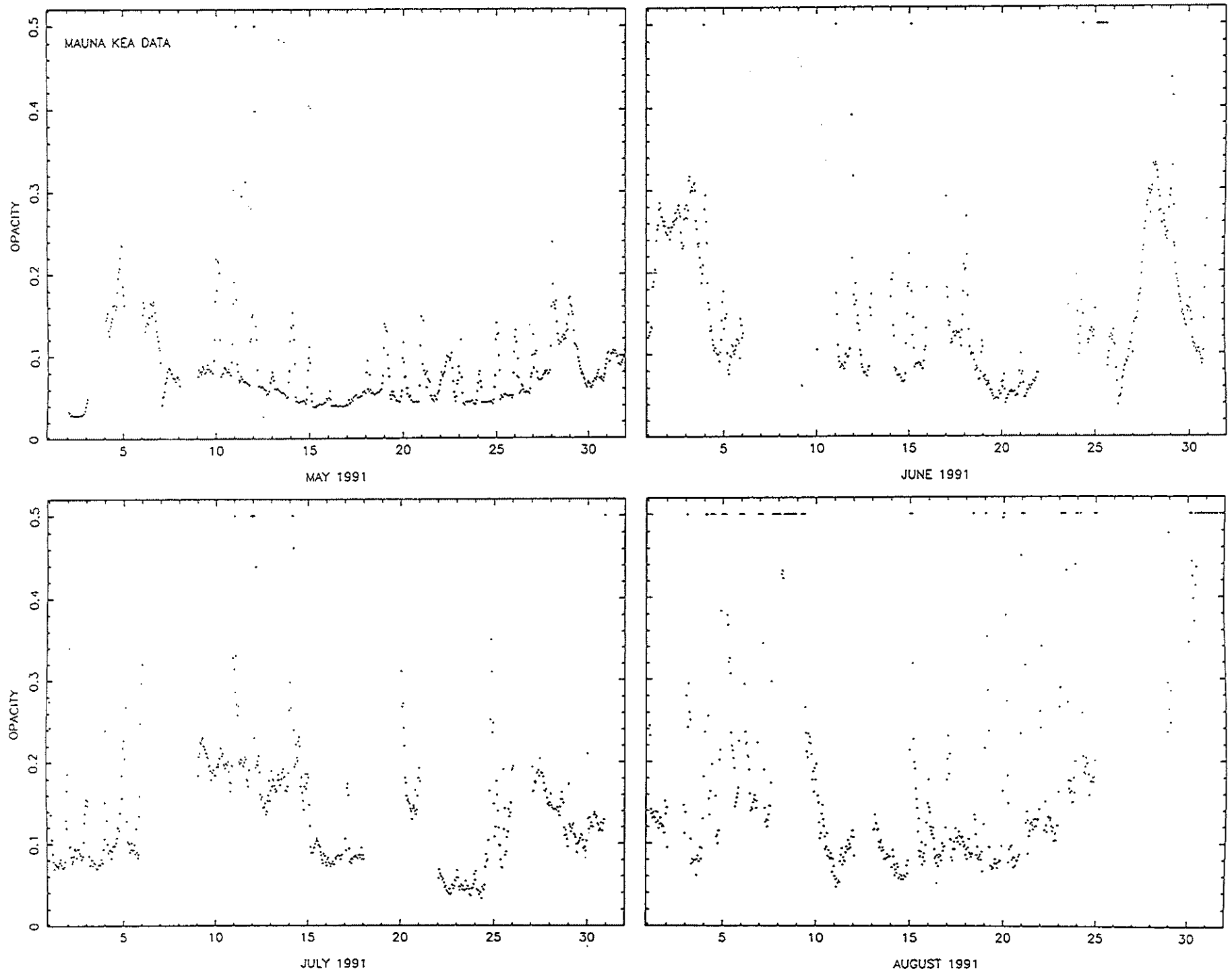
MAUNA KEA DATA
OPACITY
0
0.1
0.2
0.3
0.4
0.5
5
10
15
20
25
30
MAY 1991
JUNE 1991
JULY 1991
AUGUST 1991

Figure 1b

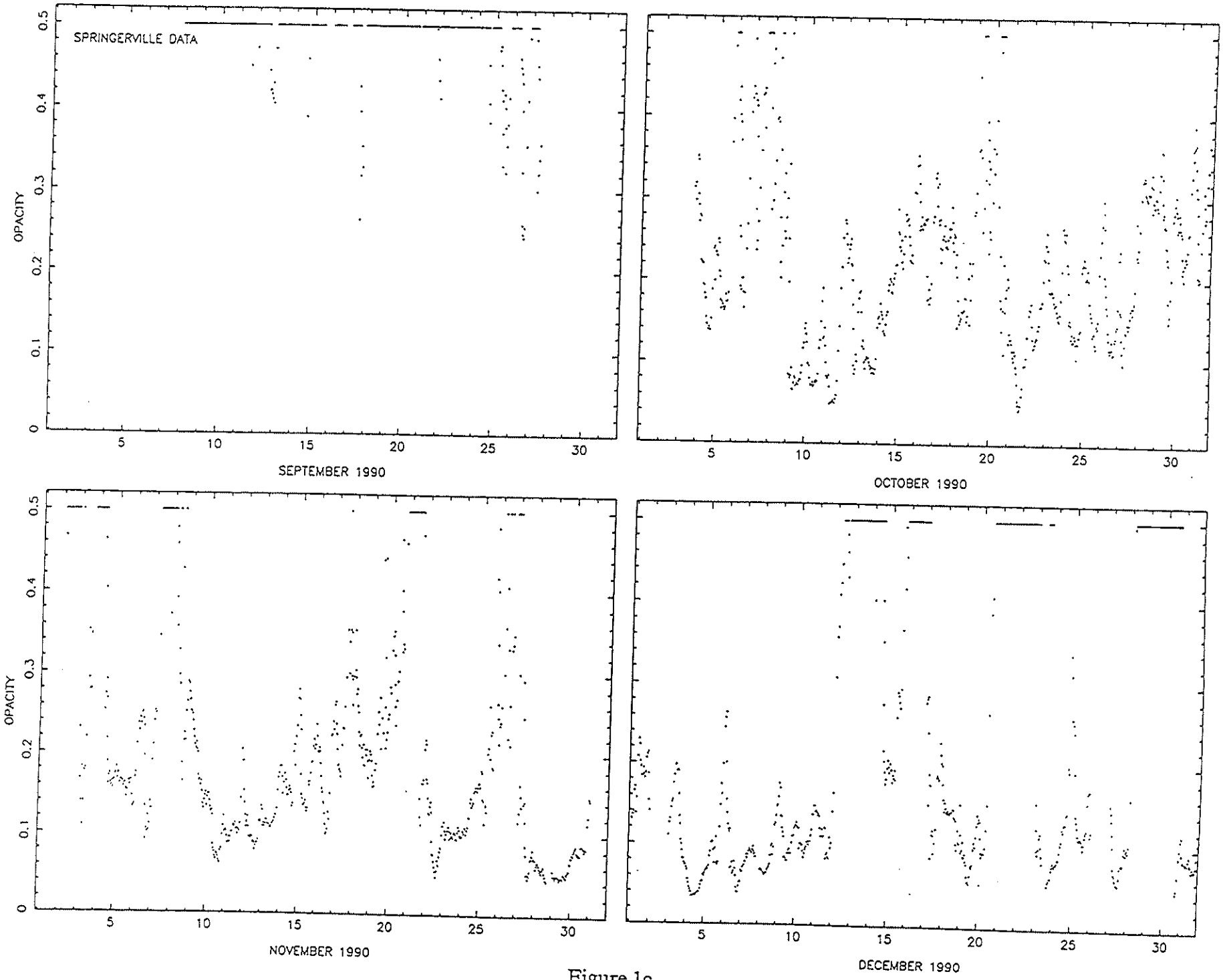
SPRINGERVILLE DATA
OPACITY
0
0.1
0.2
0.3
0.4
0.5
5
10
15
20
25
30
SEPTEMBER 1990
OCTOBER 1990
NOVEMBER 1990
DECEMBER 1990

Figure 1c

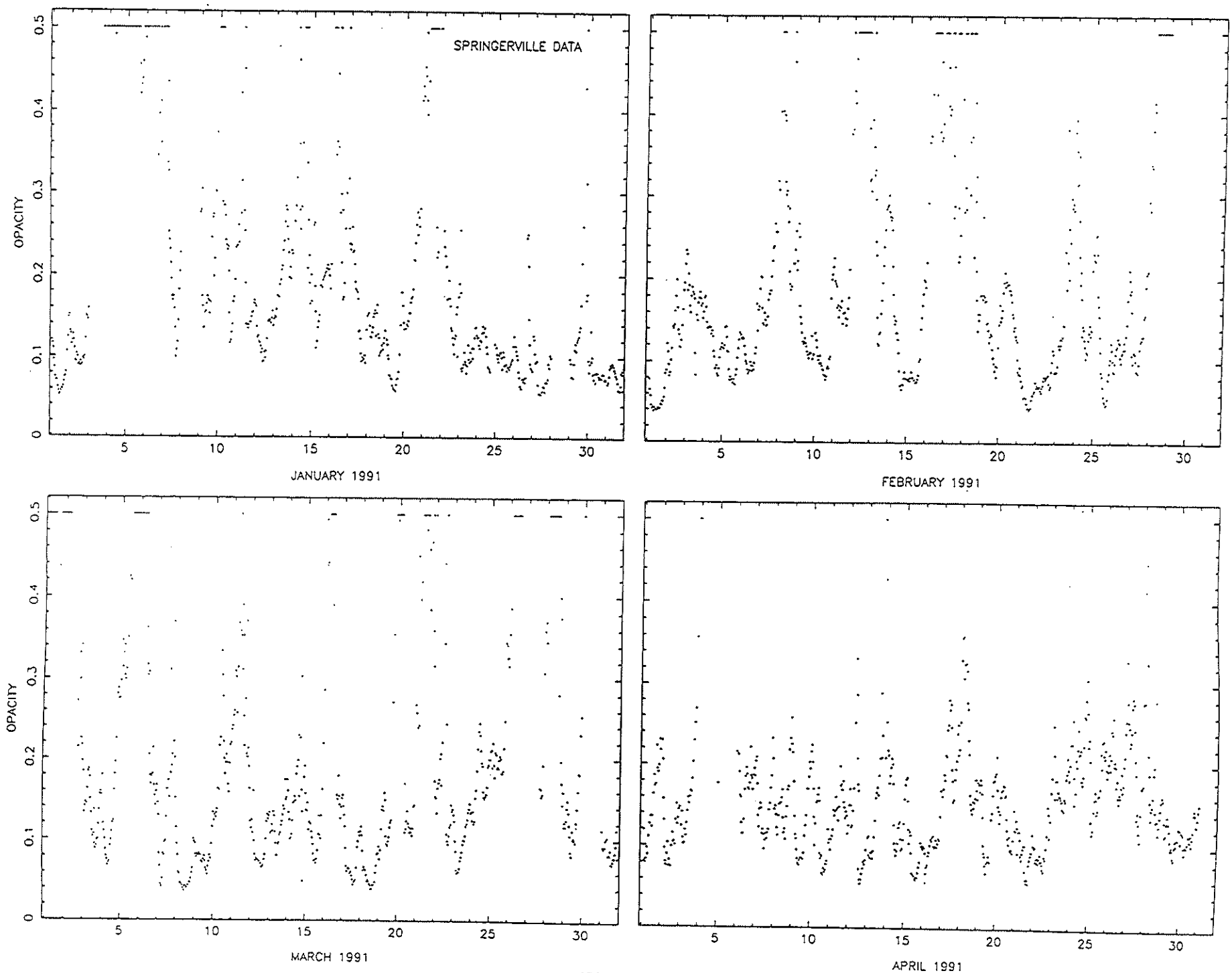
SPRINGERVILLE DATA
OPACITY
0
0.1
0.2
0.3
0.4
0.5
5
10
15
20
25
30
JANUARY 1991
FEBRUARY 1991
MARCH 1991
APRIL 1991

Figure 1c

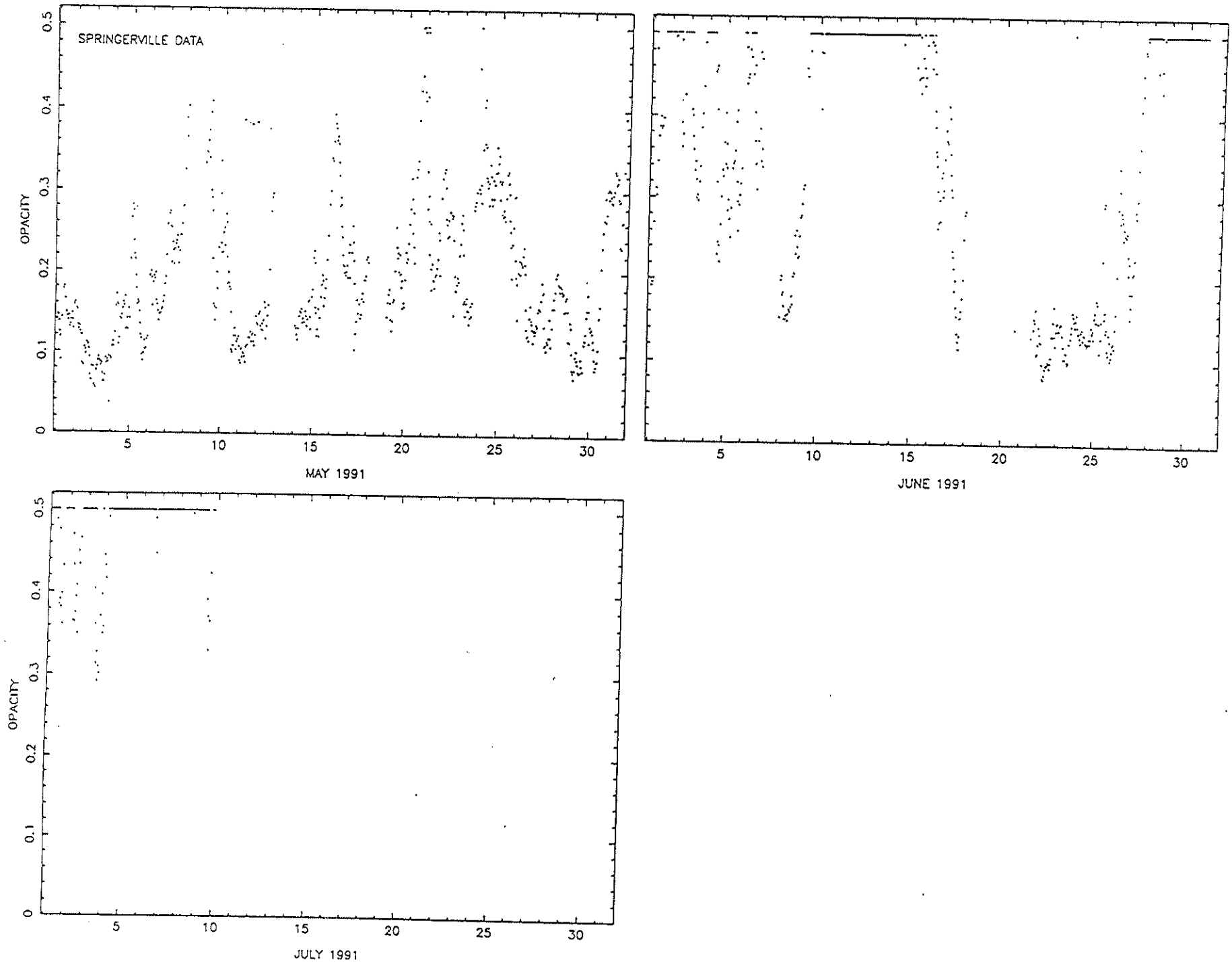
SPRINGERVILLE DATA
OPACITY
0
0.1
0.2
0.3
0.4
0.5
5
10
15
20
25
30
MAY 1991
JUNE 1991
JULY 1991

Figure 1c

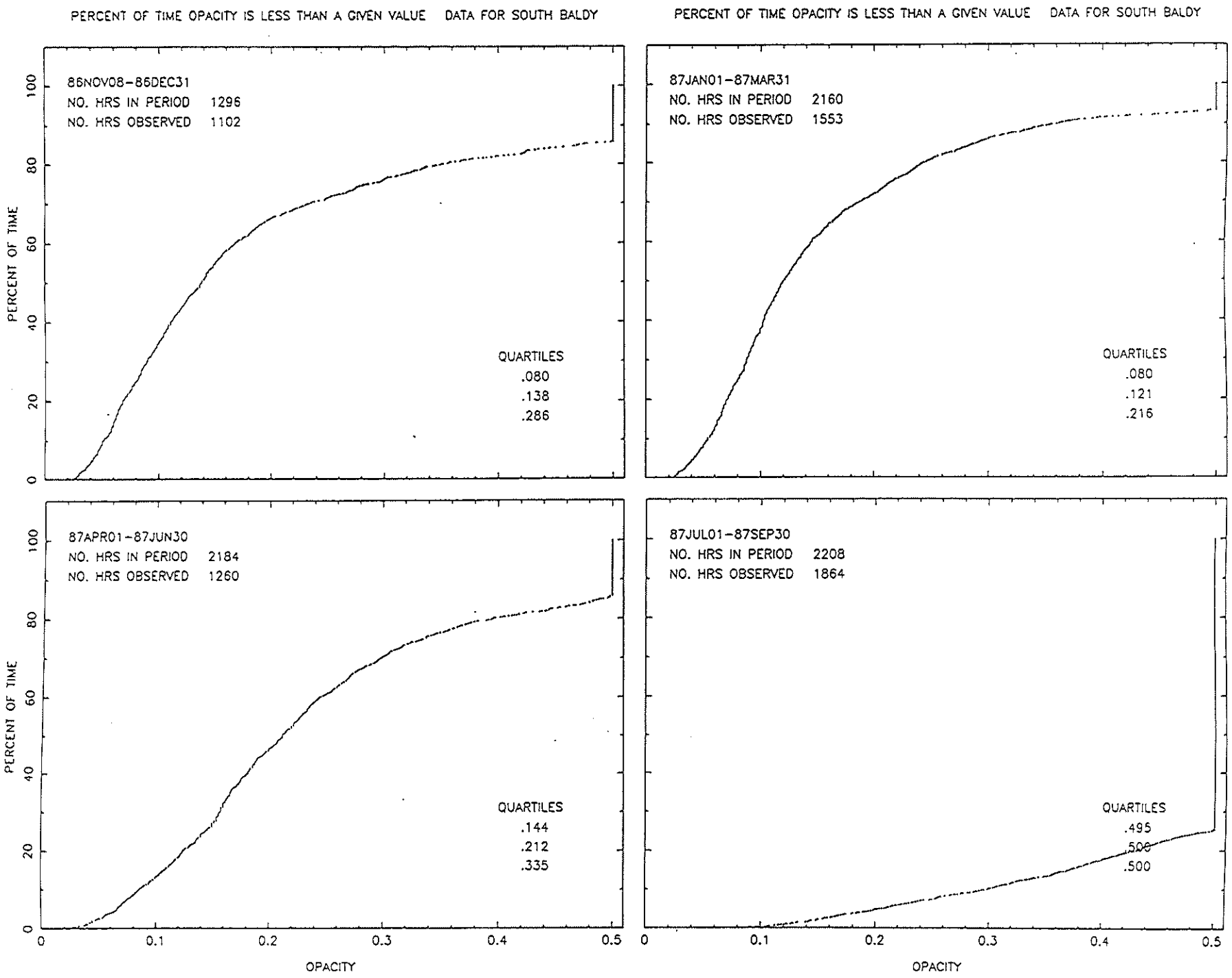
PERCENT OF TIME OPACITY IS LESS THAN A GIVEN VALUE DATA FOR SOUTH BALDY
86NOV08-86DEC31
NO. HRS IN PERIOD 1296
NO. HRS OBSERVED 1102
QUARTILES
.080
.138
.286
87JAN01-87MAR31
NO. HRS IN PERIOD 2160
NO. HRS OBSERVED 1553
QUARTILES
.080
.121
.216
87APR01-87JUN30
NO. HRS IN PERIOD 2184
NO. HRS OBSERVED 1260
QUARTILES
.144
.212
.335
87JUL01-87SEP30
NO. HRS IN PERIOD 2208
NO. HRS OBSERVED 1864
QUARTILES
.495
.500
.500
PERCENT OF TIME
0
20
40
60
80
100
0
0.1
0.2
0.3
0.4
0.5
OPACITY

Figure 2a

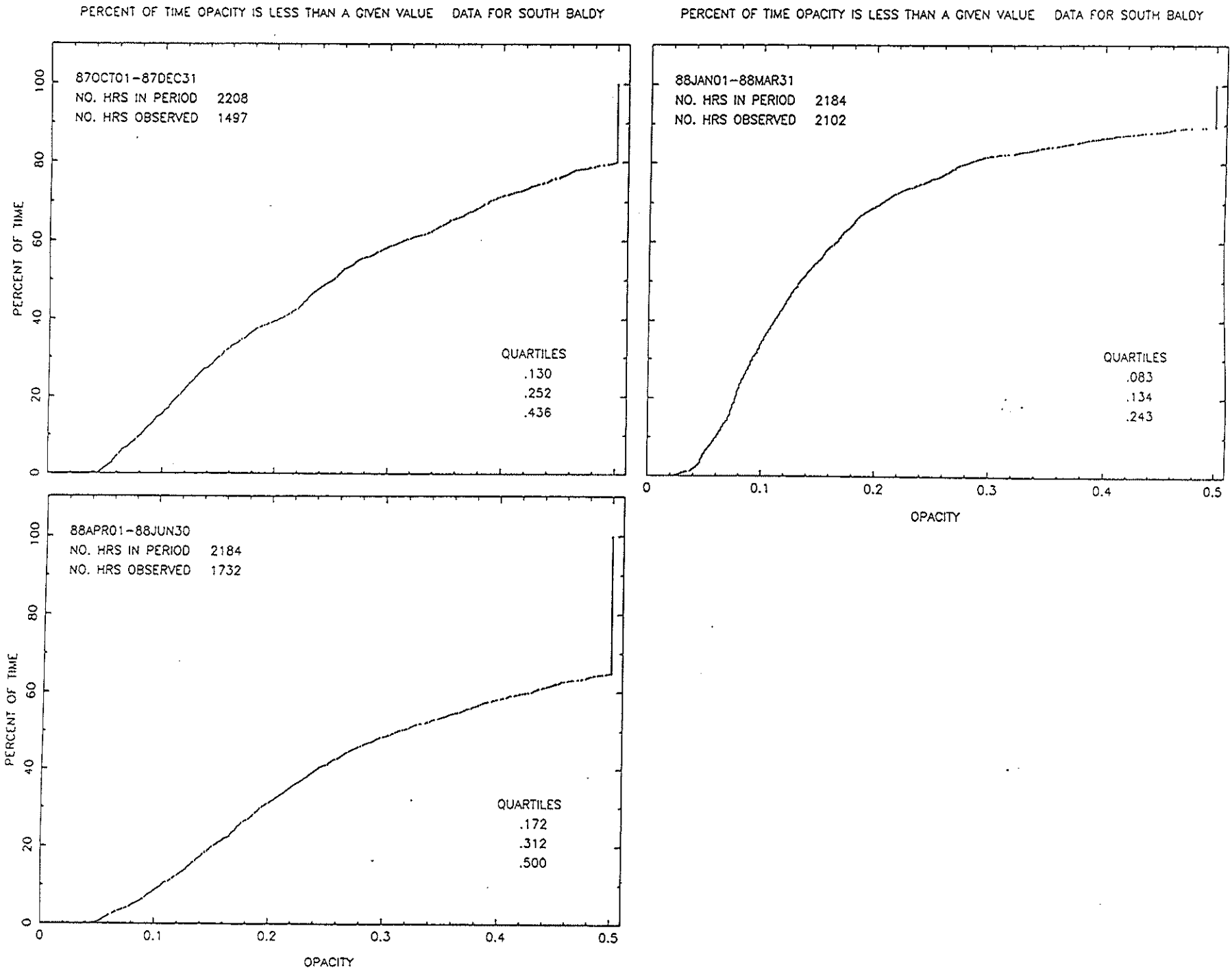
PERCENT OF TIME OPACITY IS LESS THAN A GIVEN VALUE DATA FOR SOUTH BALDY
87OCT01-87DEC31
NO. HRS IN PERIOD 2208
NO. HRS OBSERVED 1497
QUARTILES
.130
.252
.436
PERCENT OF TIME
0
20
40
60
80
100
PERCENT OF TIME OPACITY IS LESS THAN A GIVEN VALUE DATA FOR SOUTH BALDY
88JAN01-88MAR31
NO. HRS IN PERIOD 2184
NO. HRS OBSERVED 2102
QUARTILES
.083
.134
.243
0
0.1
0.2
0.3
0.4
0.5
OPACITY
88APR01-88JUN30
NO. HRS IN PERIOD 2184
NO. HRS OBSERVED 1732
QUARTILES
.172
.312
.500
PERCENT OF TIME
0
20
40
60
80
100
0
0.1
0.2
0.3
0.4
0.5
OPACITY

Figure 2a

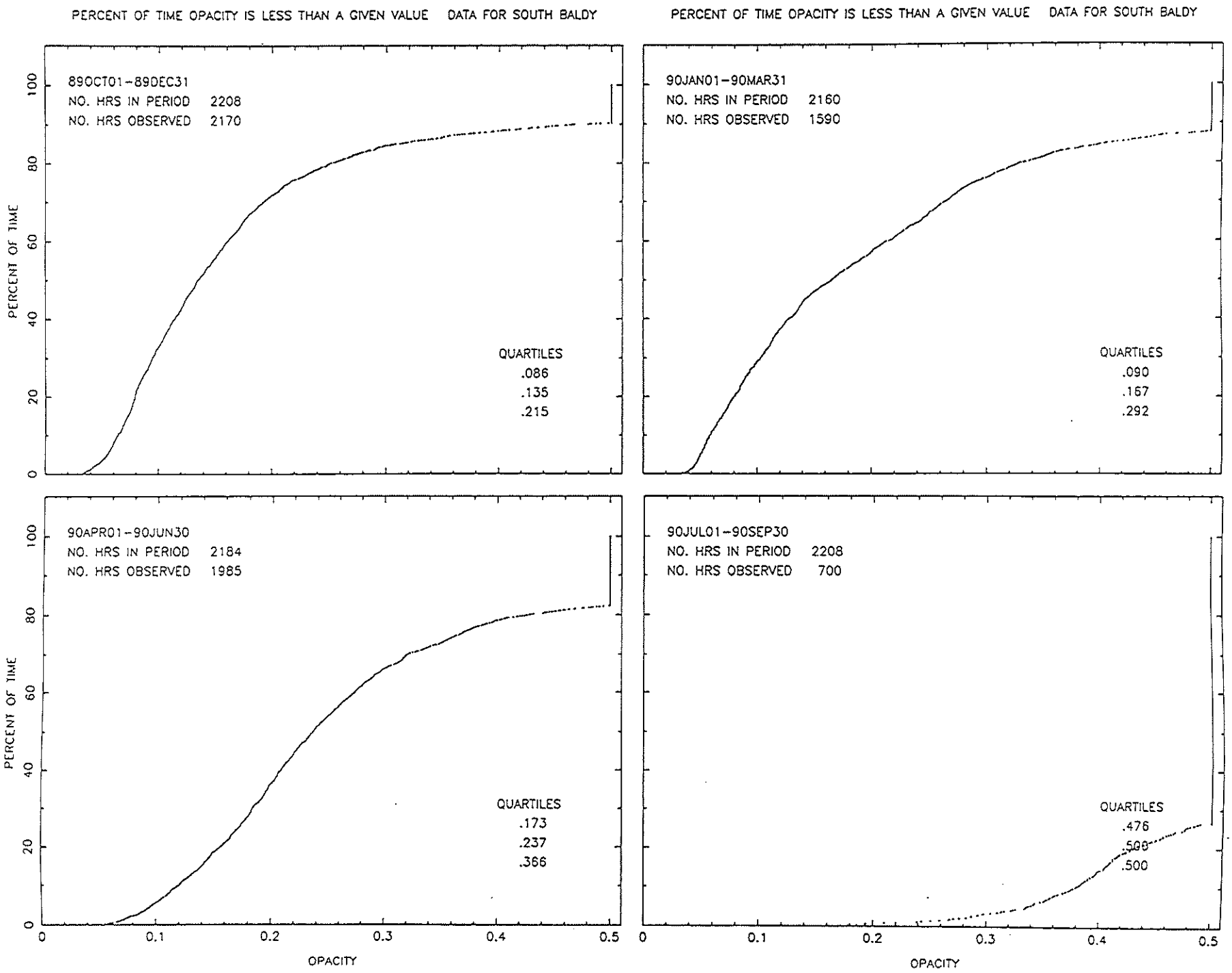
PERCENT OF TIME OPACITY IS LESS THAN A GIVEN VALUE DATA FOR SOUTH BALDY
89OCT01-89DEC31
NO. HRS IN PERIOD 2208
NO. HRS OBSERVED 2170
QUARTILES
.086
.135
.215
PERCENT OF TIME OPACITY IS LESS THAN A GIVEN VALUE DATA FOR SOUTH BALDY
90JAN01-90MAR31
NO. HRS IN PERIOD 2160
NO. HRS OBSERVED 1590
QUARTILES
.090
.167
.292
90APR01-90JUN30
NO. HRS IN PERIOD 2184
NO. HRS OBSERVED 1985
QUARTILES
.173
.237
.366
90JUL01-90SEP30
NO. HRS IN PERIOD 2208
NO. HRS OBSERVED 700
QUARTILES
.476
.500
.500
PERCENT OF TIME
0
20
40
60
80
100
0
0.1
0.2
0.3
0.4
0.5
OPACITY

Figure 2a

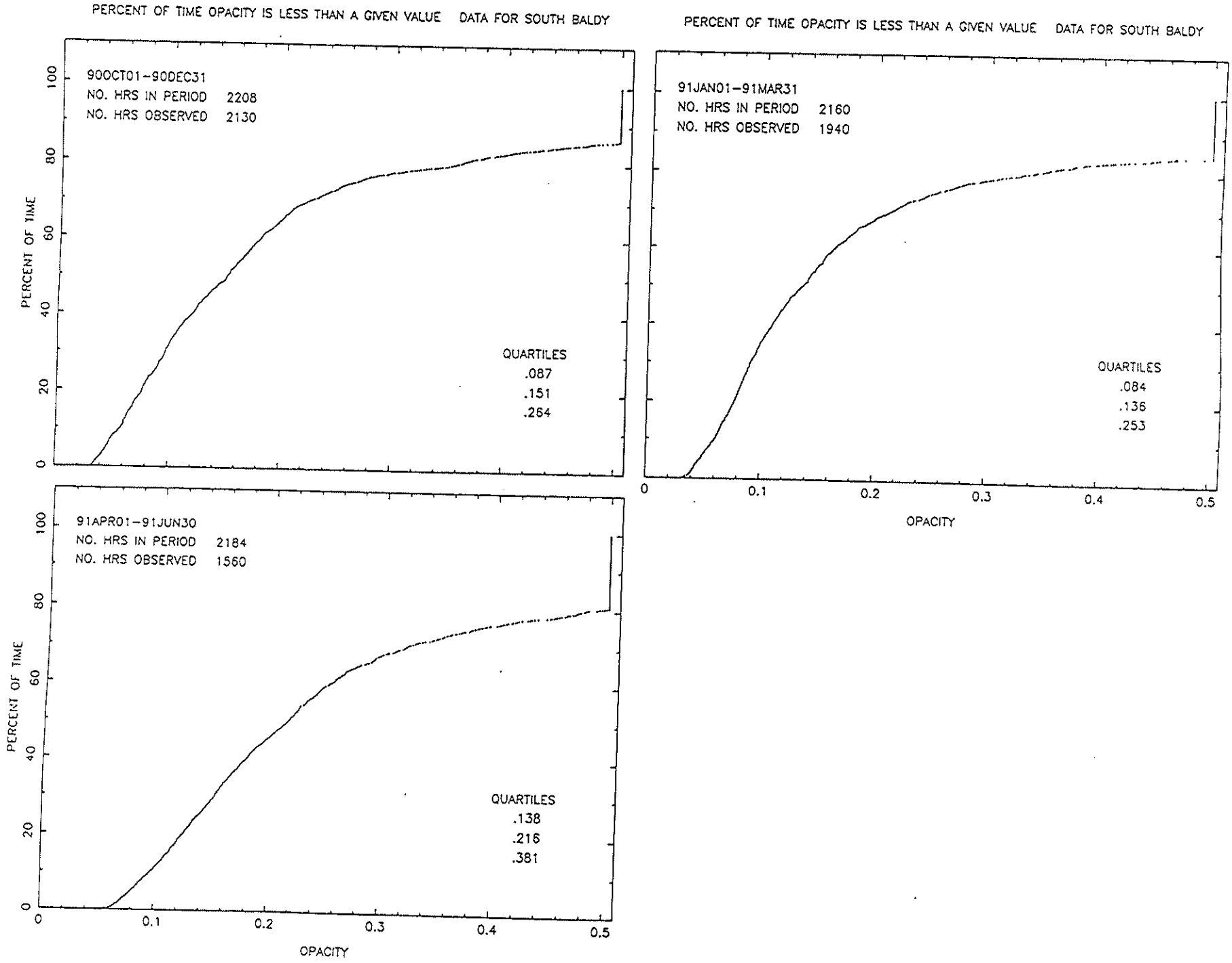
PERCENT OF TIME OPACITY IS LESS THAN A GIVEN VALUE DATA FOR SOUTH BALDY
90OCT01-90DEC31
NO. HRS IN PERIOD 2208
NO. HRS OBSERVED 2130
QUARTILES
.087
.151
.264
PERCENT OF TIME
OPACITY
PERCENT OF TIME OPACITY IS LESS THAN A GIVEN VALUE DATA FOR SOUTH BALDY
91JAN01-91MAR31
NO. HRS IN PERIOD 2160
NO. HRS OBSERVED 1940
QUARTILES
.084
.136
.253
OPACITY
91APR01-91JUN30
NO. HRS IN PERIOD 2184
NO. HRS OBSERVED 1560
QUARTILES
.138
.216
.381
PERCENT OF TIME
OPACITY

Figure 2a

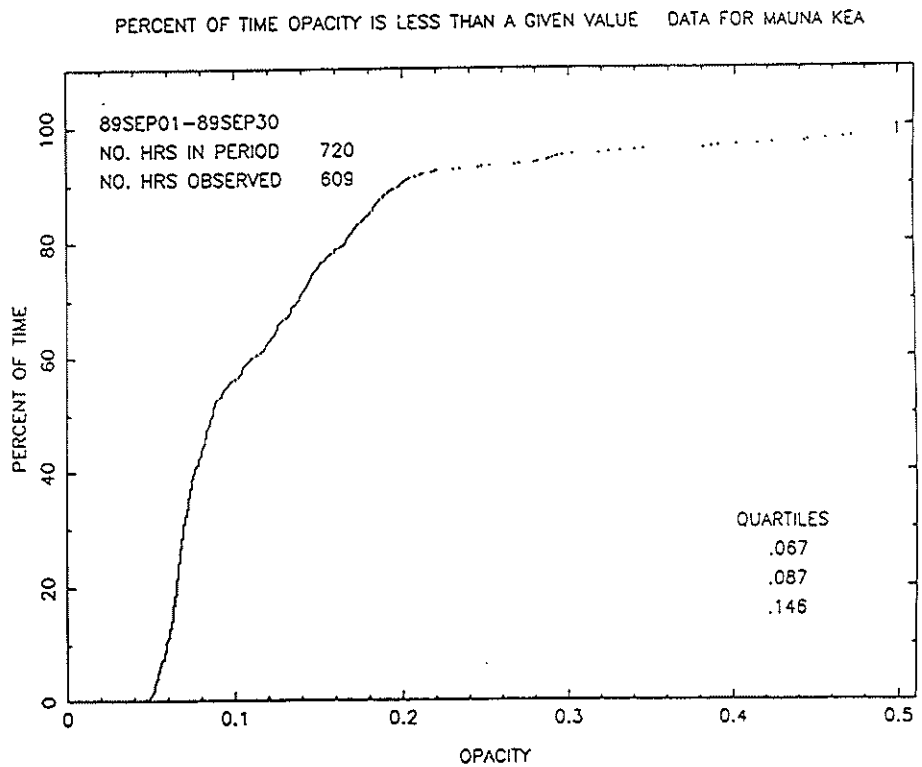
PERCENT OF TIME OPACITY IS LESS THAN A GIVEN VALUE DATA FOR MAUNA KEA
89SEP01-89SEP30
NO. HRS IN PERIOD 720
NO. HRS OBSERVED 609
QUARTILES
.067
.087
.146
PERCENT OF TIME
OPACITY
0
20
40
60
80
100
0
0.1
0.2
0.3
0.4
0.5

Figure 2b

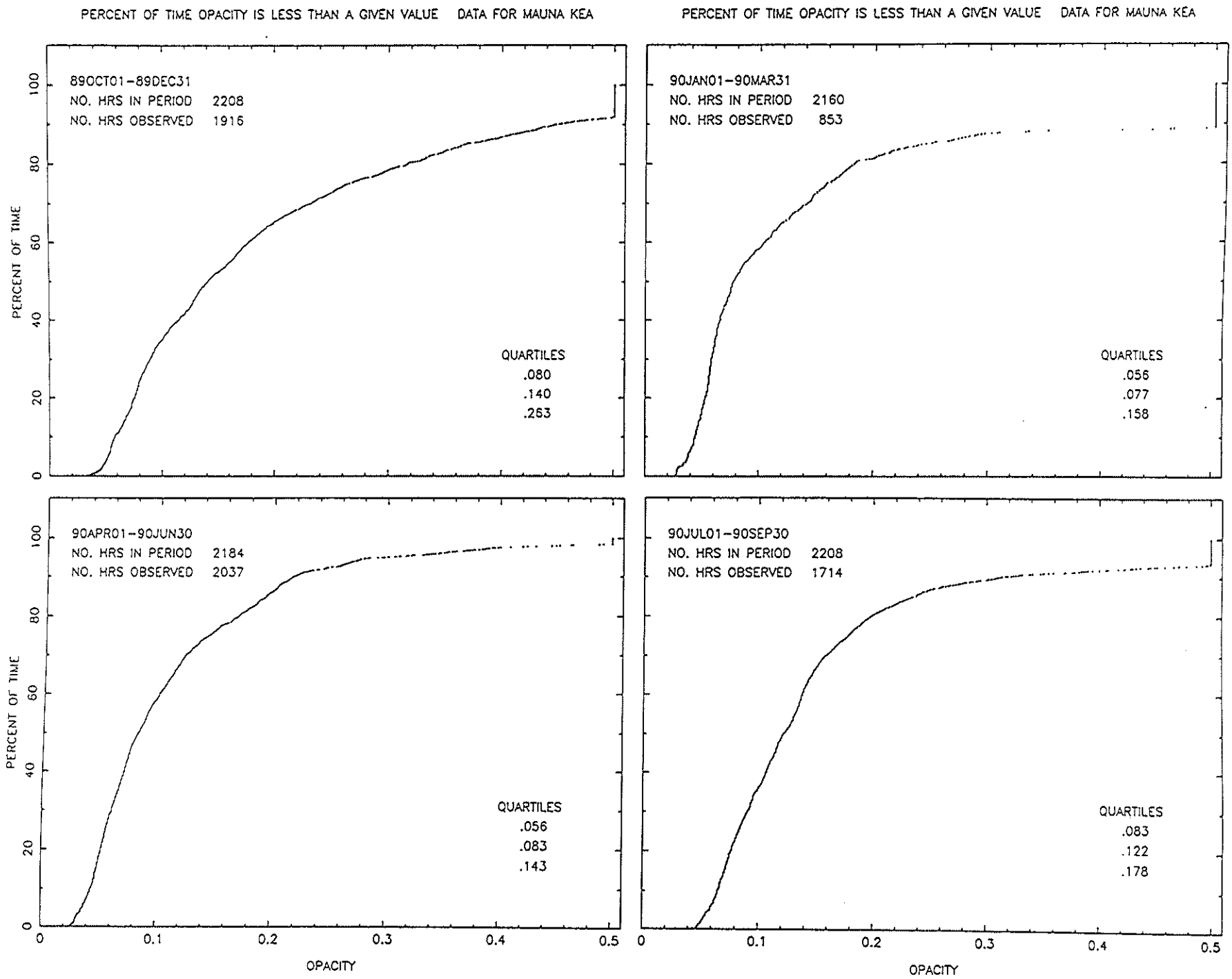
PERCENT OF TIME OPACITY IS LESS THAN A GIVEN VALUE DATA FOR MAUNA KEA
89OCT01-89DEC31
NO. HRS IN PERIOD 2208
NO. HRS OBSERVED 1916
QUARTILES
.080
.140
.263
PERCENT OF TIME OPACITY IS LESS THAN A GIVEN VALUE DATA FOR MAUNA KEA
90JAN01-90MAR31
NO. HRS IN PERIOD 2160
NO. HRS OBSERVED 853
QUARTILES
.056
.077
.158
90APR01-90JUN30
NO. HRS IN PERIOD 2184
NO. HRS OBSERVED 2037
QUARTILES
.056
.083
.143
90JUL01-90SEP30
NO. HRS IN PERIOD 2208
NO. HRS OBSERVED 1714
QUARTILES
.083
.122
.178
PERCENT OF TIME
0
20
40
60
80
100
0
0.1
0.2
0.3
0.4
0.5
OPACITY

Figure 2b

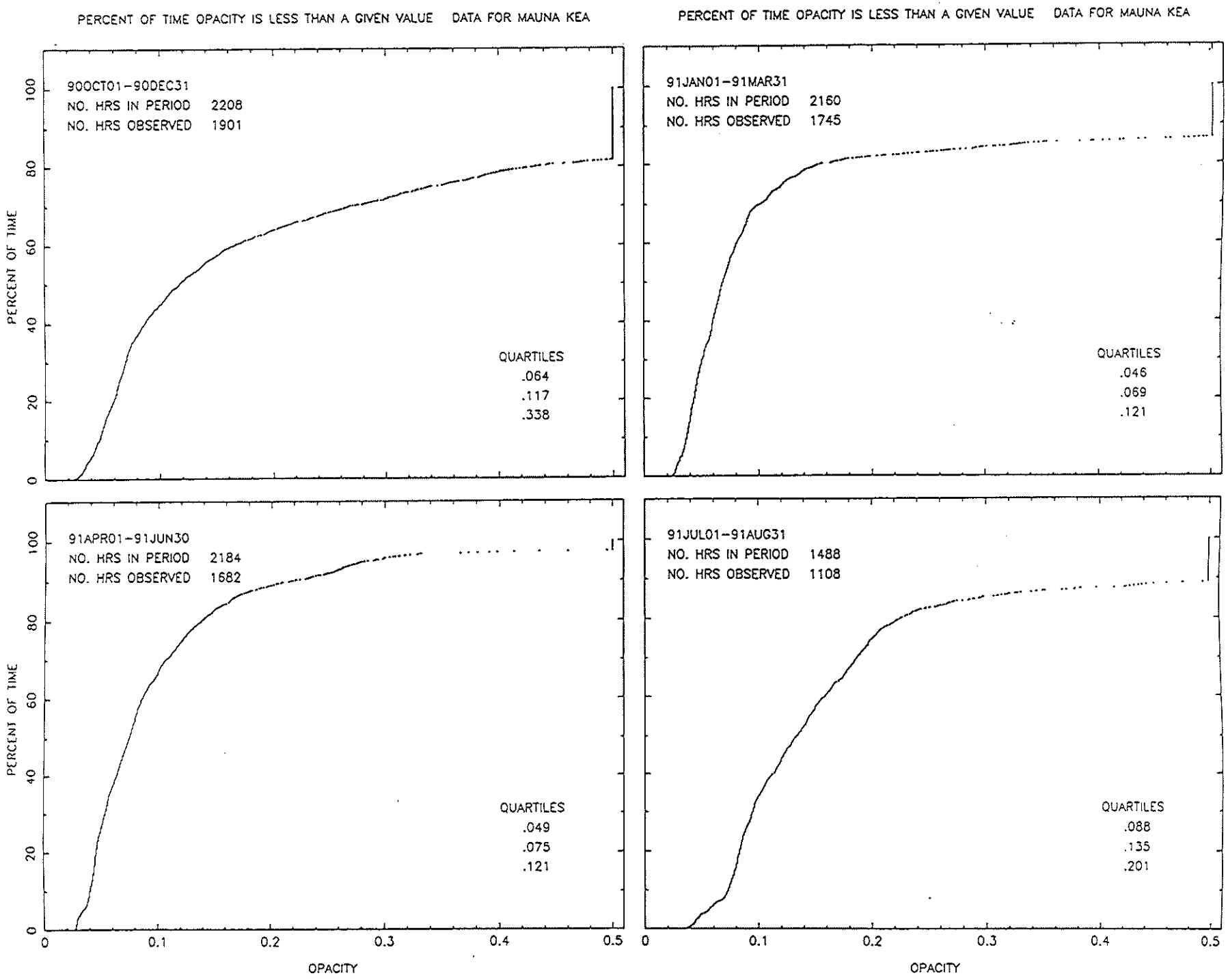
PERCENT OF TIME OPACITY IS LESS THAN A GIVEN VALUE DATA FOR MAUNA KEA
90OCT01-90DEC31
NO. HRS IN PERIOD 2208
NO. HRS OBSERVED 1901
QUARTILES
.064
.117
.338
91JAN01-91MAR31
NO. HRS IN PERIOD 2160
NO. HRS OBSERVED 1745
QUARTILES
.046
.069
.121
91APR01-91JUN30
NO. HRS IN PERIOD 2184
NO. HRS OBSERVED 1682
QUARTILES
.049
.075
.121
91JUL01-91AUG31
NO. HRS IN PERIOD 1488
NO. HRS OBSERVED 1108
QUARTILES
.088
.135
.201
PERCENT OF TIME
0
20
40
60
80
100
0
0.1
0.2
0.3
0.4
0.5
OPACITY

Figure 2b

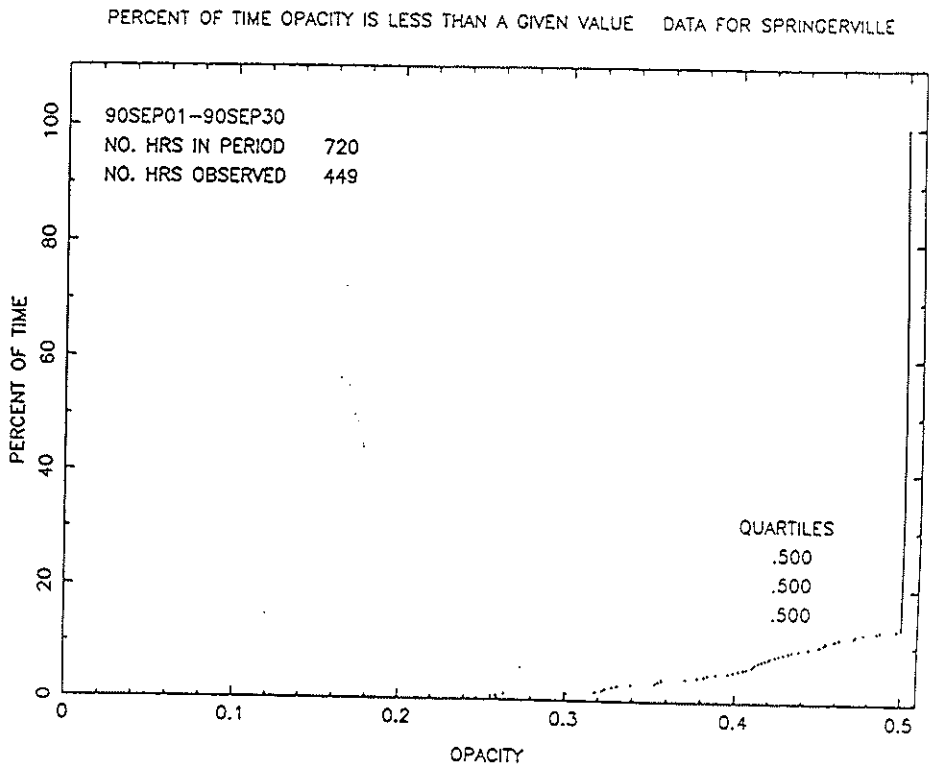
PERCENT OF TIME OPACITY IS LESS THAN A GIVEN VALUE DATA FOR SPRINGERVILLE
90SEP01-90SEP30
NO. HRS IN PERIOD 720
NO. HRS OBSERVED 449
QUARTILES
.500
.500
.500
PERCENT OF TIME
0
20
40
60
80
100
0
0.1
0.2
0.3
0.4
0.5
OPACITY

Figure 2c

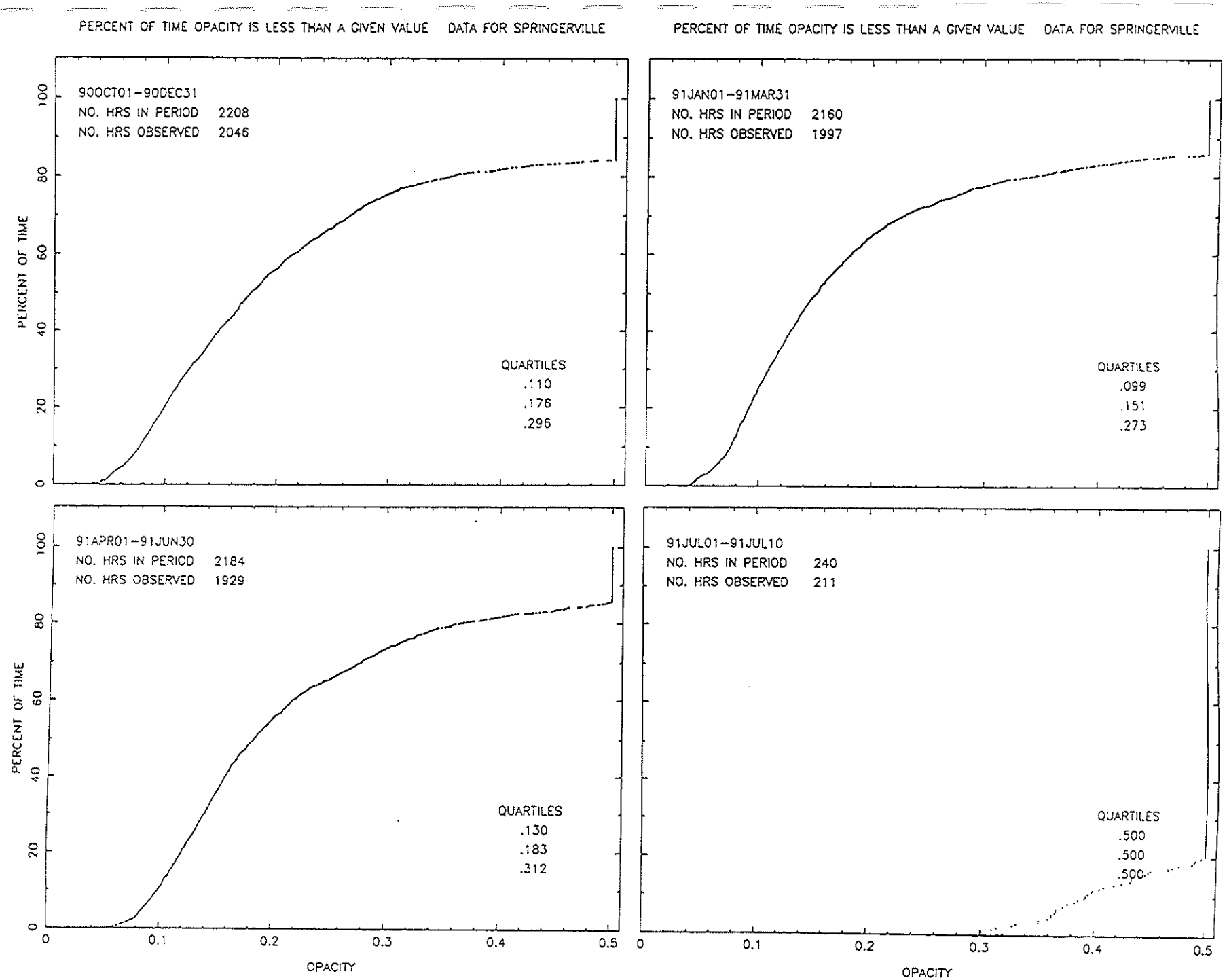
PERCENT OF TIME OPACITY IS LESS THAN A GIVEN VALUE DATA FOR SPRINGERVILLE
90OCT01-90DEC31
NO. HRS IN PERIOD 2208
NO. HRS OBSERVED 2046
QUARTILES
.110
.176
.296
PERCENT OF TIME OPACITY IS LESS THAN A GIVEN VALUE DATA FOR SPRINGERVILLE
91JAN01-91MAR31
NO. HRS IN PERIOD 2160
NO. HRS OBSERVED 1997
QUARTILES
.099
.151
.273
91APR01-91JUN30
NO. HRS IN PERIOD 2184
NO. HRS OBSERVED 1929
QUARTILES
.130
.183
.312
91JUL01-91JUL10
NO. HRS IN PERIOD 240
NO. HRS OBSERVED 211
QUARTILES
.500
.500
.500
PERCENT OF TIME
OPACITY
0
20
40
60
80
100
0.1
0.2
0.3
0.4
0.5

Figure 2c

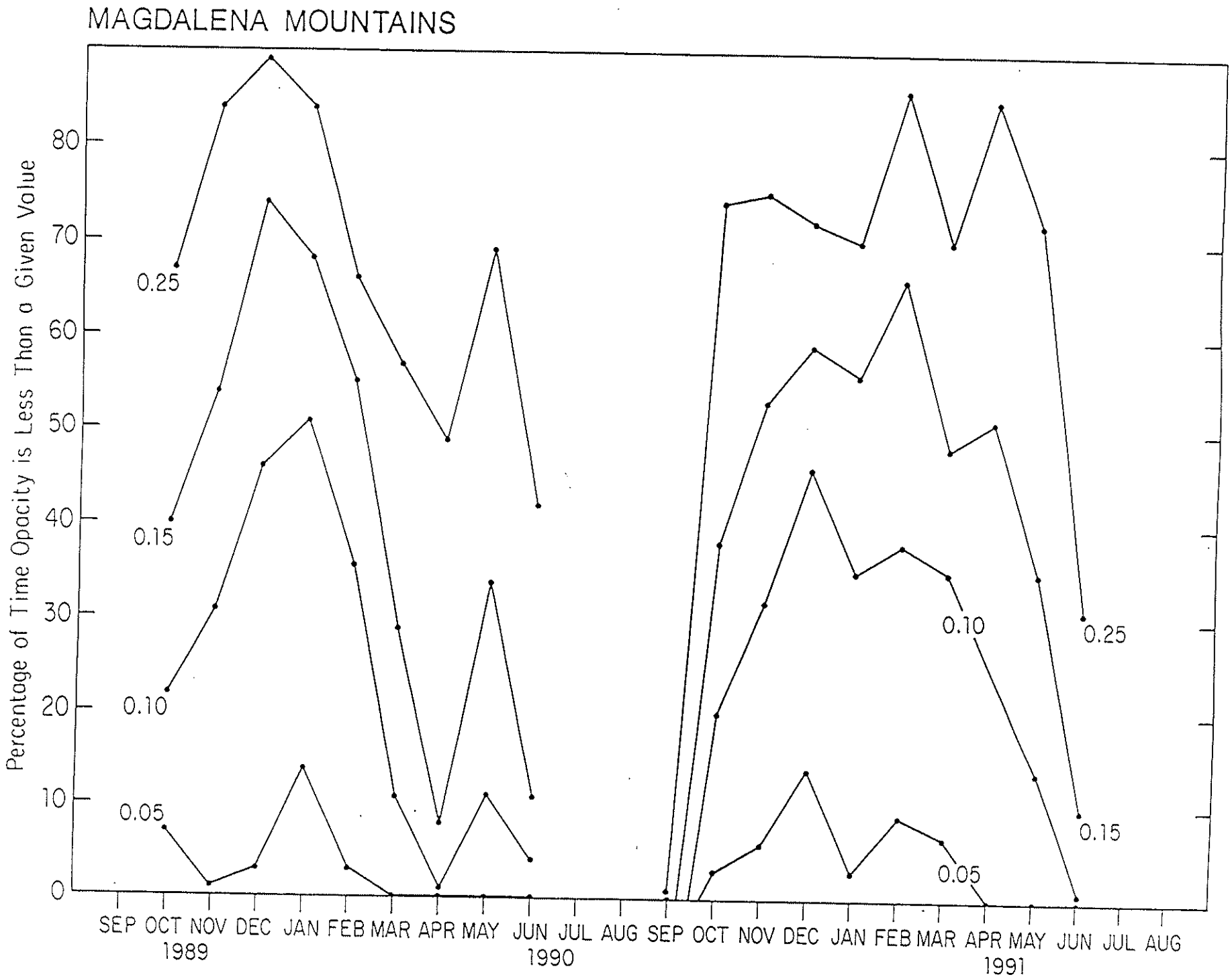
MAGDALENA MOUNTAINS
Percentage of Time Opacity is Less Than a Given Value
0
10
20
30
40
50
60
70
80
0.25
0.15
0.10
0.05
0.10
0.25
0.15
0.05
SEP OCT NOV DEC JAN FEB MAR APR MAY JUN JUL AUG SEP OCT NOV DEC JAN FEB MAR APR MAY JUN JUL AUG
1989
1990
1991

Figure 3a

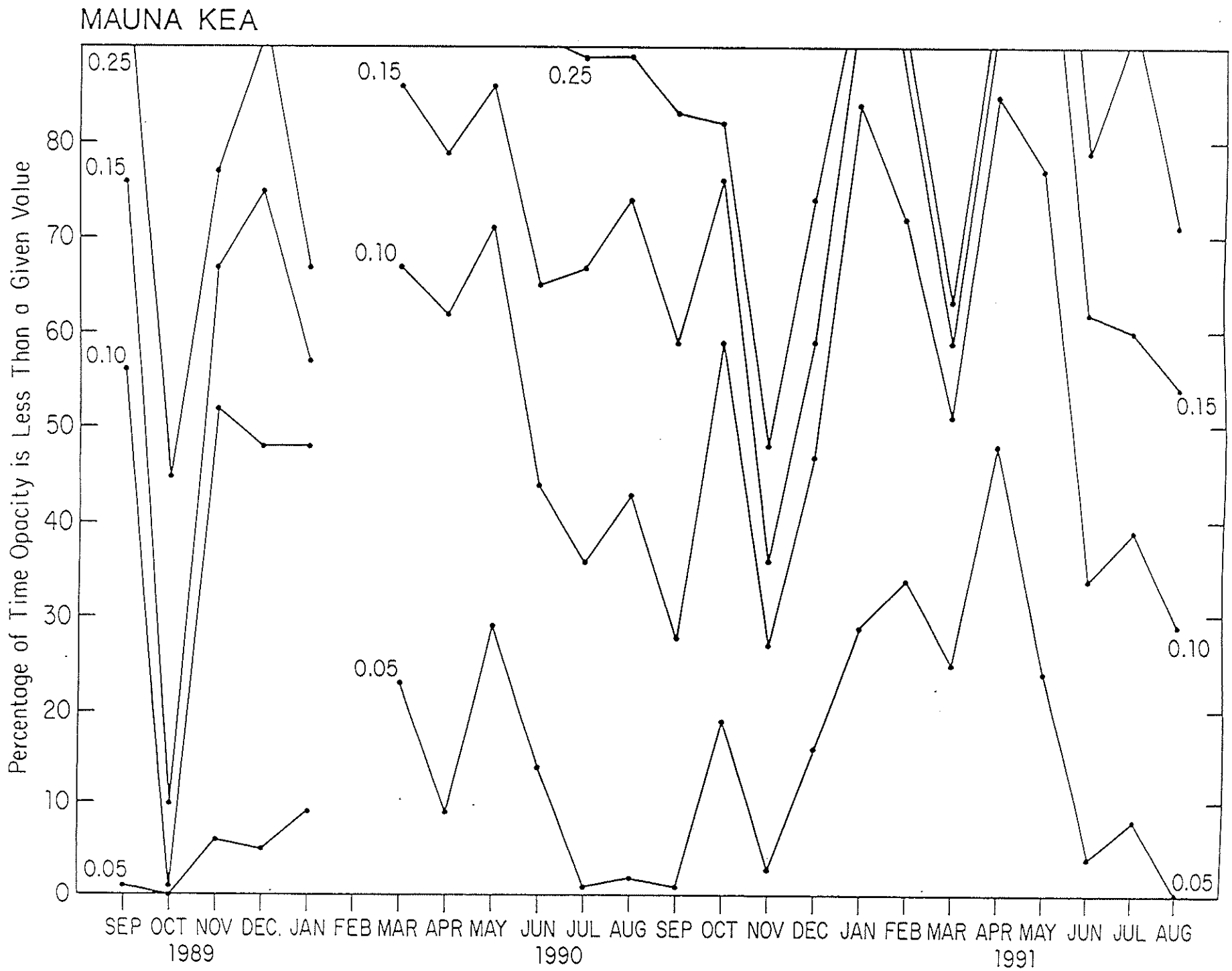
MAUNA KEA
Percentage of Time Opacity is Less Than a Given Value
0.25
0.15
0.10
0.05
0.15
0.25
0.10
0.05
0.15
0.10
0.05
0
10
20
30
40
50
60
70
80
SEP OCT NOV DEC. JAN FEB MAR APR MAY JUN JUL AUG SEP OCT NOV DEC JAN FEB MAR APR MAY JUN JUL AUG
1989
1990
1991

Figure 3b

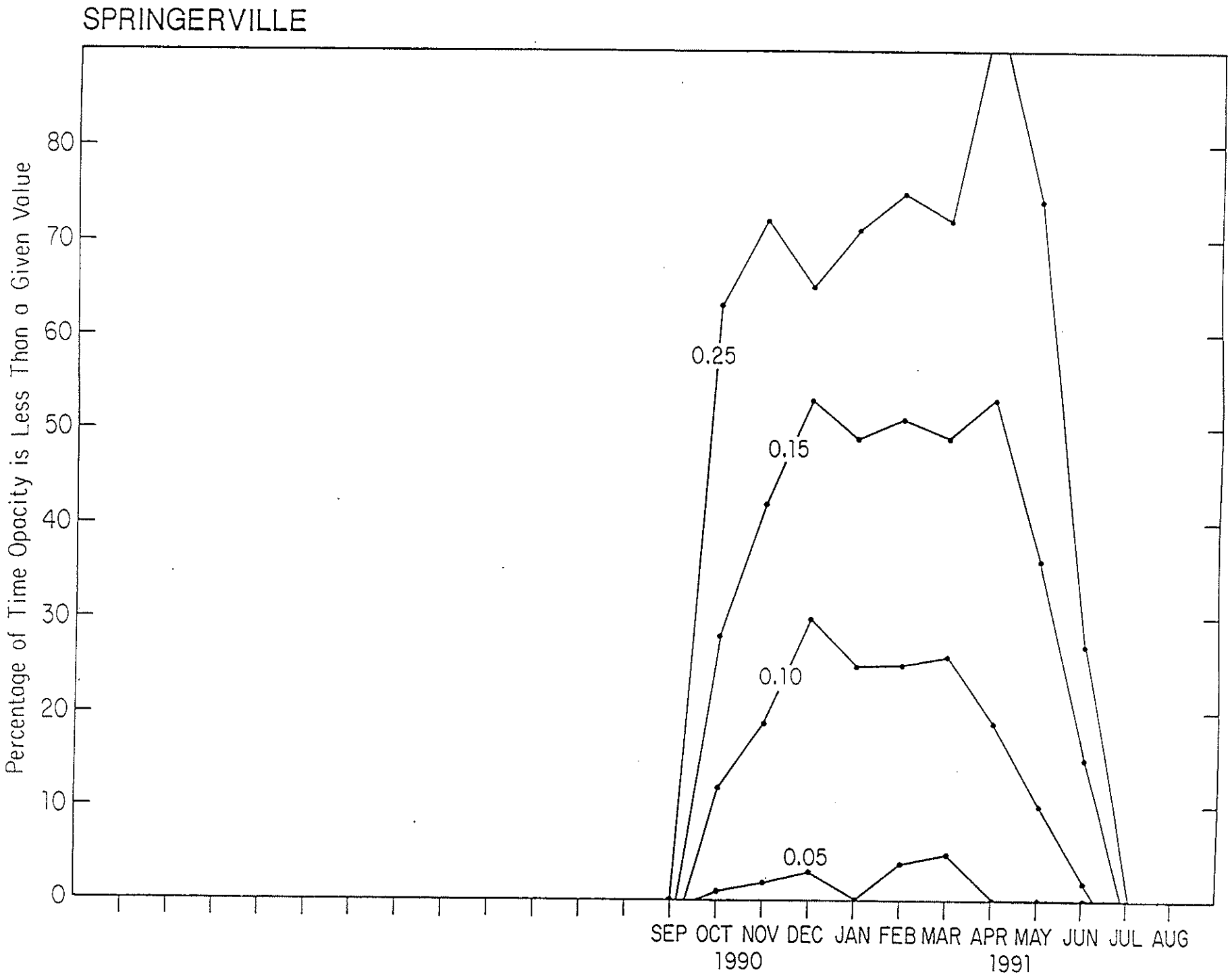
SPRINGERVILLE
Percentage of Time Opacity is Less Than a Given Value
0
10
20
30
40
50
60
70
80
0.25
0.15
0.10
0.05
SEP
OCT
NOV
DEC
JAN
FEB
MAR
APR
MAY
JUN
JUL
AUG
1990
1991

Figure 3c

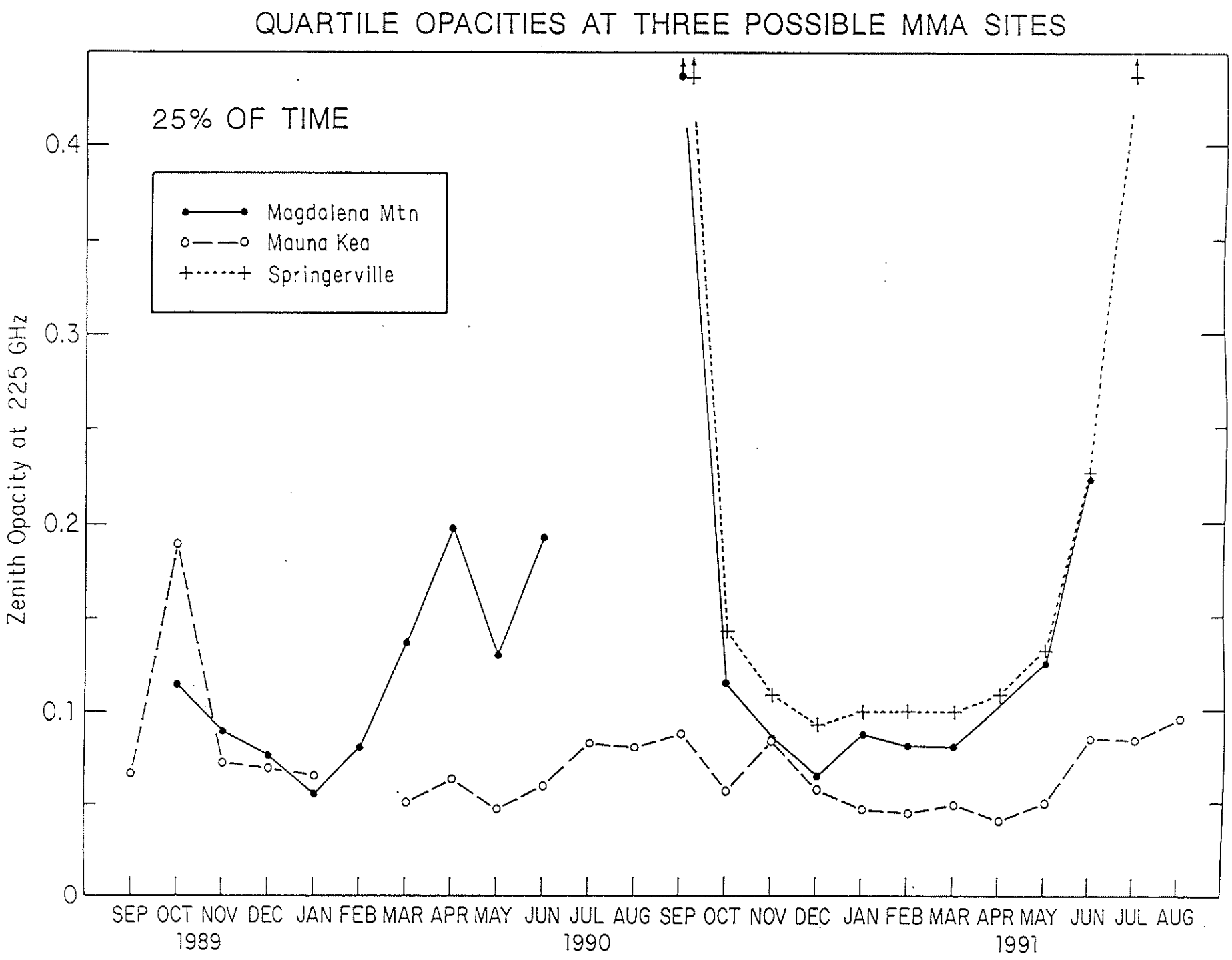
QUARTILE OPACITIES AT THREE POSSIBLE MMA SITES
25% OF TIME
Magdalena Mtn
Mauna Kea
Springerville
Zenith Opacity at 225 GHz
0
0.1
0.2
0.3
0.4
SEP OCT NOV DEC JAN FEB MAR APR MAY JUN JUL AUG SEP OCT NOV DEC JAN FEB MAR APR MAY JUN JUL AUG
1989
1990
1991

Figure 4a

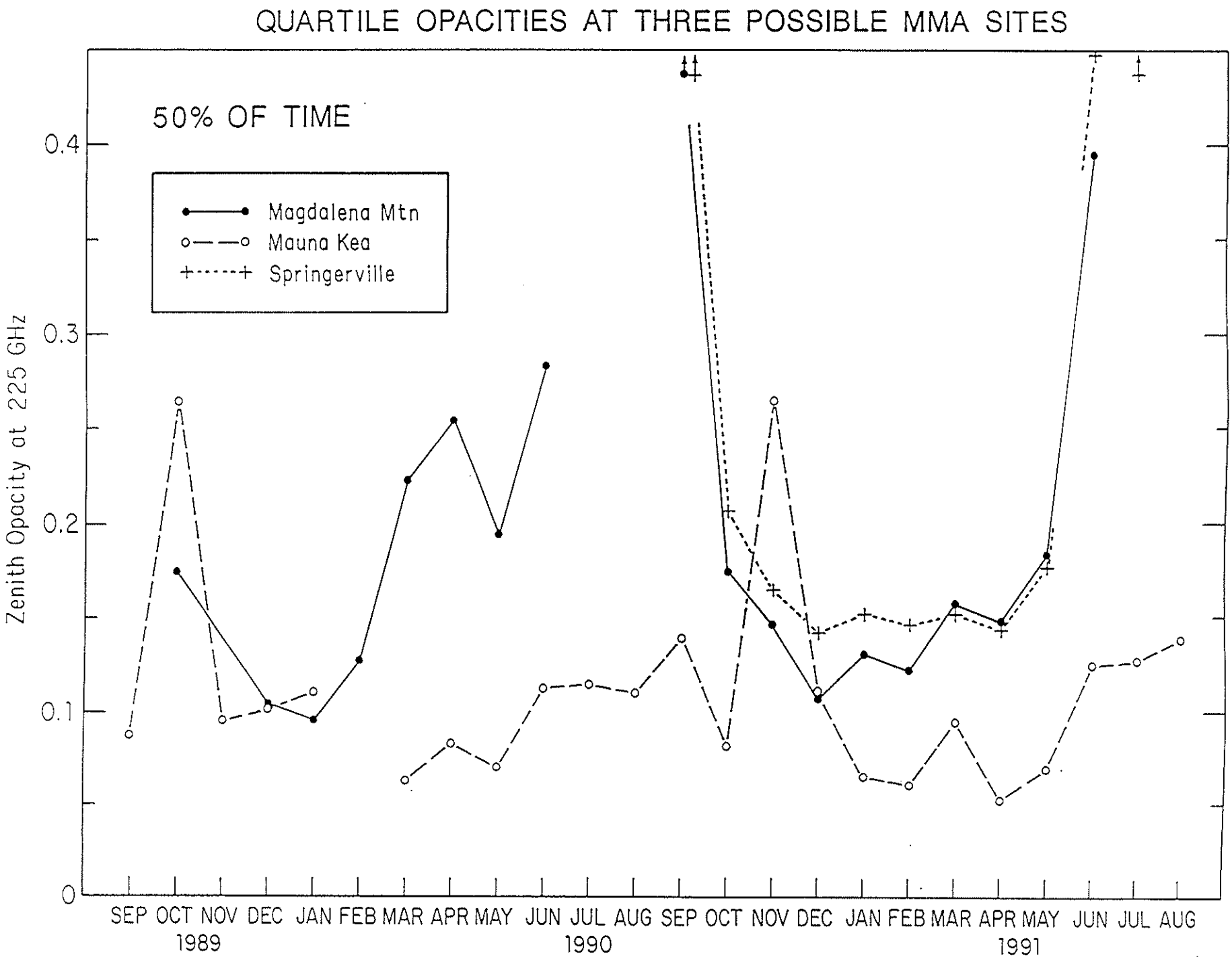
QUARTILE OPACITIES AT THREE POSSIBLE MMA SITES
50% OF TIME
Magdalena Mtn
Mauna Kea
Springerville
Zenith Opacity at 225 GHz
0
0.1
0.2
0.3
0.4
SEP OCT NOV DEC JAN FEB MAR APR MAY JUN JUL AUG SEP OCT NOV DEC JAN FEB MAR APR MAY JUN JUL AUG
1989
1990
1991

Figure 4b

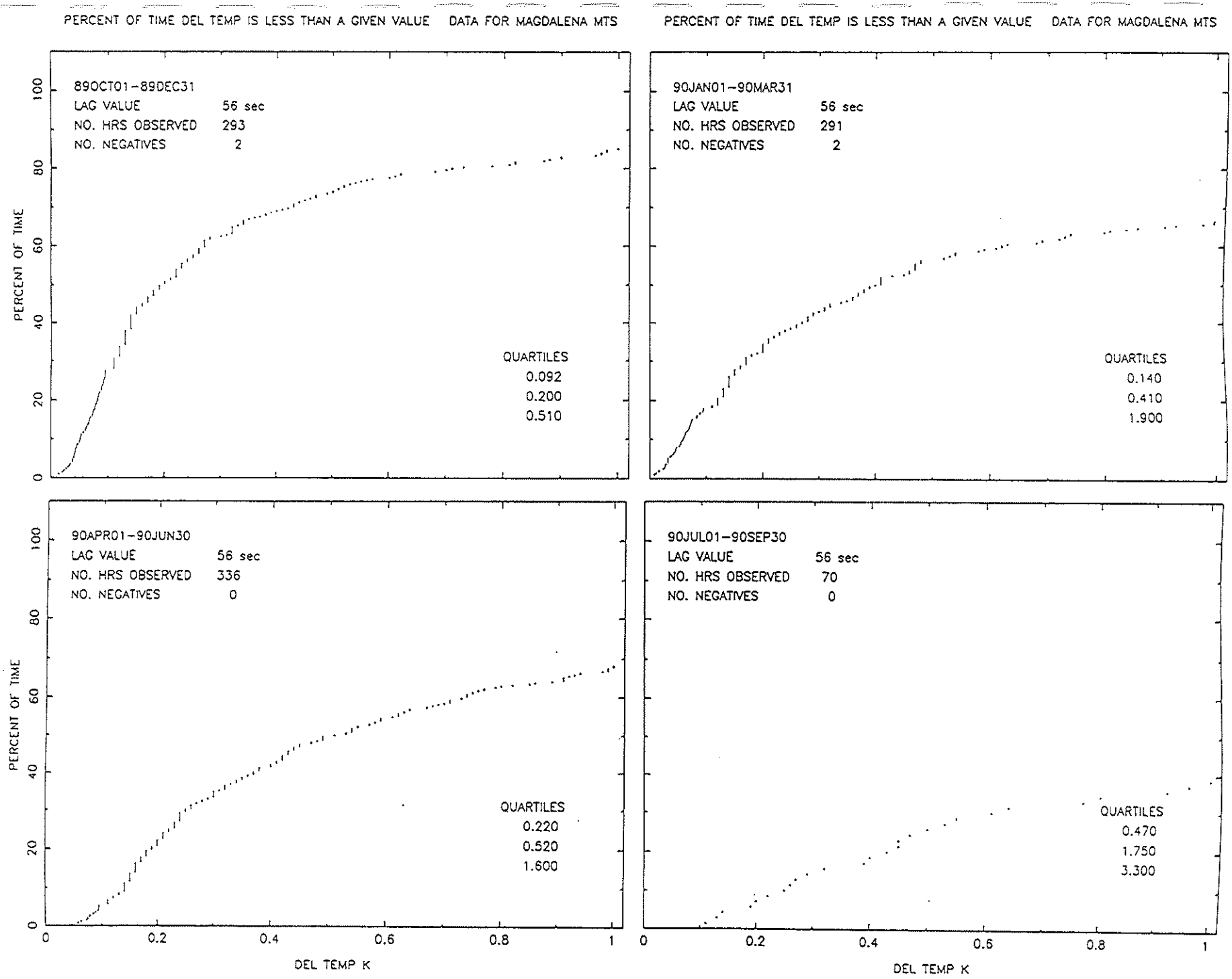
PERCENT OF TIME DEL TEMP IS LESS THAN A GIVEN VALUE DATA FOR MAGDALENA MTS
89OCT01-89DEC31
LAG VALUE 56 sec
NO. HRS OBSERVED 293
NO. NEGATIVES 2
QUARTILES
0.092
0.200
0.510
90JAN01-90MAR31
LAG VALUE 56 sec
NO. HRS OBSERVED 291
NO. NEGATIVES 2
QUARTILES
0.140
0.410
1.900
90APR01-90JUN30
LAG VALUE 56 sec
NO. HRS OBSERVED 336
NO. NEGATIVES 0
QUARTILES
0.220
0.520
1.600
90JUL01-90SEP30
LAG VALUE 56 sec
NO. HRS OBSERVED 70
NO. NEGATIVES 0
QUARTILES
0.470
1.750
3.300
PERCENT OF TIME
DEL TEMP K
0
20
40
60
80
100
0.2
0.4
0.6
0.8
1

Figure 5a

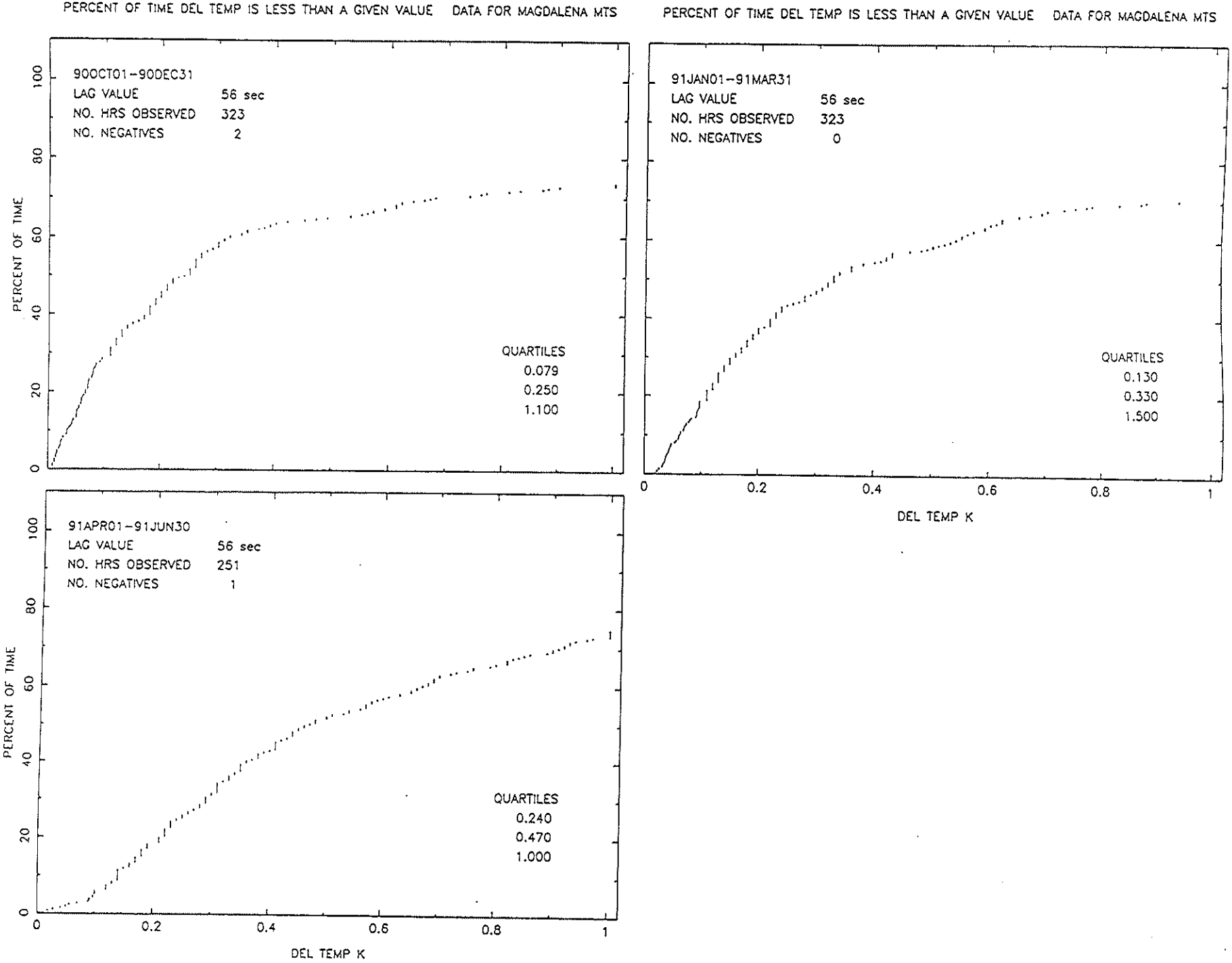
PERCENT OF TIME DEL TEMP IS LESS THAN A GIVEN VALUE DATA FOR MAGDALENA MTS
900CT01-90DEC31
LAG VALUE 56 sec
NO. HRS OBSERVED 323
NO. NEGATIVES 2
QUARTILES
0.079
0.250
1.100
PERCENT OF TIME
DEL TEMP K
PERCENT OF TIME DEL TEMP IS LESS THAN A GIVEN VALUE DATA FOR MAGDALENA MTS
91JAN01-91MAR31
LAG VALUE 56 sec
NO. HRS OBSERVED 323
NO. NEGATIVES 0
QUARTILES
0.130
0.330
1.500
DEL TEMP K
91APR01-91JUN30
LAG VALUE 56 sec
NO. HRS OBSERVED 251
NO. NEGATIVES 1
QUARTILES
0.240
0.470
1.000
PERCENT OF TIME
DEL TEMP K

Figure 5a

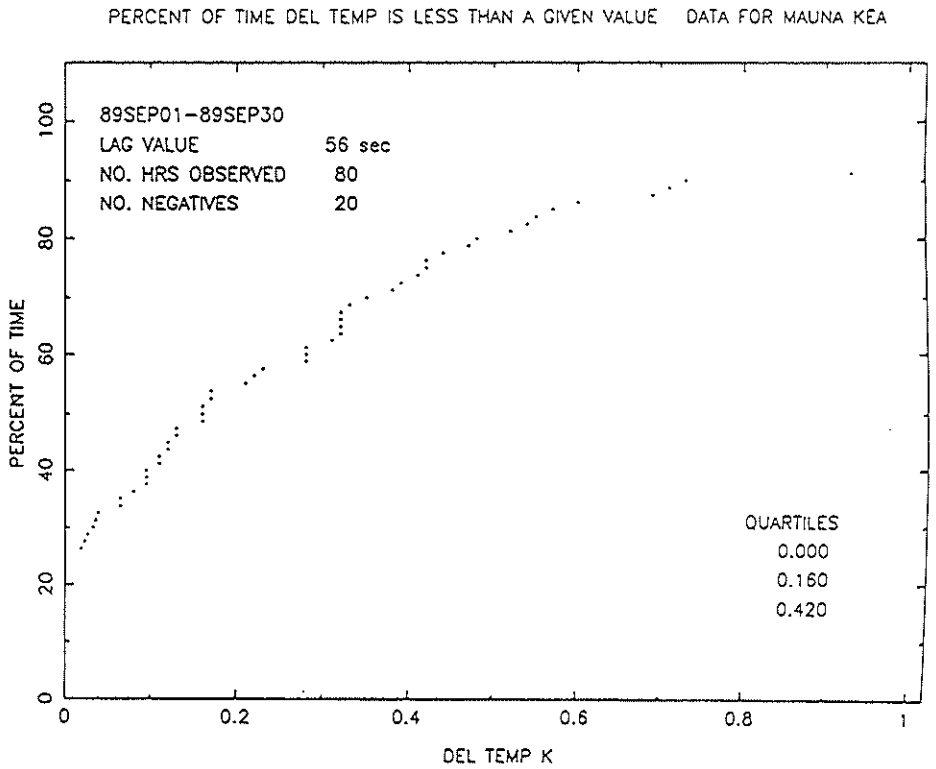
PERCENT OF TIME DEL TEMP IS LESS THAN A GIVEN VALUE DATA FOR MAUNA KEA
89SEP01–89SEP30
LAG VALUE 56 sec
NO. HRS OBSERVED 80
NO. NEGATIVES 20
QUARTILES
0.000
0.160
0.420
PERCENT OF TIME
0
20
40
60
80
100
0
0.2
0.4
0.6
0.8
1
DEL TEMP K

Figure 5b

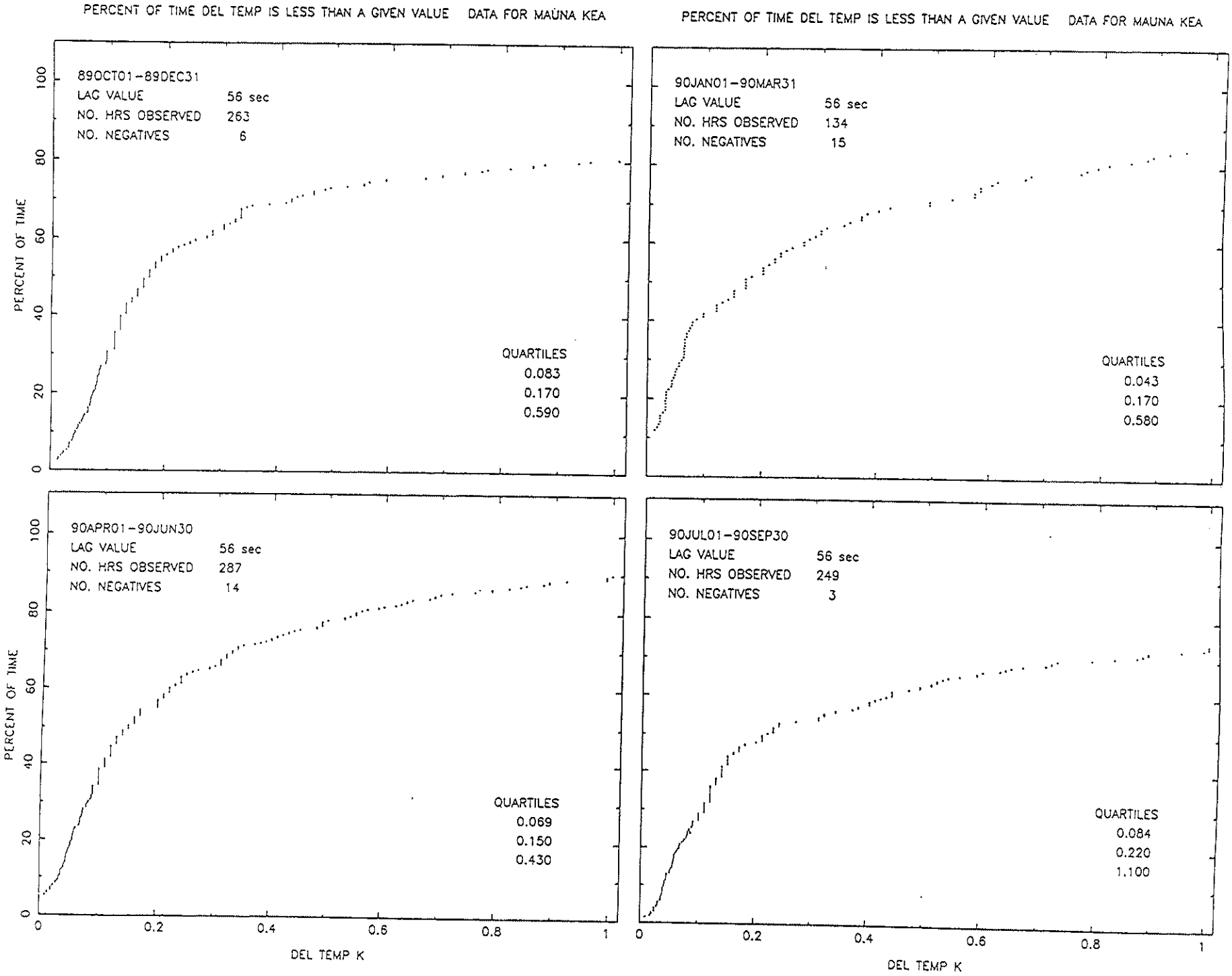
PERCENT OF TIME DEL TEMP IS LESS THAN A GIVEN VALUE DATA FOR MAUNA KEA
89OCT01-89DEC31
LAG VALUE 56 sec
NO. HRS OBSERVED 263
NO. NEGATIVES 6
QUARTILES
0.083
0.170
0.590
PERCENT OF TIME DEL TEMP IS LESS THAN A GIVEN VALUE DATA FOR MAUNA KEA
90JAN01-90MAR31
LAG VALUE 56 sec
NO. HRS OBSERVED 134
NO. NEGATIVES 15
QUARTILES
0.043
0.170
0.580
90APR01-90JUN30
LAG VALUE 56 sec
NO. HRS OBSERVED 287
NO. NEGATIVES 14
QUARTILES
0.069
0.150
0.430
90JUL01-90SEP30
LAG VALUE 56 sec
NO. HRS OBSERVED 249
NO. NEGATIVES 3
QUARTILES
0.084
0.220
1.100
PERCENT OF TIME
DEL TEMP K
0
20
40
60
80
100
0.2
0.4
0.6
0.8
1

Figure 5b

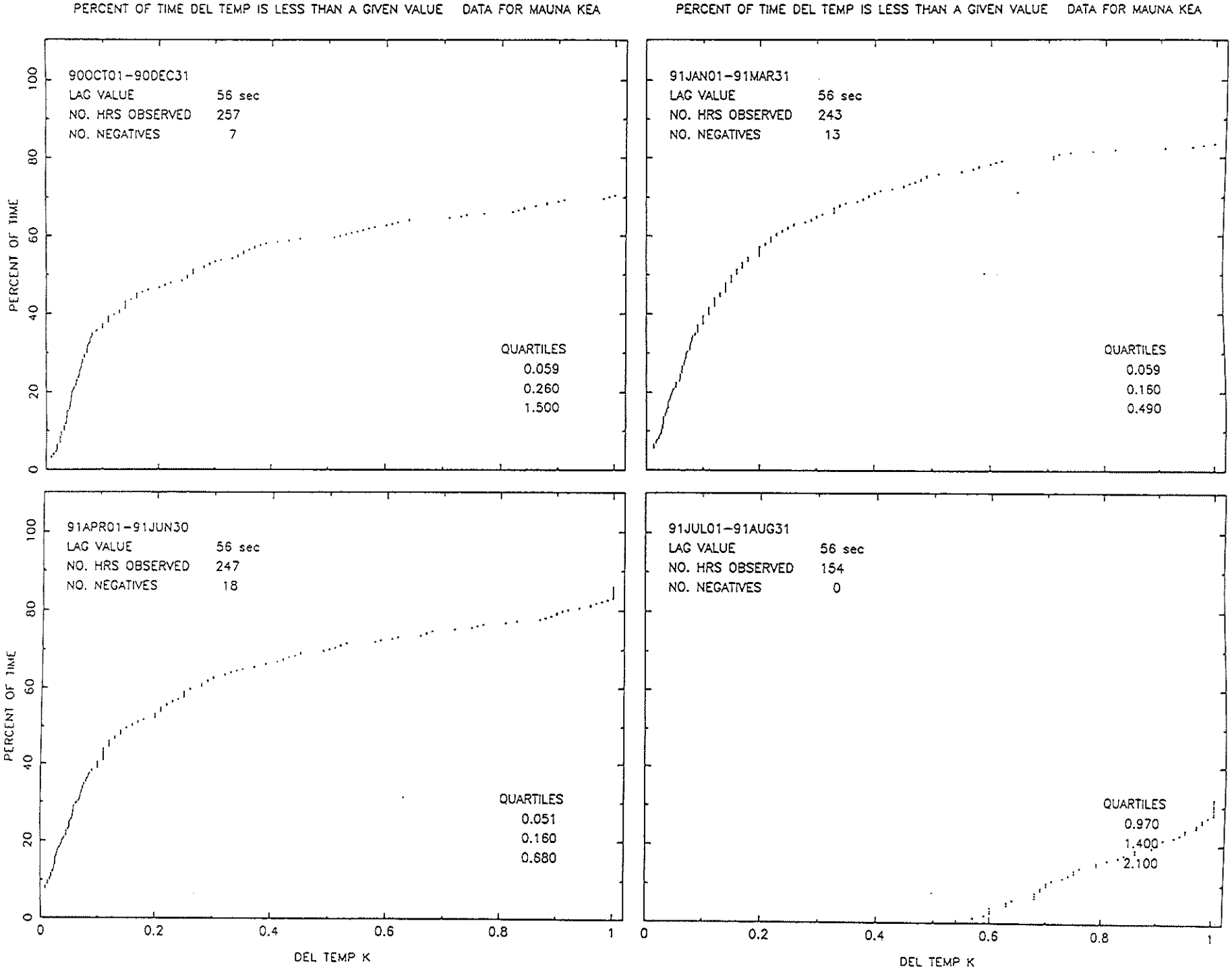
PERCENT OF TIME DEL TEMP IS LESS THAN A GIVEN VALUE DATA FOR MAUNA KEA
90OCT01-90DEC31
LAG VALUE 56 sec
NO. HRS OBSERVED 257
NO. NEGATIVES 7
QUARTILES
0.059
0.260
1.500
PERCENT OF TIME
PERCENT OF TIME DEL TEMP IS LESS THAN A GIVEN VALUE DATA FOR MAUNA KEA
91JAN01-91MAR31
LAG VALUE 56 sec
NO. HRS OBSERVED 243
NO. NEGATIVES 13
QUARTILES
0.059
0.160
0.490
91APR01-91JUN30
LAG VALUE 56 sec
NO. HRS OBSERVED 247
NO. NEGATIVES 18
QUARTILES
0.051
0.160
0.680
PERCENT OF TIME
DEL TEMP K
91JUL01-91AUG31
LAG VALUE 56 sec
NO. HRS OBSERVED 154
NO. NEGATIVES 0
QUARTILES
0.970
1.400
2.100
DEL TEMP K

Figure 5b

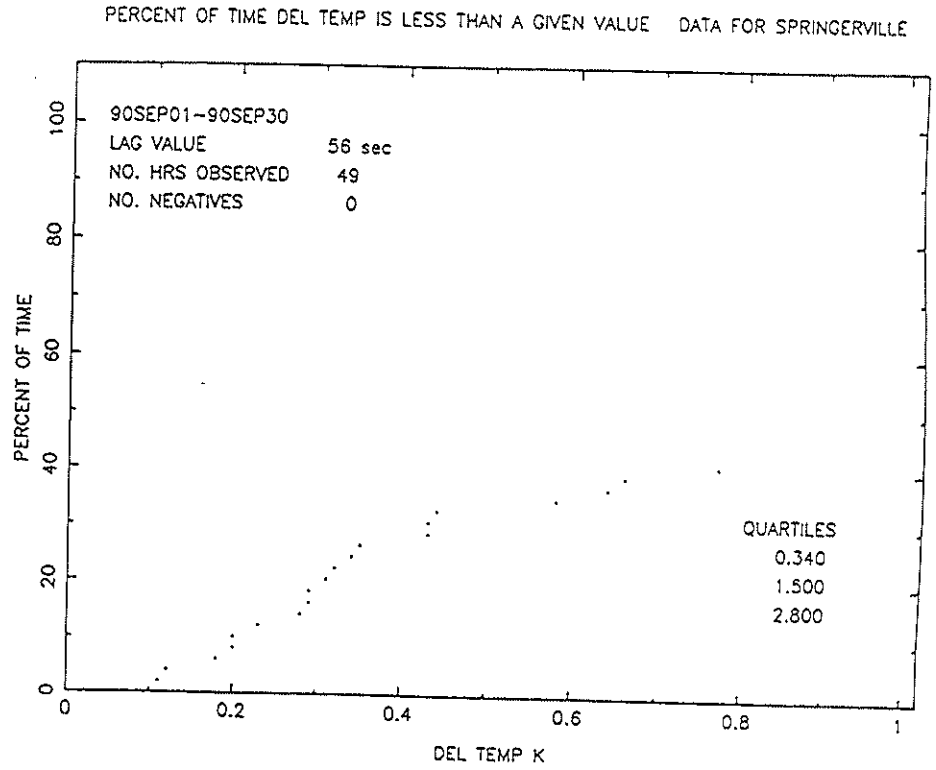
PERCENT OF TIME DEL TEMP IS LESS THAN A GIVEN VALUE DATA FOR SPRINGERVILLE
90SEP01-90SEP30
LAG VALUE 56 sec
NO. HRS OBSERVED 49
NO. NEGATIVES 0
QUARTILES
0.340
1.500
2.800
PERCENT OF TIME
0
20
40
60
80
100
0
0.2
0.4
0.6
0.8
1
DEL TEMP K

Figure 5c

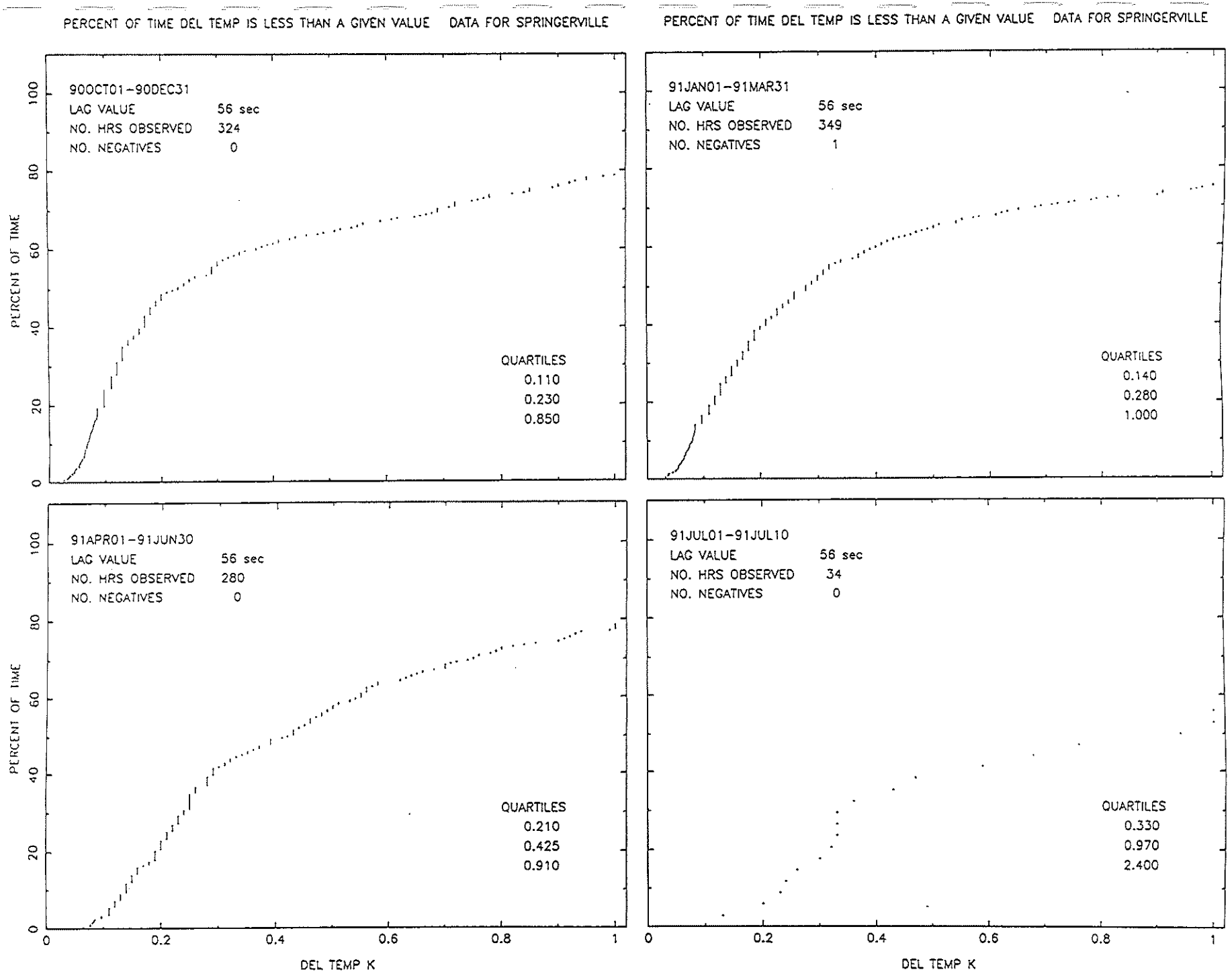
PERCENT OF TIME DEL TEMP IS LESS THAN A GIVEN VALUE DATA FOR SPRINGERVILLE
900CT01-90DEC31
LAG VALUE 56 sec
NO. HRS OBSERVED 324
NO. NEGATIVES 0
QUARTILES
0.110
0.230
0.850
PERCENT OF TIME DEL TEMP IS LESS THAN A GIVEN VALUE DATA FOR SPRINGERVILLE
91JAN01-91MAR31
LAG VALUE 56 sec
NO. HRS OBSERVED 349
NO. NEGATIVES 1
QUARTILES
0.140
0.280
1.000
91APR01-91JUN30
LAG VALUE 56 sec
NO. HRS OBSERVED 280
NO. NEGATIVES 0
QUARTILES
0.210
0.425
0.910
91JUL01-91JUL10
LAG VALUE 56 sec
NO. HRS OBSERVED 34
NO. NEGATIVES 0
QUARTILES
0.330
0.970
2.400
PERCENT OF TIME
DEL TEMP K
0
20
40
60
80
100
0.2
0.4
0.6
0.8
1

Figure 5c

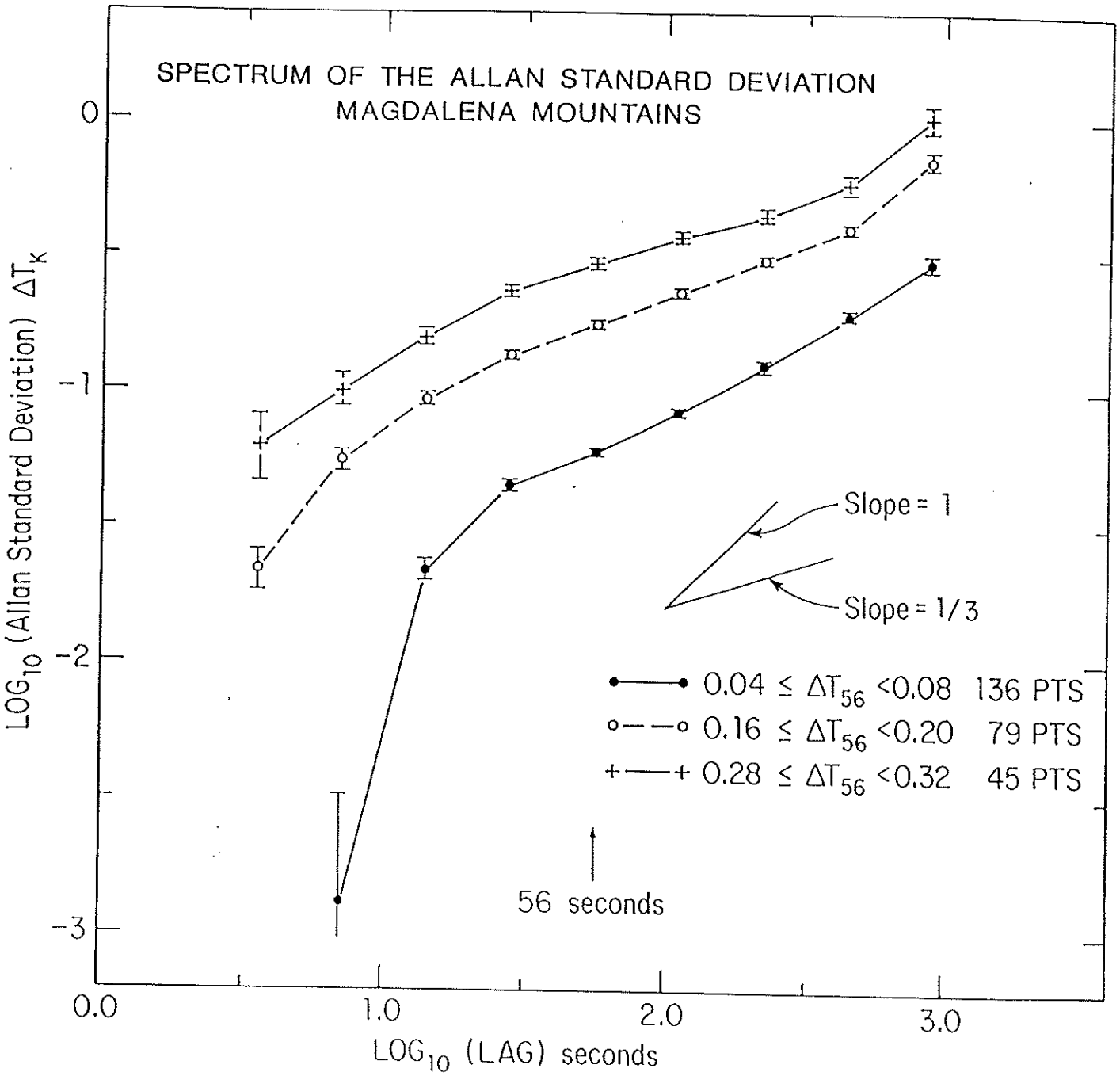
SPECTRUM OF THE ALLAN STANDARD DEVIATION
MAGDALENA MOUNTAINS
LOG10 (Allan Standard Deviation) ΔTK
0
-1
-2
-3
0.0
1.0
2.0
3.0
LOG10 (LAG) seconds
Slope = 1
Slope = 1/3
0.04 ≤ ΔT56 <0.08 136 PTS
0.16 ≤ ΔT56 <0.20 79 PTS
0.28 ≤ ΔT56 <0.32 45 PTS
56 seconds

Figure 6

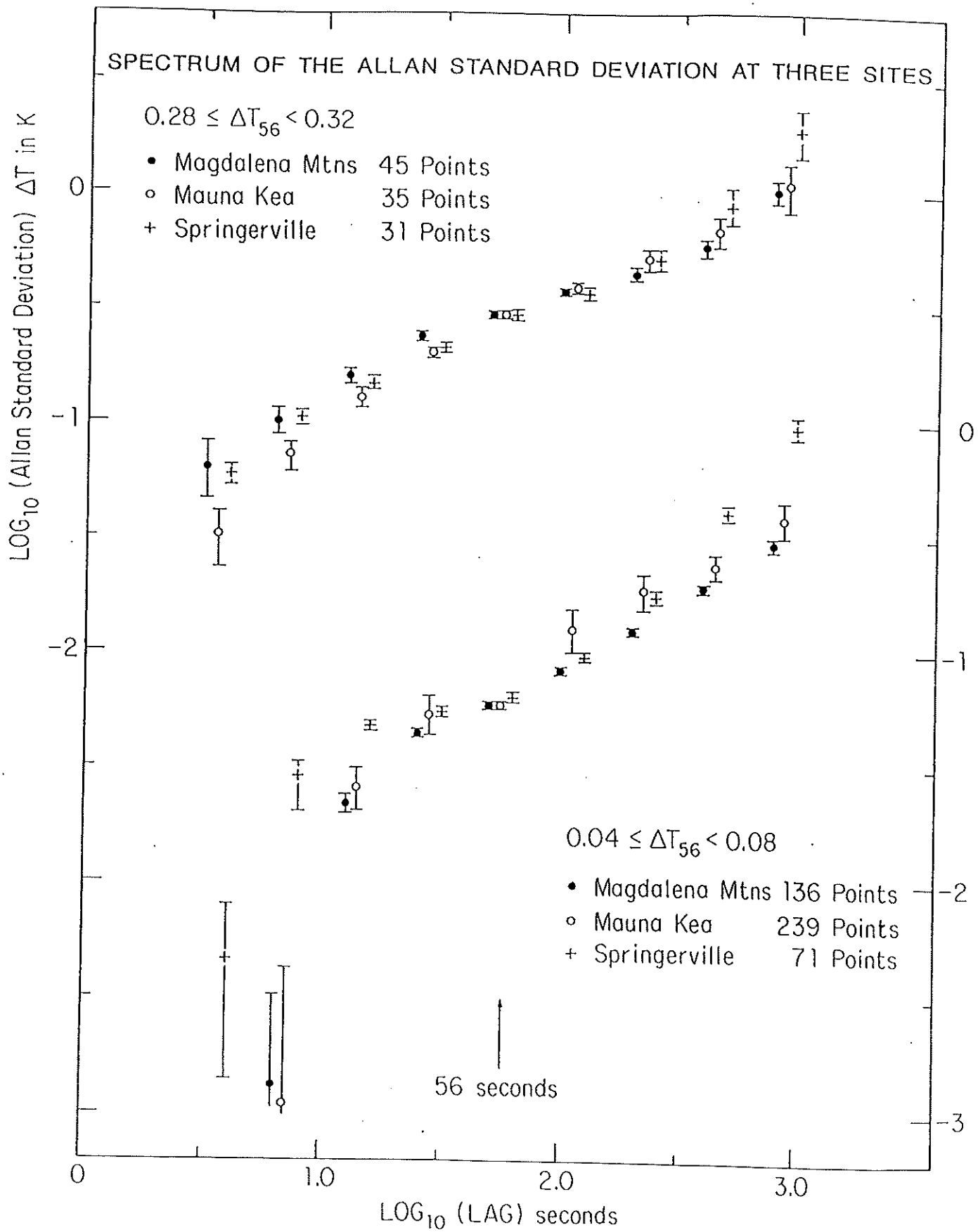
SPECTRUM OF THE ALLAN STANDARD DEVIATION AT THREE SITES
0.28 ≤ ΔT56 < 0.32
• Magdalena Mtns 45 Points
○ Mauna Kea 35 Points
+ Springerville 31 Points
0.04 ≤ ΔT56 < 0.08
• Magdalena Mtns 136 Points
○ Mauna Kea 239 Points
+ Springerville 71 Points
56 seconds
LOG10 (Allan Standard Deviation) ΔT in K
LOG10 (LAG) seconds
0
-1
-2
1.0
2.0
3.0
-3

Figure 7

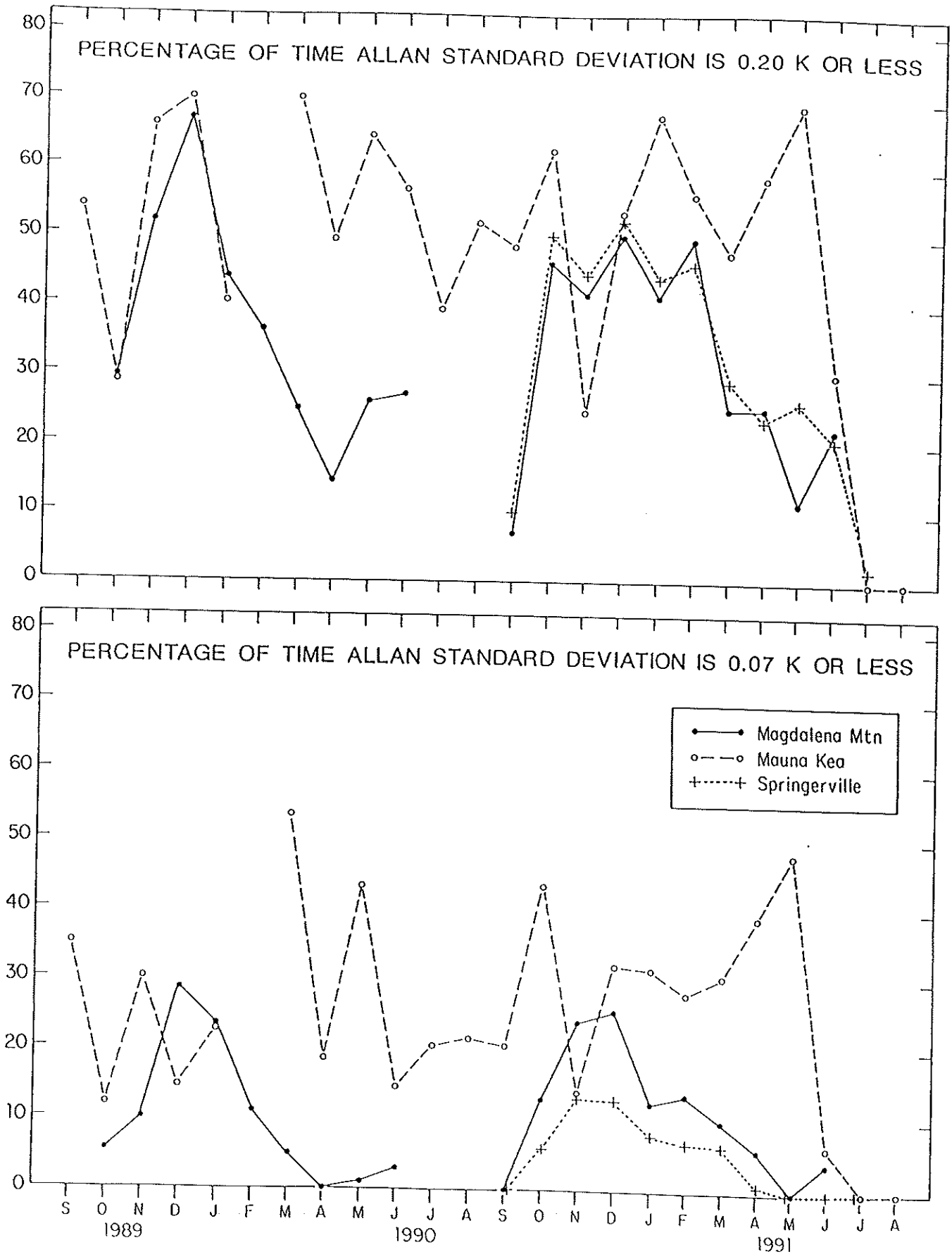
PERCENTAGE OF TIME ALLAN STANDARD DEVIATION IS 0.20 K OR LESS
PERCENTAGE OF TIME ALLAN STANDARD DEVIATION IS 0.07 K OR LESS
Magdalena Mtn
Mauna Kea
Springerville
0
10
20
30
40
50
60
70
80
S O N D J F M A M J J A S O N D J F M A M J J A
1989
1990
1991

Figure 8

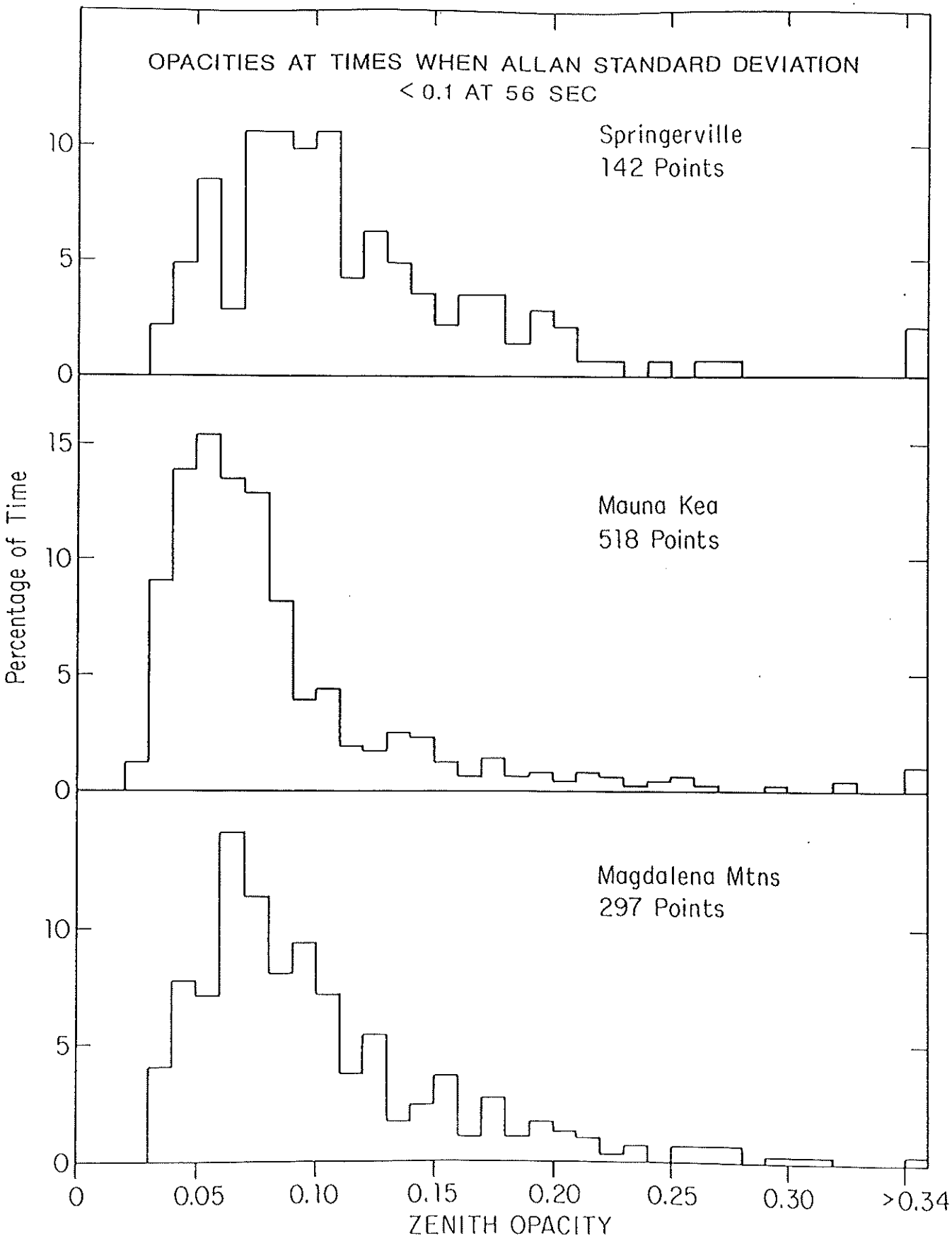
OPACITIES AT TIMES WHEN ALLAN STANDARD DEVIATION
< 0.1 AT 56 SEC
Springerville
142 Points
Mauna Kea
518 Points
Magdalena Mtns
297 Points
Percentage of Time
ZENITH OPACITY
0
0.05
0.10
0.15
0.20
0.25
0.30
>0.34

Figure 9

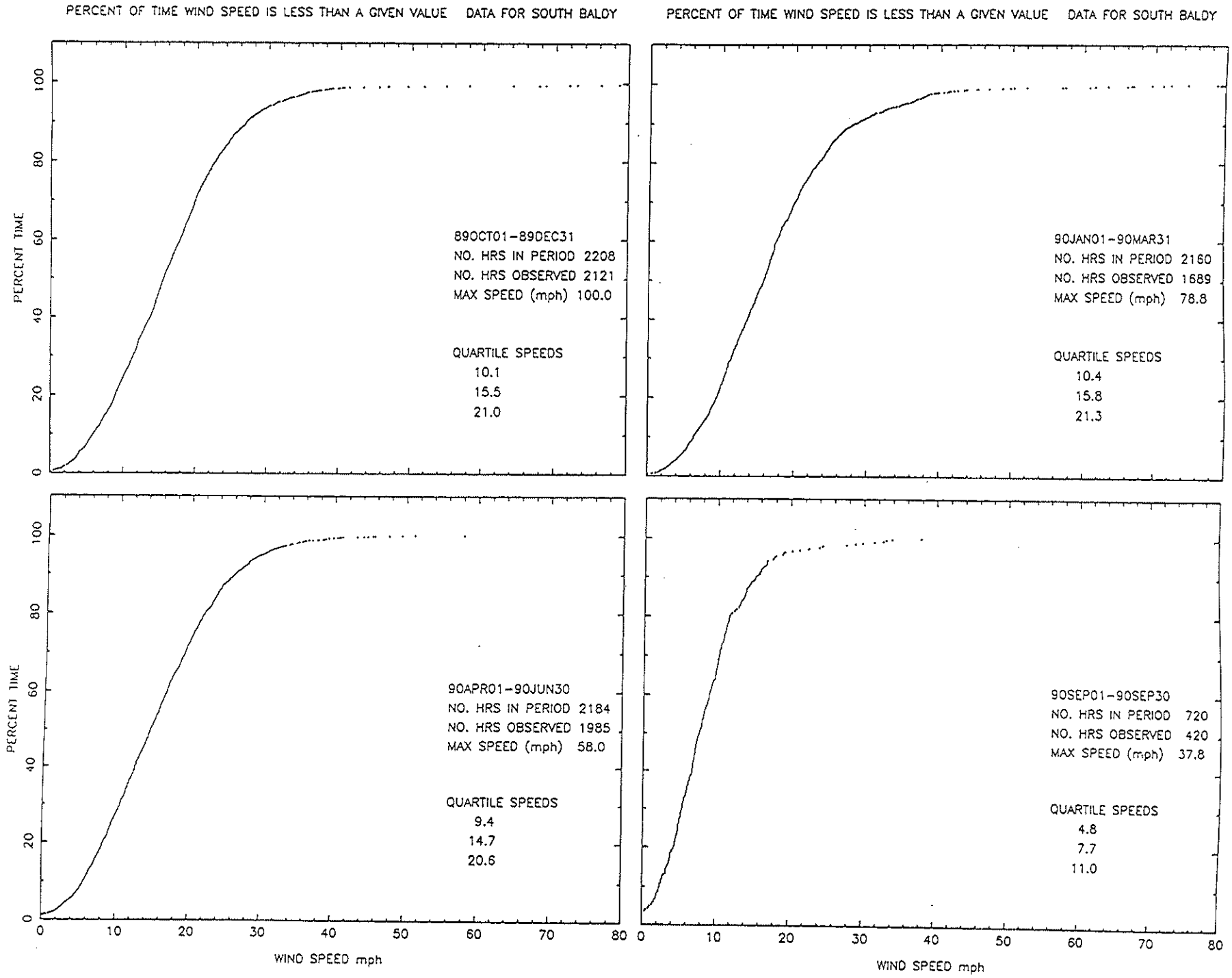
PERCENT OF TIME WIND SPEED IS LESS THAN A GIVEN VALUE DATA FOR SOUTH BALDY
PERCENT TIME
WIND SPEED mph
89OCT01-89DEC31
NO. HRS IN PERIOD 2208
NO. HRS OBSERVED 2121
MAX SPEED (mph) 100.0
QUARTILE SPEEDS
10.1
15.5
21.0
90JAN01-90MAR31
NO. HRS IN PERIOD 2160
NO. HRS OBSERVED 1689
MAX SPEED (mph) 78.8
QUARTILE SPEEDS
10.4
15.8
21.3
90APR01-90JUN30
NO. HRS IN PERIOD 2184
NO. HRS OBSERVED 1985
MAX SPEED (mph) 58.0
QUARTILE SPEEDS
9.4
14.7
20.6
90SEP01-90SEP30
NO. HRS IN PERIOD 720
NO. HRS OBSERVED 420
MAX SPEED (mph) 37.8
QUARTILE SPEEDS
4.8
7.7
11.0

Figure 10a

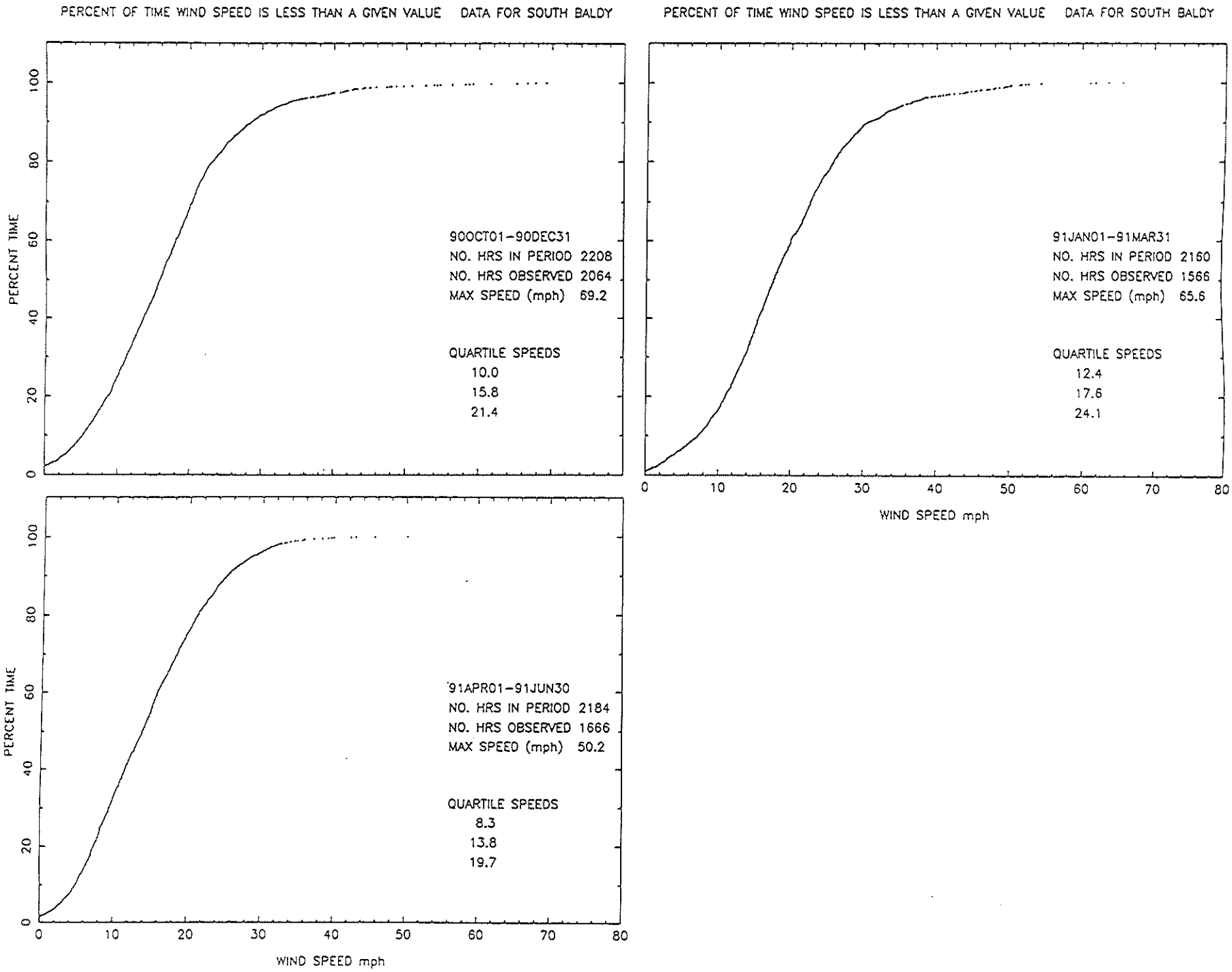
PERCENT OF TIME WIND SPEED IS LESS THAN A GIVEN VALUE DATA FOR SOUTH BALDY
PERCENT TIME
WIND SPEED mph
90OCT01-90DEC31
NO. HRS IN PERIOD 2208
NO. HRS OBSERVED 2064
MAX SPEED (mph) 69.2
QUARTILE SPEEDS
10.0
15.8
21.4
91JAN01-91MAR31
NO. HRS IN PERIOD 2160
NO. HRS OBSERVED 1566
MAX SPEED (mph) 65.6
QUARTILE SPEEDS
12.4
17.6
24.1
91APR01-91JUN30
NO. HRS IN PERIOD 2184
NO. HRS OBSERVED 1666
MAX SPEED (mph) 50.2
QUARTILE SPEEDS
8.3
13.8
19.7

Figure 10a

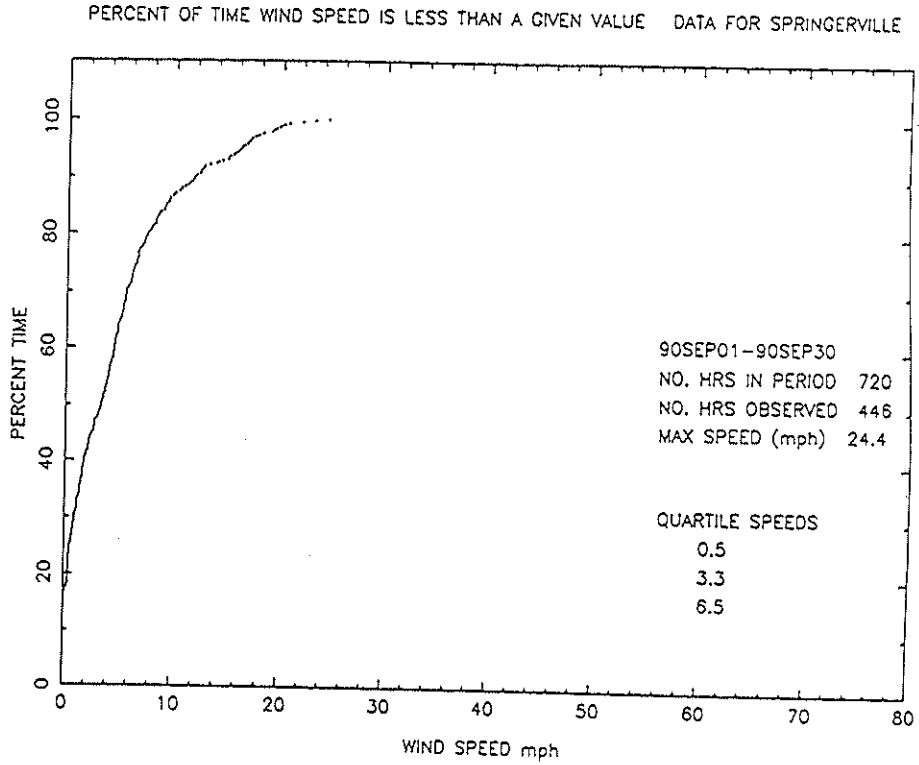
PERCENT OF TIME WIND SPEED IS LESS THAN A GIVEN VALUE DATA FOR SPRINGERVILLE
PERCENT TIME
0
20
40
60
80
100
0
10
20
30
40
50
60
70
80
WIND SPEED mph
90SEP01-90SEP30
NO. HRS IN PERIOD 720
NO. HRS OBSERVED 446
MAX SPEED (mph) 24.4
QUARTILE SPEEDS
0.5
3.3
6.5

Figure 10b

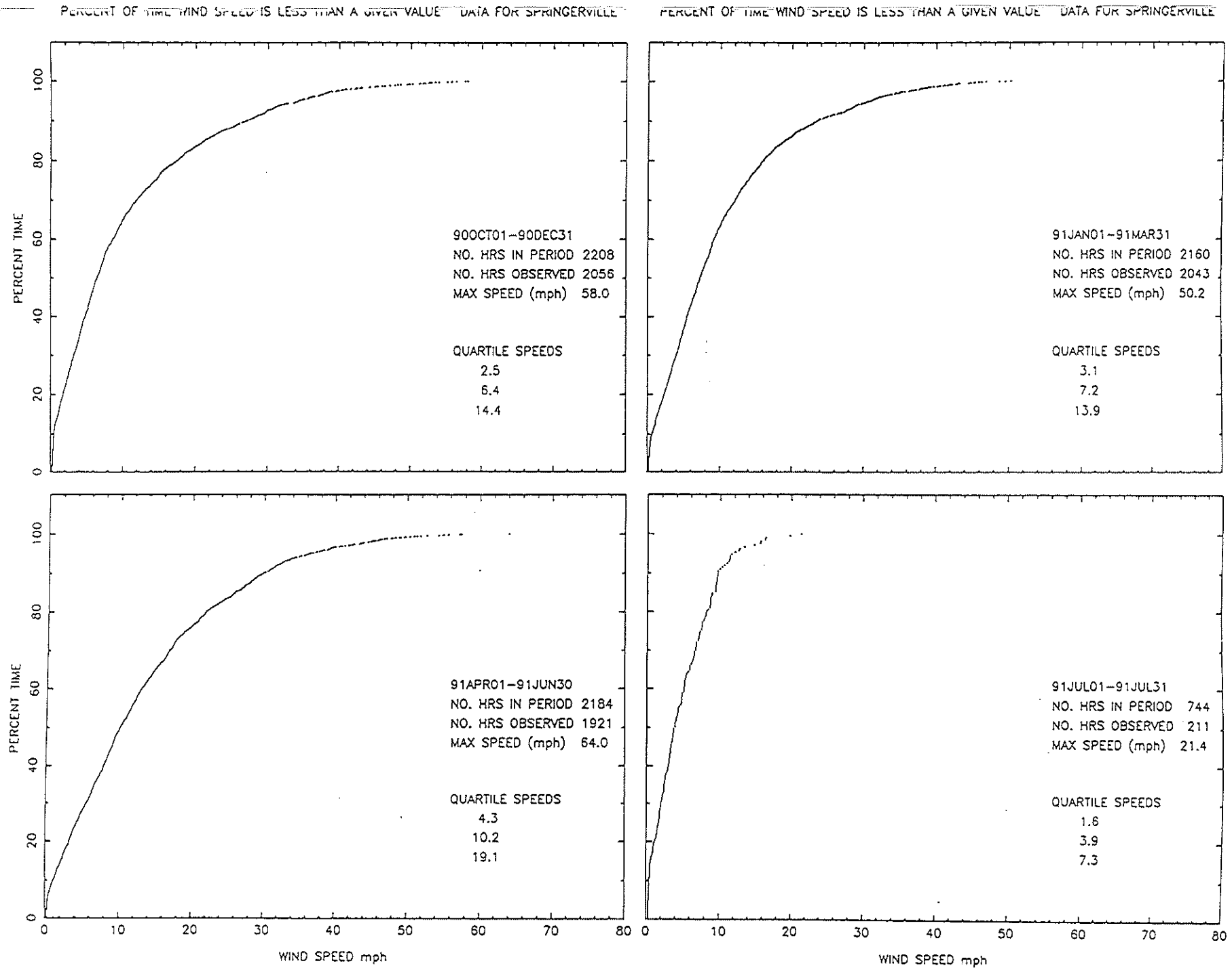
PERCENT OF TIME WIND SPEED IS LESS THAN A GIVEN VALUE DATA FOR SPRINGERVILLE
PERCENT TIME
WIND SPEED mph
900CT01-90DEC31
NO. HRS IN PERIOD 2208
NO. HRS OBSERVED 2056
MAX SPEED (mph) 58.0
QUARTILE SPEEDS
2.5
6.4
14.4
91JAN01-91MAR31
NO. HRS IN PERIOD 2160
NO. HRS OBSERVED 2043
MAX SPEED (mph) 50.2
QUARTILE SPEEDS
3.1
7.2
13.9
91APR01-91JUN30
NO. HRS IN PERIOD 2184
NO. HRS OBSERVED 1921
MAX SPEED (mph) 64.0
QUARTILE SPEEDS
4.3
10.2
19.1
91JUL01-91JUL31
NO. HRS IN PERIOD 744
NO. HRS OBSERVED 211
MAX SPEED (mph) 21.4
QUARTILE SPEEDS
1.6
3.9
7.3

Figure 10b

MILLIMETER ARRAY
MEMO NO. 83

THERMAL CONSIDERATIONS FOR mmA ANTENNAS

James W Lamb
5 May ,1992

1 Introduction

As an open facility the mmA is expected to be heavily scheduled and it is reasonable to expect it to perform within specifications even during the rapid temperature changes which occur on a clear exposed site at dawn and dusk. Furthermore, solar observing is specified as a major capability of the instrument, so special precautions need to be taken to allow high-precision operation during and after pointing at the sun, as well as avoiding damage by the focused IR and visible radiation. This note summarizes and supplements existing information on thermal problems from a variety of sources, and outlines areas to be studied.

A glance at a von Hoerner diagram for telescope structural limits shows that the thermal design of the mmA antennas is of critical importance [1]. The antenna specifications place them close to the limits predicted for a steel structure, for gravitational bending as well as thermal distortion. von Hoerner's calculations were based on a simplified model with assumptions about temperature gradients, etc., so it is necessary to look at the thermal performance in more detail to determine whether special materials or thermal controls will be required. Of the instruments listed in Fig. 1, the

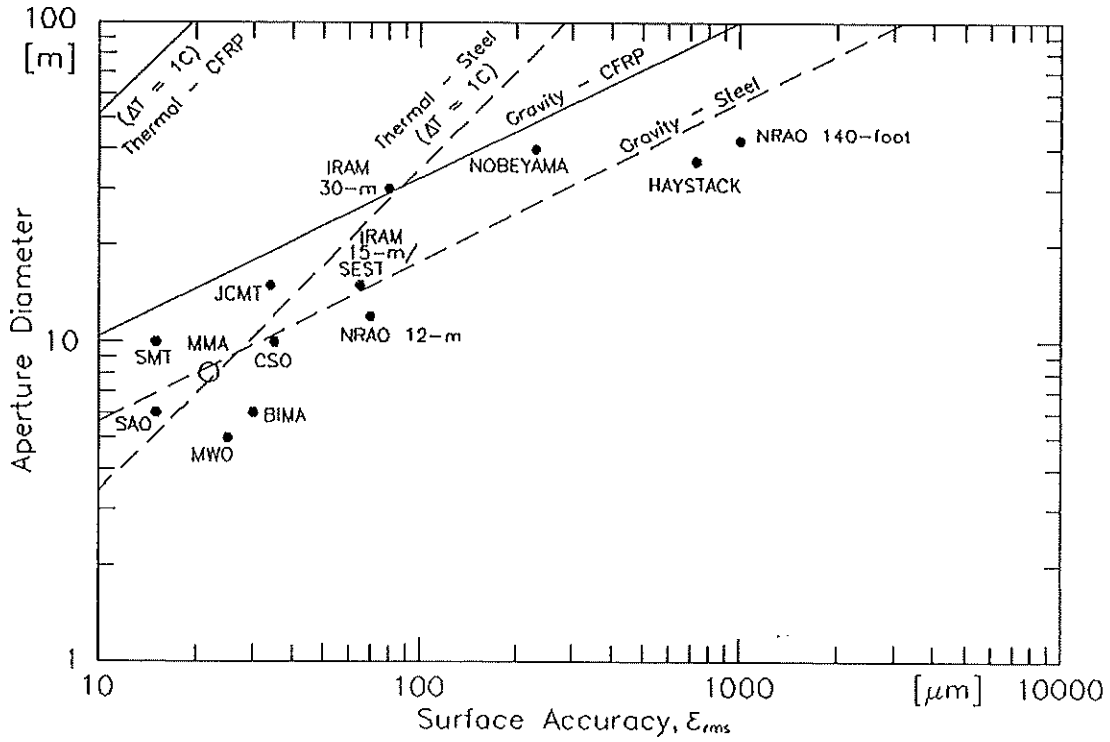

Figure 1 von Hoerner diagram showing achievable surface accuracies as limited by thermal and gravitational effects.

ones which surpass the thermal limit are: the IRAM 30-m, which has thermal controls, the JCMT, which is in an enclosure with adjustable louvers; the SMT which uses carbon fiber and an enclosure; and the SAO, which will probably use carbon fiber. Note that of the last two, the SMT is still under construction and the SAO antennas are in the design stage.

2 Design Options

In principle, it is possible to achieve very good immunity to thermal problems by using low thermal expansion materials such as Carbon Fiber Reinforced Plastic (CFRP). Practical constraints (primarily cost) dictate the use of other materials, however, so the intrinsic thermal performance will be compromised. To meet the specifications other methods of counteracting the thermal errors may be required.

Table I lists some of the design approaches to the thermal questions. The basic design should be made as good as possible within reasonable cost constraints. Although cost will limit the use of low expansion materials, judicious use of these along with suitable insulation and minimization of solar heating could be used to approach the design specifications.

If CFRP is not used further improvement of performance to meet the specifications with either temperature control or active compensation of distortions will probably required. Controlling the temperature could be expensive and complex, but circulation of air to minimize gradients is a possibility. Other options such as removing pointing and focus components of the errors are virtually cost-free, but compensation of these errors requires that they be measured first. Radiometric

Strategy	Methods	Comments	Cost
Basic Design	□ $\alpha \approx 0$	Special materials (Invar, CFRP)	V. High
	□ Insulation	Affects time constants, temperatures	Low
	□ Radiation Control	Paint, Foil	Low
	□ Enclosure	Hard to transport, pack together	High
Active Temperature Control	□ Circulation	Fans, ducts, cladding	Low
	□ Heaters	High Power consumption	Low
Measurement of Errors	□ Radiometric	Periodic, Interrupts observing	Low
	□ Ancillary Instr.	Continuous, Needs development	Mod.
Compensation	□ Active Surface	Complex, Potentially unreliable	High
	□ Re-pointing	No extra hardware required	Low
	□ Re-focusing	No extra hardware required	Low

Table I Strategies for meeting specifications of the antennas under expected thermal conditions.

measurements will be required periodically under any circumstances for atmospheric calibration and can yield information on pointing, focus etc., but direct measurements of the structure will probably be needed to interpolate between or replace some of the astronomical calibrations, as well reducing their frequency and duration, to maintain the highest precision.

Once the errors are measured corrections can be applied. In principle small scale distortions can be corrected with an active mirror, but the high cost and reliability questions make this very undesirable and such errors should be guaranteed small by the fundamental design. Large scale errors can be compensated by re-pointing and re-focusing using mechanisms which will be on the antenna anyway. The challenge lies in developing suitable instrumentation and relating the measurements to focus and pointing models.

3 General Considerations

For the present it will be assumed that the antennas will be operated without any enclosure and will be exposed to the full sun and extreme temperatures. On a typical site the temperatures may be expected to vary by as much as 20 C daily and 50 C annually. As well as changes in absolute temperature there will be gradients within the antenna structure and differences in temperature between antennas, particularly when they are in the large configurations. In the compact configurations the thermal environment of one antenna may be influenced by neighboring ones by shadowing of the sun or shading from wind.

3.1 Materials

The materials which are likely to be considered for major structural parts are listed in Table II along with some relevant thermal data. CFRP and Invar both have very low thermal expansion coefficients, but their expense will limit their use to critical parts of the structure. An attractive feature of CFRP is the possibility of tailoring its properties for different applications. Aluminum has a high thermal expansion coefficient, but its electrical properties make it desirable for the reflector

Property	ASTM A36 Carbon Steel	6061-T6 Aluminum	Carbon-Fiber-Reinforced-Plastic	Invar
Density, ρ ($kg\ m^{-3}$)	7 860	2 700	1 600	8 000
Specific Heat, c_p ($J\ kg^{-1}\ C^{-1}$)	418	962	710	503
Thermal Expansion Coefficient, α ($\times 10^{-6}\ C^{-1}$)	12.7	23.0	0 - 4	0.9
Thermal Conductivity, κ ($W\ m^{-1}\ C^{-1}$)	52	17.2	4.2	16

Table II Thermal properties of suitable structural materials.

surface. Steel has moderate expansion coefficient and conductivity, and its cost, availability and general suitability mean that it should be used in major structural components, such as the mount.

3.2 Heat Sources and Sinks

Solar radiation, which has a maximum flux of about 1.2 kW m^{-2}, is the major heat source. Generally the solar flux on the antenna surfaces will be lower than this because of atmospheric absorption and angle of incidence. Radiated heat to or from ambient will be proportional to the temperature difference, ΔT, between the structure, T_s, and the surroundings, T_0.

$$q = 4\sigma T_0^3 \Delta T \tag{1}$$

where σ is Stephan's constant. For a black body at $T_0 = 290$ K this corresponds to about 5.5 W $m^{-2}C^{-1}$ and will be less for materials with lower emissivity. Radiation to the sky will be larger since the atmosphere is relatively transparent at $\lambda 10$ μm where the peak in the 300 K black-body spectrum lies. Convective heat transfer is dependent on the geometry and orientation of the structure. Natural convection is proportional to $\Delta T^{1\frac{1}{3}}$, while forced convection is proportional to ΔT. Typical cooling rates are of the order of 2-10 W m^{-2} C^{-1}, comparable to the radiative transfer rates to ambient, but the actual value is dependent on the, wind, and temperature.

Another significant source of heat is the dissipation from compressors, air-conditioning units, and electronics, which will amount to several kW.

3.3 Absolute Temperature Effects

Some degradation in performance will result when the mean temperature of the structure changes from that at which the surface was adjusted, or from the temperature at the last calibration of pointing, phase, or focus. Pathlength changes will depend on the thermal expansion coefficients, α, of the materials used, while surface accuracy will depend on differences between expansion coefficients of different materials. Pointing will be unaffected in a symmetrical antenna. Expansion coefficients for several typical materials are given in Table II. Values of α are around 10^{-5} C^{-1} so that a structure of order 10 m will experience pathlength changes of about 100 μm C^{-1}. Temperature differences between antennas should not vary by more than about 0.1 C hr^{-1} to maintain phase stability of better than 10 μm hr^{-1}

3.4 Temperature Gradients

Temperature gradients can have severe effects on pointing and surface accuracy. The effects will be proportional to the expansion coefficients, α, and temperature gradients, ∇T.

3.5 Thermal Time Constants

Thermal time constants characterize the rate at which heat is distributed through or removed from a body. An intrinsic time constant, τ_i may be defined which describes the rate of change of

temperature of a body when it is limited by the thermal conductivity of the material. For a body of characteristic size L_c , thermal conductivity κ, density ρ, and specific heat c_p, τ_i is given by [2]

$$\tau_i = \frac{\rho c_p L_c^2}{4\kappa} \tag{2}$$

When the rate of change is governed by the rate, h, at which heat can be removed from the body an extrinsic time constant, τ_e, can be defined as

$$\tau_e = \frac{\rho c_p L_c}{h} \tag{3}$$

When $\tau_e \gg \tau_i$ the overall time constant is independent of the thermal conductivity of the material. This will be true when

$$L_c < \frac{4\kappa}{h} \tag{4}$$

For a heat transfer coefficient of 4 W m^{-2} C^{-1} the right hand side is about 50 m for steel and 5 m for CFRP.

3.6 Analysis

It is convenient to break the antenna down into parts for analysis: mount, backing structure, primary surface, secondary reflector and its support. These can be considered individually but their mutual influences also have to be studied. In a properly designed structure the interactions between major components should be minimized and well defined.

4 Mount

Steel is the preferred material for the mount, though it has a moderately high expansion coefficient of $\alpha_{steel} = 12\times10^{-6}$ C^{-1}. Uniform temperature changes produce pathlength changes, while gradients cause pointing offsets. If the mount has a height h and width w then the tilt for a temperature change ΔT is approximately

$$\beta = \frac{\alpha_{steel} h \Delta T}{w} \approx \frac{2.5 h \Delta T}{w} \quad [arcsec] \quad for\ steel \tag{5}$$

Typically $h \approx w$ so that temperature differentials need to be less than 0.1 C to keep the pointing offset less than 0.25 arcsec. Clint Janes has measured temperature distributions on VLA and VLBA antennas using an IR camera [3]. He measured 4 to 5 C differences vertically in the yoke on a VLA antenna, and 0.25 C along a beam at the base of a VLBA antenna. While those antennas are considerably larger than the proposed mmA design, the results give an estimate of the magnitude of the gradients which can exist. Bregman and Casse [4] predicted temperature differences of 22 C across the JCMT design if it were unenclosed with no insulation. This would drop to 5.1 C with appropriate insulation. Clearly, to make the mount intrinsically accurate will involve very careful precautions to keep the temperature uniform.

Uniformity may be achieved by minimizing the heat flux into and out of the mount and by making the time constant long compared to the rate of change in heating by the sun, etc. The thermal time constant for heat to be transferred from one side of the structure to the other is approximately

$$\tau_t = \frac{\rho c_p w^2}{4\kappa_{steel}} \tag{6}$$

where ρ and c_p are for steel. If $w = 4$ m this gives $\tau_i = 3.3$ day, so that the structure will never come close to equilibrium during the diurnal solar heating cycle if one side of the mount is significantly heated. The time it takes to heat one side of the structure through a layer of insulation with thermal conductivity κ_{ins}, and thickness t_{ins} is about

$$\tau_e = \frac{\rho c_p t_s t_{ins}}{\kappa_{ins}} \tag{7}$$

where t_s is the thickness of the steel members, Taking $t_s = 13$ mm and $\kappa_{ins} = 0.05$ W m^{-1} C^{-1} indicates that the insulation thickness should be about 350 mm with a corresponding heat transfer rate of 0.14 W m^{-2} C^{-1}.

Alternatively, some pointing deviations can be accepted provided that they are calibrated out by some means. If β is to be predicted from temperature measurements then the average ΔT also needs to be known to an accuracy of about 0.1 C. A brief look at commercial temperature sensors shows that resolutions of this order are typical, although accuracy is generally a few tenths of a kelvin. Probably a few (e.g. 4-8) sensors would be used on each side of the mount so that the effect of statistical variations will be reduced. Thermistors with tolerances of ±0.05% over a range of 50 C are available, so this method seems feasible.

Another possibility is to measure the relative movements of the structure directly using lasers, or CFRP rods as temperature stable distance measures. The end of the rod would have a displacement transducer which would measure the relative motion of part of the structure. This would require a length measurement accuracy of

$$\Delta l = w\beta \tag{8}$$

For $\beta = 0.25$ arcsec and $w = 2$ m, Δl will be 2.5 μm. The range would be

$$R = h\alpha\Delta T \tag{9}$$

which for $\Delta T = 50$ C, $h = 2$ m, $\alpha = 12\times10^{-6}$ C^{-1} is 1.2 mm, giving a dynamic range of 500. This accuracy and range is achievable with an LVDT, for example.

Tilts may also be measured directly with a commercial electronic tiltmeter. If these devices are placed above the azimuth bearing, radial forces due to tracking at sidereal rates will give errors of order 10^{-4} arcsec which is quite negligible, but settling times after slewing may be a problem. The tiltmeter should be located as close to the azimuth axis as possible to minimize this.

Temperature differences between antennas will introduce a differential pathlength error. This will be calibrated out if it is constant, but could be important if it is variable. To hold the rate of change of pathlength below 10 μm hr^{-1} the differential rate of temperature change between antennas

must be less than about 0.2 C hr^{-1}. This will depend on the topography as well as the antenna design. If the mount time constant is made sufficiently long it may not be a problem.

5 Backing Structure

There are several approaches to minimizing the thermal effects in the backing structure. These may be divided into three groups. (a) the structure may be made insensitive to temperature changes and gradients (e.g. the SMT which uses CFRP with a very low expansion coefficient), (b) the temperature gradients (and/or temperature) may be controlled to a high degree (e.g. IRAM 30-m antenna has fans in the backing structure and active thermal control of the secondary mirror support legs), or (c) a combination of (a) and (b). In addition, measurements of temperature or position on the structure will allow compensation of some of the focusing and pointing terms. Another form of thermal control is to use an enclosure, such as a radome or astrodome. For the present we will ignore the possibility of a enclosure because of the added difficulties in transportation and close-packing of antennas.

Space frames appear to be the best choice for backing structures. These are relatively simple to analyze accurately and can easily be made from combinations of different materials such as CFRP and steel. This type of structure will be assumed in the following discussion.

5.1 Estimates of Distortions

To get some understanding of whether an active temperature control system is required for the mmA we need to estimate the magnitude of some of the thermal effects. Some elementary calculations have been done using the model in Fig. 2*a* for the backing structure. A radial rib is represented as a plane lattice framework, where the expansion coefficients of the radial and transverse members are allowed to be different, α_r, and α_t, respectively. A gradient from the front to the back of the reflector tends to warp it as shown in Fig. 2*b*, while gradients along the rib will tend to cause a change in thickness (Fig. 2*c*). Local inhomogeneities can potentially have quite damaging effects

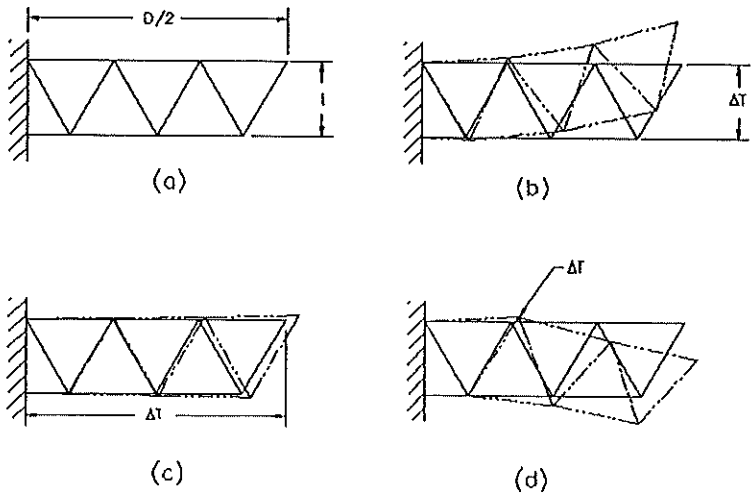

Figure 2 Model structure used in the calculations. a. Undistorted, b. Gradient through rib, c. Gradient along rib, d. Local gradient.

as they affect large parts of the structure through some type of lever action. The size scale of these is such that refocusing or repointing cannot remove them. Several specific cases are now considered.

Fig. 3 shows the temperature distributions over the reflector which will be considered along with the appropriate distribution from Fig. 2.

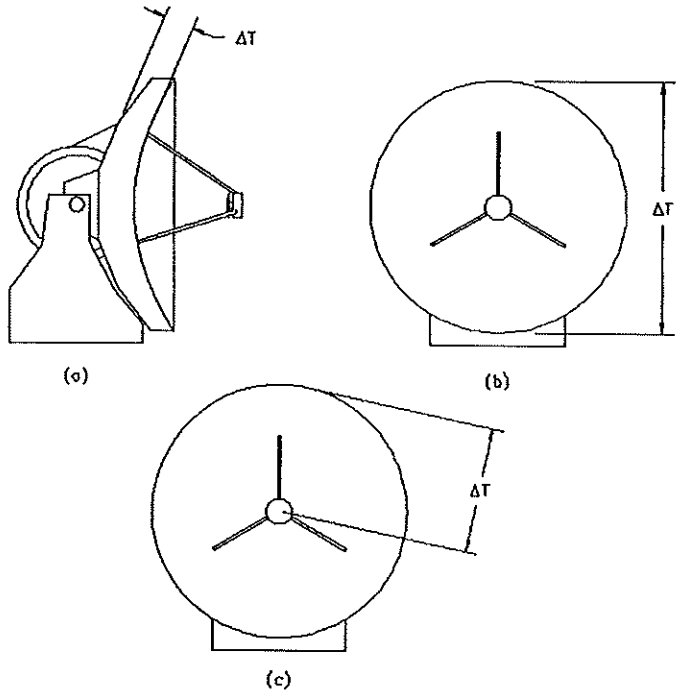

Figure 3 Temperature distributions considered in text. a. Front-to-rear, b. Top-to-bottom, c. Radial.

Case I: Assume a linear gradient, ΔT, from the front to the rear of the reflector (Fig. 2*b*, Fig. 3*a*). This causes the rib to bend and produces a focus change of

$$\frac{\Delta f}{f} = \frac{2f\alpha_r \Delta T}{t} \tag{10}$$

without any degradation to the surface accuracy. If the time-constant of the change is short compared to the interval between focus checks there will be a focusing loss which will be roughly equivalent to a degradation of surface accuracy of

$$\epsilon_{df} \approx \frac{0.02}{(f/D)^2}\Delta f \tag{11}$$

Of course, the movement of the secondary must also be considered, and it may increase or decrease this depending on the temperature distribution and properties of the support legs.

As a check, take the following numbers as being representative of the SAO 6-m design [5]. $f = 2.5$ m, $t = 0.7$ m, $\alpha_r = \alpha_{CFRP+steel} = 3\times10^{-6}$ C^{-1}, $\Delta T = 2$ C. This yields $\Delta f = 110$ μm which compares favorably with the finite element analysis value of 54 μm, considering the simplifications used. For numbers more appropriate to the mmA take $f = 3.2$ m, $t = 1$ m, $\alpha_r = 12\times10^{-6}$ C^{-1} for which

the change in focal length of the primary is $\Delta f = 250\ \mu m\ C^{-1}$. If the secondary mirror is not refocused this leads to an equivalent surface error of $\epsilon_{eff} = 30\ \mu m\ C^{-1}$. Replacement of the steel with CFRP could reduce this by a factor of 4 to 8.

Case II: Assume a linear temperature gradient of $\Delta T/D$ across the aperture, Fig. 2*c*, Fig. 3*b*. To a first approximation this induces a beam squint of

$$\Delta\theta = \frac{\alpha_t t \Delta T}{2D} \tag{12}$$

with no contribution to the surface error. For the SAO design $\alpha_t = 12\times10^{-6}\ C^{-1}$, $t = 0.7$ m, $\Delta T = 2$ C, and $D = 6$ m, so that $\Delta\theta = 0.3$ arcsec which is of the same order as the finite element analysis value of 0.7 arcsec. Using $\alpha_t = 12\times10^{-6}\ C^{-1}$, $t = 1$ m, $D = 8$ m gives $\Delta\theta = 0.75$ arcsec C^{-1}.

Case III: Assume a linear radial gradient of $2\Delta T/D$ along all the ribs, Fig. 2*c*, Fig. 3*c*. This produces a focusing error of approximately

$$\frac{\Delta f}{f} = 10\frac{f t \alpha_t \Delta T}{D^2} \tag{13}$$

and an rms surface error which is of order

$$\epsilon = \frac{\alpha_t t \Delta T}{40\sqrt{2}} \tag{14}$$

Taking $\alpha_t = 12\times10^{-6}\ C^{-1}$, $t = 1$ m, $f = 3.2$ m, $D = 8$ m, gives $\Delta f = 18\ \mu m$ and $\epsilon = 0.2\ \mu m\ C^{-1}$. With no refocusing there would be an additional equivalent surface error of $\epsilon_{eff} = 2\ \mu m\ C^{-1}$.

It is clear, then, that these large scale distributions cause changes which can be largely removed by repointing or refocusing, provided that they can be calibrated either astronomically or by ancillary instrumentation. Obviously there will be higher order terms which are not represented in this analysis but which will appear in a numerical model of a specific structure. This analysis should at least give some kind of upper bound on those terms, which will probably be an order of magnitude smaller. More complicated temperature distributions, such as shown in Fig. 2*d*, cannot be easily analyzed analytically, but it may be expected that these would produce more severe distortions of the surface figure. In general, the smaller the spatial scale of the temperature gradients the less effect on pointing and the greater the effect on the surface accuracy so that local sources of heating should be avoided.

The primary heat sources for the backing structure are direct solar radiation, indirect solar heating *via* the panels, ground radiation, and dissipation from compressors, electronics, etc. The interactions between these can be manipulated to some extent. For example, it will be worthwhile looking at treatment of the rear of the panels and selection of panel mount conductance so that the backing structure is heated uniformly by convection and radiation from the panel rear surface rather than locally at the mounting points. This will also ensure that there are no large gradients along a panel.

5.2 Thermal Time Constants

Generally the time constants of the structure will be determined by the heat capacity of the material and the rate at which heat can be removed from the members (the extrinsic time constant). Equation (3) can be used with the thickness of the members, t, as the characteristic length. All members should have a similar thickness to keep the time constants uniform. From this point of view

the "box" type of structure, such as used on the NRAO VLA and 12-m antennas for the central part of the backing structure is preferable to the "strong ring" support used on the Bonn 100-m and the JCMT, for example. For typical values take a thickness of 4 mm and a heat transfer rate of 8 W m^{-2} K^{-1}. For steel this gives τ_e = 0.45 hr, and for CFRP, τ_e = 0.16 hr.

The time constants can also be used to estimate the spatial extent and distorting effects of local heating. Consider a part of the backing structure which is heated at one end at a rate q, such as a tube heated through a panel support. The heat will diffuse a distance l down the member in a time τ_i given by equation (2)

$$\tau_l = \frac{\rho c_p l^2}{4\kappa} \tag{15}$$

The rate at which heat is removed from the walls is given by the extrinsic time constant (equation (3)),

$$\tau_e = \frac{\rho c_p t}{h} \tag{16}$$

The temperature gradient along the member will be over a distance of order l_0, which is found by setting $\tau_e = \tau_i$ to give

$$l_0^2 = \frac{4\kappa t}{h} \tag{17}$$

For a thickness of 4 mm and heat flow h = 8 W m^{-2} K^{-1} this is 0.35 m and for CFRP it is 0.11 m. These relatively small scales indicate that the backing structure will come to equilibrium by exchanging heat with the surroundings rather than by conduction through the material itself. Over this distance the temperature change will be about

$$\Delta T = \frac{q}{p l_0 h} \tag{18}$$

where p is the perimeter distance of the tube, and the length change will be

$$\Delta l = \alpha \Delta T = \frac{\alpha q}{p\sqrt{4\kappa t h}} \tag{19}$$

Values obtained from this equation cannot be expected to be accurate, but it should at least be useful for comparing different materials. The ratio for two materials denoted by subscripts 1 and 2 is

$$\frac{\Delta l_1}{\Delta l_2} = \frac{\alpha_1}{\alpha_2}\sqrt{\frac{\kappa_1}{\kappa_2}} \tag{20}$$

For steel and CFRP this ratio is about unity, so that the relatively low thermal conductivity of the CFRP is not a disadvantage.

5.3 Expected Temperature Gradients

There is little detailed information on temperature distributions in antenna structures available, though there are some sources which give partial measurements. It should be noted that gradients need to be known with a resolution of 0.1 C or better. Akabane [6] reports some temperature distributions in the Nobeyama 45-m antenna which give average temperature gradients radially along the ribs of 0.13 C^{-1} m^{-1} (day time), and -0.09 C^{-1} m^{-1} (night time) with forced air circulation at a rate of about 1.5 m s^{-1} in the backing structure. In terms of an 8 m antenna this translates to about a 1 C gradient across the aperture which is not negligible. Akabane's data also show differences of 0.5 C (day) and 0.3 C (night) between the front and rear of the backing structure, also a significant amount. For these temperature distributions the computed contribution to the surface error is 50 μm (day) and 30 μm (night). The temperature distribution is apparently not a simple gradient and there is some scatter among the nodes which were monitored. For example, there are a few nodes on the front surface which have the same temperature as those on the rear while most are significantly different. It is not stated what the accuracy of the measurements, but if it is not a calibration uncertainty then these nonuniformities probably contribute substantially to the surface error budget. Akabane also describes a 6 m diameter antenna of steel and aluminum which exhibits temperature differences of 20 C (day) and 5 C (night), leading to severe variations in the antenna efficiency.

Greve *et al.* [7] describe the thermal design of the IRAM 15-m and 30-m antennas. The 15-m antennas have a mixed CFRP/Steel backing structure with thermally insulating rear cladding. Individual sensor data are not given but differences between the averages of sensors on the upper half of the dish and the lower half vary from about 2 C at night to 12 C during the day. There are rms temperature variations of about 1 C at night and 2 - 3 C in the day. The 30-m antenna is steel with insulation and tangential airflow of several m s^{-1}. Variations in temperature with an rms between 0.3 C and 2 C were recorded in backing structure.

The above results demonstrate that even with active thermal control significant thermal gradients can exist within the backing structure. Diurnal variations are seen in all the measurements with most of the changes taking place over a couple of hours near sunrise and sunset. If the structure is thermally sensitive there will be significant focusing and pointing shifts which will reduce the antenna efficiency if they are not compensated for. Either temperature control or monitoring of the changes will be required if full accuracy is to be maintained over this period when the change is too rapid for focusing and point calibrations to be effective.

6 Panels

Several types of panel have been used or proposed for millimeterwave and sub-millimeterwave antennas. These include: aluminum skins with aluminum ribs epoxied on the rear (eg ESSCO panels on the 12-m, U. Mass Antennas); aluminum honeycomb with aluminum facings (eg JCMT); aluminum honeycomb with CFRP facings (eg SMT, IRAM 15-m); cast, machined aluminum (eg BIMA 6-m antennas); and CFRP honeycomb with CFRP facings. These all have different thermal properties which must be taken into account when choosing the type and dimensions of the panels.

Thermal effects may be divided into absolute temperature (T) effects, and gradient (ΔT) effects. These effects can be quite complex in detail and depend on the construction and materials of the panels, the method of mounting them, and the temperature distributions. Some simplifications can be used to estimate the relative merits of different panel types.

6.1 *Absolute Temperature Effects*

Consider first the absolute temperature effects. Clearly, if the panels and backing structure are made from the same material then a change in temperature will require (at most) refocusing the secondary. If there is a difference in temperature between the backing structure and the surface panels, or they have a different expansion coefficient the curvature of the panels will not match that of the backing structure and there will be a contribution to the surface error budget.

To estimate the magnitude of this effect, assume that the backing structure has a expansion coefficient of α_b, and that the panels are homogeneous and isotropic with a expansion coefficient of α_p. Further assume that the panels are supported at their front surfaces at the edges and that the typical linear size of a panel is d_p. It may then be shown that the rms surface error is approximately

$$\epsilon = \frac{|(T_p - T_0)\alpha_p - (T_b - T_0)\alpha_b|}{8\sqrt{3}R_0} \qquad (21)$$

T_p and T_b are the panel and backing structure temperatures and T_0 is the temperature at which the surface was set. R_0 is the panel radius of curvature (averaged over the sagittal and tangential directions) and depends on the focal length of the primary mirror.

For an 8 m diameter antenna with a focal ratio of 0.4 the radii of curvature at a 2 m radius on the aperture are 6.7 m and 7.4 m, so the average value is about $R_0 = 7$ m. For material expansion coefficients take $\alpha_{CFRP} = 2\times10^{-6}\ C^{-1}$, $\alpha_{Al} = 23\times10^{-6}\ C^{-1}$, $\alpha_{steel} = 12\times10^{-6}\ C^{-1}$.

Case I: CFRP backing structure, aluminum panels.

$$T_p = T_b = T_0 + 30\ C$$

then

$$\epsilon = 7\ \mu m \times d_p^{\,2} \qquad d_p \text{ in m}$$

eg 7 μm for a 1 m panel, 1.5 μm for a 0.5 m panel.

Case II: Steel backing structure, aluminum panels.

$$T_p = T_b = T_0 + 30\ C$$

then

$$\epsilon = 2.5\ \mu m \times d_p^{\,2} \qquad d_p \text{ in m}$$

eg 2.5 μm for a 1 m panel, 0.6 μm for a 0.5 m panel.

Case III: Steel backing structure, aluminum panels.

$$T_b = T_0,\ T_p = T_0 + 10\ C$$

then

$$\epsilon = 2.3\ \mu m \times d_p^{\,2} \qquad d_p \text{ in m}$$

eg 2.3 μm for a 1 m panel, 0.6 μm for a 0.5 m panel.

6.2 *Gradient Effects*

A thermal gradient between the front and back of the panel will cause it to warp. For a uniform panel with an expansion coefficient of α_p the change in curvature is

$$c = \alpha \frac{\Delta T}{t} \tag{22}$$

For a given thermal flux, I, and thermal conductivity, κ, the temperature difference will be

$$\Delta T = \frac{It}{\kappa} \tag{23}$$

so that the curvature is

$$c = \frac{\alpha_p I}{\kappa} \tag{24}$$

i.e. *independent* of panel thickness. Table III shows values of α_p/κ for typical materials.

Material	α (C^{-1})	κ (m C^{-1})	α/κ (m^{-1})
Aluminum	23×10^{-6}	156	1.5×10^{-7}
CFRP	$0 - 5\times10^{-6}$	4.2	$0 - 12\times10^{-7}$
Carbon Steel	12×10^{-6}	52	2.3×10^{-7}
Invar	0.9×10^{-6}	16	5.6×10^{-8}

Table III Some thermal properties of common materials.

6.3 *Estimated Gradients*

It is difficult to make accurate estimates of actual temperature distributions, and numerical studies and measurements will be required for definitive answers. It is, however, possible to make some rough estimates of the thermal flux through a panel.

Assumptions are as follows: direct solar flux of 1.2 kW m^{-2}; emissivity for solar flux, 0.3; ambient temperature, 290 K; infra-red emissivity, 0.08. Heat input to the panel is from the solar flux on the front surface and radiation from ambient on the rear. Heat outflow is from thermal radiation and natural convection on both surfaces, and it is assumed that the conduction through the supports is about 0.5 W K^{-1}. With some reasonable assumptions about convective heat transport [8] the energy balance equation may be solved to yield a thermal flux through the panel of about 140 W m^{-2}.

For an aluminum panel of 1 m size the rms surface accuracy would be about 1.5 μm. If the panel has stiffening ribs on the rear the convective dissipation on the rear surface could increase with a corresponding increase in the gradient, though probably by a factor of only about 2 at most , which would still be acceptable. If the ribs were made separately and bonded using epoxy the thermal resistance at the bond line could be a significant problem. A panel made from aluminum skins on an aluminum honeycomb will have an rms which is greater than that of a solid one by a factor m, where m is the inverse of the fractional filling of the aluminum in the honeycomb. Typically this may range from 10 to 80, so that this type of panel could be as bad as 15-120 μm. Unless a suitable surface treatment to reduce the solar absorption was used this construction must be ruled out as a possibility. Panels of mixed materials are hard to analyze, but for a crude estimate for CFRP panels with aluminum honeycomb assume that the expansion coefficient of the CFRP is modified by the aluminum to give the value estimated by Delannoy [9] to be about 4.5×10^{-6} C^{-1}, and the conductivity to be that of the aluminum honeycomb, which gives $\alpha/\kappa = 2.9 \times 10^{-8} \times m$ m W^{-1}. The rms for a 1 m panel is then $0.3\times m$ μm. It is therefore comparable to a cast aluminum panel for $m \approx 5$. A CFRP panel with CFRP honeycomb would be perfect if α were adjusted to zero, but for $\alpha = 2\times10^{-6}$ C^{-1} the accuracy for a 1 m panel would be $2 \times m$ μm. Some current designs for CFRP panels have highly reflective surfaces so that the flux calculation given above will be an over estimate, and ϵ would be correspondingly smaller. It should also be remembered, however, that the high reflectivity is not necessarily desirable since much of the energy will be focused towards the secondary mirror and receiver optics during solar observations.

These estimates indicate that an aluminum panel is thermally good, possibly better than a CFRP or CFRP/aluminum-honeycomb one.

6.4 Gaps Between Panels

There will be gaps between panels partly to make mounting feasible, but also to allow for thermal expansion between the panels and the backing structure. If the backing structure is steel and the panels are aluminum the panel gap needs to be about 0.04% of the panel size for a 40 C change in temperature. For a 1 m panel this is about 0.4 mm, but practically the panels would probably be separated by at least 1 mm. This corresponds to an average scattering of about -24dB relative to isotropic.

7 Secondary Mirror Support

Changes in the temperature of the secondary mirror support temperature will lead to changes in pointing and focus. Depending on how the struts are attached to the secondary mirror mount and the backing structure or mount, differential thermal effects could potentially disrupt the surface figure but this may be avoided with careful design. If steel struts are used they would probably need to have air circulated to keep them at equilibrium with the backing structure. This would partially compensate for some of the changes in the backing structure shape with temperature. An alternative would be to make the struts from CFRP, which would be a relatively small part of the overall costs, and avoid the need for any forced circulation. Material with suitably high solar reflectivity would be required.

Shifts in pointing could also be monitored using a laser beam and a quadrant detector, as on the 12-m telescope. If it is possible to locate the quadrant detector behind the secondary, at its center of curvature, pointing offsets due to both lateral shifts and tilts would be measured. It would also be possible to measure the focus position relative to the primary by using a laser ranger such as that developed by J. Payne for the Green Bank Telescope [10]

8 Secondary Mirror

The secondary mirror is subjected to the same thermal gradient problems as the panels. In general the effect will be less as the secondary will generally be at an oblique angle to the sun. In addition, simple changes in curvature may be removed by re-focusing. An exception to this is for solar observing which is discussed more in detail below. Differences in temperature relative to the primary mirror will cause some change in the focus. A difference of 10 C will change the focal length of the secondary by an amount of order 0.05 mm if the mirror is aluminum. This is probably negligible in most cases, especially as it will periodically be refocused.

8.1 Solar Observing

The requirement for observing the sun places heavy demands on the antenna. If the primary diameter is D, the secondary diameter d, the primary mirror reflectivity R, and the solar constant $s = 1.2$ kW m^{-2}, then the power density at the secondary will be

$$I_s = sR\left(\frac{D}{d}\right)^2 \tag{25}$$

Typically, $D/d = 10$ - 20, and $R = 0.6$ - 0.92, so that $I_s = 72$ - 450 kW m^{-2}. The effect on the secondary will depend on the reflectivity of the secondary mirror — if it is small the secondary will be severely affected and if it is large the energy will be transmitted to the receiver optics. Some of the solutions to investigate are to have small scale roughness on the primary to diffuse the power over a range of angles large compared to the angle subtended by the secondary as seen from the primary, or to use a membrane such as Goretex, which is transparent to mm-waves but has a high solar reflectance, over the receiver optics. Hills [11] and Welch [12] have both discussed the role of surface finish in scattering sunlight.

9 Site Dependence

Dependence of thermal effects on different sites is generally rather weak. The main factors are the air density, and the wind speeds which affect the convective cooling. For an extreme change of altitude from 2 km to 4 km the air density falls by about 27%. Natural convection depends on the kinematic viscosity and thermal conductivity of the air and the net difference in cooling between these altitudes is only about 20%. Forced convection is proportional to the thermal conductivity and changes by less than 5% between these altitudes. It is also proportional to $v^{-1/2}$, where v is the wind speed. Considering that the range of elevations of the possible sites is smaller than this it is clear that the site dependence of thermal effects is small compared to the accuracy of the modeling.

A site-dependent effect which could be of importance is the uniformity of temperature variation over the array (particularly in the large configuration), as this will affect the relative phase stability of the antennas.

10 Conclusions

The concept of a simple, reliable, cheap antenna is very attractive. Fabrication using CFRP extensively could satisfy the first two attributes but will probably be relatively expensive, so the limits of more conventional materials has to be investigated in depth.

Clearly there is much to be understood about the thermal design. The mount can probably be well understood and appropriate steps taken to minimize or compensate for thermal effects. Even if gradients cannot be eliminated, the time constant could be made long enough that they are not a problem, Proper account needs to be taken of heating by electronics, compressors, etc.

Analysis of the backing structure is much more complex. To meet the specifications without any compensation for thermal distortions with a steel construction requires thermal gradients across the aperture to be less than a few tenths of a degree Celsius. However, many of the gross thermal effects can be viewed as changes in pointing or focusing and if these can be calibrated or monitored in real time the ultimate limitation becomes the effect of the residuals on the surface accuracy. This relaxes the temperature uniformity needs and it is then not clear that a steel backing structure cannot meet the specifications, even without control of forced circulation.

If the thermal time constants are on the order of an hour astronomical calibrations may not always be frequent enough to remove the systematics, and supplementary instrumentation will be required. Time constants in the backing structure will probably be short (0.1-1 hr) and the changes will be determined by the ambient conditions (0.1-24 hr). Enclosure of the backing structure may increase the time constant, but it might then be necessary to install fans to ensure that no stratification occurs within the enclosure. The mount will have much longer time constants than the backing structure, so it is important to decouple these effectively.

Thermal considerations for panels rule out the aluminum-aluminum honeycomb-aluminum construction but otherwise is not very restrictive on construction. The choice will be based more on cost, and gravitational and wind loading deflections.

Although it is relatively easy to compute what a given temperature distribution has on the structure it is very difficult to predict what that temperature distribution should be, particularly on scales small compared to the aperture diameter. These small scale inhomogeneities will place the ultimate limit on thermal performance. To resolve these questions we need to make measurements on comparable existing structures. We propose to do this on the 12-m antenna and also on one of the new BIMA 6-m antennas. The BIMA antennas are more appropriate since they are not in an enclosure and are more comparable in size to the proposed mmA antennas. This will be done using arrays of thermistors and we also propose to borrow the IR camera from the MMT. Typically, it is expected that temperature differences of tenths of a kelvin will be the maximum that can be tolerated.

Some methods of instrumentation need to be looked at, and experience with the quadrant detectors for the 12-m and the GBT, the laser ranger and auto-collimator for the GBT, and tiltmeters within NRAO and at other institutions should be extended.

10.1 Suggested Thermal Error Budget

For both the panels and the backing structure the thermal errors may have the same form as those due to gravity and wind loading so that their component in the error budget should be more conservative than would be obtained by quadrature addition. It is probably true, however, that the

thermal and wind effects will not be maximum simultaneously since wind tends to smooth out the temperature gradients.

The values in Table IV are therefore suggested as reasonable components for the surface error and pointing:

Surface Error	Panel: Absolute Temperature	3 μm
	Panel: Thermal Gradient	3 μm
	Backing Structure: Thermal Gradient	3 μm
Pointing	Mount: Thermal Gradient (after correction)	0.25 arcsec
	Backing Structure: Thermal Gradient (after correction)	0.25 arcsec

Table IV Proposed thermal components of surface accuracy and pointing error budgets.

11 References

[1] S. von Hoerner: "Design of large steerable antennas", Ap. J. Vol. 72, No. 1, February 1967, pp 35-47.

[2] R. N. Bracewell: *The Fourier transform and its applications*, McGraw-Hill, 1986: New York

[3] C. James: "VLA and VLBA antenna temperature measurements", VLA Test Memo., No. 160., NRAO, December 1991.

[4] J. D. Bregman and J. L. Casse: "A simulation of the thermal behaviour of the UK-NL millimeter wave telescope", Int. J. IR and Millimeter Waves, Vol. 6, No. 1, 1985, pp 25-40.

[5] P. Raffin: "Analysis of reflector back-up structure", Submillimeter Array Tech. Memo., SAO No.51, Sept 1991.

[6] K. Akabane: "A large millimeterwave antenna", Int. J. IR and Millimeterwaves, Vol. 4, No. 5, 1983, pp 793-808.

[7] A. Greve, M. Dan, and J. Penalver: "Thermal design and thermal behavior of mm-wavelength radio telescopes", IRAM Internal Report

[8] E. Guyer (Ed): *Handbook of applied thermal design*, McGraw-Hill, New York, 1989.

[9] J. Delannoy: "The design of high frequency antennas", IAU Coll. 131, 8-12 Oct, 1990.

[10] J. M. Payne, D. Parker and R.Bradley: "A rangefinder with fast multiple range capability", GBT Memo No. 73, NRAO, 1992

[11] R. E Hills: "Detailed results of panel development programme: I Surface finish and 'figure' ", JCMT Report ASR/MT/T/443/REH(83), July, 1983.

[12] W. J. Welch, Private communication.

MILLIMETER ARRAY
MEMO NO. 84

Possible Phase Calibration Schemes for the MMA

M.A. Holdaway
National Radio Astronomy Observatory
Socorro, NM 87801

June 15, 1992

1 INTRODUCTION

The 225 GHz tipping radiometers which were used in the MMA site survey measured the atmospheric opacity and zenith total power fluctuations (Hogg, 1992). In MMA Memo 68 (Holdaway, 1991), I demonstrated how the phase stability can be estimated from the total power time series taken with the tipping radiometer and reported the raw phase stability (with no calibration) for various atmospheric conditions as a function of time and baseline, in essence, the phase structure function. When the rates of occurance of the various atmospheric conditions are folded into the phase stability estimates, we can estimate how much time the MMA could operate productively at high frequencies in each configuration. It was assumed that rms phase fluctuations of 30° would permit the formation of images with reasonable quality. If the phase fluctuations were less than or equal to 30° over the 1 hour simulation period, phase stable interferometry of very weak objects was possible. If phase fluctuations were greater, then selfcalibration was required. For these cases, only sources which are bright enough to be detected in the time over which 30° phase fluctuations occurred were assumed to be observable.

This method for estimating phase stability from the fluctuations in total power radiated by the atmosphere has not yet been verified against simultaneous direct measurements of the atmospheric phase with an interferometer. A set of approximate structure functions parameterized in the Allan standard deviation is presented for the South Baldy site. We compare our phase structure functions with recent literature, and we find that the South Baldy phase structure function is generally consistent with the results from other phase monitoring programs.

Since there is a need for a better understanding of the relationship between the phase structure function and the resulting images, we simulated the effects of the atmospheric phase errors on images using South Baldy's A configuration. Selfcalibration simulations were also performed.

The relationship between the phase structure function and the structure function of the calibrated phase (ie, the dependence of the residual phase errors upon baseline) is derived and used to analyze a number of different calibration schemes. Among the schemes considered by this document are traditional phase calibration, nutating the subreflector between the calibrator and the target source, simultaneous off-axis calibration, phase extrapolation from low to high frequencies, selfcalibration, and measuring the water vapor column density and determining the atmospheric phase by dead reckoning. Each scheme except the last requires some bright

calibration source to track the atmospheric phase fluctuations. The dead reckoning scheme requires a bright calibrator to track slower fluctuations in atmospheric temperature. It is seen that the calibrator list must include sources down to about 0.15 Jy and the calibrator must be reobserved on timescales of <10 s to be highly effective. Methods for collecting such an extensive calibrator list are discussed.

The Springerville atmosphere is reevaluated in light of the promise some of these phase calibration techniques hold. The differences between the two sites which favored South Baldy for long baseline, high frequency observations in MMA Memo 68 (Holdaway, 1991) are deemphasized by the findings of the current work.

2 FUTURE CONFIRMATION OF METHOD WITH DIRECT PHASE MEASUREMENTS

In the winter of 1988-1989, a number of one hour observations of strong point sources were made with the VLA simultaneously with stability measurements made with the tipping radiometer. The VLA was in its A configuration which has baselines ranging from 1 km to 35 km. Unfortunately, with wind velocities of 12 m/s, the 1 hour radiometer stability measurements are sensitive to atmospheric features ranging from about 100-200 m to about 3-5 km. Hence, the VLA's *direct* phase measurements and the radiometer's *indirect* phase measurements have little overlap in their regime of applicability. When the radiometer data is inverted according to the method presented in MMA Memo 68, the predicted interferometer phases agreed with the VLA phases to no better than a factor of two.

A comparison between direct phase stability measurement and indirect phase stability measurement could be performed with the VLA in its C configuration which has baselines ranging from about 100 m to 3 km. However, the LO is only stable to something like a degree of phase per GHz. To see the atmospheric phase noise above the electronic noise requires very large phase fluctuations which only occur during bad atmospheric conditions. Since we are most interested in the atmospheric conditions with very good phase stability, comparison with VLA data may not be meaningful.

For the last six months of the radiometer's operation on South Baldy, the Smithsonian Astrophysical Observatory's 100 m two element interferometer was directly measuring the atmospheric phase at 12 GHz. The SAO interferometer is sensitive to atmospheric features ranging up to about 100 m. The regime of applicability for the direct and indirect phase stability determination methods have very little overlap. At this time, the Smithsonian data has not been analized.

Some of the work presented here makes the assumption that the rms phase is proportional to baseline raised to the 5/6 power for baselines less than about 150 m, but increase more gently for longer baselines, ie, proportional to baseline raised to the 1/3. This is quite consistent with what is seen in other millimeter and centimeter wavelength atmospheric phase fluctuation studies. Sramek (1990) sees a power law which with a median power of about 0.34. However, most of the data were on baselines much longer than 150 m. When only D array data were

used, and observations dominated by instrumental phase instabilities were excluded, the power law steepened to 0.59, arguing for a change in power law on baselines less than 1000 m. Other observations indicate that there is a steep phase power law for short spacings. For example, the 100 m interferometer on Mauna Kea (Masson, 1991) typically sees power laws of 0.75. The IRAM Interferometer, observing on baselines of 24-288 m, find the average power law to be 0.71. IRAM sees a power law of 0.92 during the day and 0.55 during the night. The steep power law is consistent with what we see on short baselines, Sramek's long baseline power law is consistent with what we see on long baselines, and the IRAM nighttime result is consistent with what we see during the very best conditions, which are likely at night. Keep in mind that in all of these studies there is a fair amount of scatter in the power law exponents, and that the average power law represent a trend.

Both the SMA and IRAM are measuring phase stability on the steep part of the structure function. However, they are extrapolating the steep power law to longer baselines to estimate the utility of future long baseline, high frequency expansions of their arrays. If the phase fluctuations increase less steeply with baseline for longer baselines, then these phase stability estimates are unnecessarily pessimistic.

2.1 PARAMETERIZED PHASE STRUCTURE FUNCTION

Some of the calculations in the following sections estimate the calibrated phase in terms of the phase structure function at some baseline relevant to the calibration process. (The phase structure function is defined as the variance of the phase over long times as a function of baseline, so the RMS phase error is the square root of the phase structure function.) The calculation of the relevant baseline is independent of the model used for the atmosphere and the phase structure function. However, to convert this baseline into an RMS phase error (after calibration), we must know the phase structure function. For this reason, we present the model phase structure functions for South Baldy in terms of the Allan Standard Deviation at 56 s (ASD_{56}). For $ASD_{56} \leq 0.07$, the phase structure function is given by

$$D_\phi(\rho) = \left(8.3 ASD_{56} \rho^{0.54}\right)^2, \tag{1}$$

where ρ is the baseline in meters and the phase deviation is in degrees. For $ASD_{56} > 0.07$, the phase deviation is given by

$$D_\phi(\rho) = \left(4 ASD_{56} \rho^{0.76}\right)^2 \qquad \rho < 150m \tag{2}$$

$$D_\phi(\rho) = \left(28 ASD_{56} \rho^{0.36}\right)^2 \qquad \rho > 150m. \tag{3}$$

These expressions are approximate and are derived from averaging the Allan standard deviations from several stability observations during similar atmospheric conditions (see Holdaway, 1991). In the analysis below, these approximations of the phase structure functions will be used in the short baseline regime (<100 m) where the tipper's uncertainty is high. However, it does not seem unreasonable to extrapolate in this region since this is consistent with the Kolmogorov prediction.

3 A ARRAY SIMULATIONS

Any differential phase errors between the two antennas will result in a phase error in the visibility, which will result in an error in the image. For the simple case of a point source in the image plane, a snapshot of $N(N-1)/2$ visibilities in the (u,v) plane, and small random phase errors of RMS ϕ radians, the *dynamic range* DR (image peak divided by off-source RMS) is estimated by Perley (1989) as

$$DR \approx N/\phi. \tag{4}$$

The MMA design calls for 40 antennas, so a DR of 100 requires the phase errors to be less than 30°. In MMA Memo 68 we used this criteria to define conditions which would permit useful imaging with the MMA.

This naive treatment does not account for the fact that phase errors on short baselines will be less severe than phase errors on longer baselines. It is not straightforward to generalize from a *fictitious* snapshot with uncorrelated Gaussian phase errors to a long integration with phase errors that are coherent over some baseline-dependent time. Finally, this treatment must break down for large phase errors. These complications can be readily dealt with by performing numerical simulations. Our model atmosphere (a 2-D phase screen) is blown over the array, and the simulated visibilities at each time are corrupted by the appropriate gains.

We present in Table 1 the results from a campaign of some simple simulations. A bright point source (no thermal noise) is observed for one hour with South Baldy's current A configuration design (Ge, 1992) at 230 GHz. Observations are performed with four different atmospheric models, looking directly overhead and at 30° elevation. Calibration timescales of both one hour and 60 seconds were used. The simulated data were imaged by Fourier transform and CLEAN deconvolution. The success of the image was gauged by the dynamic range (peak over off-source RMS). The dynamic range is not exactly inversely proportional to the RMS phase error in a given column because the form of the phase structure function changes down the column. The dynamic range is not proportional to the RMS phase error *across* columns because the phase errors will be correlated over long times in the 3600 s column but will be largely uncorrelated in the 60 s column. For example, for zenith observations through the 0.04 K model atmosphere without calibration, the dynamic range and the RMS phase error indicate that in the one hour observation there are ~5 observing intervals with independent phase on a 3000 m baseline. With 60 s calibration intervals, there are ~23 observing intervals with independent phase. The RMS phase error on a representative baseline is not a very good indicator of the potential dynamic range; something else must be specified about the degree of correlation of the phase errors over time and position. Until we get more sophisticated, we will just keep in mind that the phase errors are largely uncorrelated after calibration.

Phase-stable (calibrating once) observations are possible for the 0.04 K and 0.07 K models at zenith and the 0.04 model at 30° elevation. Some sort of calibration will be required for reasonable imaging with worse atmospheric conditions. When simulations are performed with complicated sky brightness distributions, the dynamic range decreases by a factor of about 2.

In addition to decreased DR, the phase fluctuations will artificially "resolve" the source due to loss of coherence on the longest baselines. As the atmospheric conditions deteriorate

	Zenith				30° Elevation			
ASD(56 s), K	3600 s		60 s		3600 s		60 s	
	ϕ	DR	ϕ	DR	ϕ	DR	ϕ	DR
0.04	14°	370	5°	2190	28°	130	10°	720
0.07	26°	180	10°	1150	52°	50	20°	390
0.13	42°	80	19°	500	84°	17	38°	180
0.20	69°	40	31°	240	138°	4	62°	85

Table 1: Dynamic range of simulated point sources viewed with the 3000 m configuration at zenith (one air mass) and 30° elevation (two air masses), with 3600 s calibration time intervals and 60 s calibration time intervals at 230 GHz. The RMS phase error on a 2000 m baseline is also shown.

in our simulations, the integrated flux in the map decreases only by about 15% for the 0.20 K atmosphere, indicating that the loss of coherence on the shortest baselines is not significant. However, the image peak drops by 50% for the 0.20 K atmosphere, indicating that we have reached the seeing limit of the atmosphere.

4 CALIBRATION SCHEMES

The typical observation strategy at existing radio interferometers include the observation of an external calibrator about once every half hour. Antenna slewing rates and on-line computer setup times of existing arrays limit the source/calibrator cycle time to a minimum of a few minutes. At millimeter wavelengths, atmospheric phase errors are a bigger problem and may require more drastic measures. First, we determine the structure function of the calibrated phase analytically and through simulations. Then we apply this relationship to understanding the capabilities of several novel phase calibration schemes.

4.1 STRUCTURE FUNCTION OF THE CALIBRATED PHASE

First, we will analytically determine the structure function of the calibrated phase. Figure 1 illustrates a two element interferometer with baseline ρ alternately observing a target source and a calibrator. The distance between the lines of site to the source and to the calibrator in the atmospheric phase screen is d. We assume frozen-in turbulence and (for now) a velocity of zero. After calibration, the residual atmospheric phase on this baseline will be

$$\phi_{cal}(d,\rho) = (\phi(r) - \phi(r+\rho)) - (\phi(r+d) - \phi(r+\rho+d)). \quad (5)$$

The phase structure function (Tatarski, 1961) is defined by

$$D_\phi(\rho) = \langle(\phi(r+\rho) - \phi(r))^2\rangle, \quad (6)$$

and is expressed in terms of the correlation function as

$$D_\phi(\rho) = 2 - 2\langle\phi(r+\rho)\phi(r)\rangle. \tag{7}$$

The average is an ensemble average which can be approximated by a time average over some time which is large compared to ρ/v, where v is the atmospheric velocity. The RMS residual calibrated phase can be expressed in terms of the phase structure function:

$$\langle\phi^2_{cal}(d,\rho)\rangle = 2\left(D_\phi(\rho) + D_\phi(d) - (D_\phi(\rho+d) + D_\phi(\rho-d))/2\right), \tag{8}$$

or for $\rho \gg d$ we have

$$\langle\phi^2_{cal}(d,\rho)\rangle \approx 2D_\phi(d). \tag{9}$$

The RMS phase error made with such a calibration is then essentially independent of ρ and is equal to $\sqrt{2}$ times the square root of the phase structure function on a baseline of d. A more complicated analysis must be made if the turbulent layer is thick. If the atmosphere is moving with velocity v and the interferometers cycle through the source/calibrator observations in time t, then

$$\langle\phi^2_{cal}(d)\rangle \approx 2D_\phi(vt+d). \tag{10}$$

Of course, v and d are vectors, and adding them as scalars represents the worst case.

Similar arguments can be made for the residual calibrated phase structure function when selfcalibration is used to determine and correct the phase. For selfcalibration, there is no difference in the lines of site between calibrator and source, only the atmosphere velocity and the gain averaging time come into the expression:

$$\langle\phi^2_{cal}(d)\rangle \approx 2D_\phi(vt). \tag{11}$$

4.2 CALIBRATION SIMULATIONS

We can check the above arguments for the structure function of the calibrated phase with our atmospheric simulation machinery and atmospheric models.

Consider observations of a bright point source in which we artificially divide the data up into calibration observation and target source observation. We use the calibration data, recorded every t_{cycle} s, to calibrate the target source data which is taken in between the calibration data. If the atmosphere is moving with velocity v, then atmospheric features larger than vt_{cycle} can be effectively removed from the target source data, while smaller features cannot be removed. Figure 2 illustrates the behavior of the atmospheric phase on a 60 m and a 3000 m baseline with selfcalibration timescales of 3600 s, 60 s, and 7 s. As can be seen, there is still a great deal of short time scale structure in the phases, and the short baseline phases are not improved by the calibration. Figure 3a shows the structure function for the model atmosphere and the structure function for the residual 60 s calibrated phase while Figure 3b shows the residual 7 s calibrated phase. With the 12 m/s wind velocity used in the simulations, calibration is expected to improve the phase for baselines greater than $vt_{cycle} = 720$ m for the 60 s case and

84 m for the 7 s case. For baselines shorter than vt, calibration *corrupts* the phase. A similar argument can be made for an external calibrator. If the distance in the turbulent atmospheric layer between the line-of-sight to the source and the line-of-sight to the calibrator is d, the phase on baselines longer than d can be improved by calibration. So, a calibrator can improve the phase only on baselines longer than $vt_{cycle} + d$. After calibration, the residual phase structure function is almost flat and the level of residual phase errors can be estimated for a particular atmospheric model by the RMS (uncalibrated) phase on baselines of order $vt + d$.

For a classical Kolmogorov phase structure function with phase error proportional to $\rho^{5/6}$ for baselines less than ρ_o and to $\rho^{1/3}$ for baselines more than ρ_o, calibration will improve the phase greatly for $vt + d \ll \rho_o$, but the improvement is mild for $vt + d > \rho_o$ where the phase structure function is fairly flat. It should be noted that Truehoft and Lanyi (1987) indicate that there is not a sharp switch between the steep and flat phase power laws, but rather a continuous change in power law slope. Observationally, a flattening has not been observed, but steep power laws are observed on short baselines and flatter power laws are observed on longer baselines. Since our observations indicate that ρ_o is only about 100-300 m, highly effective calibration requires that the source/calibrator cycle time be $\ll$ 25 s and the distance in the atmosphere be $\ll$ 150 m, or $\ll 15°$ on the sky, for a source at the zenith and a turbulent atmospheric layer 1000 m above the array traveling at 12 m/s.

During the best atmospheric conditions on the candidate sites, the RMS phase error is proportional to $\rho^{1/2}$, and no flattening is seen. Hence, there is no critical baseline beyond which phase improvements from calibration become slight. During these good conditions, which occur about 20% of the time during the winter months on South Baldy, there is no compelling argument for extremely short cycle times or extremely close calibrators. Under these conditions, the magnitude of the atmospheric phase fluctuations are small anyway and frequent calibration will be needed only for low elevation observations.

4.3 FAST CALIBRATION

To optimize phase calibration, the quantity $vt_{cycle} + d$ must be minimized. There is a trade-off between close, weak calibrators (long integration times, short slew times, close by in the atmosphere) and further, strong calibrators (shorter integration times, longer slew times, and further away in the atmosphere). We estimate the value of $vt_{cycle} + d$ for MMA observations. The dependence of $vt_{cycle} + d$ on the minimum calibrator source strength and the antenna slew rate will indicate the optimal values of these parameters. The value of the phase structure function at a baseline of $vt_{cycle} + d$ will indicate the level of phase errors that is possible to achieve using external calibration.

The atmospheric velocity as a function of height has been studied by Schwab (1992). A typical value for v_{atmos} is 12 m/s. If the atmosphere cannot be described as a thin phase screen, then a single value of the velocity will not be valid.

The total cycle time will be

$$t_{cycle} \approx t_{source} + t_{cal} + 2\psi/v_{slew} + 2t_{setup} \qquad (12)$$

where t_{cal} is the time spent integrating on the calibrator, t_{source} is the time spent integrating on the target source, ψ is the slew distance in degrees, v_{slew} is the slew rate in degrees per second, and t_{setup} is the time required for the online computers to set up prior to taking data.

We parameterize t_{source} in terms of $X = \frac{t_{cycle}}{t_{cycle}-t_{source}}$, so $t_{cycle} = X(t_{cycle} - t_{source})$. The value adopted for X depends upon how much time the observer is willing to sacrifice to calibration. In our analysis, we consider $X = 1.5$, or $\sqrt{3}$ loss in SNR compared to no time spent on calibration. For many combinations of atmospheric conditions, target sources, and array configurations, the image quality will be limited by atmospheric phase errors rather than SNR if such a scheme is not adopted, so throwing away a large fraction of the time to calibrate actually means gaining some time for high frequency, long baseline observing.

An estimate for t_{cal} can be obtained by considering the required accuracy of the gains. Thermal noise will lead to errors in the *complex* antenna gains of order

$$\sigma_G = \frac{\sigma_V}{S\sqrt{N-3}} \tag{13}$$

where σ_V is the noise for a single visibility, N is the number of antennas in the array and S is the calibrator strength (Cornwell, 1989). For high SNR, the gain phases have a Gaussian distribution with RMS of $\sigma_G/\sqrt{2}$ radians (Thompson, Moran, and Swenson, 1986). We assume a Gaussian distribution in spite of the low SNR. Then the RMS error in the gain phase varies as $\sigma_\phi = 6°/R$, where R is the SNR per baseline. We assume here that $R = 1$, as 6° phase errors yeild a DR of 500-1000:1. If higher DR is required, then selfcalibration is probably possible.

For the MMA, the noise per baseline (two Stokes, one IF) will be

$$\sigma_V = 0.001\frac{T_{sys}(\nu)}{\epsilon_a(\nu)\sqrt{t}} \tag{14}$$

where ϵ_a is the aperture efficiency and t is the observing time in seconds and $T_{sys} = T_{rec}+T_{atmos}$, and $T_{atmos} = T_{sky}(1 - e^{-\tau/\sin(\theta)})$, where θ is the elevation angle and T_{sky} is the physical temperature of the air in the moist turbulent layer. We assume everywhere that we can use one IF at a continuum bandwidth of 1 GHz for calibration (or selfcalibration), that T_{rec} is equal to the frequency in GHz (Hjellming, 1989), and that the optical depth τ_ν is related to the column density of precipitable water vapor via $\tau_\nu = A_\nu w$, where w is millimeters precipitable water vapor, and A_ν has been read off of Schwab and Hogg's 1 mm opacity figure (1989) and reproduced here in Table 2. Hence, the amount of time required to obtain a signal to noise ratio of R on a source of brightness S is

$$t = \left(\frac{0.001RT_{sys}}{\epsilon_a S}\right)^2 \approx \left(\frac{0.001R(\nu + 253(1 - e^{-A_\nu w/\sin(\theta)}))}{\epsilon_a S}\right)^2 \tag{15}$$

In the case where the antennas slew to the calibrator position, this time is divided by two since both IFs can observe the calibrator.

At λ 3 mm, there are about 200 compact flat spectrum sources in the sky which are 1 Jy or brighter (Kühr et al, 1979). Hence, the average distance, in degrees, from the target source

ν, GHz	A_ν	ϵ_a
30	0.007	0.9
90	0.01	0.8
200	0.05	0.7
340	0.15	0.6
410	0.3	0.5
650	0.6	0.3

Table 2: Frequency dependence of scaling factor A_ν in $\tau_\nu = A_\nu w$, where w is millimeters of precipitable water vapor; and values of ϵ_a, the aperture efficiency, used in the simulations.

to a calibrator of strength S Jy is

$$\psi \approx \frac{\sqrt{\frac{40000}{200S^{-1.5}}}}{2} \approx 7.1S^{0.75} \tag{16}$$

Most of these sources have a sizable flux in milliarcsecond structure, so will be unresolved to the longest baselines of the MMA.

The slew velocity v_{slew} is not yet determined. The VLA antennas slew at about 0.33°/s, and smaller, modern antennas could probably slew faster. However, the problem will be actually accelerating and decelerating in less than a second, and once on the target or calibrator source, pointing with reasonable accuracy. In most cases where fast external calibration would be required, pointing worse than 1″ would be tolerated since the atmospheric phase fluctuations would limit the DR to a lower value than the pointing errors would.

The online system setup time t_{setup} is also not yet determined. Typically, the setup time for arrays is 10-40 seconds. Several concerns push the MMA setup time to very low values:

- Fast external calibration arguments. These arguments are most compelling for long baseline observations.
- Very large mosaics of bright spectral lines; mosaics with several 1000 pointings, each requiring only 10 seconds or so. The setup time should be much less than 10 seconds for efficient use of the array. This applies to the compact configurations.
- The effects of some sorts of pointing errors on mosaic images are reduced if the entire mosaic is scanned over several times. Again, efficient use of the array requires short setup times. This applies to the compact configurations.
- For low declination sources, the beamshape of the compact arrays depends strongly on the hour angle of the observation (Ge, 1992). This implies that the synthesized beam will change over a mosaic image, and flux in the residuals will be inaccurately determined. One way of getting around this problem is to scan through all pointings many times

over a range of hour angle to yeild more similar synthesized beams for each pointing. This will also improve the performance of the computationally inexpensive linear mosaic algorithm, which assumes the (u, v) coverage is identical for all pointings. This applies to the compact configurations.

We assume that $t_{setup} = 1$ s. Altering t_{setup} will not affect the optimal calibrator source strength, but it will affect the value of $vt + d$, and therefore, the achievable calibrated phase.

The relationship between d, the distance in the atmosphere between the lines of sight, and ψ, the distance on the sky between the calibrator and the source, is optimal when the source and the calibrator are at the same elevation:

$$d = h \sin(\psi) / \sin(\theta) \quad (17)$$

$$d = h \sin(7.1 S^{0.75}) / \sin(\theta) \quad (18)$$

where h is the height of the turbulent layer of water vapor above the array and θ is the elevation angle above the horizon of the source.

Combining the above expressions, we see we must minimize the quantity

$$\begin{aligned} d + vt &= h \sin(7.1 S^{0.75}) / \sin(\theta) \\ &+ X v_{atmos} \left(\left(\frac{0.001 R(\nu + 253(1 - e^{-A_\nu w / \sin(\theta)}))}{\epsilon_a \sqrt{2} S} \right)^2 + 2(7.1 S^{0.75} / v_{slew}) + 2 t_{setup} \right) \end{aligned} \quad (19)$$

This expression can be analyzed as a function of elevation θ, atmospheric optical depth τ, calibrator strength S, and slew rate v_{slew}. This analysis does not depend upon any assumptions on the form of the phase structure function and indicates that the optimal calibrator flux is around 0.15 Jy. There will be about 3500 calibrators brighter than 0.15 Jy at λ 3 mm, or a calibrator within 2° of the target source.

Figure 4 illustrates the behavior of the left hand side of Equation 20 ($vt + d$) for a range of slew rates and elevation angles. A few trends are apparent:

- there is almost no difference between the zenith and 60° elevation curves, and little difference between these two curves and the 30° elevation curve. Things fall apart at very low elevation.
- the optimal calibrator flux (ie, the calibrator flux which minimizes the curves) increases as elevation angle decreases (as the atmosphere becomes more important).
- the curves become flatter with higher slewing rates, indicating that less is gained by compiling a calibrator list complete down to the optimal calibrator flux. The curve for 10° elevation is still fairly steep.

The quantity $vt + d$ has been studied as a function of optical depth for a range of elevations angles and source strength, and the main trends are:

	Zenith		30° Elevation	
ASD(56 s), K	no cal	fast cal	no cal	fast cal
0.04	14°	5.5°	28°	12°
0.07	26°	10°	52°	22°
0.13	42°	25°	84°	54°
0.20	69°	41°	138°	90°
0.30	105°	63°	210°	136°

Table 3: RMS phase in degrees over one hour on 2000 m baselines observing the zenith and at 30° elevation for five atmospheric models. The left phase represents essentially no calibration, and the right phase is what is possible with the fast calibration described in the text.

- the difference between curves at different elevations increases with increasing opacity.
- the optimal calibrator flux increases with increasing opacity, the strongest increase coming from the low elevation curves.

The minimum value of $vt + d$ obtained from Equation 20 can be combined with the atmospheric phase structure function to give an estimate of the best possible calibrated phase for a set of parameters θ, τ, v_{slew}, S. We have calculated the value of $vt + d$ for a variety of atmospheric conditions assuming $v_{slew} = 1°/s$, the appropriate τ for each condition, the optimal value of S, and looking at the zenith as well as 30° elevation. Estimates of the best possible residual phase errors are given in Table 3. For observations near the zenith using fast calibration, all of these atmospheric conditions would permit some sort of useful imaging. After fast phase calibration, the phase errors will not be highly correlated over time, so even 50° phase errors may result in an image with dynamic range greater than 100:1. At 30° elevation, the 0.04-0.13 K conditions will result in reasonable images, and the 0.20 K atmosphere may be used for observations which require ~50:1 dynamic range.

4.3.1 REQUIREMENTS ON THE ARRAY: FAST CALIBRATION

For conventional external calibration to effectively remove the effects of the atmosphere at millimeter wavelengths during all but the best atmospheric conditions, the antennas would have to slew at 1-2°/s, the antennas would have to accelerate and decelerate almost instantaneously, the online computers would have to setup in 1 s or less, and an extensive calibrator list would need to be generated.

4.4 BEAM SWITCHING-PHASE REFERENCING

As determined in Section 4.3, highly effective phase calibration at millimeter wavelengths is only possible when the antennas and online computers are extremely agile. Instead of actually moving the antennas, it might be possible to beam switch[1] to the calibrator, or to design the antenna optics such that the calibrator can be observed at the same time as the target source without moving the antenna. The field of view of the antenna will be between 30 and 100 primary beam widths. From our analysis of the density of calibrators on the sky, we know that we need to travel two degrees or more from the target source to get to a suitable phase calibrator. While nutating the subreflector two degrees will not be possible at 230 Ghz, it *will* be possible to see sources 1-2 degrees off axis at 30 GHz, the lowest proposed frequency for the MMA.

If we are beam switching between the calibrator and the target source, the travel time and setup time terms no longer contribute to the cycle time. The atmospheric opacity and the receivers will be more favorable at 30 GHz. There will likely be more suitable calibrator sources at 30 GHz. A new expression for $vt + d$ for beam switching to a calibrator is:

$$vt + d = X v_{atmos} \left(\frac{0.001(\nu_1/\nu_2)(\nu_2 + 253(1 - e^{-A_{\nu_2} w/\sin(\theta)}))}{\epsilon_a S} \right)^2 + h \sin(10 S^{1.25})/\sin(\theta). \quad (20)$$

If it were possible to observe the phase calibrator and the target source simultaneously through a novel optical design, then the factor X becomes 1 and the cycle time is simply the amount of time required to detect the calibrator. One concern here is that the required accuracy of the gains, and hence the required SNR R per visibility and the required observing time increases if we are to know the gains well enough to extrapolate to higher frequencies. The $(\nu_1/\nu_2)^2$ increase in observing time balances out the improvement due to T_{sys} and ϵ_a being more favorable at low frequencies.

It is clear that this technique is not only much easier to perform than the fast slewing, but it also yeilds better calibrations as the quantity $vt + d$ will be much smaller. Figure 5b illustrates the levels of $vt + d$ which can be achieved with beam switching onto the calibrator.

[1] In the literature, *beam switching* usually refers to the total power technique in which the on-signal and off-signal are differenced to remove the effects of atmospheric emission. In this document, *beam switching* refers exclusively to a new technique in which the subreflector is nutated between source position and calibrator position, but the signals are not differenced; rather, the correlated visibilities are stored as two separate sources and the calibrator visibilities are used to solve for the atmospheric gain phases and amplitudes. If both total power and phase beam switching are required, three different beam positions on the sky will be required.

4.4.1 REQUIREMENTS ON THE ARRAY: BEAM SWITCHING

The array must be able to observe at 30 GHz simultaneously or almost simultaneously with each high frequency (115 GHz, 230 GHz, 345 GHz). The beam switching phase calibration method puts tight constraints on the design of the antenna and subreflector. The antenna must have a fairly wide field of view, and the subreflector must be able to move about 3 degrees quickly ($\ll$ 1 second) and accurately (10 arcseconds). The online control system must handle bizarre switching patterns, such as: CAL(2 degrees; 1 second)::25 times { ON-SOURCE(0 arcminutes; 0.02 seconds)::OFF-SOURCE(2 arcminutes; 0.02 seconds) }. The OFF-SOURCE and ON-SOURCE total power signals would be differenced on-line to remove the atmospheric emission from the total power data. Interferometric data would be taken at all three positions. The on-line system would have to accumulate the visibilities for all three positions and store them separately, and the beam switched total power would have to be stored and tagged with the on and off positions. The pointing for both the ON-SOURCE and OFF-SOURCE positions must meet the 1 arcsecond specification. Other specifications must be determined for things like the off-axis gain. In essence, the beam switching phase calibration scheme represents a paradigm shift in array operation and antenna functionality.

4.5 SIMULTANEOUS PHASE REFERENCING

Selfcalibration is the best way to calibrate the atmospheric phase since the calibrator and target source share the same line of sight and there is no time sharing between the calibrator and the target source. If the source is not bright enough to selfcalibrate on, then the next best way to calibrate the source of interest is to simultaneously phase reference on a nearby calibrator. It may be possible to arrange the antenna optics to allow *simultaneous* observations of a target source at high frequency and a calibrator source 1-2° away at 30 GHz. If simultaneous observations are possible, then the residual phase errors after calibration will be about $\sqrt{2D_\phi(vt+d)}$, where $vt+d$ is now given by

$$vt + d = v_{atmos}\left(\frac{0.001(\nu_1/\nu_2)(\nu_2 + 253(1 - e^{-A_{\nu_2} w/\sin(\theta)}))}{\epsilon_a S}\right)^2 + h\sin(10S^{1.25})/\sin(\theta). \quad (21)$$

This is nearly identical to the beam switching case, but the X term is set to 1 (the total observing time is equal to the calibration time). This represents only a small gain in the phase errors, but a $\sqrt{3}$ gain in SNR, since no time is taken away from the target source to perform the required frequent calibration. The values of $vt + d$ as a function of source strength for several values of elevation angle are illustrated by Figure 5c.

4.6 DIRECTIONAL CALIBRATION

I have shown in Section 4.1 that the residual calibrated phase structure function is a function of $vt+d$, at least for baselines long compared to $vt+d$. Up until now, v and d have been considered to be scalars, which is the worst case. Since v and d are really vectors, it is possible to do significantly better phase calibration by measuring the atmospheric phase of the calibrator upwind or downwind from the target source. A delay in the interpolation of the gains can then be calculated based on the wind velocity and the distance d between the target and calibrator sources' lines of site. Such a method would require accurate real time information about the direction and speed of the winds aloft and the height of the turbulent layer. This method works best if the sky velocity and the slewing speeds are matched (ie, if v = 10 m/s and h = 1000 m, it takes 1.7 s for an atmospheric feature to move 1°, so the antenna slewing and on-line setup time should conspire to take 1.7 s to move the same 1°) or if the beam switching frequency is matched with the wind velocity. This method will be limited by the agreement of the wind direction and the calibrator-source orientation, the accuracy of the wind speed, the validity of the assumption that the atmospheric turbulence is "frozen in", and the validity of the assumption that the turbulent layer is thin and therefore has unique height and wind speed. As the sky rotates or the wind changes directions, a new calibrator with the proper orientation to the target source would need to be chosen for optimal calibration. While this method seems promising, it is a messy enough problem that we probably should not count on any great benefit from it.

4.7 SELFCALIBRATION

Selfcalibration is included here for comparison with the fast calibration and the beam switching techniques. Figure 5d shows vt as a function of the flux in compact components (ie, useful flux for selfcalibration). These curves assume an SNR of 1 on each baselines, which leads to phase errors simply due to thermal noise of 6°. Bright sources for which SNR of 1 is reached over times so short that the atmospheric phase fluctuations are less than 6° will require higher SNR and longer integration. It follows that the curves underestimate vt for real observations of bright objects. Also, there will probably be some range of spacings in the (u, v) plane for which selfcalibration is effective, leading to a loss in sensitivity. Again, the curves underestimate the value of vt.

As with the other methods, selfcalibration requires long integration times for sources which are much weaker than about 150 mJy, and hence results in large values of vt. However, since the calibrator and the target source share the same line of sight, there is no penalty in atmospheric distance or slew time in going to brighter and brighter sources, and the phase structure function does not need to be multiplied by $\sqrt{2}$ to get the residual phase error after calibration.

After one of the external calibration schemes has been used to remove most of the gross atmospheric phase fluctuations, the residual phase fluctuations will be not be highly correlated over time. The phase errors will have a mean of zero, timescales of several seconds, and amplitude depending upon the atmospheric conditions. In cases of very bad phase stability

where the residual phase errors are still greater than a radian, there is probably no hope, and selfcalibration will not improve the situation. For somewhat better atmospheric conditions, the residual phase errors after external calibration will be smaller and selfcalibration may help. However, since the remaining phase errors will be over very short timescales, we may not be able to detect the source in the amount of time which the phase fluctuates an appreciable amount. More work needs to be done on the noise characteristics of images made by selfcalibrating data with these very fast residual phase fluctuations.

4.8 COMPARING CALIBRATION METHODS

A comparison of the curves of $vt + d$ can be found in Figure 5. Using the minimum values of $vt+d$ on these curves, Equation 1 through Equation 3 for the phase structure functions, and the relationships between phase structure function and the residual phase errors, we calculate the expected residual phase errors from fast calibration, beam switching calibration, simultaneous calibration, and selfcalibration. The results for zenith observing are shown in Table 4, and the results for observing at 30° are shown in Table 5. The variations in opacity and Allan standard deviation for the various atmospheric stability conditions have been taken into consideration in calculating $vt + d$. Note that the residual phase errors at an airmass of two are worse than twice the residual phase errors at the zenith. This is because T_{sys} increases for low elevation observations, requiring a longer integration on the calibrator, and the distance in the atmosphere between the lines of sight to the calibrator and the source is larger. Also, note that during the best conditions, the residual atmospheric phase is less than 6° for some methods. In calculating $vt + d$ we assumed that we would need to determine the gain phases to within 6°. For the best cases, the gains from the calibrator must be determined with more accuracy; the minimum residual phase error should probably be around 7°. For some of the worse cases where the residual phase error is 30° or higher, we are determining the gains on the calibrator with too much accuracy. For example, letting the error in the phase gains go to 12° requires that we integrate on the calibrator for one quarter the time used in the calculations. This reduction in time will reduce the residual phase errors, but since the d term is not affected and the phase error is proportional to $vt + d$ raised to some power less than one, this will be about a 25% reduction for phase errors greater than 30° for the methods which do not have any overhead in setting up and slewing.

The rate of occurrence of the various atmospheric conditions (see MMA Memo 68) can be folded into these tables to get an idea of the amount of time the MMA can be used with the various calibration schemes. Using the beam switching phase calibration scheme or the simultaneous scheme, zenith observations could be performed during all atmospheric conditions listed here, or over 50% of the time during the winter months. Observations at 30° elevation could be made about 40-50% of the time, but the dynamic range would dip below 100:1 for the 0.20 K and 0.30 K atmospheric conditions.

ASD(56 s), K	fast	beam switch	simult	selfcal
0.04	5.5°	3.2°	3.0°	1.9°
0.07	10°	5.9°	5.5°	3.6°
0.13	25°	13°	12°	7.6°
0.20	41°	22°	20°	13°
0.30	63°	34°	31°	21°

Table 4: Estimates of the residual phase errors after calibration for the fast calibration scheme, the beam switching calibration scheme, simultaneous calibration, and selfcalibration on a 200 mJy continuum source, all looking at zenith at 230 GHz. If there is more continuum flux, the gain solution interval can decrease and smaller phase errors result.

ASD(56 s), K	fast	beam switch	simult	selfcal
0.04	12°	8.6°	8.0°	4.0°
0.07	22°	16°	15°	7.6°
0.13	54°	40°	36°	17°
0.20	90°	66°	62°	31°
0.30	136°	102°	94°	49°

Table 5: Estimates of the residual phase errors after calibration for the fast calibration scheme, the beam switching calibration scheme, simultaneous calibration, and selfcalibration on a 200 mJy continuum source, at 30° elevation at 230 GHz.

4.9 PHASE BOOT-STRAPPING

Because the very high frequency long baseline work is so demanding, it has been proposed that the atmospheric phase be determined at a lower frequency (either by observing the calibrator at a lower frequency or by selfcalibrating at the low frequency while simultaneously observing at the higher frequency), scaled, and applied to the higher frequency source observations. There are a number of reasons why this is a good idea:

- For some source geometries and emission mechanisms, there will be more flux at lower frequencies, thereby decreasing t_{cal}.
- The receivers have lower system temperatures at lower frequencies, decreasing t_{cal}.
- The phase coherence time is much longer at lower frequencies since the additional atmospheric path length is a smaller fraction of a wavelength.

The last point is not really valid since phase fluctuations which occur on timescales shorter than t_{cycle} (or t_{cal} for selfcalibration) will be lost anyway and the phases must be determined more accurately to be scaled up to the higher frequency.

Phase boot-strapping will be most beneficial when there is a great deal of power in large scale phase fluctuations. During the very best conditions, the $\phi \propto \rho^{1/2}$ phase law indicates that there is relatively more power in large scale fluctuations than in small when compared to the usual Kolmogorov case, and phase boot-strapping may have more success. Also, atmospheric phase fluctuations are not the only cause of phase errors in radio interferometers. Poorly calibrated baselines, fluctuating signal pathlengths, and unstable electronics will cause phase errors which may change smoothly through several turns over timescales large compared to t_{cal}, and a low frequency phase-bootstrapping method will remove such phase errors from high frequency observations.

If phase boot-strapping is used, the time required to detect the source will be reduced by a factor

$$\left(\frac{T_{sys}(\nu_1)}{T_{sys}(\nu_2)}\frac{S(\nu_2)}{S(\nu_1)}\frac{\epsilon_a(\nu_2)}{\epsilon_a(\nu_1)}\right)^2 \tag{22}$$

where ν_1 is the lower (calibration) frequency and ν_2 is the higher (target) frequency, T_{sys} is the system temperature, ϵ_a is the aperture efficiency, and $S(\nu)$ is the source flux at frequency ν. Both spectrum and beam size need to be factored into $S(\nu)$. If the phase boot-strapping is to be used in conjunction with selfcalibration of the continuum signal, the source may be weaker at the lower frequency and any gain must be made up by the improvement in T_{sys}.

If the phase is to be scaled from ν_1 to ν_2, it must be determined with greater precision at ν_1. Instead of a SNR of 1 on each baseline, a SNR of about ν_2/ν_1 will be required. A large contribution to T_{sys} is T_{rec}, and the working assumption is that T_{rec} is proportional to ν. While some speed may be gained from aperture efficiency, source spectrum and structure, and atmospheric opacity changing with frequency, this method does not gain a great deal. More is gained at submillimeter wavelengths, especially at low elevation angles, where the atmosphere has a sizable opacity and $T_{sys}(\nu_2)$ increases more quickly than ν.

4.10 TOTAL POWER MEASUREMENTS FOR PHASE FLUCTUATIONS

At millimeter wavelengths, total power measurements are dominated by emission from atmospheric water vapor. Since the MMA is designed to measure total power and interferometric data simultaneously, the non beam switched total power data could be used to determine the atmospheric phases, assuming that the atmospheric phase is dominated by the water vapor path length difference. Analysis of the South Baldy SMA 100 m interferometer and 230 GHz tipper databases should indicate if and under what conditions the bulk of the atmospheric phase truly is due to inhomogeneously distributed water vapor.

The column density of precipitable water vapor w can be determined from

$$T_B = T_{sky}(1 - e^{-A_\nu w}), \tag{23}$$

where T_{sky} is the physical temperature of the moist turbulent air and A_ν is defined in Table 2. This expression breaks down when the water is in the form of droplets. It is difficult to determine w accurately when the atmosphere is optically thick, but who want to observe then? The atmospheric component of the gain phase is then given by

$$\phi = 2\pi 6.5 w/\lambda. \tag{24}$$

Strong signals from astronomical sources must be removed. An accurate value of the kinetic sky temperature averaged over the height range in which the turbulent water vapor is concentrated could be obtained by comparing the phase determined by this method with the phase determined by observations of a calibrator source. In the optically thin limit, any error in T_{sky} propagates into a phase error of

$$\Delta\phi \simeq 2\pi 6.5 w \Delta T_{sky}/T_{sky} \tag{25}$$

indicating that under typical atmospheric conditions at 230 GHz, an error of 1 K in sky temperature results in a 10° phase error.

Neglecting the phase error due to errors in the sky temperature, the residual calibrated phase errors will be on the order of $\sqrt{D_\phi(vt + D)}$, where t is now the amount of time needed to achieve the required SNR for the atmospheric water vapor, D is the dish diameter. The noise in a single total power measurement will be

$$\sigma_{SD} = \frac{T_{rec}}{\sqrt{\Delta\nu t}}, \tag{26}$$

or using 1 GHz bandwidth and the earlier approximation for T_{rec}, the time required to achieve some noise level σ is

$$t = \left(\frac{\nu_{GHz}}{\sigma}\right)^2 10^{-9}. \tag{27}$$

From Equation 24, we see that the water vapor column density must be determined with an accuracy of 0.003 mm for a 5° phase error in the gain phase at 230 GHz. For optically thin skies, this implies that the noise must be

$$\sigma_{SD} < T_{sky} A_\nu 0.003, \tag{28}$$

which is 0.045 K for 230 GHz ($A_\nu \simeq 0.06$) and $T_{sky} = 253$ K. Plugging into Equation 27, the time required for 5° errors is 0.026 s. Hence, $vt + D = 8.3$ m.

Excluding temperature fluctuations, the atmospheric contribution to the residual phase errors should then be $< 5°$ during the 0.30 K atmospheric conditions, the worst conditions which we consider in this memo. Assuming we have an error budget of about 30° of phase per baseline, we can tolerate temperature fluctuations of almost 3 K. The water vapor weighted average of T_{sky} along the line of sight could be calculated from the structure function of T_{sky}. Under the types of conditions which we consider in this memo, the fluctuations of the average temperature will be less than 3°. However, variations in T_{sky} of a few degrees over tens of meters can occur during midday convective conditions, and these sorts of fluctuations are not well described by the Kolmogorov theory of isotropic homogeneous turbulence and may be highly correlated vertically. During these conditions, the fluctuations in T_{sky} may sometimes be large enough to prevent this phase calibration method from being useful.

To summarize, the potential problems with this "dead reckoning" phase calibration scheme:

- This method is not applicable when an appreciable amount of the water is in the form of water droplets rather than water vapor, as ΔT_B is no longer related to w in a simple way.
- What is the nature of the air temperature fluctuations? During what conditions will the air temperature fluctuations be too large for this calibration method to be effective?
- Under what conditions is the atmospheric phase dominated by water vapor?

Since the temperature fluctuations are not well understood at this point, and the residual phase errors will probably be dominated by temperature fluctuations rather than by the variable atmospheric water vapor, we will not attempt to compare this calibration scheme with the other methods discussed above.. This is a promising technique, and more will be written about it when we better understand the sky temperature fluctuations.

4.11 REQUIREMENTS ON CALIBRATORS

For most of the phase calibration schemes discussed above, the sensitivity of the MMA puts a lower limit of about 150 mJy on the strength of the source for which calibration is feasible.

How many calibrator sources are there which are stronger than 150 mJy? We have made very naive arguments based on known point sources at 90 GHz. There may be more 150 mJy sources at 30 GHz. It is possible to identify candidate MMA calibrator sources from flat spectrum objects in Condon's 5 GHz and 1.4 GHz all-sky surveys. Observations of promising fields at 22 GHz with the VLA D and C configurations would provide additional information. Better information on the distribution of sources at 30 GHz would help tighten up the antenna requirements and the estimates of the residual phase errors.

Since there may be on the order of 3500 sources 150 mJy or brighter at 30 GHz, or one source within 1.7° on average, it would not be practical to compile a calibrator list from an all sky survey. Rather, a region of the sky around the target source would need to be surveyed

for calibrators prior to the actual observations. Assume that $(2x)^2$ square degrees must be surveyed. We could first start with each antenna observing an independent field in total power. Sampling at $\lambda/2D$, or 0.032 degrees, requires $7500x^2$ individual pointings. Assuming we need a 5σ detection of our 150 mJy calibrator source, and considering the 2.5-fold increase in sensitivity due to the overlap of the primary beams, each sky position needs to be observed by one antenna for only 0.15 seconds. Using the nutating subreflector, we should be able to scan over the entire field with very little dead time. The entire array of 40 antennas could survey the region of interest in total power in $30x^2$ seconds, or six minutes for a 50 square degree region.

The total power survey local to the target source would presumably reveal a large number of unresolved sources. Each of these could be observed with the MMA in interferometric mode to accurately determine the position, flux, and source structure. Determination of these quantities should take a few seconds. In only ten minutes, the candidate calibrator sources for your big observation next week can be located. This requires an integrated expert system which calibrates the total power data, identifies unresolved sources, determines their approximate positions and fluxes, then reobserves them with the entire interferometer, and repeats the identification step. The characteristics of the candidate calibrators should be stored in a database which could be reaccessed the next time the target source was observed.

5 SPRINGERVILLE REVISITED

MMA Memo 68 (Holdaway, 1991) estimated the raw phase stability at both the South Baldy and the Springerville sites but paid little attention to how the phase could be corrected with clever calibration schemes. The results indicated that South Baldy and Springerville were comparable on short baselines or at low frequencies, but that South Baldy had significantly better phase stability on long baselines at high frequency. This was due to two factors: first, the Springerville phase structure function appeared to steepen on long baselines, leading to much higher phases on the longest baselines; second, there was more time on South Baldy when the Allan Standard Deviation at 56 s was as low as 0.04 K or 0.07 K, the atmospheric conditions during which permit phase stable observations on long baselines.

If the phase calibration techniques which have been explored in this memo can be used, the differences between the South Baldy and Springerville sites are not great. The first factor against Springerville disappears because the residual phase after calibration depends only upon $D_\phi(vt + d)$, and $vt + d$ can be made much smaller than the baseline at which the steepening occurs. The second factor is also not highly significant: the very best atmospheric conditions are not required. The fast calibration, beam switching calibration, and probably the total power phase calibration schemes should work well for the atmospheric model characterized by an Allan Standard Deviation at 56 s averaging time of 0.13 K, and South Baldy has conditions this good or better 33% of the time during the winter months, while Springerville has conditions this good or better 30% of the time during the winter months. However, as reported in MMA Memo 68, pages 4-5, the phase structure function at Springerville does not seem to have a

steep section for very *short* baselines, implying that the calibrated phases on South Baldy will still be somewhat better than the calibrated phases on Springerville.

6 SUMMARY

The estimates of usable high frequency time for each configuration of the MMA given in MMA Memo 68 are somewhat conservative. Simulations of the Baldy A Array with model atmospheres overhead and no active phase correction indicate that the 30° phase error criterion results in almost 200 : 1 DR imaging of a simple point source. The improved dynamic range comes about because the phase errors are not correlated over the entire one hour simulation. But even the 0.20 K model atmosphere permits 40:1 DR imaging of a source near the zenith without active phase correction. When the data can be selfcalibration, the correlated parts of the phase errors drop out and the residuals are largely uncorrelated in time, so the same RMS phase error will result in higher DR. The current work indicates that the large configurations may be used for "medium quality imaging" more of the time than estimated in Tables 3 and 4 of MMA Memo 68. The inability of the RMS phase error to uniquely indicate the resulting image quality requires a new way to represent the severity and nature of phase errors. Something like the Allan variance at different averaging times would be appropriate.

Empirical phase structure functions have been derived from the South Baldy data. It has been found that the residual calibrated phase error is given by $\sqrt{2D_\phi(vt+d)}$. We have measurements for v; d can be estimated based on source counts, the calibrator strength, and geometry; t follows from d, the calibrator strength, and other parameters. An analysis of the standard external calibration scheme indicates that it is not very effective at removing the short timescale atmospheric fluctuations unless the online system setup time is very small (1 s), the antennas can slew very quickly (1°/s), and the calibrator source is nearby (2°). It may not be feasible to get the antennas moving back and forth so quickly, but it may be possible to quickly nutate the subreflector between the calibrator and the target source. The field of view is probably wide enough to do this at 30 GHz. It is not clear that the antennas can actually do this. Such a calibration scheme would place new constraints on the antenna design, such as distance of beam throw, accuracy of beam throw, and a highly programable nutating subreflector.

Phase extrapolation from low to high frequencies does not seem very promising except for very high frequencies. Dead reckoning of the atmospheric phases from total power measurements of the water vapor column density may sometimes be limited by the accuracy to which the temperature of the air aloft is known. A scenario is presented for finding very weak calibrator sources; the MMA could find nearby 150 mJy sources in 5-10 minutes, so it could actually be done just prior to the observations.

7 REFERENCES

1. Cornwell, T.J., 1989, *in 'Synthesis Imaging', Publ, A.S.P., eds. Perley, R.A., Schwab, F.R. and Bridle, A.H.*, 185.

2. Ge, Jinp Ping, 1992, "Further Simulations of (Possible) MMA Configurations", MMA Memo 80.

3. Hjellming, R.M., 1989, "Update of MMA Sensitivity Estimates", MMA Memo 59.

4. Hogg, D.A., 1992, "A Summary of the Data Obtained During the mmA Site Survey", MMA Memo 79.

5. Holdaway, M.A., 1991, "A Millimeter λ Phase Stability Analysis of the South Baldy and Springerville Sites", MMA Memo 68.

6. Kühr, H., et al, 1979, "A Catalogue of Radio Sources", Max-Planck-Institute für Radioastronomie, Preprint No. 55.

7. Masson, C., 1991, SMA Memo.

8. Perley, R.A., 1989, *in 'Synthesis Imaging', Publ, A.S.P., eds. Perley, R.A., Schwab, F.R. and Bridle, A.H.*, p. 291.

9. Olmi, L., and Downes, D., 1992, "Interferometric Measurement of Tropospheric Phase Fluctuations at 86 GHz on Antenna Spacings of 24 m to 288 m", *submitted to A.A.*.

10. Schwab, F.R., and Hogg, D.A., 1989, "Millimeter-Wave Atmospheric Opacity and Transparency Curves", MMA Memo 58.

11. Schwab, F.R., 1992, "Lower Tropospheric Wind Speed Statistics...", MMA Memo 75.

12. Sramek, R.A., 1990, in: Radio Astronomical Seeing, eds. J.E. Baldwin & Wang Shouguan, Pergamon, Oxford, p. 21.

13. Tatarski, V.I., 1961, *Wave Propagation in a Turbulent Medium*, Dover, New York.

14. Thompson, Moran, and Swenson, 1986, *Interferometry and Synthesis in Radio Astronomy*, John Wiley & Sons, New York, p. 259.

15. Treuhoft, R.N., and Lanyi, G.E. 1987, Radio Science, 22, 2, p. 251.

Figure 1: Schematic diagram of a two element interferometer observing a target source and a calibrator through a thin atmospheric phase screen. ρ is the baseline, ϕ are the atmospheric phases, and d is the distance in the atmosphere between the line of sites to the source and to the calibrator.

Figure 2: Simulated 230 GHz phase time series for 60 m and 3000 m baselines, uncalibrated, calibrated with $t_{cycle} = 60$ s, and calibrated with $t_{cycle} = 7$ s.

Figure 3: Simulated 230 GHz phase structure function of uncalibrated data compared to phase structure function for calibrated data: 60 s calibration cycle time (a) and 7 s calibration cycle time (b). The distance vt_{cycle} is marked in the baseline axis.

Figure 4: The quantity $d + vt_{cycle}$ with fast slewing calibration as a function of calibrator strength for a variety of elevation angles and *slew rates*. $\tau = .1$, $v_{atmos} = 12$ m/s, $X = 1.5$, $t_{setup} = 1$ s, and $\nu = 230$ GHz were assumed.

Figure 5: (a) The quantity $vt + d$ for fast calibration, assuming 1 mm water vapor, 1°/s slewing, and 1 s of setup time. (b) The quantity $vt + d$ with beam switching calibration assuming $X = 1.5$. (c) The quantity $vt + d$ with simultaneous observations of calibrator and target source. (d) The quantity $vt + d$ with selfcalibration.

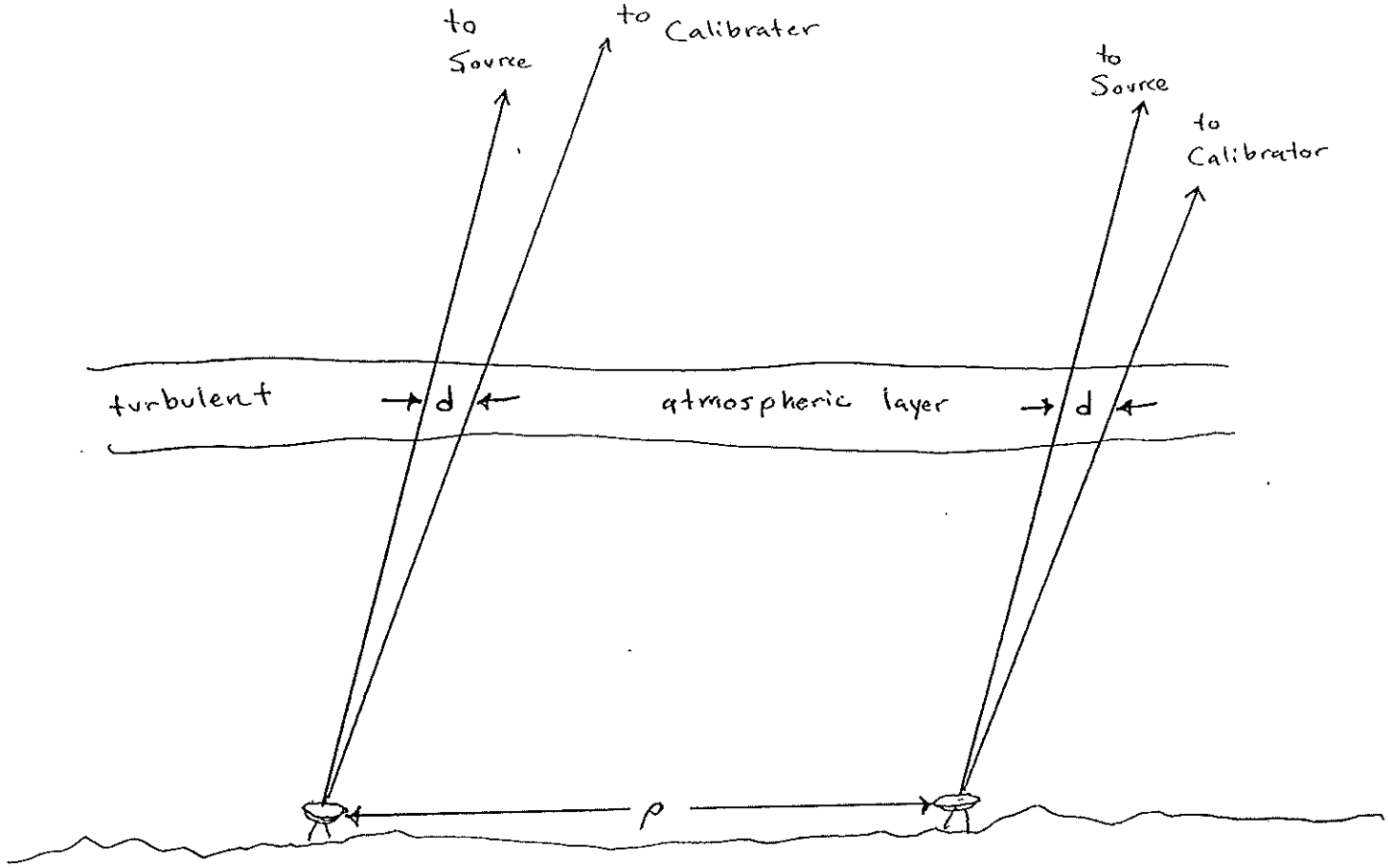

Figure 1

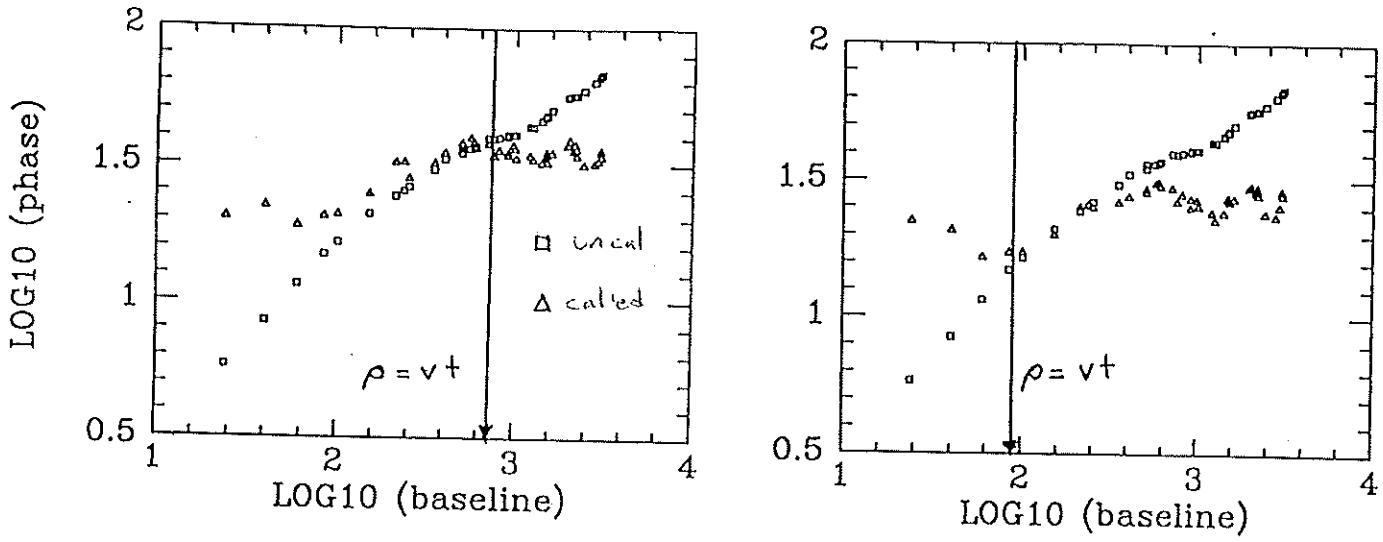

Figure 3: Phase structure function of uncalibrated data compared to phase structure function for calibrated data: 60 s calibration cycle time (a) and 7 s calibration cycle time (b). The distance vt_{cycle} is marked in the baseline axis.

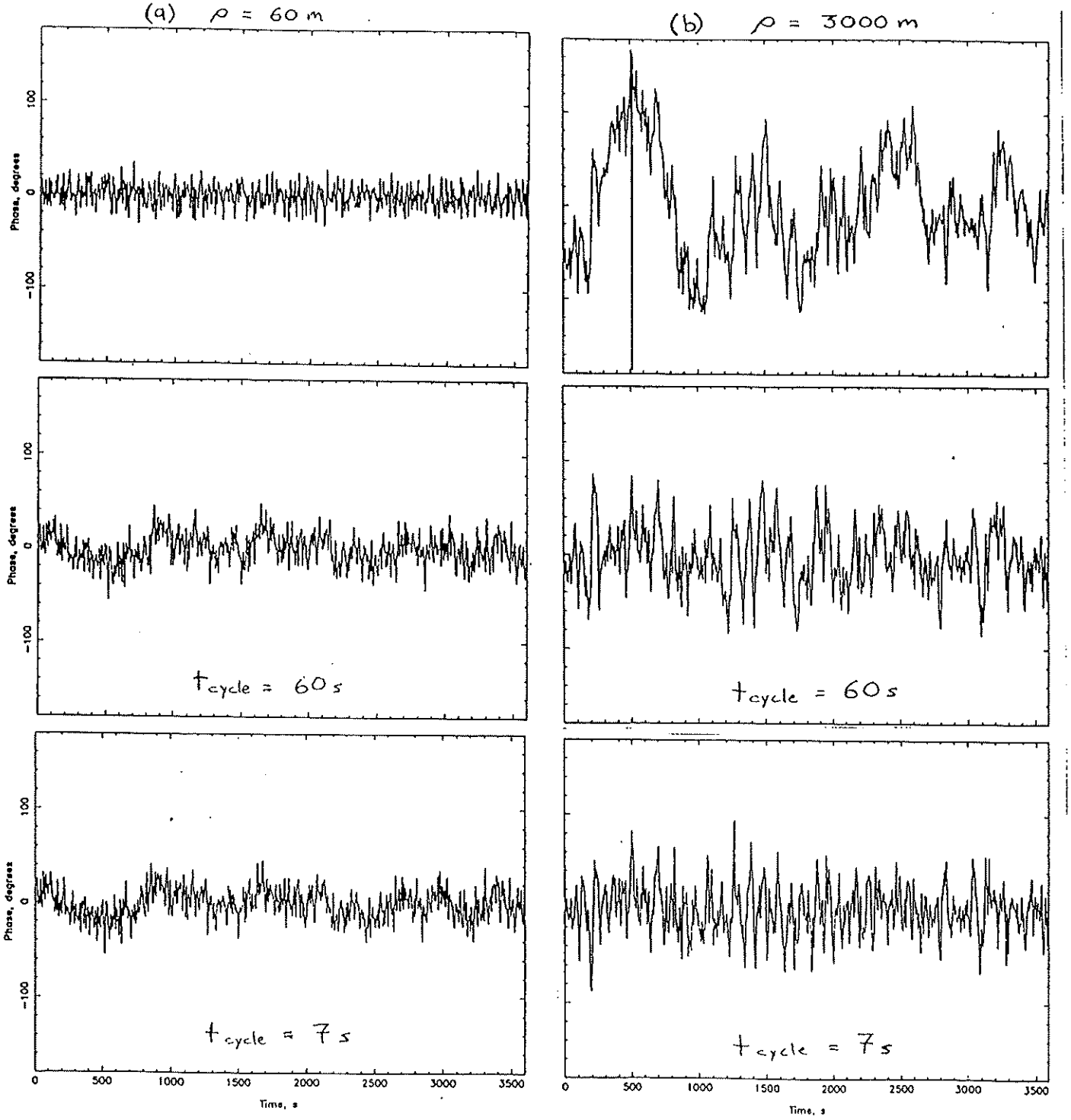

Figure 2: Phase time series for 60 m and 3000 m baselines, uncalibrated, calibrated with 60 s t_{cycle}, and calibrated with 7 s t_{cycle}.

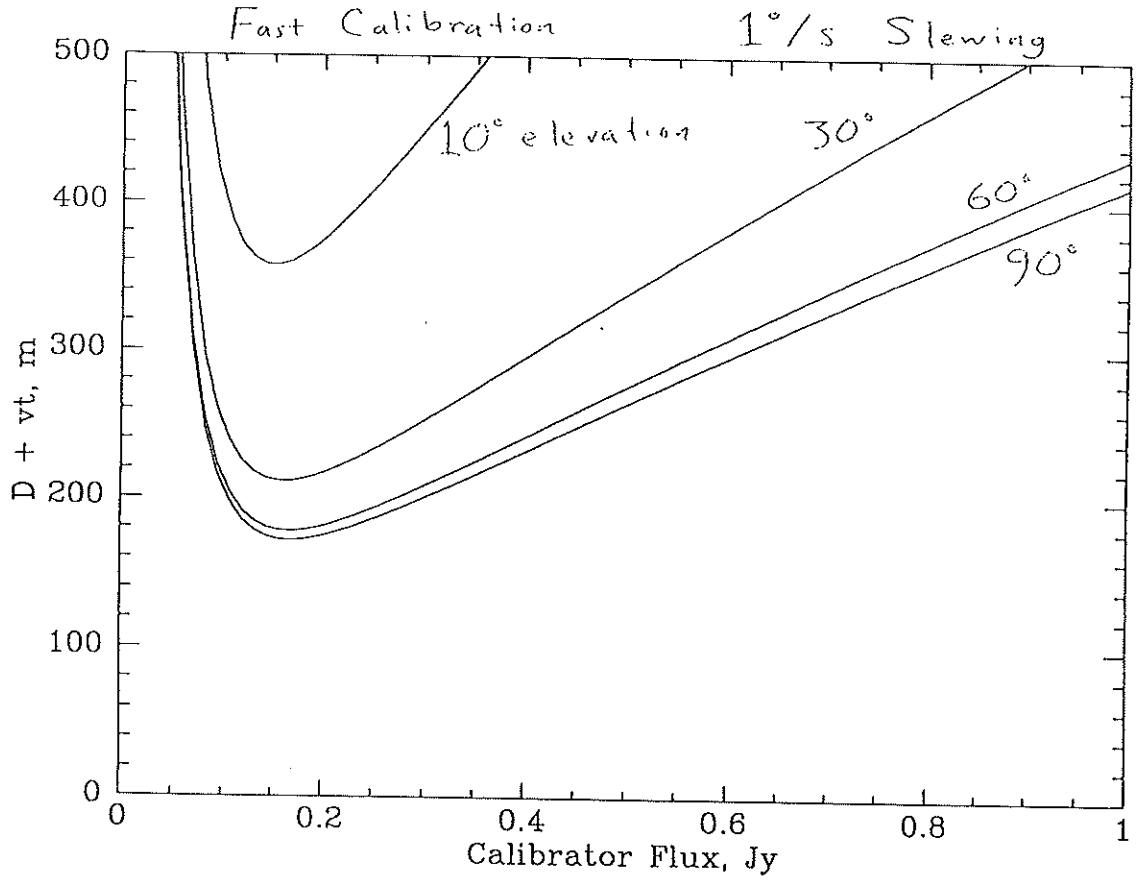
Fast Calibration
1°/s Slewing
10° elevation
30°
60°
90°
D + vt, m
Calibrator Flux, Jy
0
100
200
300
400
500
0.2
0.4
0.6
0.8
1

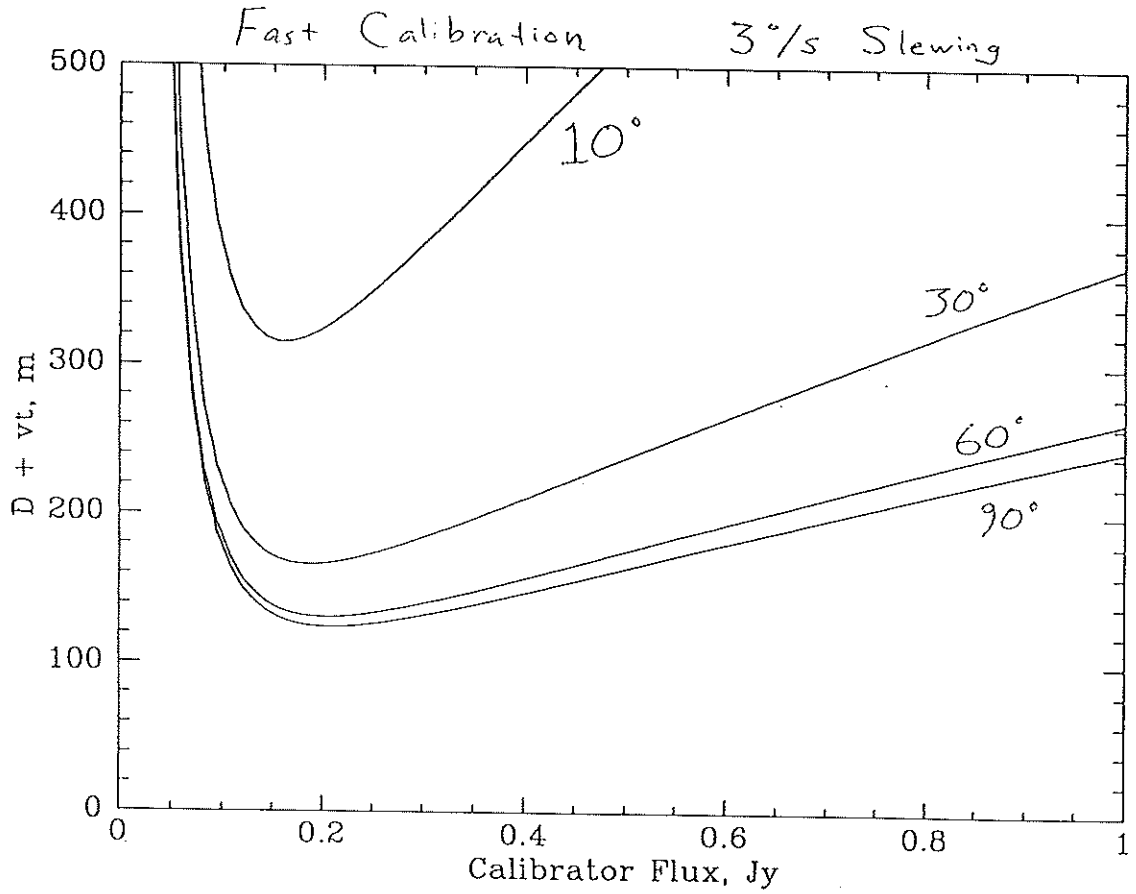
Fast Calibration
3°/s Slewing
10°
30°
60°
90°
D + vt, m
Calibrator Flux, Jy
0
100
200
300
400
500
0.2
0.4
0.6
0.8
1

Figure 4

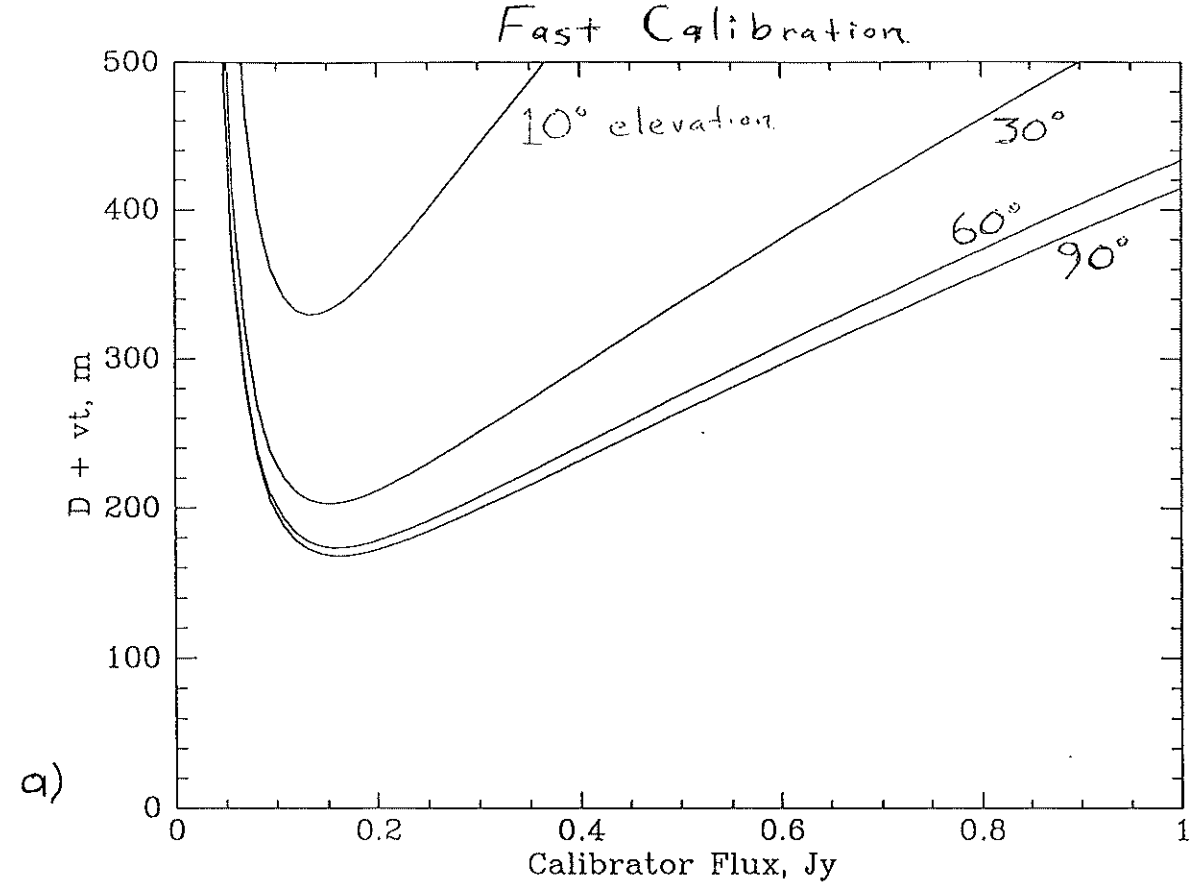
Fast Calibration
10° elevation
30°
60°
90°
D + vt, m
Calibrator Flux, Jy
0
100
200
300
400
500
0
0.2
0.4
0.6
0.8
1

a)

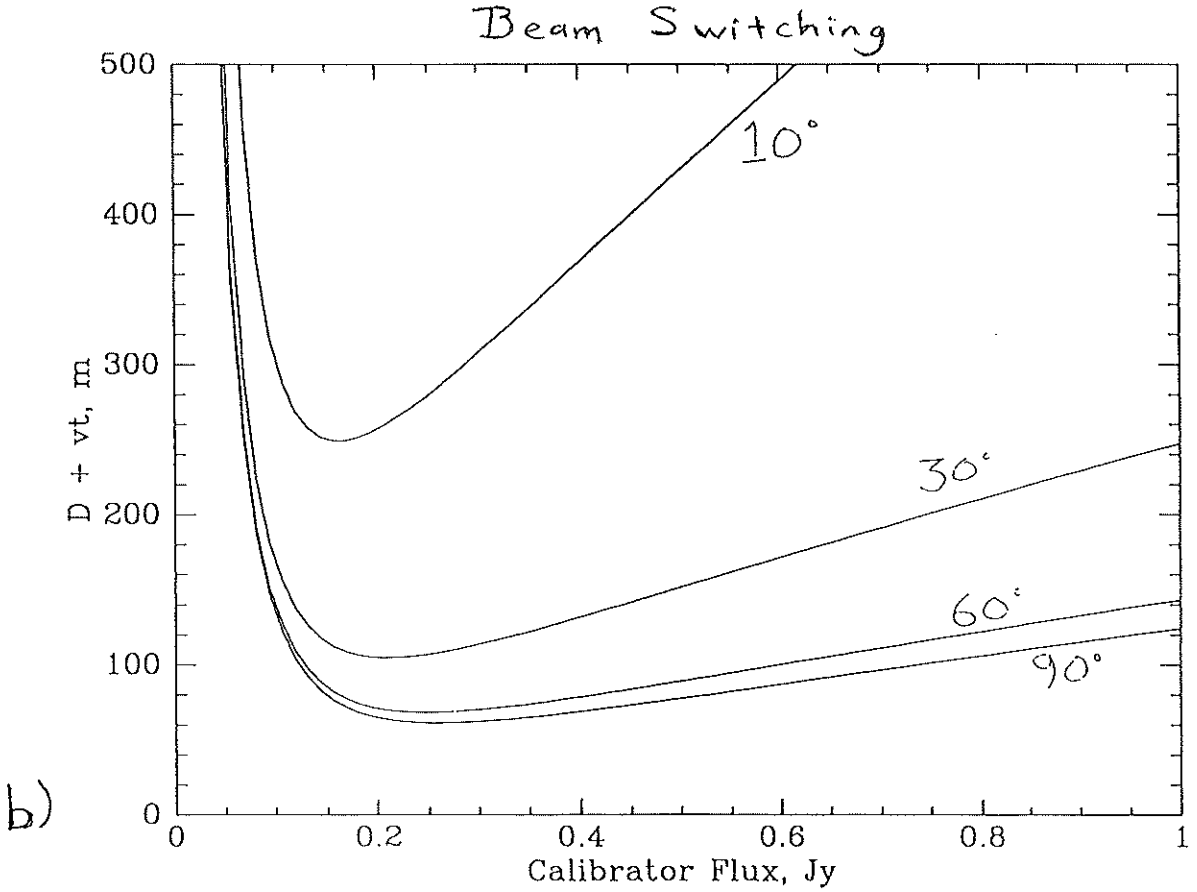
Beam Switching
10°
30°
60°
90°
D + vt, m
Calibrator Flux, Jy
0
100
200
300
400
500
0
0.2
0.4
0.6
0.8
1

b)

Figure 5

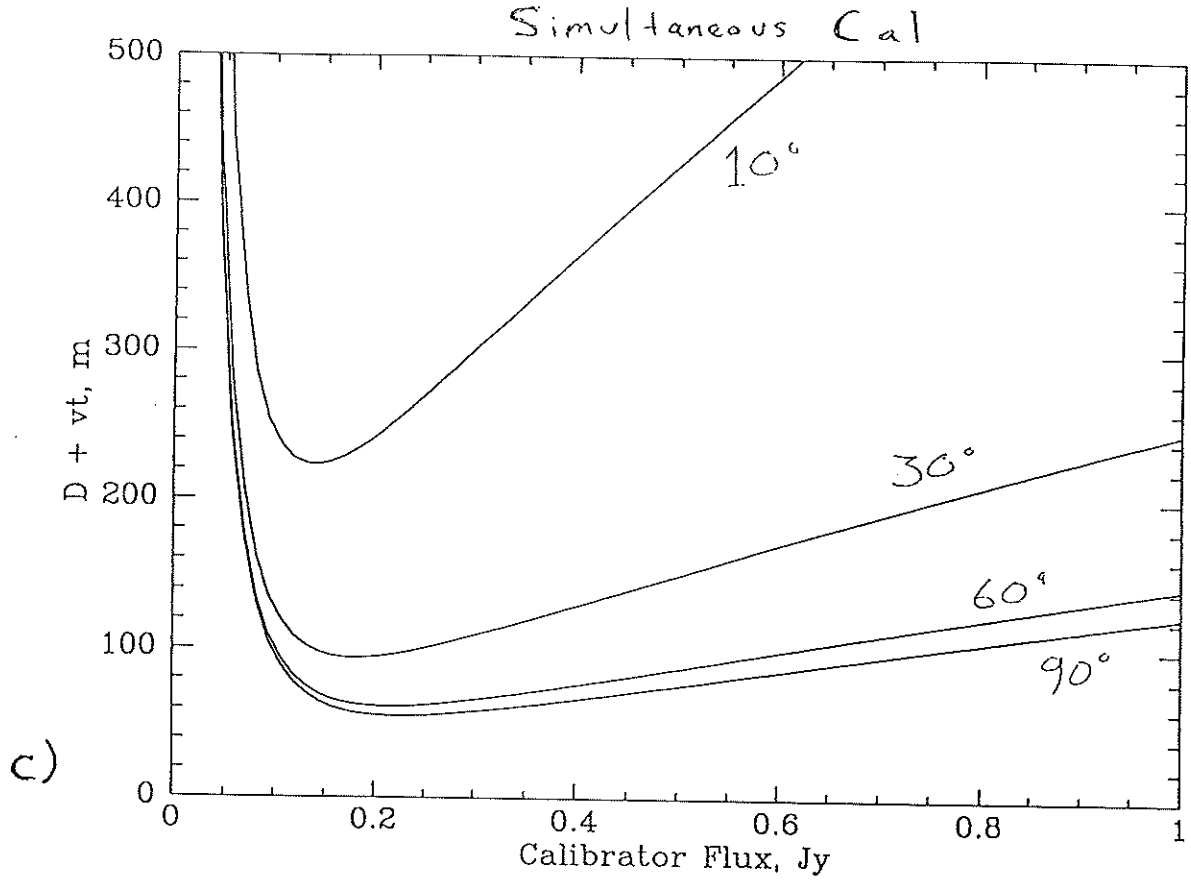
Simultaneous Cal
500
400
300
200
100
0
D + vt, m
10°
30°
60°
90°
0
0.2
0.4
0.6
0.8
1
Calibrator Flux, Jy

c)

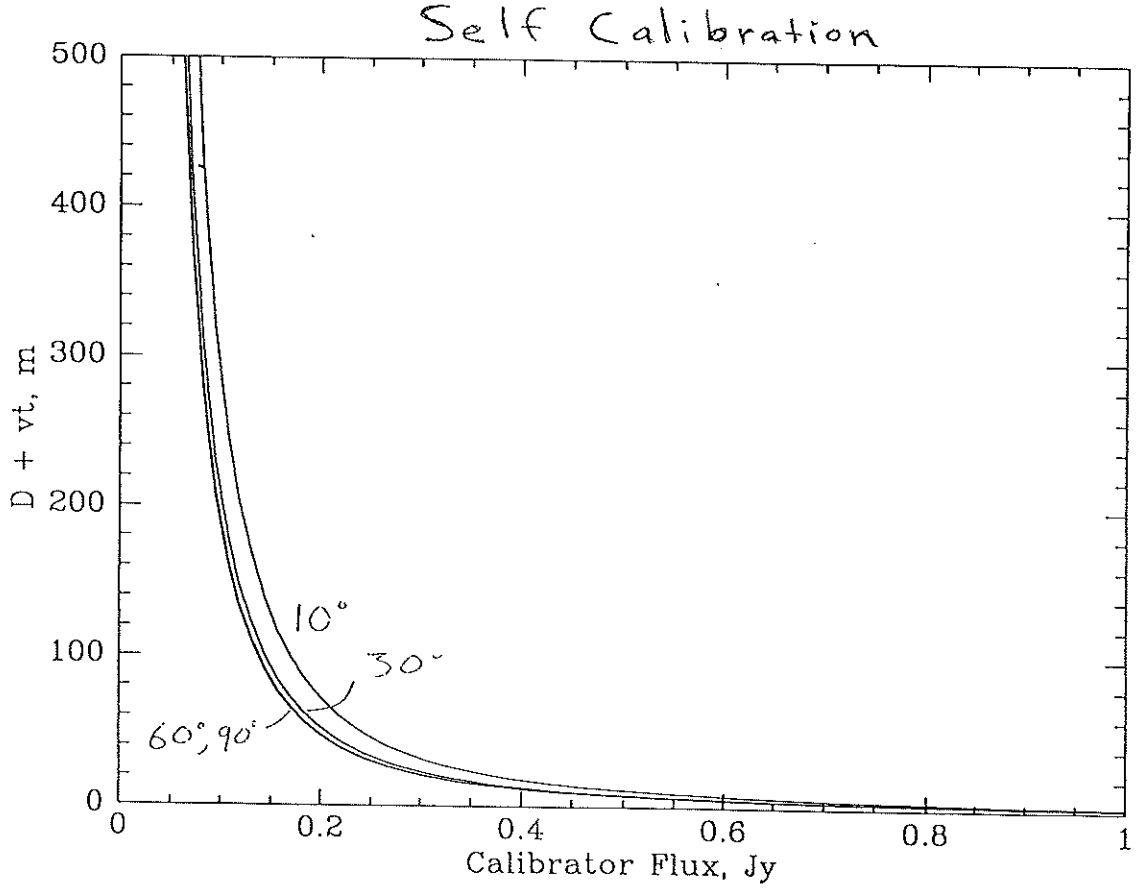
Self Calibration
500
400
300
200
100
0
D + vt, m
10°
30°
60°, 90°
0
0.2
0.4
0.6
0.8
1
Calibrator Flux, Jy

d)

Figure 5

MILLIMETER ARRAY
MEMO NO. 85

Some Remarks on MMA System Design

B.G. Clark

June 1992

Despite the conclusions of the MMA proposal, I feel that there are substantial advantages to an all digital, FX approach to signal processing, because it gives rise to a conceptually simple, highly modular system. I shall discuss a system based on the technology of the VLBA correlator: an FX system built around special purpose butterfly chips with a 32MHz clock rate.

The scientific question to be decided is how much bandwidth should be instantaneously analysed for spectroscopy. The scientists, naturally, will want as much as possible. On the other hand, the cost of the correlator will increase nearly linearly with that bandwidth, and will be a very expensive part of the system, even with a minimum acceptable bandwidth.

Just for purposes of discussion, lets consider an analysed bandwidth of 128 MHz, which is surely near the minimum, if not below it. This is 450 km/s at 86 GHz, only 170 at 230 GHz. This could be used to analyse a single spectrum of that width, or split in two to analyse two spectra of half that width (which could be at quite different frequencies if two LOs are provided in front of the sampler). This is, however, clearly too little bandwidth be make it worthwhile splitting it four ways. If many lines are to be covered simultaneously, for variability or phase referencing reasons, it is more effective to timeshare between them on a rapid cycle.

I shall describe below a definitely non-optimised straw-man system built on these principles.

The IF, after final frequency conversion, would be fed into a sampler module with a 2 GHz sample clock. There would be two (one/polarization) of these samplers (if enough money is invested in the correlator to get enough bandwidth analysed to justify splitting it in 4, one might have 4 samplers). After the VLA experience with bandpass problems introduced in the analog data transmission system, I favor locating the samplers at the antennas, even without an analysis of what the problems are likely to be with a modern data transmission system. I do not address here the question of the number of bits per sample - I suspect that two or three is an appropriate answer.

These bits would be sent to the correlator building, presumably on a bundle of optical fibers.

After the sample stream is reconstructed at the correlator building, it would be delayed to a common clock, and then sent to a serial to parallel converter which would send successive blocks of 64 samples to a string of butterfly chips. A seven chip deep FFT string would apply fringe rotation, apply the sub-sample portion of the delay, and do the FFT such that the output is a set of complex samples of 32MHz wide channels. Successive samples of the same channel may then be obtained from successive FFT strings in the engine. This stage of processing requires 7*64 = 448 butterfly chips for each sampler, a large but not oppressively large number. Two such boxes (one for each polarization (sampler)) would be required for each antenna.

To provide the further spectral analysis, one could in principle select some (4 for a 128 MHz analysed bandwidth) of these datastreams and feed them into a further set of FFT strings, which for a very small price (perhaps 40 chips) will then analyse the spectrum to whatever degree of fineness is desired. In practice it is probably possible to do rather better than this, in effect factoring the FFT to produce much lower response to out-of-band signals than just taking the raw 32MHz channels. Most such schemes seem to involve some data exchange among the last stages of the FFT strings, and the complexity of that is not yet clear to me.

The spectral correlator then consists of a set of 4*40*40 cross correlators. The VLBA correlator is, by comparison, 8*20*20, just half the size. This spectral correlator is about 3200 chips. However, the complexity of the correlator is not adequately measured by the number of chips; the need for having long runs of wire on a two dimensional grid, and preserving clocking integrity over these fairly large chip arrays makes the job more difficult than the antenna based engines, despite the larger total number of chips in the latter.

The size of the correlator doubles, of course, if it is desired to produce full polarization cross products. I suspect that this is sufficiently uncommonly needed in the spectroscopic case that sacrificing half the analysed bandwidth to get it would be acceptable.

The remaining 32MHz channels could be analysed in a continuum correlator. Little thought has gone into the question of how best to do continuum correlation in modern digital logic. It seems to me that it might be just possible to design a chip that would accept samples from 20 antennas, shifted in at a 32MHz rate, and perform the 210 cross multiplications in the time that the next set of 20 samples was being shifted in. If necessary to simplify the logic, assumptions could be made about the RMS and correlation of the samples, which would be acceptable for a continuum correlator. Then, a 32MHz continuum correlator would consist of 160 chips, or the full continuum, cross polarized correlator for 1 GHz in each polarization, of 20,000 chips. Per unit bandwidth, this approach would need only about one fifth as many chips as a full spectral correlator.

All of the above depend on a rather specialized form of "glue" to hold things together, shuffling samples from various FFT strings to arrange the data in the correct order for the next stage of processing. It it might be worthwhile to design special "sample shuffler" chips to do this. Actually, a modest number of gates is needed for these functions, but the number of pins is critical. The correlator would contain perhaps 2000 such "sample shuffler" chips if they could have of the order of 100 pins, but might need 20,000 if they can have only 24 pins.

To summarize, the advantages of this sort of digital approach are:

- Only two LO synthesizers per antenna, with widely spaced lockpoints (say 200 MHz spacing).
- Only two sampler modules per antenna.
- Digital data transmission, with no effect of the transmission system on bandpasses.
- No analog lobe rotators.
- A very modular construction, with the largest module only about 1000 chips.

MILLIMETER ARRAY
MEMO NO. 86

POSSIBILITIES FOR WIDE-ANGLE BEAM-SWITCHING

James W Lamb
26 June, 1992

1 Introduction

One possible scheme for calibrating atmospheric phase variations on short time scales is to switch between the source being observed and a near-by calibration source [1]. In essence, it is assumed that the pathlength variations are due to variations in the water vapor in a thin layer in the atmosphere. The temporal variation is due to this layer being blown over the array. If the irregular layer is blowing by at some velocity v then length scales greater than ℓ can be calibrated if the calibrator is observed with a period $T \lesssim \ell/v$. This means that calibrators which are further from the source will not give such good phase measurements, but it also means that they do not need too be observed as frequently and the speed of switching may be lower. In fact the speed at which the telescope has to move is dependent on v but not on the distance to the calibrator. If there is a calibrator at an angular distance α from the source being observed and the irregular layer is at a height h then the corresponding length scales are $\ell = h/\alpha$.

Parameters which have been proposed are to switch by up to about 1° from the source to the calibrator with a 2 s integration time. This magnitude of beam switching was considered be difficult to do by moving the antenna so some optical switching scheme, such as a focal plane chopper or nutating secondary, has been proposed. Any such arrangement should not compromise the overall sensitivity of the instrument. In this note we compare some methods and conclude that moving the whole telescope is probably the best solution.

2 Comparison With Single-Dish Requirements

Beam-switching has been used for many years on millimeterwave telescopes and several techniques have been devised. Although these methods may serve as a useful basis for developing the required switching mechanism it should be recognized that the use of it proposed for phase calibration differs in several ways from traditional applications. The following points should be considered (for position switching as well as beam switching in the optics)

2.1 Beam Throw

The beam throw is very large compared to traditional beam-switching. Typically throws of a few beamwidths are required, but in this case the throw may be as large as 100 beamwidths. There are several reasons that the throw has been limited. Large throws generally lead to poor beam shapes, reduced aperture efficiency, and increased spillover noise. In addition, when the switching angle is relatively large, the two beam do not overlap in the atmosphere and the desired cancellation of atmospheric fluctuations is not achieved. Deterioration of cancellation can be evident at quite small throws (for example, Jewell [2]). For the proposed mmA antennas the beams become completely separate in the atmosphere after less than 500 m for a 1° throw. This means that the small scale

fluctuations in phase will not be calibrated out, but presumably most of the effect should be in the larger scale structure.

2.2 Switching Speeds

The 2 s integration time is long compared to the rates used in single-dish astronomy, but is commensurate with the larger beam throw required.

2.3 Beam Equality

Usually single dish switching requires that the "signal" and "reference" beam be very similar in terms of beam shape, efficiency, and spillover. In the case being considered here the two beams will be looking at different sources with different requirements. It will be necessary to maintain optimum beam properties for the source being observed but the conditions may be relaxed for the calibrator. Because of the large offsets being considered between the calibrator and the source, it is probable that the source beam would be on or close to the antenna boresight and the calibrator beam would be considerably offset and the attendant degradations accepted. The frequency of observation need not even be the same in the two positions and it may be that the calibrator is observed at a lower frequency than the source.

2.4 Beam Direction

Since the calibrators will be at arbitrary positions relative to the source being studied the beam switching system must be able to move in any direction. This is not usually a requirement for single-dishes, though it is be coming more common (e.g. JCMT, SMT, CSO).

2.5 Phase stability

For the calibration to be effective the phase difference between the source and calibrator beams needs to be stable.

3 Focal Plane Switching

The telescope beam may be switched between the source and calibrator by moving the feed or an image of the feed in the focal plane. Generally the aberrations resulting from a displacement of the feed are smaller than those caused by nutating the secondary mirror to give the same beam displacement, but there is a problem with vignetting by the hole in the primary (assuming that the feed is behind the primary vertex). If the telescope effective focal length is F then the displacement Δx of the feed required to displace the beam by θ is

$$\Delta x = \theta F \qquad (1)$$

For an antenna with a diameter D = 8 m, primary focal length f = 3.2 m, and secondary focal ratio F/D = 12, a 1° beam displacement requires a feed displacement of 1.68 m. This is impractical since an excessively large hole in the primary would be required. Even if the beam were switched by ±0.5° the vignetting would be excessive and the beam degradation in the source beam would be unacceptable.

Another problem with focal plane switching is that the direction the beam must be switched is variable, which could lead to a rather complicated mechanical arrangement.

4 Chopping Secondary

Chopping secondaries have been used on many telescopes because of their versatility, low loss, and wide bandwidth. The primary performance specifications are switching speed, switching angle, and beam degradation. A typical scheme is shown in Figure 1, with the notation used in this document.

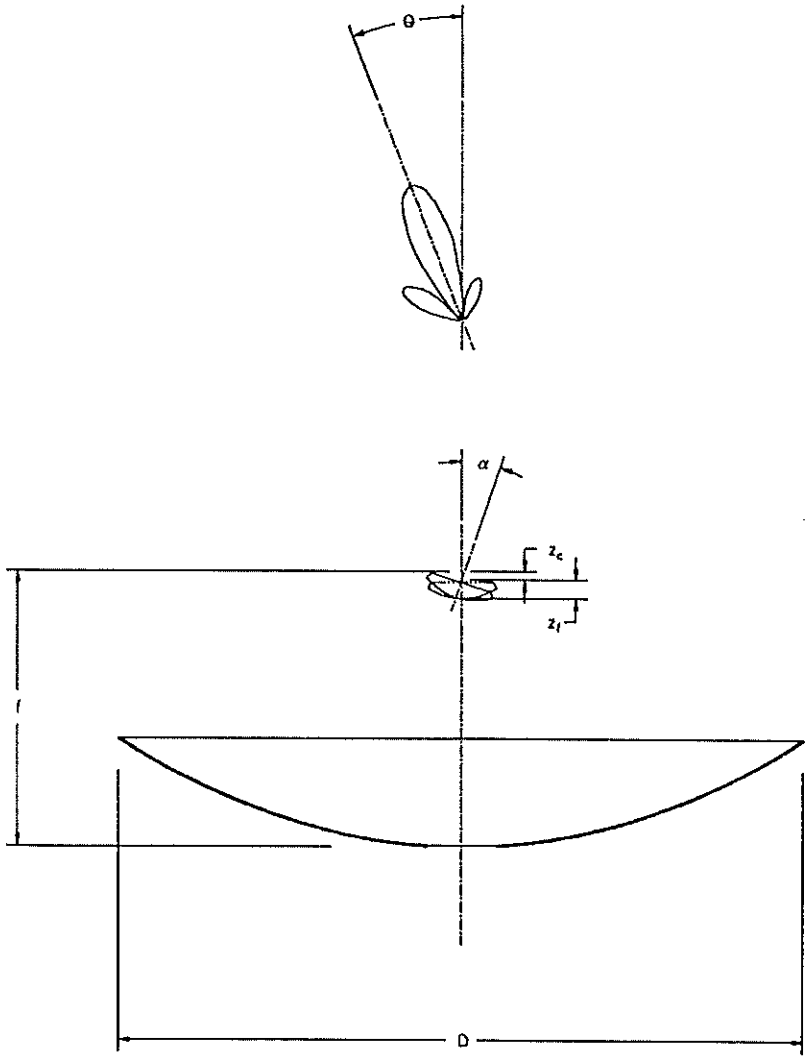

Figure 1 Geometry of the nutating secondary reflector.

4.1 Optical Performance

When the secondary is tilted (Figure 1) there will be aberrations introduced into the beam, and some spillover round the edge of the primary mirror. From the perspective of the aberrations the optimum rotation center for the secondary is at the prime focus ($z_c = 0$), as discussed in detail by Lamb and Olver [3] and van de Stadt [4]. When this point is used the comatic aberrations are very small and the dominant term is the astigmatism. Astigmatic

path length errors increase as the square of the secondary reflector rotation angle so that the gain is reduced in proportion to the fourth power of the beam throw (for small angles). When the center of rotation is about any other point, the errors are mainly comatic. The phase errors are then linear in the rotation angle so that the gain varies as the square of the beam throw. For small beam throws the prime focus center gives the best beam quality, but at larger angles the astigmatism grows too fast. At large angles the higher order aberrations need to be considered also and numerical studies are required to give reasonably accurate results.

Some preliminary studies have been made using ray tracing in the plane of tilt. The cases which were investigated had rotation centers at the prime focus, the secondary vertex, and halfway between these two points: The phase of the aperture field is shown in Figure 2 where a linear term corresponding to the desired beam squint has been removed. For the situation where the prime focus is the rotation center the astigmatic phase error can be seen while the other two cases show the characteristic phase errors for comatic aberrations. It may be seen that the phase error is rather large for the three cases. The pathlength errors were calculated for a number of offset angles and the rms error along the cut through the aperture was calculated — the results are given in Figure 3*a*. As predicted by the first order theory, for small angles the error is quadratic in angle for $z_c = 0$ and linear otherwise, but for large angles the increase is more rapid. It should be noted that the effective pathlength errors will be smaller than these numbers, firstly because the rms over the circular aperture will be less than that along a line through the center, and secondly because the amplitude taper will reduce the weighting at the edges of the dish. However, the numbers are still not negligible in proportion to the wavelengths involved.

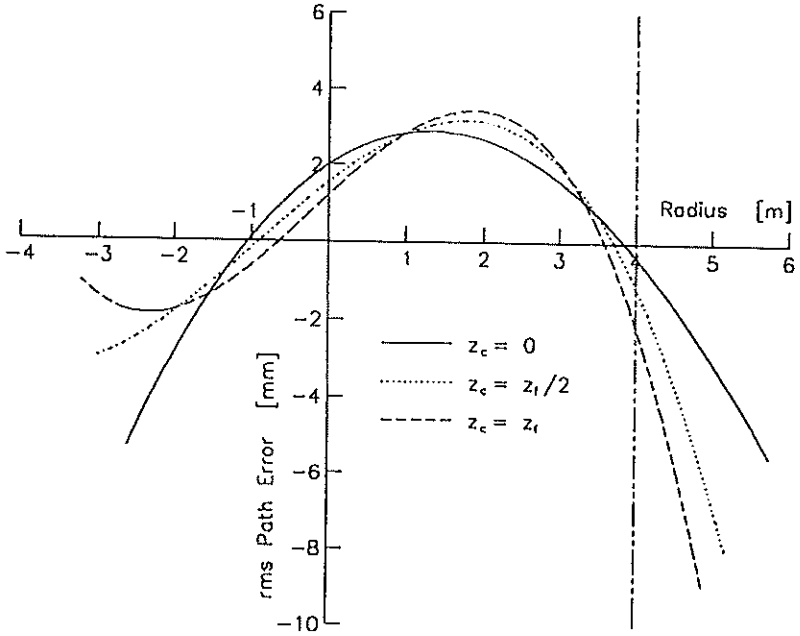

Figure 2 Phase errors in the plane of tilt induced by rotating secondary about different points. The beam squint is 1°.

The other effect which degrades the system is the displacement of the amplitude illumination pattern on the aperture. This leads to reduced gain and an increase in the spillover noise. Figure 3*a* shows an estimate for the magnitude of the pattern displacement for the different cases. It is worst when the rotation is about the focus and reduced by about a factor of two when the rotation axis passes through the vertex. The shift in the pattern is linearly proportional to the beam squint and the spillover noise and gain degradation will both be proportional to this.

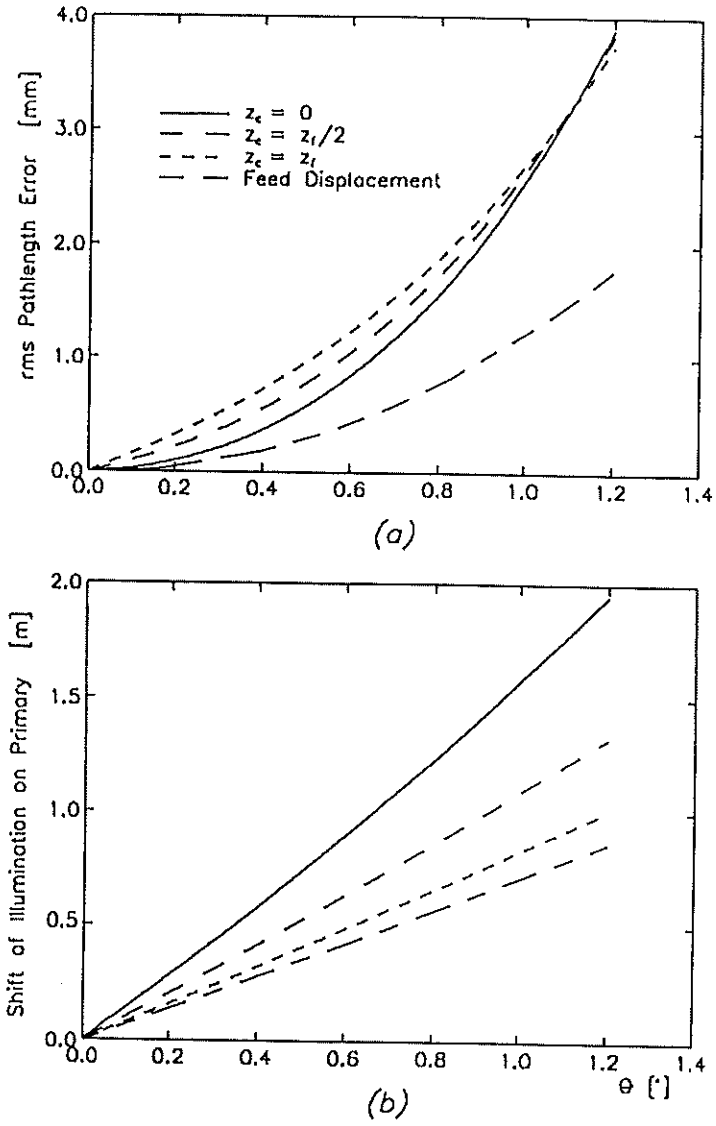

Figure 3 *(a)* Estimated path length error along principal axis in aperture plane. *(b)* Shift of illumination pattern on aperture.

To get a more accurate estimate of the degradation, some beam pattern calculations were made by constructing an aperture field with a Gaussian amplitude shifted by the appropriate amount, and a phase varying in one direction according to the ray tracing results. The beam is broadened in the direction of tilt as expected, and the gain is reduced by about 4.8 dB at 30 GHz. Some of the gain may be recovered by re-focusing the secondary reflector to give about equal phase errors in the two orthogonal directions. This was calculated by adding a defocusing term to the phase which was adjusted to optimize the gain, but the improvement was only about 0.4 dB because of the higher order aberrations which are present. If asymmetrical beam switching was used the secondary would need to be re-focused between positions, but this could be accomplished by moving the rotation center off axis.

The extra spillover noise was determined by integrating the power which spills past the aperture, and it was found that the additional noise temperature for a reasonable range of parameters is given approximately by

$$T_{spill} = 8.7s^2 + 9.3s + 0.23 \quad [kelvin] \tag{2}$$

where s is the shift of the amplitude pattern in m. s is proportional to the beam throw as shown in . This could easily add 10 - 50 K to the antenna temperature, a range comparable to the receiver noise temperatures. The reduction in sensitivity would reduce the number of sources detectably in a given time or increase the integration time required on the source by significant amounts.

For comparison, the pathlength error and the shift in the illumination pattern are both shown for a feed displaced in the focal plane, assuming no vignetting. Both are about half the values for nutation of the secondary about the prime focus.

4.2 Choice of Parameters

The antenna parameters are not yet fixed so it may be that there is a better set of parameters than those chosen here. Variation of the rms pathlength error with so the antenna parameters is shown in Figure 4. The results are insensitive to the value of the secondary focal ratio, but depend strongly on the secondary size and the primary focal ratio. The pathlength error is inversely dependent on the secondary size, but a significant improvement could be achieved only with an unrealistically large secondary. Similarly, only marginal improvements can be obtained by increasing the primary focal length within a reasonable range as the path error is also inversely dependent on the primary focal ratio.

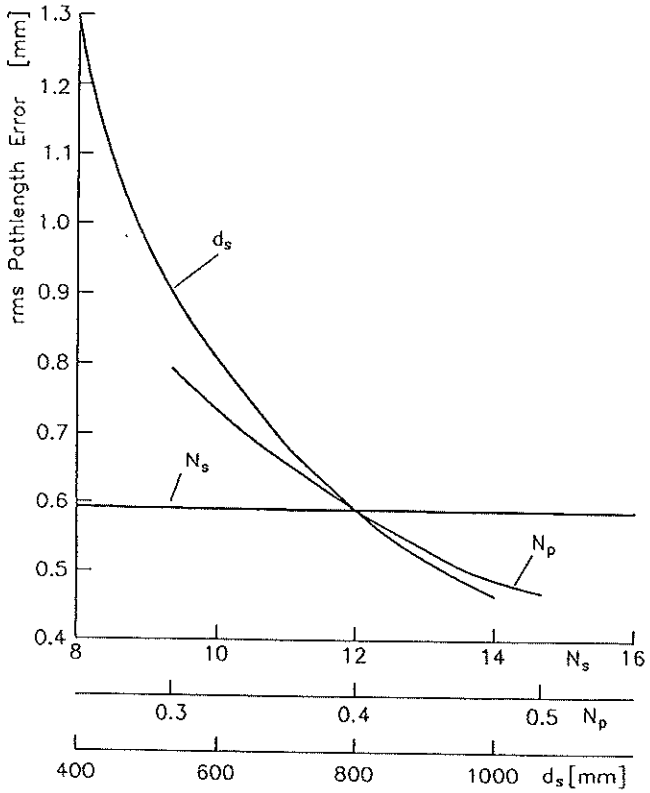

Figure 4 Pathlength error *vs* d_s. $N_s = MfID$, and $N_p = fID$. Nominal: d_s = 800 mm, N_s = 12, and N_p = 0.4.

4.3 Mechanical Considerations

For a constant actuator force the switching time varies as

$$t \propto \sqrt{\alpha} \tag{3}$$

where α is the angle of rotation of the secondary mirror. On the 12-m the switching frequency may be up to 5 Hz and the beamthrow on the sky is ±3 arcmin. In principle, a 1° throw could be achieved with a frequency of about 1.3 Hz for the same system. In practice, the larger beam throw will probably require that the secondary be rotated about the prime focus (rather than a point closer to the secondary vertex) which makes the rotational inertia larger and the required secondary rotation greater for the same beam throw. Additionally, the necessity of two-axis switching will require a more sophisticated mechanism. Use of a relatively light CFRP secondary mirror and a well designed servo system could make this feasible.

5 Ritchey-Chretien Design

The Ritchey-Chretien (RC) design [5] has sometimes been mentioned as a way of obtaining a larger field of view, but this is generally not relevant to millimeterwave antennas. The RC telescope uses two reflectors with equal and opposite coma aberrations to produce an acomatic final design. However, a long focal ratio telescope has very little comatic aberration and astigmatism is dominant at millimeter wavelengths. This is because the path errors increase linearly for the coma term and quadratically for the astigmatism term as a function of the off-set distance in the focal plane. There is therefore a distance where the astigmatic term becomes larger than the comatic term, and it turns out that when this occurs the path errors are still negligibly small compared to a wavelength — when the off-set is large enough to produce appreciable phase errors the astigmatism overwhelms the coma.

It is possible that some comparable scheme could be used to correct astigmatism, but two-reflector schemes which have been devised have the secondary focus in an inaccessible place. A multi-reflector solution may be possible. A further complication is that the RC design is to increase the field of view at the secondary focus whereas the requirement here is to be able to nutate the secondary so that the aberrations are different.

6 Position Switching

Position switching by moving the whole antenna should not be ruled out. Some simple estimates can be based on existing antennas. If the drive system is capable of exerting a torque T and the rotational inertia of the antenna is I then the antenna can be moved to a new position an angular distance θ away in a time t given by

$$t = \sqrt{\frac{2\theta I}{T}} \tag{4}$$

For example, for the 45-ft antenna in Green Bank, the motors can deliver a torque of $T = 1.5 \times 10^4$ kg m, and the moment of inertia is about 3.8×10^4 kg m s^{-2}, giving a switching time of 0.42 s. A number for the mmA may be obtained by scaling the values in some appropriate way. For a given geometry, a direct scaling of the antenna diameter leads to a change in the moment of inertia in proportion to D^5 and the switching time scales according to $D^{2.5}$, giving a switching time of *0.11 s for a 1° position change*. (Note that for now we have neglected the secant elevation term which actually requires that the antenna should rotate more than this for a 1° movement on the sky.) This scale factor may be optimistic since the higher precision requirements of the mmA antennas may require a proportionately greater amount of material in the backing structure to minimize the effects of wind loading. On the other hand, a higher torque motor could be designed in from the start, and the use of a material with a higher stiffness-to-weight ratio, such as CFRP, could be used. It appears, then, that this would be a feasible technique

provided that the necessary specifications were placed on the servo performance from the start. To put things in perspective, a 1° movement of the antenna will move the prime focus position or the edge of the dish by ~100 mm.

The switching time required depends on the off-set to the calibrator. If these are linearly related, a constant velocity movement will give equal performance for all off-sets, but the constant acceleration implied in (4) actually favors the larger off-sets.

An advantage of moving the antenna as opposed to the feed or secondary is that there are no additional spillover noise or aberrations.

7 Other Techniques

Beam switching with the secondary or focal plane switching were proposed because of the difficulty of position switching the whole antenna, although it appears that the latter may not be as much of a limitation as originally thought. It may be possible to use a combination of these methods by position switching the antenna, but using a nutating secondary to "track" the source or calibrator at the ends of the switching half-cycles.

Another possibility is to attempt to correct the aberrations in the feed system. Several implementations could be used. If a single frequency was used the secondary could be nutated symmetrically. If the center of rotation is the prime focus, the phase errors are reduced by a factor of four and as the astigmatism errors are the same for the plus and minus rotations so that a single correction is required for both beams. (Coma is asymmetric so that the optics would need to be rotated by 180° between beams if a rotation center other than the prime focus was used.) If two frequencies were used, the source beam could be on-axis and a corrector could be used for the calibrator beam only. Further work would need to be done to demonstrate that adjustable correcting optics could be designed and constructed.

8 Calibration Frequency

The frequency at which the calibrator is observed need not necessarily be the same as that at which the source is observed. When there are aberrations present the gain will be reduced when the phase errors are a significant fraction of a wavelength so that a lower frequency is preferred.

Another important consideration is the optics needed to diplex the two signals. Dichroic mirrors tend to be relatively lossy, limited in bandwidth, and difficult to construct at short wavelengths. A better solution may be to use a Martin-Puplett Diplexer [6]. Even such a diplexer could be difficult to fabricate if the two frequencies are significantly different since the high frequencies require fine wires and the low frequencies require large grids. The spot size at the Cassegrain focus is about

$$s = 4F/D\lambda \tag{5}$$

For the antenna parameters considered here this is about 480 mm at 30 GHz. Although a smaller secondary f-ratio would apparently reduce the optics size, this is not so in practice since the size of the diplexer also depends on the beam divergence which becomes greater for smaller f-ratios. The minimum diplexer size is around 400 mm and the length of the wires in the grid is almost 700 mm.

Since the beams two frequencies need not be coincident the feeds could be located in different places in the focal plane. This favors higher frequencies since the off-set need not be as large.

9 Conclusions

Simple application of traditional focal plane or subreflector chopping techniques of beam switching will not be adequate for large beam throws required for switching to calibration sources. The beam degradation and system temperature increase could be severely limiting factors. If the calibrator is at a lower frequency then the degradation may be acceptable provided that the beam for the source at the observing frequency is not significantly affected. A frequency of 30 GHz may be acceptable, but the design and layout of the optics would be greatly eased if a higher frequency (90 GHz or greater) can be used.

Position switching the antenna seems to be quite feasible, possibly in conjunction with "fine tuning" the pointing in real time with the secondary mirror. This would need to be included in the specifications for the servo drive system. Dual-frequency operation could be done by offsetting the feeds for the source and calibrator by some small distance in the focal plane. We favor moving this as being the simplest solution. Initial calculations indicate that the switching times could be made very short even for a degree. In addition, the unlimited switching angle means that there is less reliance on having a calibrator within a degree or so of the source.

Since the aberrations are strong functions of the beam throw it is important that some realistic information on the density of suitable sources is obtained — small changes could have a large impact on the design. In addition, the switching time could affect the choice of method considerably. To get a better idea of the requirements we need to know more precisely the distribution of possible calibration sources on the sky, and the length of integrations on the calibrator. A comparison with the possible merits of the calibration source scheme with an alternative method using continuous measurements of the atmospheric emission as measure of the pathlength change should be made.

Although this preliminary analysis shows that there are probably no trivial solutions, it seems likely that some method of switching can be implemented. The optimum solution currently appears to be to move the antenna and possibly to have a calibration feed off-set by a suitable amount in the focal plane. The calibration receiver could be the 65-90 GHz band which would be at the observing frequency while that band was used, or tuned to, say, 90 GHz if a higher band was used.

10 References

[1] M. Holdaway: "Possible phase calibration schemes for the mmA", Millimeter Array Memo No. 84, June 1992.

[2] P. R. Jewell: "Report of 345 GHz Receiver tests", NRAO Tucson Internal Report No. 2, February 1992.

[3] J. W. Lamb and A. D. Olver: "Gain loss and noise temperature degradation due to subreflector rotations in a Cassegrain antenna", *Proc. Int. Conf. Antennas Propagat. 85*, April 1985.

[4] H van de Stadt: "Optimum location of the wobble axis of secondary mirrors in Cassegrain-type telescopes", *IEEE Trans. Antennas Propagat.*, vol. AP-32, no. 10, October 1984, pp 1128-1129.

[5] D. J. Schroeder: *Astronomical Optics*, Academic Press, San Diego, 1987.

[6] D. H. Martin and E. Puplett: "Polarised interferometric spectrometry for the millimetre and submillimetre spectrum", *Infrared Phys.*, vol. 10, pp 105-109, 1969.

National Radio Astronomy Observatory
Charlottesville, Virginia

MMA MEMORANDUM # 87
(also distributed as EDIR No. 291)

Progress on Tunerless SIS Mixers for the 200-300 GHz Band

A. R. Kerr, S.-K. Pan, A. W. Lichtenberger[1] and D. M. Lea[1]

23 July 1992

INTRODUCTION

In the last few years, designers of SIS mixers have begun to exploit the potential of superconducting integrated circuits for achieving full waveguide bandwidths without mechanical tuning. Coplanar and microstrip mixer designs have given promising results at 100 GHz [1, 2], but have not yet approached the performance of the best mechanically tuned SIS mixers [3, 4].

This report describes recent progress on an integrated SIS mixer for the 200-300 GHz band, similar in concept to the coplanar mixer described in [1]. A coplanar circuit allows a much thicker substrate than is possible with a microstrip circuit if higher modes and troublesome parasitic reactances are to be avoided. (A thick substrate greatly simplifies mixer fabrication and assembly.)

The failure of the mixers reported in [1] to match the performance of the best tunable SIS mixers was unexplained at the time of writing of [1]. Since then, we have found strong indications that the upper Nb layer in the tested mixers was very lossy. The evidence is as follows: (i) The conversion loss of the mixers was about 10 dB greater than expected. (ii) The IF output impedance was much lower than expected. (iii) Other (non-integrated) mixers, from the same wafer and with similar tuning circuits, had much higher conversion loss than subsequent mixers of similar design. (iv) Analysis by Mears, *et al.*, [5, 6], of our I-V curves, measured with LO power applied, indicated a substantially capacitive embedding admittance, which suggests that the inductive tuning circuit was not operating properly. Furthermore, the Nb interconnection layer (M3) was an unusual brown-orange color, and had poor adhesion to the wafer.

---

[1] Department of Electrical Engineering, University of Virginia.

MIXER DESIGN

Figs. 1 and 2 show the configuration of the mixer. For operation in the band 200-300 GHz, of interest to radio astronomers, the critical dimensions of the mixer block are scaled by a factor of 0.37 from the WR-10 design of [1]. The resulting non-standard waveguide has inside dimensions 0.0370 x 0.0185 inches, and falls between WR-3 and WR-4. (In the spirit of the EIA waveguide numbering scheme[2], we refer to the new size as WR-3.7.) Energy from the waveguide is coupled to a 50-ohm suspended-stripline via a broadband transducer. A transition is then made to a 50-ohm coplanar line which leads to a series array of six SIS junctions, each with its own tuning circuit [7, 3] as shown in Fig. 2. The inductance of the array of junctions in the hole in the ground plane is tuned out by capacitor C_H in Fig. 2. A four-element low-pass filter consisting of $\sim\lambda/4$ coplanar lines and capacitors acts as an RF choke, while passing DC and IF to a bonding pad at the end of the substrate. This filter was designed [8] to present a relatively low impedance to the SIS junctions from DC to 90 GHz, thereby reducing the likelihood of instability and premature saturation due to high embedding impedances between the IF and RF bands [9].

The mixer was designed according to the procedure described in [3]. The RF source impedance, R_S, and IF load impedance were chosen, for convenience, as 50 ohms. For junctions with a given J-V curve (J is the current per unit area), it is then possible to predict a desirable normal resistance R_N for which the mixer noise temperature is near its minimum, the conversion loss is close to unity, and the input VSWR $\lesssim 2$. In the light of further analysis since writing [3], we have found that for typical Nb/Al-Al_2O_3/Nb SIS mixers, this optimum value $R_N = 2.4\ R_S(100/f(GHz))^{0.72}$. Accordingly, in the present design, $R_N = 62$ ohms. At 250 GHz, a critical current density $J_C = 4500$ A/cm^2 and a specific capacitance $C_S = 45$ fF/μm^2 [10] gives $\omega R_N C \simeq 3$ (the exact value depends on the amount of stray capacitance), and requires an effective (single) junction area of 0.64 μm^2 to give the desired value of R_N. The choice of $\omega R_N C \simeq 3$ is larger than the value of 1.6 suggested in [3] partly to avoid junctions too small to be reliably fabricated using the present process, but also to prevent the inductive junction tuners becoming too long, thus increasing the size of the hole required in the ground plane and its associated inductance which appears in series with the junctions. In this design we used six junctions in series, each with an area of 3.9 μm^2 (diameter 2.2 μm).

In designing the integrated tuning circuits for the individual junctions (Fig. 2), it was found that the (nominally) quarter-wave open circuit stub could be shortened considerably with only a small effect on the embedding impedance, provided the length l_L of the higher impedance line (the inductor) was slightly increased to compensate [8].

---

[2] In the EIA WR-# scheme, # is the waveguide inside width in hundredths of an inch, rounded to a whole number.

MIXER FABRICATION

Nb/Al-Al_2O_3/Nb tri-layers were deposited on z-axis crystal quartz wafers 0.010 inches thick using a process similar to that described in [10]. However, during Nb deposition, the DC magnetron power was held constant while the Ar pressure was adjusted to maintain constant current. This results in a constant deposition rate and uniform film stress from wafer to wafer over the life of the sputtering target.

Following deposition of the tri-layer, the main lithographic steps were as follows:

(i) The Nb/Al-Al_2O_3/Nb trilayer was etched by RIE to define the final pattern of the lower Nb layer (M1).

(ii) The upper Nb layer (M2) was removed by RIE in the vicinity of the $\sim\lambda/4$ stubs, and the lower Nb anodized to produce a 100 nm layer of Nb_2O_5.

(iii) The junctions were defined, and 450 nm of SiO deposited, using the tri-level resist and RIE process described in [11]. M2 now remains only on the junctions.

(iv) The Nb interconnection layer (M3) was deposited and patterned by lift-off.

(v) A layer of Au for bonding and contact pads was deposited by sputtering and patterned by etching.

After dicing the wafer into individual mixers, each mixer was waxed facedown and ground to 0.0035" thick using a dicing saw as a surface grinder.

EXPERIMENTAL RESULTS

The mixers were tested in a liquid helium cooled vacuum cryostat [12] containing 4.2 K IF calibration components, similar to that described in [13]. The incoming RF signal enters the cryostat through a mylar film vacuum window supported by polystyrene foam [14]. It passes through a PTFE infrared filter at 77 K, and enters a scalar feed horn at 4.2 K. LO power is injected through a 20 dB branch-line coupler, also at 4.2 K. A 1.39 GHz IF was used, and all measurements were made with a 50 MHz bandwidth. The IF noise temperature, including a coaxial switch, two isolators, and a directional coupler, was 6.4 K. No IF impedance transformer was used, and no external magnetic field was applied to the mixers.

Using a chopper wheel to switch the input beam between room temperature and 77 K loads, and a Y-factor meter synchronized to the chopper wheel, the LO power and mixer bias voltage were adjusted for minimum receiver noise temperature. Fig. 3 shows the DSB receiver noise temperature as a function of frequency for three mixers from two different wafers, and, for comparison, the corresponding results for an NRAO type 401 (WR-4) mixer with two mechanical tuners [3]. At the higher end of the frequency band it was found that, for normal LO power levels, structure appeared on the pumped I-V curve and the receiver output became unstable, indicating interference from Josephson currents. This Josephson interference could be reduced either by biasing

closer to the gap voltage or by reducing the LO power. The points (Δ) and (□) in Fig. 3 (but not the two isolated points (□) at 230 GHz) were obtained with the LO level reduced sufficiently to eliminate Josephson effects. The points (+), were obtained at normal LO level but with increased bias voltage. The pair of isolated points (□) at 230 GHz, were obtained at normal LO power and with the mixer biased as usual near the middle of the first photon step. Despite the apparently better receiver noise temperature at the two isolated points (□), we believe operation in the presence of Josephson interference is undesirable because of the likelihood of nonlinear response and non-heterodyne detection. Furthermore, when sharp features are present on the photon steps of the pumped I-V curve, the mixer gain also shows sharp variations with bias. The dynamic range of the receiver is likely to be reduced as the IF voltage excursions become comparable with the width of the gain peak [15, 16].

The properties of the mixers were deduced from the measured IF output power from the receiver with hot and cold RF and IF loads [13]. For the three mixers (+, □, and Δ) in Fig. 3, at 230 GHz, L = 0.9 dB, 2.5 dB and 2.6 dB DSB, T_M = 17 K, 12 K and 21 K DSB, and the IF output impedance R_{IF} = 490, 235, and 250 ohms, respectively.

DISCUSSION

Fig. 4 shows the theoretical mixer gain and receiver noise temperature at several LO power levels for the mixer represented by (+) in Fig. 3. It appears that the pronounced rise in the measured receiver noise temperature at higher frequencies is partly inherent in the present circuit design, and partly a result of the need to operate with lower LO levels at higher frequencies if the Josephson effects (mentioned above) are to be avoided. In the future, we plan to use a magnetic field to suppress the Josephson currents, which may eliminate the need to operate with reduced LO power.

At low frequencies, the mixers were limited by an apparent biasing instability. This is understood in terms of the RF embedding admittance (seen by the junction conductance), shown in Fig. 5, which becomes inductive at the low end of the band. Under this condition, a single SIS junction can exhibit negative DC (and IF) output conductance. For a series array of junctions, it is suspected that this can be an unstable situation in which the individual junctions become unequally biased, and ultimately reach one of a number of possible stable dynamic states in which the junctions remain unequally biased. As we have seldom seen this bias instability in tunable mixers using similar arrays of individually tuned SIS junctions, we surmise that it can be avoided by appropriate design of the embedding admittance as a function of frequency. We are now developing a new tunerless mixer designed to prevent this difficulty.

ACKNOWLEDGEMENTS

The authors thank N. Horner, F. Johnson, F. L. Lloyd, and G. Taylor for their invaluable work in fabricating and assembling the mixers.

REFERENCES

[1] A. R. Kerr, S.-K. Pan, S. Whiteley, M. Radparvar, and S. Faris, "A fully integrated SIS mixer for 75-110 GHz," *IEEE Int. Microwave Symp. Digest*, pp. 851-854, May 1990.

[2] D. Winkler, N. G. Ugras, A. H. Worsham, D. E. Prober, N. R. Erickson, P. F. Goldsmith, "A full-band waveguide SIS receiver with integrated tuning for 75-110 GHz," *IEEE Trans. Magnetics*, vol. MAG-27, no. 2, pp. 2634-2637, March 1991.

[3] A. R. Kerr and S.-K. Pan, "Some recent developments in the design of SIS mixers," *Int. J. Infrared Millimeter Waves*, vol. 11, no. 10, Oct. 1990. (Originally presented at the First International Symposium on Space Terahertz Technology, March 1990.)

[4] H. Ogawa, A. Mizuno, H. Hoko, H. Ishikawa, and Y. Fukui, "A 110 GHz SIS receiver for radio astronomy," *Int. J. Infrared & Millimeter Waves*, vol. 11, no. 6, pp. 717-726, June 1990.

[5] C. A. Mears and P. L. Richards, private communication, May-June 1990.

[6] C. A. Mears, Qing Hu, and P. L. Richards, "Numerical simulation of experimental data from planar SIS mixers with integrated tuning elements," *IEEE Trans. Magnetics*, vol. MAG-25, no. 2, pp. 1050-1053, March 1989.

[7] A. R. Kerr, S.-K. Pan, and M. J. Feldman, "Integrated tuning elements for SIS mixers," *Int. J. Infrared Millimeter Waves*, vol. 9, no. 2, pp. 203-212, Feb. 1988. This paper was presented at the International Superconductivity Electronics Conference, Tokyo, Japan, Aug. 1987.

[8] The MMICAD microwave integrated circuit design program was used for circuit simulation and optimization. MMICAD is a product of Optotek, Ltd., Ontario, Canada K2K-2A9.

[9] L. R. D'Addario, "Saturation of the SIS mixer by out-of-band signals," *IEEE Trans. Microwave Theory Tech.*, vol. MTT-26, no. 6, June 1988.

[10] A. W. Lichtenberger, C. P. McClay, R. J. Mattauch, M. J. Feldman, S.-K. Pan, and A. R. Kerr, "Fabrication of Nb/Al-Al_2O_3/Nb junctions with extremely low leakage currents," *IEEE Trans. on Magnetics*, vol. MAG-25, no. 2, pp. 1247-1250, March 1989.

[11] A. W. Lichtenberger, D. M. Lea, R. J. Mattauch, and F. L. Lloyd, "Nb/Al-Al_2O_3/Nb junctions with inductive tuning elements for a very low noise 205-250 GHz heterodyne receiver," *IEEE Trans. Microwave Theory Tech.*, vol. MTT-40, no. 5, pp. 816-819, May 1992.

[12] Infrared Laboratories, Inc., Tucson, AZ, model HD-3(8) (modified).

[13] S.-K. Pan, A. R. Kerr, M. J. Feldman, A. Kleinsasser, J. Stasiak, R. L. Sandstrom, and W. J. Gallagher, "A 85-116 GHz SIS receiver using inductively shunted edge-junctions," *IEEE Trans. Microwave Theory Tech.*, vol. MTT-37, no. 3, pp. 580-592, March 1989.

[14] A. R. Kerr, in preparation.

[15] A. D. Smith and P. L. Richards, "Analytic solutions to SIS quantum mixer theory," *J. Appl. Phys.*, vol. 53, no. 5, pp. 3806-3812, May 1982.

[16] M. J. Feldman, S.-K. Pan, and A. R. Kerr, "Saturation of the SIS mixer," *International Superconductivity Electronics Conference, Tokyo, Digest of Technical Papers*, pp. 290-292, Aug. 1987.

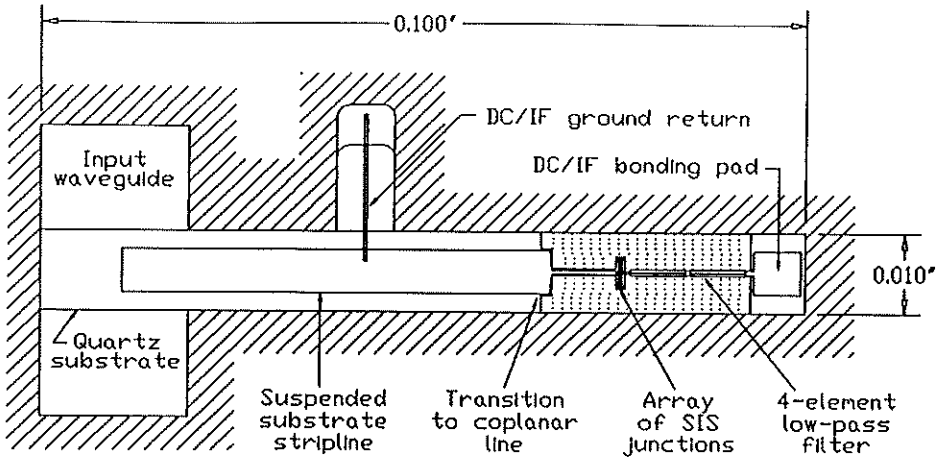

Fig. 1. The complete mixer, showing the waveguide to suspended stripline transducer, DC and IF ground return stub, and the coplanar mixer circuit. The quartz substrate is 0.100" x 0.010" x .0035" thick.

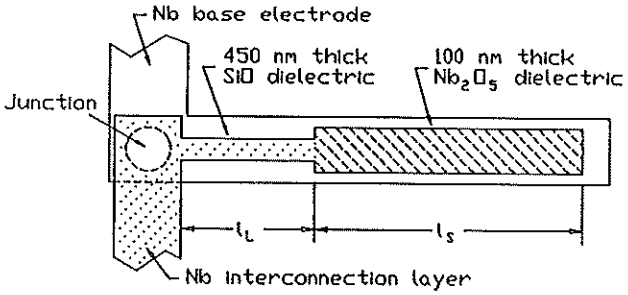

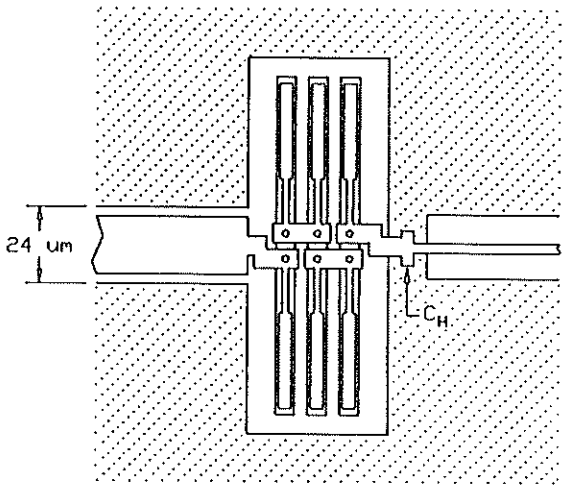

Fig. 2. (Upper) Details of an inductively tuned SIS junction. (Lower) Array of six inductively tuned junctions connected to the coplanar input line. The inductance of the hole in the ground plane in the vicinity of the array is tuned out by the capacitor C_H.

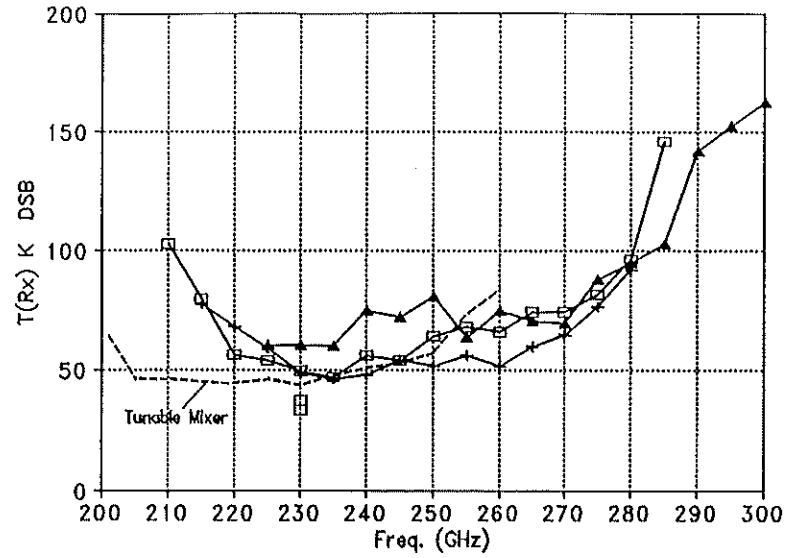

Fig. 3. DSB receiver noise temperature (measured outside the vacuum window) for three mixers from two different wafers. Also shown (dashed) for comparison is the noise temperature of a receiver using an NRAO 401 mixer with two mechanical tuners. Points (▲) and (□) in Fig. 3 (but not the two isolated points (□) at 230 GHz) were obtained with the LO level reduced sufficiently to eliminate Josephson effects. Points (+) were obtained at normal LO level but with increased bias voltage. The pair of isolated points (□) at 230 GHz were obtained at normal LO power and with the mixer biased near the middle of the first photon step. All measurements were made at 4.2 K.

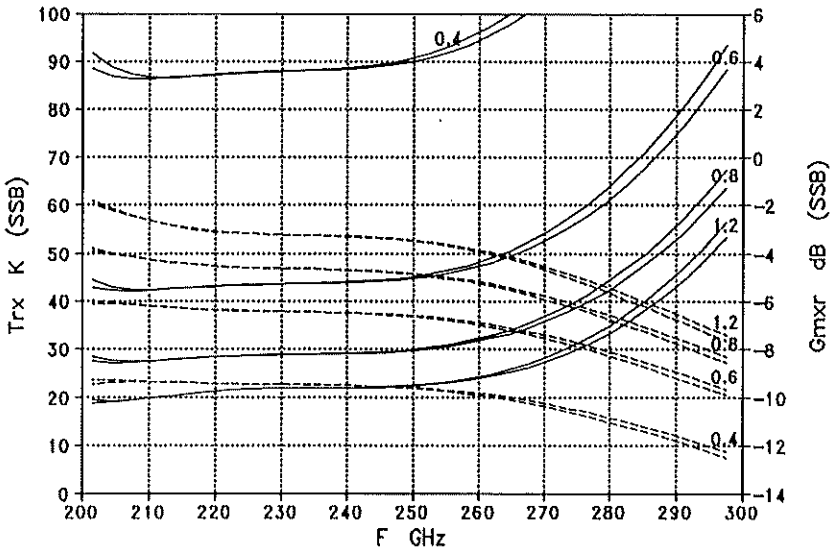

Fig. 4. Theoretical upper- and lower-sideband gain and receiver noise temperature (SSB) versus frequency for the mixer represented by (+) in Fig. 3. The parameter is the normalized LO amplitude $\alpha = eV_{LO}/hf$. The IF noise temperature is 6.4 K corresponding to the measured value for these experiments. No correction has been made for the loss of the vacuum window, infrared filter, feed horn, or LO coupler ahead of the mixer.

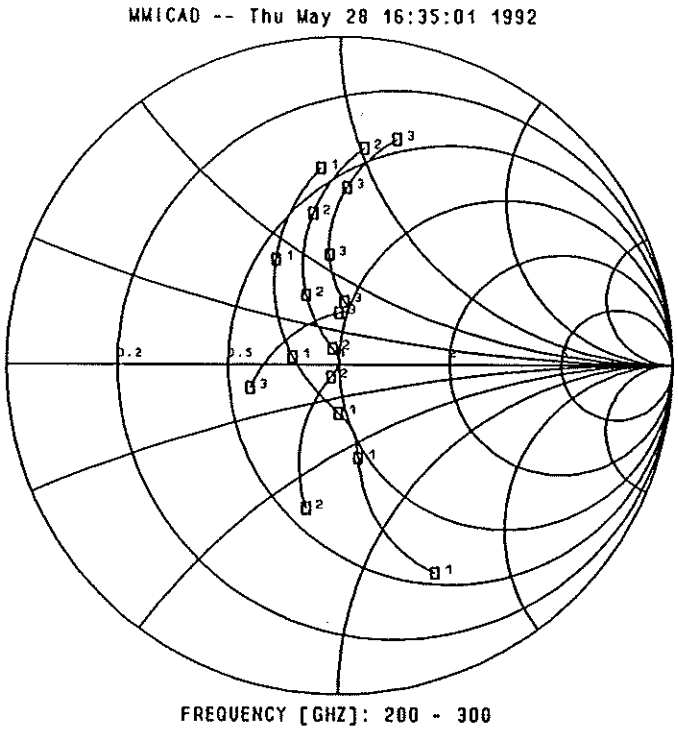

Fig. 5. The embedding admittance seen by the array of junctions, as a function of frequency, for inductor lengths l_L = 10.6 μm, 12.5 μm, and 14.5 μm, shown on a Smith (admittance) chart normalized to (50 ohms)$^{-1}$. Frequency markers are every 20 GHz.

MILLIMETER ARRAY
MEMO NO. 88

Paired Antenna Phase Calibration: Residual Phase Errors and Configuration Study

M.A. Holdaway
National Radio Astronomy Observatory
Socorro, NM 87801

Aug 17, 1992

1 Introduction

In MMA Memo 68, it was shown how the MMA site survey data could be converted into atmospheric models which could be used in interferometer simulations, leading to estimates of the phase stability and the phase structure function. MMA Memo 84 developed a method of analyzing calibration schemes which can be summarized by the following steps:

- A calibration scheme implies a cycle time t and a distance between the lines of site to the calibrator and the target source in the atmosphere d.
- After calibration, the rms phase errors on baselines which are long compared to $\mathbf{v}t + \mathbf{d}$, will be approximately $\sqrt{2D_\phi(\mathbf{v}t + \mathbf{d})}$, where $D_\phi(\rho)$ is the phase structure function and $\mathbf{v}$ is the velocity of the atmosphere.
- The phase structure functions for a range of atmospheric conditions have been determined from the method of MMA Memo 68 and are presented in MMA Memo 84.
- Interferometric simulations using the method of Memo 68 and the residual phase structure function indicate the image quality which results from the calibration scheme.

Several novel approaches to phase calibration were presented in Memo 84, but because of hardware limitations, none of them are sure to work. This memo looks at another calibration scheme called *paired antenna calibration*, in which the MMA's 40 antennas are paired spatially, and in conditions of poor phase stability, one antenna from each pair will view a calibrator while the other 20 antennas view the target source. The phase fluctuations seen on the calibrator antenna are then applied to its paired antenna for the astronomical observations. The main advantage to this scheme is that there are no technical or hardware problems which will prevent it from working.

In the D, C, and B arrays, the antennas are already close enough to permit a paired antenna scheme to work. However, paired antenna calibration is incompatible with mosaicing in the D and C configurations, which requires complete Fourier plane coverage when imaging

fields which are filled with emission, and hence, all 40 antennas are required for observing the astronomical source. This is not a problem since the phase stability in the D and C arrays will usually be quite good anyway, and calibration schemes like paired antennas calibration will not be required. In the A array, observations will be split between bright quasars, which permit selfcalibration, and very weak spectral line or dust continuum objects with fairly simple source structure, which may require hours of integration to get enough signal to meet the scientific objectives. A paired antenna array design must permit high quality imaging of the bright objects using all 40 antennas. Reducing the astronomical part of the array to only 20 antennas for observations of weak sources will half its sensitivity and degrade its (u, v) coverage. For these simple, weak sources, the sensitivity loss is important, but the loss of (u, v) coverage is probably not important. During the best atmospheric conditions, all 40 antennas can observe the astronomical source coherently and at full sensitivity.

In this memo, I analyze the improvement in phase stability due to paired calibration, present a prototype paired antenna A configuration, gauge the effects of the poorer (u, v) coverage, and point out various tradeoffs due to the paired calibration.

2 Analysis of "Pair Calibration"

Following the analysis scheme of MMA Memo 84, the quantity $\mathrm{v}t + \mathrm{d}$ becomes $\mathrm{v}t + \mathrm{d} + \mathrm{B}$, where B is the typical baseline between the paired antennas in meters. While v, d, and B are all vectors, we will not treat them as vectors in this document. Treating them as scalars is a worst case. With 20 antennas looking at the calibrator, there is no need for fast slewing, fast switching, or short setup times, so the "cycle time" is simply the time required to detect the calibrator. Using an expression appropriate to 20 antennas and the notation of Memo 84, we get that

$$vt + d + B = v\left(\frac{.002RT_{sys}}{\epsilon_a S}\right)^2 + \frac{h\sin(7.1S^{0.75})}{\sin\theta} + B. \qquad (1)$$

R is the required signal to noise per calibrator visibility (R=1 leads to 12° phase errors in the gains for 20 antennas), T_{sys} is the system temperature, ϵ_a is the aperture efficiency, tabulated in Table 2 on MMA Memo 84, S is the brightness of the calibrator in Jy, h is the height of the turbulent layer of water vapor above the array, and θ is the elevation of the target source. T_{sys} depends upon frequency, water vapor column height, and elevation angle as indicated by Equation 15 of MMA Memo 84.

Optimal values for $vt+d$ and the minimum calibrator flux (assuming $h = 1000$ m, $v = 12m/s$ (Schwab, 1992), and $B = 0$) are presented in Table 1. The rms phase errors at 230 GHz can be determined for South Baldy from the phase structure functions given in Equations 1-3 of MMA Memo 84 for these values of $vt + d$ and various values of B and are listed in Table 2. With the paired antennas 100 m apart, phases are 30-40% worse than if the antennas are as close together as possible. Comparing the phase errors in Table 2 and those in Tables 4 and 5 in MMA Memo 84, we see that the paired antenna calibration scheme yields phase errors which are comparable to or better than position switching calibration (referred to as *fast calibration*

Elevation	$vt + d$	S
90.000	92	0.45
60.000	103	0.425
30.000	160	0.375
10.000	393	0.300

Table 1: Optimal values of $vt+d$ and S assuming $B = 0$. The calibrator list should be complete down to flux S to ensure calibrators are near enough. For nonzero B, the optimal value of S is unchanged and the optimal $vt + d$ is increased by B.

in MMA Memo 84), but not as good as beam switching phase calibration or simultaneous phase calibration.

Phase errors in Table 2 cannot be directly compared to the phase errors in Tables 4 and 5 in MMA Memo 84. From the imaging simulations reported in Memo 84, a 60° rms residual phase error will permit moderate dynamic range imaging (85:1) with the 40 element MMA. However, using 20 elements to image the target source would require 30° phase errors to obtain the same dynamic range. If we use a paired antenna approach and switch the antennas which view the source every couple of minutes, then phase errors go down by $\sqrt{2}$ and dynamic range goes up by $\sqrt{2}$ if the residual phase errors in each 20 element subarray are independent.

It is assumed that 60° phase errors are required for an image dynamic range of ~85:1 for position switching calibration, beam switching calibration, and simultaneous calibration; 43° for paired antenna calibration, and 38° for infrequent calibration (10 minutes). Using the interpolation scheme used in MMA Memo 68, we can estimate the fraction of time the array will be usable at high frequencies with each calibration method (see Table 3). We can also look at the fraction of time when high quality observations will be possible. 30° phase errors result in an image dynamic range of 250:1 for position switching calibration, beam

ASD(56 s)	Zenith			30 degrees		
	$B = 10$ m	$B = 100$ m	$B = 500$ m	$B = 10$ m	$B = 100$ m	$B = 500$ m
0.04K	2.9°	4.0°	7.4°	7.5°	9.5°	16°
0.07K	7.9°	11°	20°	21°	26°	43°
0.13K	19°	26°	39°	50°	59°	82°
0.20K	31°	43°	65°	83°	97°	135°
0.30K	48°	66°	98°	126°	147°	205°

Table 2: RMS phase errors after paired antenna calibration for atmospheres of various Allan standard deviation (ASD) at 56 s averaging time at zenith and at 30 degrees elevation, for the distance between paired antennas B of 10 m, 100 m, and 500 m.

switching calibration, and simultaneous calibration; 21° for paired antenna calibration, and 20° for infrequent calibration (~10 minutes). Brightness temperature calibration has not been included in these tables because the main contributors to the residual phase errors, namely fluctuations in the atmosphere temperature and the receiver temperature, have not yet been properly analyzed. We also list the increase in noise which goes along with each method and how certain we are that the calibration method will work. The increase in noise is due to three factors: less time, fewer antennas, and less bandwidth (one IF instead of two) on the target source. The assumptions which have entered into the increase in noise are:

- infrequent calibration, it is assumed that the loss in time due to calibration is insignificant.
- Paired antenna calibration utilizes both IFs all of the time for half of the antennas.
- Position switching calibration utilizes both IFs in all of the antennas, but only one third to one half of the time.
- Beam switching calibration uses only one IF since it requires observations at two different frequencies, and only one half to one third of the time will be spent on source.
- Simultaneous calibration allows us to observe the target source all of the time with all of the antennas, but only in one of the IFs.

These assumptions will need to be revised as the MMA design changes, but the basic truth of the matter is that we are trading sensitivity for phase stability. The "technical challenges" column indicates that some of these methods present technical problems in the antenna design which have not been solved at the present time:

- For position switching to be competitive, the antennas must switch position very quickly and remain stable.
- For beam switching calibration to work, the subreflector must be able to switch $1 - 2°$ quickly, point reasonably accurately to both positions, and not distort the antenna's shape too much.
- For simultaneous calibration to work, the optics must be designed to track two different beams separated by 1-2° on the sky.

The Springerville phase structure functions have also been determined. There has been some concern that the calibration techniques would not work as well at Springerville due to a flatter structure function on short baselines. The same analysis has been performed for the Springerville site's A array usability, and is presented in Tables 4 and 6. In this memo, I will deal with the South Baldy data since the residual phase errors after calibration are smaller at South Baldy. Note that this depends solely upon the phase structure function. A future comparison between the Springerville and South Baldy sites will take another look at the phase structure functions at the two sites.

Calibration Method	A array usability at zenith	A array usability at 30° elevation	noise increase	technical challenges?
infrequent calibration	22%	9%	1	no
paired antennas ($B = 10$m)	46%	24%	2	no
paired antennas ($B = 100$m)	38%	22%	2	no
paired antennas ($B = 500$m)	28%	14%	2	no
position switching calibration	46%	27%	$\sqrt{2} - \sqrt{3}$	yes
beam switching calibration	>52%	35%	$2 - \sqrt{6}$	yes
simultaneous calibration	>52%	37%	$\sqrt{2}$	yes

Table 3: **South Baldy.** Estimates of the fraction of time the A array will be usable at high frequencies at zenith and 30° elevation using various calibration schemes. "Usable" means that residual atmospheric phase fluctuations will not limit the dynamic range to below 85:1 at 230 GHz, or below 60:1 at 345 GHz. Much of the usable time will permit higher dynamic range.

Calibration Method	A array usability at zenith	A array usability at 30° elevation	noise increase	technical challenges?
infrequent calibration	15%	3%	1	no
paired antennas ($B = 10$m)	42%	17%	2	no
paired antennas ($B = 100$m)	38%	14%	2	no
paired antennas ($B = 500$m)	27%	6%	2	no
position switching calibration	38%	15%	$\sqrt{2} - \sqrt{3}$	yes
beam switching calibration	>50%	21%	$2 - \sqrt{6}$	yes
simultaneous calibration	>50%	22%	$\sqrt{2}$	yes

Table 4: **Springerville.** Estimates of the fraction of time the A array will be usable at high frequencies at zenith and 30° elevation using various calibration schemes.

Calibration Method	A array usability at zenith	A array usability at 30° elevation	noise increase	technical challenges?
infrequent calibration	10%	4%	1	no
paired antennas ($B = 10$m)	27%	14%	2	no
paired antennas ($B = 100$m)	21%	11%	2	no
paired antennas ($B = 500$m)	14%	7%	2	no
position switching calibration	29%	17%	$\sqrt{2} - \sqrt{3}$	yes
beam switching calibration	45%	21%	$2 - \sqrt{6}$	yes
simultaneous calibration	47%	22%	$\sqrt{2}$	yes

Table 5: **South Baldy.** Estimates of the fraction of time the A array will produce *high quality images* at high frequencies at zenith and 30° elevation using various calibration schemes. "High quality images" means that residual atmospheric phase fluctuations will not limit the dynamic range to below 250:1 at 230 GHz, or below 170:1 at 345 GHz.

Calibration Method	A array usability at zenith	A array usability at 30° elevation	noise increase	technical challenges?
infrequent calibration	$\sim 0\%$	$\sim 0\%$	1	no
paired antennas ($B = 10$m)	22%	4%	2	no
paired antennas ($B = 100$m)	16%	3%	2	no
paired antennas ($B = 500$m)	6%	2%	2	no
position switching calibration	17%	4%	$\sqrt{2} - \sqrt{3}$	yes
beam switching calibration	29%	6%	$2 - \sqrt{6}$	yes
simultaneous calibration	32%	7%	$\sqrt{2}$	yes

Table 6: **Springerville.** Estimates of the fraction of time the A array will produce *high quality images* at high frequencies at zenith and 30° elevation using various calibration schemes. "High quality images" means that residual atmospheric phase fluctuations will not limit the dynamic range to below 250:1 at 230 GHz, or below 170:1 at 345 GHz.

3 Configuration Feasibility

The current designs for the D and C configurations would not need to be changed as the shortest baseline from any antenna is much less than 100 m. If the B configuration is a randomized ring 800 m in diameter, the average distance between antennas will be 60 m. The configuration design might need to be tweaked up to ensure all antennas' nearest neighbor is less than 100 m away. Hence, such a scheme would result in no loss of flexibility of the D, C, and B arrays: during excellent atmospheric stability, all 40 antennas could be used to observe the source and calibration could be performed on timescales of tens of minutes. For the three smallest configurations, a different calibration method might be used: half of the array would observe the calibrator and solve for a 2-D image of the atmospheric phase as a function of time. The phase error and array usability analysis is the same as for paired antenna calibration, but the appropriate B must be used.

In the A configuration, the average spacing to the nearest neighbor is greater than 100 m, and some antennas will be several hundred meters away from their nearest neighbors. Some improvement will result from performing the paired antennas calibration on the nearest neighbor, but the A configuration can get much more benefit out of this scheme if it is redesigned to have closer nearest neighbors. This illustrates one of the fundamental tradeoffs inherent in the paired antenna calibration scheme: the array is usable for more time if the antennas are placed very close together, but the (u, v) coverage is optimized when the antennas are placed further apart.

To demonstrate the feasibility of a 3 km array of 40 paired antennas, we have performed a configuration study using Ge's configuration toolkit (1992b). The antennas in each pair are located about 100 m distant from each other. The resulting configuration is not intended to be an optimal configuration, but merely indicates that such an array is feasible. To find an optimal array of 40 paired antennas, a modification could be made to the simulated annealing array design scheme presented in Cornwell (1986) and Holdaway (1992b).

A possible paired array design is found in Figure 1. When all 40 antennas are used to look at a source, the (u, v) coverage has a nice banding due to the four correlations between any two pairs of antennas. The result is not unlike the (u, v) coverage which one gets from multi-frequency synthesis, except that the offset between the tracks in the band are not necessarily radial. Examples of the full tracking[1] (u, v) coverage obtained from all 40 antennas is shown in Figure 2. While the (u, v) coverage is good, it is clear that better (u, v) coverage can be obtained in a 40 element array of *unpaired* antennas (see MMA 80, Appendix B, Figure 2b). The snapshot coverage is not very good for the paired configuration.

If the paired antenna calibration scheme is employed, the (u, v) coverage will be much thinner. Some of the coverage can be made up by switching which antennas are in the target source subarray and which are in the calibrator source subarray. The easiest way to switch is to just switch subarrays. However, it is possible to obtain (u, v) coverage which approaches the 40 antenna coverage of Figure 1 by randomly switching antennas in each antenna pair.

[1] Full tracks are defined as observing while the maximum air mass is less than 1.4 times the transit air mass, or 9 hours at $\delta = 60°$, 7 hours at $\delta = 30°$, 6 hours at $\delta = 0°$, and 4.7 hours at $\delta = -30°$.

Array Used	Dynamic Range	Fidelity Index
40 unpaired elements	29000	121
40 paired elements	11800	112
20 element array	770	18
2 20 element subarrays switching every 5 min	1060	24

Table 7: Results of numerical simulations for a variety of arrays.

The antennas in a pair should switch about once every 20 seconds. The disadvantage to such a scheme is that it would complicate the online system and the data handling. So we show the worst case (u, v) coverage in which the two subarrays merely switch from target source to calibrator and vice versa in Figure 3.

4 Imaging Simulations

We now determine how much the image reconstruction is affected by the less complete (u, v) coverage obtained from the paired antenna calibration scheme. Consider four cases: a non-paired 40 element array, a paired antenna 40 element array, a 20 element array, and a paired 40 element array in which the 20 element subarrays take turns observing the target source, changing every 5 minutes. The arrays used in these four cases are closely related: the 20 element array is made up of one antenna from each pair of the paired 40 element array, and the unpaired 40 element array is made by moving one antenna in each pair to a more reasonable location. No errors, atmospheric or otherwise, have been introduced into the data: the questions which are asked are of the (u, v) coverage and how it limits the images. Full track simulated visibilities were calculated for a very complicated source (the M31 HII region used in all MMA imaging simulations) at $\delta = 30°$ every 5 minutes for 7 hours symmetric about transit. The resulting data were imaged and deconvolved using a maximum entropy deconvolution scheme (Cornwell, 1984), and the convolved, residuals added, maximum entropy images were gauged by dynamic range and fidelity index (Holdaway, 1990). The results are reported in Table 7. It is clear that an optimized 40 element array provides the best imaging. However, if the antennas in each pair are separated by $\sim$ 100 m, the 40 element paired array has imaging characteristics which are not that much worse than the unpaired 40 element array. If only 20 elements are used, the source is too complicated for the array, resulting in poor dynamic range and fidelity index. Switching between the target source array and the calibrator array increases both the dynamic range and the fidelity index by almost exactly $\sqrt{2}$. Higher dynamic range could be achieved for a simpler model brightness distribution.

A paired antenna array does not have very good imaging characteristics when performing paired antenna calibration. However, all bases seem to be covered. Assume the MMA is an a

paired antenna A array. If the atmospheric conditions are excellent, then no paired antenna calibration is required. If the atmosphere is not good and a bright source is being observed, (ie, a source which is bright enough to permit dynamic ranges exceeding 1000:1 if the image were noise limited), selfcalibration will be possible and paired antenna calibration does not need to be used. In this case, the simulation results for *40 paired elements* apply and dynamic ranges of 10000:1 (or greater for simple source structure) are possible. If a weak source is being observed (noise limited dynamic range is less than 1000:1) the images will either be limited by noise or by residual phase errors. Hence, poor (u, v) coverage will only be a factor for the very brightest, most complicated sources, such as Cygnus A. For this reason, it may be desirable to have both a paired 40 element array and a more optimized 40 element array with 20 stations in common. In other words, the cost for this calibration scheme is the cost of 20 extra stations in the A array.

5 Evaluation of Paired Antenna Calibration

Paired antenna calibration provides a substantial improvement over infrequent calibration, especially at low elevations.

Using half of the array to observe a calibrator and the other half of the array to observe the target source reduces the array's sensitivity by a factor of 2. This must be compared to a sensitivity reduction of $\sqrt{2} - \sqrt{3}$ for the position switching and beam switching calibration methods and no reduction at all for simultaneous calibration and the traditional infrequent calibration.

Some decrease in array usability results when the paired antennas are separated by $\sim$100 m rather than 10 m. However, the great improvement in (u, v) coverage and the improved image quality which results when using all 40 antennas in a paired antenna A configuration with 100 m spacings between paired antennas probably outweighs the small loss in observing time. Larger pair separations should also be explored in future configuration studies.

The limited (u, v) coverage obtained from the paired antenna calibration is not a problem for the weak sources which would require such a scheme. Stronger sources which might be limited in dynamic range due to the limited (u, v) coverage can use selfcalibration to correct for the atmospheric phases, and can therefore use all 40 elements for astronomical observing.

6 References

1. Cornwell, T.J., and Evans, K.F., 1985, Astron. Astrophys., 143, 77-83.
2. Cornwell, T.J., 1986, "Crystaline Antenna Arrays", MMA Memo 38.
3. Ge, Jinp Ping, 1992a, "Further Simulations of (Possible) MMA Configurations", MMA Memo 80.
4. Ge, Jinp Ping, 1992b, "Array Design Toolkit", *or something like that* MMA Memo *in preparation.*

5. Holdaway, M.A., 1990, "Imaging Characteristics of a Homogeneous Millimeter Array", MMA Memo 61.
6. Holdaway, M.A., 1991, "A Millimeter λ Phase Stability Analysis of the South Baldy and Springerville Sites", MMA Memo 68.
7. Holdaway, M.A., 1992a, "Possible Phase Calibration Schemes for the MMA", MMA Memo 84.
8. Holdaway, M.A., 1992b, "Timber Ridge A Configuration Out on a Limb", MMA Memo ??.
9. Schwab, F.R., 1992, "Lower Tropospheric Wind Speed Statistics...", MMA Memo 75.

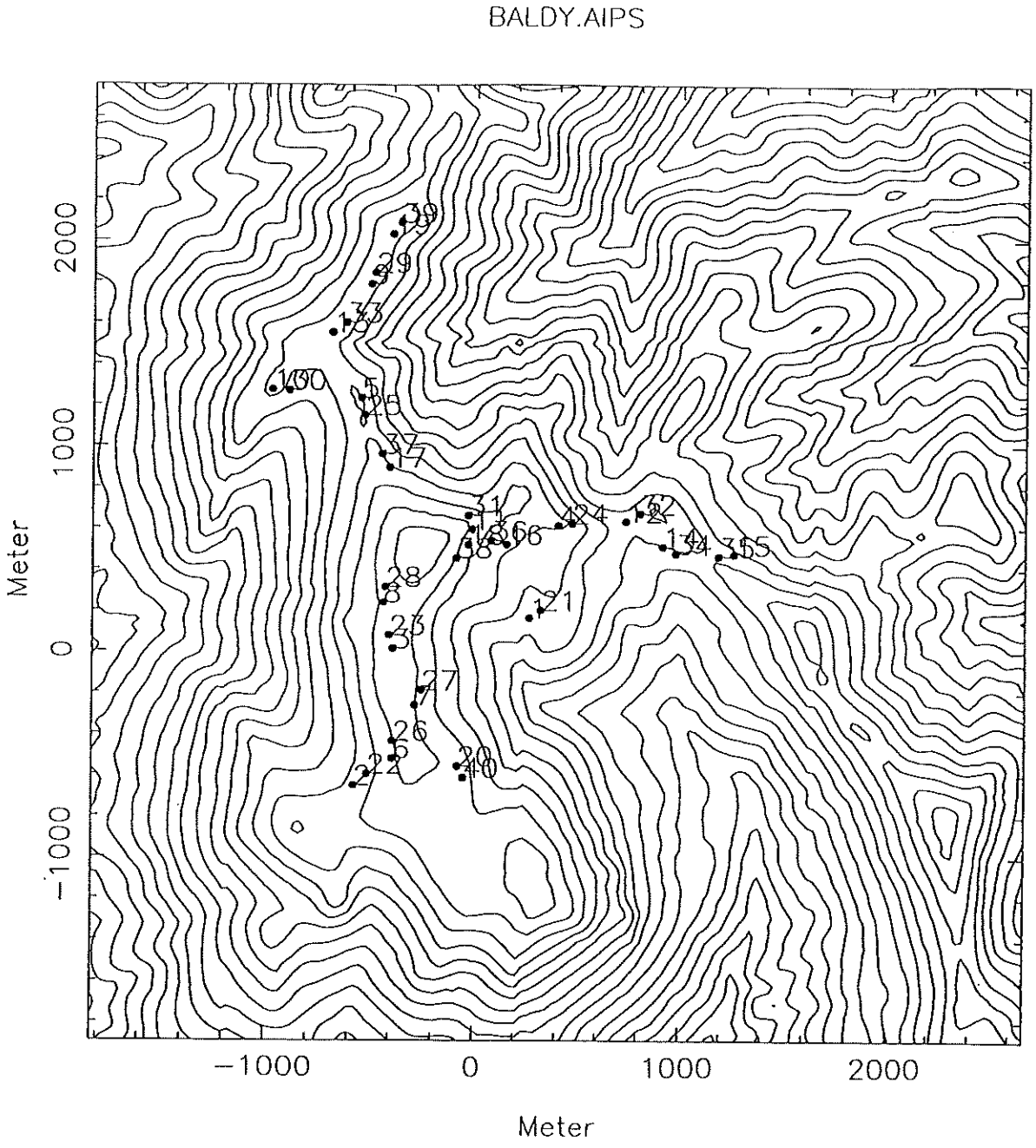

Figure 1: A possible design for an array of 40 paired antennas in the Magdalena Mountains.

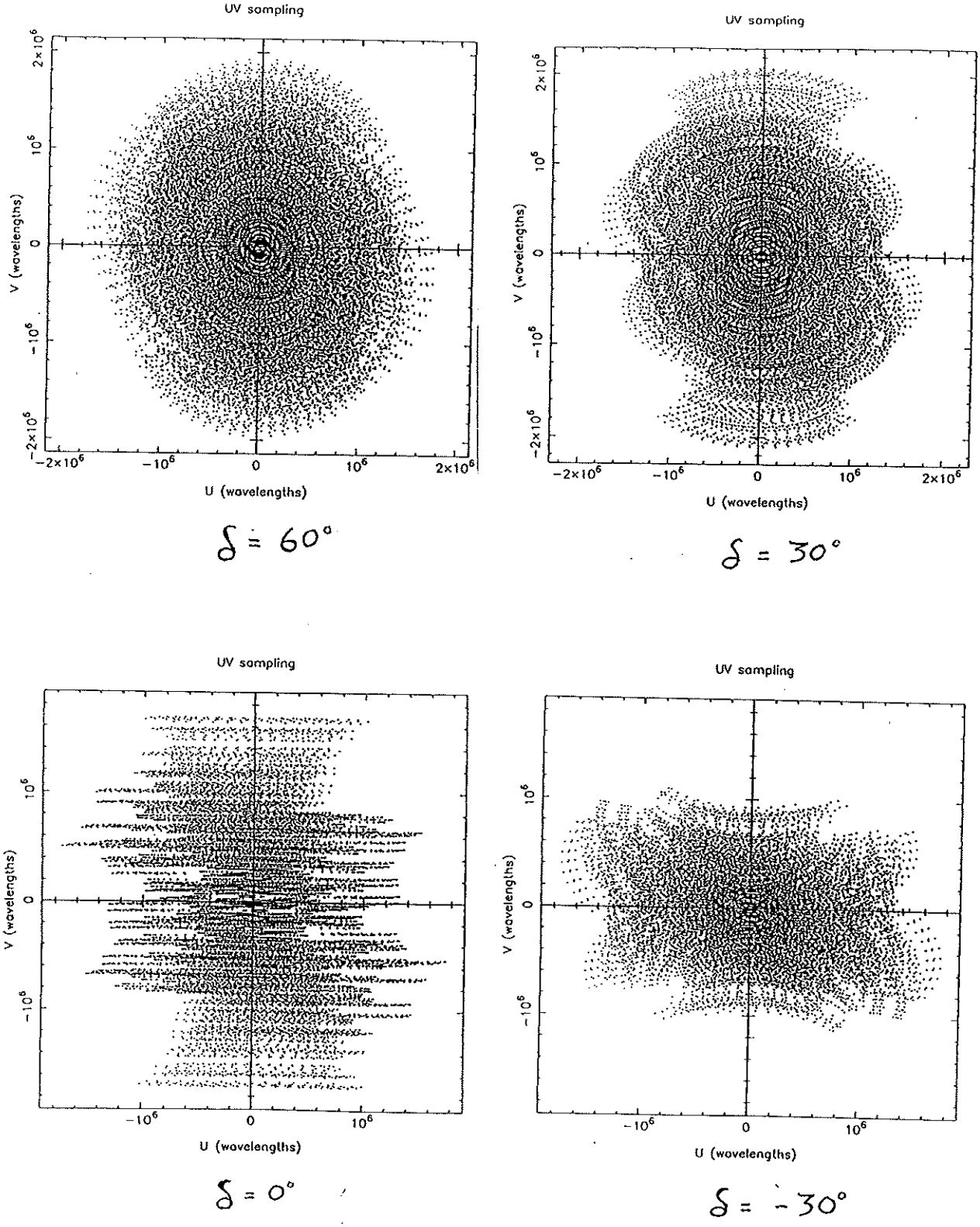

Figure 2: The full tracking (u, v) coverage for all antennas on source.

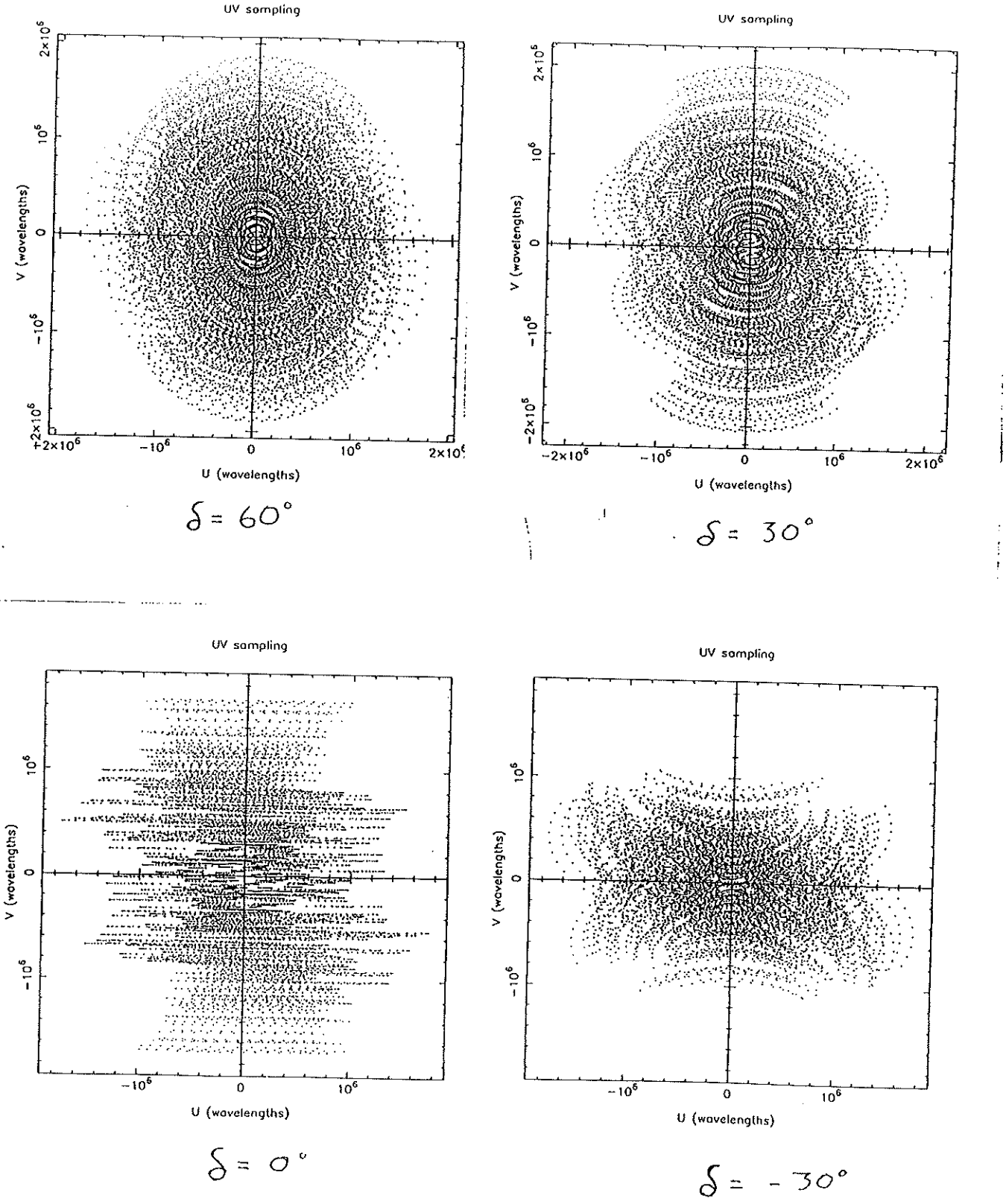

Figure 3: The full tracking (u, v) coverage for half of the antennas on the source and half tracking a calibrator, switching every 8 minutes.